David Grainger

Development of carbon membranes for hydrogen recovery

Thesis for the degree philosophiae doctor

Trondheim, September 2007

Norwegian University of Science and Technology
Faculty of Natural Sciences and Technology
Department of Chemical Engineering

NTNU

NTNU
Norwegian University of Science and Technology

Thesis for the degree philosophiae doctor

Faculty of Natural Sciences and Technology
Department of Chemical Engineering

ISBN 978-82-471-4297-4 (printed version)
ISBN 978-82-471-4302-5 (electronic version)
ISSN 1503-8181

Doctoral theses at NTNU, 2007:195

Printed by NTNU-trykk

Abstract

The recovery of hydrogen from gas mixtures with hydrocarbons may provide a commercial niche for carbon molecular sieve membranes (CMSMs). Previous work has shown that carbon membranes achieve excellent performance, with respect to hydrogen permeability and selectivity, in the separation of hydrogen from light hydrocarbons, such as CH_4, and CO_2. The intent of this work was to screen CMSMs derived from cellulose-hemicellulose for H_2 recovery and to generate performance data so that commercial application could be simulated. Three fields of application were evaluated: 1) the separation of hydrogen from a mixed H_2-natural gas network in a hydrogen-based society concept, 2) recovery from refinery waste gases and 3) capture of CO_2 in a precombustion coal-fired power plant. The key separation components were therefore H_2, CH_4 and/or CO_2, with nitrogen and C_2-C_4 hydrocarbons sometimes present as smaller fractions.

The precursor material was an 80% cellulose-20% hemicellulose mixture derived from spruce and pine pulp. The final carbonization temperature was varied between 375°C and 700°C and a separation performance maximum found at about 650°C. Membranes carbonized at the low end had not yet developed sufficient porosity, whereas those carbonized at 700°C had experienced extensive pore closure. Copper (II) nitrate and silver nitrate were also added to the precursor in the range of 0-6 wt%. Copper (II) nitrate decomposed to copper oxide during pyrolysis and silver nitrate to silver, the latter often forming a layer on the membrane surface. SEM analysis showed dispersed clusters of the additive in the carbon film. Increasing the additive loading tended to decrease the permeability of H_2, CO_2 and CH_4 but increased the selectivity of the H_2/CH_4 separation. H_2/CO_2 selectivity was best with about 4% copper nitrate loading. There was no significant advantage in doping the membrane with the more expensive silver nitrate compared with the copper nitrate.

The carbonization environment strongly affected separation properties. Deep vacuum (0.02-0.05 mbar) produced tight membranes with low hydrogen permeability and the highest H_2/CO_2 selectivity (>20 at 25°C). These membranes performed better than the productivity-selectivity trade-off for polymeric membranes. A higher carbonization pressure (0.34-0.41 mbar), which implies a higher oxygen partial pressure and more oxidation, led to more open, productive membranes that are better suited to H_2/CH_4 separation. All membranes prepared in this work exceeded the performance of polymers for this pair, with single gas H_2 permeabilities at 25°C of up to ~1400 Barrer and selectivities of 1200 observed for new membranes. Carbon membranes were also prepared under an argon gas flow (a more practical method for mass production) and found to have similar performance to those prepared at the higher pressure under vacuum. After carbonization temperature, the most important factor determining performance was the length of exposure of the material to air. Aging due to chemi- and physisorption decreased membrane productivity by as much as 80% over 14 months, although the deterioration slowed over this time.

The effect of operating conditions was also studied. Increasing the operating temperature produced an exponential increase in productivity for all gases, but decreased the hydrogen selectivity. Feed pressure had little effect on separation below 6 bar, which was the equipment limit. The permeability of hydrogen was hindered by competitive adsorption by heavier gases, but short term testing showed the productivity to be reasonable and stable, even in the presence of propane and butane.

The operating data for the simulation of applications was taken from the performance of a carbon membrane prepared by doping the cellulose-hemicellulose precursor with 4wt% copper (II) nitrate and carbonizing it at 650°C. This data was for the 'aged' membrane, which still achieved excellent performance in mixed gas tests – approximately 500 Barrer and H_2/CH_4 and H_2/CO_2 selectivities of 1000 and 19, respectively, at 25°C.

The cost and energy consumption of H_2 recovery from hydrocarbon streams varied considerably with the hydrogen partial pressure in the feed, degree of recovery and assumed membrane module cost ($50-500/m^2). Ninety percent of the hydrogen could be recovered with >95 mol% purity from a stream containing as little as 5 mol% H_2, in a single stage. Compared with a commercial polyimide membrane, the carbon molecular sieve produced purer hydrogen from leaner streams with lower energy consumption. The operating cost, which included a 15% capital charge, was similar to or lower than that of the polyimide membrane.

The separation of hydrogen from carbon dioxide and nitrogen, the main components in an IGCC precombustion stream, was simulated and compared with the performance of a CO_2-selective facilitated-transport membrane. The CO_2 compression duty in the CMSM process is higher because the nitrogen that is retained with the CO_2 must be compressed too. The CO_2 pipeline size increases because more gas must be transported. The second challenge is that the hydrogen must be recompressed as well, to turbine pressure. This is a particular issue because the H_2/CO_2 permselectivity ratio at the operating temperature of 90°C is only about 13 and so the permeate pressure was less than 3 bar to achieve good separation.

Foreword and acknowledgements

This is a well-travelled thesis. It was begun in the cold, dark, snowy winter of middle Norway and was finished in the perpetual daylight of the Norwegian summer. In between, it was assembled in Trondheim, on planes and airports between Europe and South Africa, paragraphs were scribbled in the air above Durban and graphs constructed over cappuccinos in cafes in Cape Town. For me, it is as much a reminder of places as of work done.

I wish to thank Prof. May-Britt Hägg for her invaluable guidance and for creating the opportunity for me to work on a fascinating project. The atmosphere in our group is creative and relaxed thanks to her and I will miss waltzing into her office to dump the next lot of proof-reading on her desk. The members of our membrane group – Arne, Jon, Taek-Joong, Tone, Marius, Lily, Lei and Edel – provided a friendly and supportive environment and I particularly want to thank Jon Arvid Lie and Arne Lindbråthen for their help over the years and for proof-reading this thesis. Jon is the pioneer of carbon molecular sieves in our group and my work is built on his; I won't throw out the tired 'shoulder of giants' cliché here, but I certainly will say that he provided me with solid and fertile ground to till. I wish to thank Taek-Joong Kim for finding time in his busy schedule to provide data for the simulations of the FSC membrane in CO_2 capture, and for introducing me to kimchi!

My parents, Colin and Linda, should know that I appreciate their love and support immensely; they have always been positive about my life decisions, even when they take me so far away from them. My fiancée Anette deserves mountains of gratitude for her uncomplaining support over the last four years, especially the last 6 months during which I have been more of a part-time lodger than a contributing partner. I owe you plenty of dinners!

I am also grateful to the Gas Technology Centre for funding my project. I hope that this work is interesting and useful.

Trondheim, July 2007
David Grainger

Table of Contents

Nomenclature

Symbol	Explanation	Unit/value
Latin characters		
A	area	m^2
b	2nd coefficient in van der Waal's EOS	mol m^{-3}
C	concentration	mol m^{-3}
D	diffusivity	m^2 s^{-1}
d	diameter	m
E	Activation energy	kJ mol^{-1}
f	fugacity	bar or kPa
h	Planck's constant	6.63×10^{-34} J s
i	specie	
J	flux	mol m^{-2} s^{-1} or m^3(STP) m^{-2} s^{-1}
k	constant	
l	membrane thickness	m
M	molar mass	g mol^{-1}
N	moles	mol
N	number	-
p	pressure	bar or kPa
p	probability	-
P	permeability	Barrer or m^3(STP) m m^{-2} bar^{-1} h^{-1}
Q	volumetric flowrate	m^3 h^{-1}
R	universal gas constant	8.314 J mol^{-1} K^{-1}
S	solubility	mol m^{-3} bar^{-1} or m^3(STP) m^{-3} bar^{-1}
S	activation entropy	J mol^{-1} K^{-1}
T	temperature	°C or K
t	time	h, day, s
V	volume	m^3
W	work	J mol^{-1} (in compression context)
x	distance in the x direction	m
y	mole fraction	-
Z	compressibility factor	-
Greek characters		
ϕ	fugacity coeffient	-
γ	specific heat ratio	-
α	(perm)selectivity	-
Δ	delta (finite difference)	
λ	mean free path	m

Subscripts

0	usually denotes pre-exponential constant
A, B	species A, B
Kn	Knudsen
p	pore

Abbreviations

AgN	silver nitrate
CMS	carbon molecular sieve
CMSM	carbon molecular sieve membrane
CuN	copper (II) nitrate
DP	degree of polymerisation
HC	cellulose/hemicellulose precursor
HZS	Carbolite furnace with quartz furnace tube
MG	mixed gas
PSD	pore size distribution
PSA	pressure swing adsorption
SD	standard deviation
SG	single gas
SEM	scanning electron microscopy
TGA	thermogravimetric analysis
TZF	Carbolite furnace with ceramic furnace tube

Conversions

From	To	Conversion factor
Barrer	cm^3(STP) cm cm^{-2} s^{-1} $cmHg^{-1}$	1×10^{-10}
	m^3(STP) m m^{-2} bar^{-1} h^{-1}	2.736×10^{-9}
	mol m m^{-2} bar^{-1} h^{-1}	1.217×10^{-7}
m^3(STP) m^{-2} bar^{-1} h^{-1}	mol m^{-2} kPa^{-1} h^{-1}	4.45×10^{-1}
	mol m^{-2} bar^{-1} h^{-1}	44.50
cm^3(STP) cm^{-2} s^{-1} $cmHg^{-1}$	mol m^{-2} kPa^{-1} h^{-1}	1.217×10^{3}

1 Layout of the thesis and unit conventions

The intent of this thesis is to present a continuum from the theory of carbon molecular membrane sieves through development and testing to simulated application. After a brief introduction, there follow two parts; Part I documents the theoretical and experimental work and Part II presents the results of process design and evaluation.

The units used to describe gas *permeability* (the transport coefficient) in membranes can be a controversial subject, with some preferring SI units to the traditional units. However, Barrer, which is traditional, is convenient because the range of permeability in carbon membranes is usually between 1 and 2000 Barrer. This is compared to 2.735×10^{-14} to 5.472×10^{-11} $m^3(STP)\cdot m/m^2\cdot Pa\cdot h$ for the same range in SI units or even 2.735×10^{-9} to 5.472×10^{-6} $m^3(STP)\cdot m/m^2\cdot bar\cdot h$ for the more common metric units. Furthermore, Barrer is in common use in the literature, including by the Editor-in-chief of the Journal of Membrane Science, WJ Koros, and so it is easier to compare experimental data by reporting in Barrer. The situation is different in Part II. Here, the inputs to the simulation software are *permeances* (permeability normalised by thickness) and it was more convenient to report them with the units $mol/m^2\cdot kPa.h$ or $m^3(STP)/m^2\cdot bar\cdot h$. Conversions are provided where clarity is required.

2 Introduction and motivation

There is no more important element than hydrogen. It constitutes about 75% of the elemental mass of the universe[1], and two of the three elements in water, which makes up roughly 70% of our bodies, are hydrogen. Most hydrogen is found in stars, in the plasma state, powering the thermonuclear reactions that give rise to other elements, the planets and everything else in the cosmos, including us.

It is the lightest element, with an atomic mass of 1.00794 g/mol, and in the standard state it is a colourless, odourless, tasteless, highly flammable diatomic gas. Because it reacts easily with other substances, the pure form is only found in traces in our atmosphere (Air Liquide Gas Encyclopaedia, 2007) and so we must synthesize it from hydrocarbons or water. Some of the physical properties of hydrogen are given in Table 2-1.

Table 2-1. The physical properties of diatomic hydrogen (Perry and Green, 1984)

Molar mass, g/mol	2.016
Triple point, K	13.95
Boiling point (1 bar), K	20.3
Gas density (1 atm, 0°C), kg/m^3	0.0898

The world produces approximately 50 million tons of hydrogen per year; 48% from natural gas reforming, 30% from oil, 18% from coal and 4% from water (National Hydrogen Association, 2007). The USA uses about 10 million tons of hydrogen per year for industrial purposes, 95% of it from natural gas reforming (Wise, 2006). Pure hydrogen has many industrial uses, including the formation of plastics, polyester and nylon, as a blanketing gas in the glass industry, the treatment of various metals, the desulphurization, hydrotreating and hydrocracking of hydrocarbon fuels, in the propulsion of rockets and as a fuel for fuel cells (Air Liquide Gas Encyclopaedia, 2007). Hydrogen is also used to produce ammonia for fertilizer, amongst other products.

Further investment in hydrogen technologies is particularly important to mankind for two reasons. The first, which invokes either approval or cynicism, depending on the audience, is the replacement of carbon-based energy carriers with hydrogen. One argument is that the demand for fossil fuels is outstripping the supply. The course that the oil price has taken over the last four years certainly supports this. Furthermore, geopolitical events have caused governments to consider alternative sources of energy, usually renewable, to wean their oil-hungry economies off the dependency on supply from the Middle East and Russia. The United States imported 56% of its oil in 2000 (a quarter of that from the Middle East) and Europe 60% (half of that from the Middle East) (Sanborn Scott, 2005). The danger is *not*, however, the impending depletion of fossil resources. The ratio of the conventional oil reserves added each year by discovery to the ratio of consumption has remained approximately the same since 1900. The estimated depletion time for the known reserves is about 40 years at the current rate of consumption; but it was the same value in 1900. Added to this is the vast reserve of non-conventional oil, such as oil sands, and coal. In the words of Cesare Marchetti in 1979, "'Running out' has the advantage of being easy to understand, but the disadvantage of being wrong".

[1] NASA: http://imagine.gsfc.nasa.gov/docs/ask_astro/answers/971113i.html

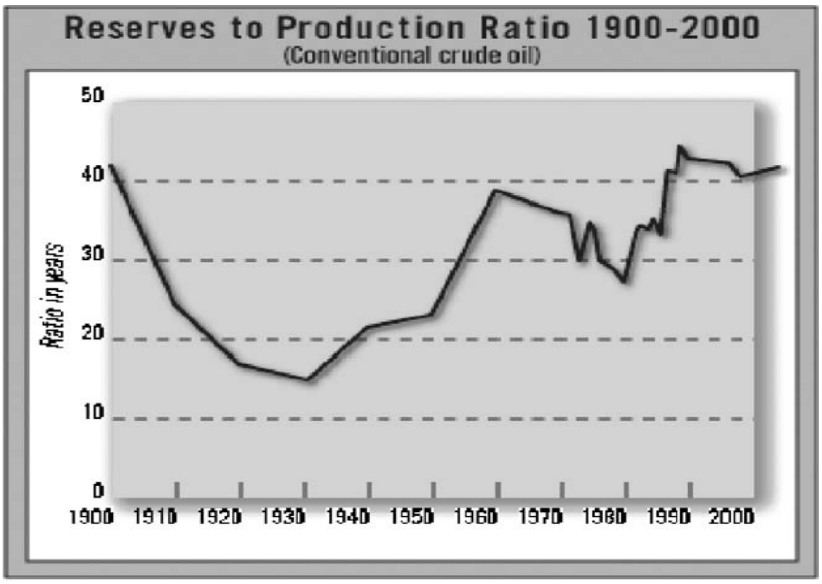

Figure 2-1A century of monitoring the ratio of reserves to production (Sanborn Scott, 2005)

The more important reason for developing hydrogen technologies is the threat of global warming; the result of fossil-fuelled power stations, cars, industry and countless other consumers spewing carbon dioxide and other greenhouse gases into the atmosphere. The exact effect of these gases and the predictions for the temperature increase are debated, but the trend in the scientific and political community is to accept that there is a problem. It was calculated in 1997 that if there were no further discoveries of fossil fuels and no further technological improvements and all the known fossil reserves were burned, that the CO_2 content in the atmosphere would rise to 700 ppmv (Sanborn Scott, 2005). The highest maximum CO_2 level over the last 300 000 years was 310 ppmv, until we entered the industrial age. It now stands at 380 ppmv. Considering that the CO_2 levels are closely tracked by global temperature, the combustion of all of the known reserves without CO_2 mitigation could cause a disaster.

One solution, possibly in the medium term, is to capture CO_2 at source and store it, a scenario that requires the conversion of the energy carrier from fossil fuel to another form that will not emit CO_2 at the end-use site, such as electricity or hydrogen. The only long-term alternatives to CO_2 mitigation are alternative energy sources. The problem with most of the candidates – nuclear, wind, solar, geothermal, current and wave action – is that they do not produce an easily transportable form of energy. A hydrogen energy system may be able to resolve this problem (Veziroglu, 2007). Although it must be acknowledged that there are serious challenges with storing hydrogen in a compact form, hydrogen can be the link between all energy sources and sinks. There are certainly signs that the hydrogen economy is being viewed seriously. For example, major car manufacturers are investing in fuel-celled vehicle development and it is estimated that there will be 15 million hydrogen-fuelled cars in 2020 and 50 million in 2030. The hydrogen field provides fertile ground for research and technology development, including the distribution of hydrogen on a massive scale. This challenge is one of the technologies explored in this thesis, through the application of carbon membranes to recover hydrogen that has 'hitched a ride' in a natural gas network, in the NaturalHy project.

Those who remain unconvinced by the arguments for fossil-fuel replacement would not dispute the second reason for investment in hydrogen-related technologies. That is the management of hydrogen resources within refineries. The demand for hydrogen is increasing

due to stricter product specifications and a decline in the quality of crude available for processing (Pacalowska et al, 1996). These increase the need for hydro-processing and hydrotreating. Where hydrogen may previously have been in excess in a refinery, it is now imported or produced separately onsite. The concept of hydrogen pinch analysis, similar to energy pinch analysis, is often applied and has resulted in significant savings for refineries (Hallale et al, 2002). Many of the off-gas streams in a plant containing hydrogen are commercially attractive as hydrogen sources. Hence, there exists an opportunity for technologies that can upgrade that hydrogen.

2.1 Carbon molecular sieve membranes (CMSMs)

The subject of this doctoral work is the use of CMSMs to separate hydrogen from other gases. Carbon molecular sieve membranes are thin carbon barriers, usually in the shape of a film or hollow fibre, that are capable of selectively transporting certain gases. The mechanisms are explained in the body of the thesis and will not be dealt with in detail here, suffice to say that the carbon material can discriminate between gases based on their size and shape. They are able to transport hydrogen, the smallest molecule after helium, through their ultra-micropores with a high degree of productivity and selectivity.

2.2 Applications

Three important applications are considered in this thesis: 1) the recovery of hydrogen from refinery off-gases, 2) the recovery of hydrogen from a syngas stream that has been CO-shifted and 3) the recovery of hydrogen from a hypothetical mixed natural gas-hydrogen distribution network. These applications are discussed in detail in Part II of the thesis and this section is only intended to be an introduction that places the experimental work in context for the reader.

1. Recovery from a mixed natural-gas hydrogen network

This hypothetical case is in fact the basis of a 6th EU Framework programme, of which the NTNU is a participant. The concept involves the injection of hydrogen from a large-scale producer into a natural gas network, with the aim of utilising existing networks in the transition to a hydrogen economy. The project, NaturalHy, consists of 39 European partners and aims to test all critical components in a mixed network by adding hydrogen to existing natural gas networks. This consortium includes network operators, hydrogen producers, specialist practitioners and academic researchers. The effect of hydrogen on technical components of the pipeline, reliability, safety and pipeline integrity as well as the possibility to separate out hydrogen for the end user are being tested.

Critical to the success of the project is the feasible separation of the hydrogen for end-use components requiring relatively pure hydrogen, such as fuel cells.

2. Hydrogen from refinery off-gases

Refineries contain off-gas streams that have hydrogen contents of 10-90%, depending on the source unit operation. Typical impurities include methane, nitrogen, carbon dioxide and higher hydrocarbons. Considering the moderate pressures these streams are available at, there exists a potential niche for carbon molecular sieve membranes to recover the hydrogen.

Commercial polymer membranes exist for the purpose already, but these are generally limited in their performance, for reasons that will be discussed in more detail later.

3. Hydrogen from a CO-shifted syngas stream

Integrated gasification combined cycle power plants have been identified as, potentially, the most efficient and environmentally-friendly form of coal-to-power conversion. Furthermore, they produce syngas (CO and H_2) as an intermediate product, which can be CO shifted with steam to produce a mixture rich in CO_2 and H_2.

A typical CO-shifted syngas would contain approximately 50 mol% H_2, 39 mol% CO_2, 10 mol% N_2, 1% mol CO and traces of carbon disulphide and hydrogen sulphide. The pressure of the feed gas depends on the gasifier pressure and can vary from 20 to 60 bar (abs). The temperature of a gas stream exiting CO-shift is usually from 500°C to 200°C (if a low-temperature shift step is present). These conditions provide a potential application for hydrogen-separating carbon molecular sieves.

The results of this application are also relevant for a closely related process – natural gas combined cycles, in which natural gas can be reformed and CO shifted to produce a similar feed for a membrane. Finally, any future reforming/gasification processes with the sole purpose of producing hydrogen would also provide applications for the results in this work.

PART I Development of hydrogen-selective carbon membranes

3 Membrane gas separation

Membranes are used to separate solids from liquids (filtration), liquids from dissolved salts (reverse osmosis), gases from liquids (pervaporation) and gases from gases (Mulder, 1997). This thesis deals with the latter and the equations developed in the next section are for gas transport.

3.1 Principles of membrane separation

Membranes are defined by Mulder (1997, pg. 7) as a permselective barrier or interface between two phases. A simple representation of a membrane is shown in Figure 3-1.

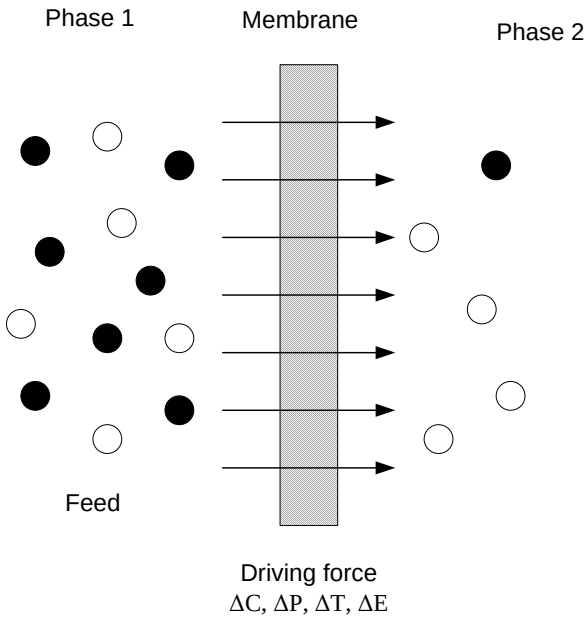

Figure 3-1 Basic representation of a membrane process (adapted from Mulder, 1997)

The driving force for transport of a species is the potential difference across the membrane, and may be in the form of a pressure (or more correctly, fugacity) difference, concentration difference, temperature difference or an electrical field. In gas separations, the driving force is usually the component fugacity difference or partial pressure difference if the gases behave ideally.

An equation describing steady state diffusion was presented in 1855 by Fick and is the basis for the flux equations commonly used in the membrane field:

$$J_i = -D_i \frac{dC_i}{dx} \qquad (1)$$

The assumption here is that a concentration gradient is the driving force across the membrane.

J is the flux (volume, mass or mole flow per unit area), *D* is the diffusivity constant of specie *i* in a medium, *C* is the concentration of the specie and x is the distance over which diffusion is considered. If the concentration of a gas species at the membrane-gas interface is in equilibrium with the partial pressure of the gas, then Equation (1) can also be expressed in terms of gas partial pressures:

$$J_i = -D_i \frac{dC_i}{dp_i} \cdot \frac{dp_i}{dx} \qquad (2)$$

The permeability, *P* (m^3(STP)·m/m^2·bar·h), of a gas is then defined as:

$$P_i = -D_i \frac{dC_i}{dp_i} \qquad (3)$$

If Henry's law applies, $C_i = S_i.p_i$, where *S* is the solubility coefficient; $dC_i/dp_i = S_i$ and hence

$$P_i = D_i \cdot S_i \qquad (4)$$

Often, in engineering applications, flux is presented in the volumetric form:

$$J_i = \frac{dQ_i}{dA} \qquad (5)$$

If the concentration gradient is assumed to be linear, then Eq. (1) can be rearranged and integrated over the membrane thickness, *l*, to yield

$$dQ_i = dA \frac{D_i}{l}(C_{i,f} - C_{i,p}) \qquad (6)$$

where dQ_i (m^3/h) is the incremental volumetric flow rate of component *i* through the membrane in an area increment, *l* (m) is the thickness of the membrane, *dA* (m^2) is an area increment and subscripts *f* and *p* refer to the feed and permeate sides, respectively. Eq. (6) can be rewritten as

$$dQ_i = dA \frac{P_i}{l}(p_{i,f} - p_{i,p}) \qquad (7)$$

Here *P* (m^3(STP)·m/m^2·bar·h) is the permeability of component *i* in the membrane, *p* is the partial pressure of *i*, and subscripts *f* and *p* refer to the feed and permeate sides, respectively. Gas separation is often performed with high pressure on the feed side, making the assumption that the gas behaves as an ideal gas invalid. In that case, the fugacities should be used (Mulder, 1997):

$$dQ_i = dA \frac{P_i}{l}(\phi_{i,f}.p_{i,f} - \phi_{i,p}.p_{i,p}) \qquad (8)$$

where ϕ is the fugacity coefficient of i. ϕ is defined as the ratio of the fugacity and the pressure of the gas, f_i/p_i.

Alternatively, the transport of gas i can be described in terms of moles (F_i) transferred per hour:

$$dF_i = dA\frac{P_i}{l}(p_{i,f} - p_{i,p}) \qquad (9)$$

Here, the permeability, P_i, has the units mol.m/m^2.bar.h. The ratio of two gases permeability coefficients is termed the permselectivity (often shortened to selectivity), which is a measure of the membranes effectiveness in separating species:

$$\alpha = \frac{P_i}{P_j} \qquad (10)$$

Figure 3-2 shows a representation of a membrane module, with the separation of H_2 from CH_4 as an illustration.

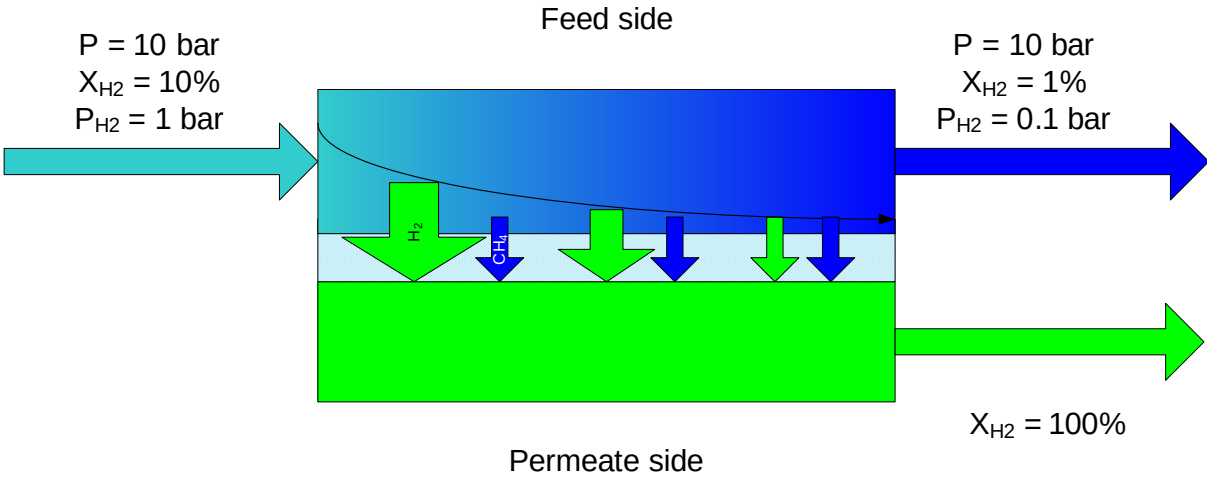

Figure 3-2 Representation of a membrane module

In this example, the continuous feed contains 10 mol% hydrogen and 90 mol% methane and is at a pressure of 10 bar, meaning that the partial pressure of hydrogen in the feed is 1 bar. The membrane in this example is only permeable to hydrogen and as the gas permeates through the membrane to the permeate side, so the fraction and partial pressure of hydrogen decreases. If 90% of the hydrogen is separated, its partial pressure will be 0.1 bar in the retentate stream that leaves the module. Since the membrane is only permeable to hydrogen, the permeate stream is pure hydrogen. As the driving force is ($p_{H2,f}$ - $p_{H2,p}$), the total pressure on the permeate side must be less than or equal to 0.1 bar for transport to occur along the entire length of the membrane.

As the fraction of hydrogen recovered increases and the partial pressure of the hydrogen decreases, so the driving force decreases and dQ_{H2}/dA decreases. Thus, recovery of the target gas is not directly proportional to the required membrane area.

In reality, most membranes are not perfectly selective and all gases will pass through the membrane to some degree. Thus, methane would also permeate at a low rate and would dilute the hydrogen on the permeate side, allowing for the total permeate pressure to be correspondingly higher. However, as the partial pressure and transport of the hydrogen decreases, so the relative rate of transport of methane increases and the purity of hydrogen in the permeate decreases. Higher recoveries, therefore, tend to result in lower product purity.

The ratio of feed to permeate pressure is also an important parameter. As shown in Figure 3-3, the purity of the component with the highest permeability increases as this ratio increases.

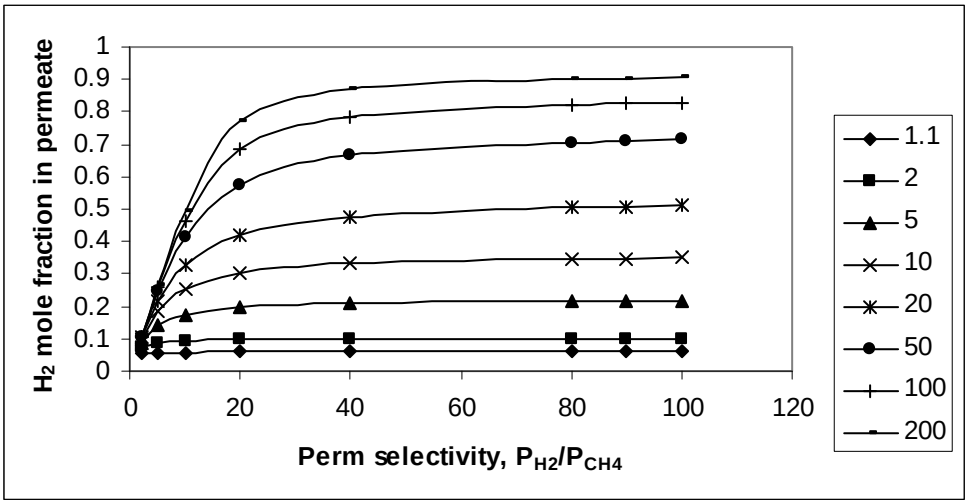

Figure 3-3 The effect of permselectivity on hydrogen fraction in the permeate, with feed to pressure ratio as a parameter. Results are shown for a cross-flow membrane, 10% H_2 in the feed and achieving 75% recovery

3.1.1 Real gas behaviour

The fugacity coefficient, *N*, of a gas is a function of the state and can be calculated from

$$\ln\phi = \int_0^p (Z-1)\frac{dp}{p} \text{ (constant T, y)} \qquad (11)$$

where Z is the compressibility factor of a gas and y is the mole fraction (Smith and Van Ness, 1987). According to San Marchi et al. (2007), who studied the permeability of hydrogen in stainless steels, the Abel-Noble equation of state (EOS),

$$V_m = \frac{RT}{P} + b \qquad (12)$$

represents the real gas behaviour of hydrogen well in the range 1-2000 bar and 223-1000 K. In Equation (12), V_m is the molar volume and *b* is the second coefficient in van der Waals

equation of state, which is only a weak function of pressure and temperature in the above range. San Marchi et al. fitted Equation (12) to hydrogen data over this range and calculated that b = 15.84 cm^3/mol. From Eq. (12) we get

$$Z = 1 + \frac{bP}{RT} \tag{13}$$

and hence Eq. (11) can be rewritten as

$$\ln\phi = \int_0^p \left(1 + \frac{bp}{RT} - 1\right)\frac{dp}{p} = \frac{bp}{RT} \tag{14}$$

Thus, for the engineering conditions relevant to this thesis, the fugacity of hydrogen is well represented by Eq. (15).

$$f = p\exp\left(\frac{bp}{RT}\right) \tag{15}$$

The fugacity of a gas in a mixture is also a function of the composition. However, if hydrogen is present in an ideal mixture, then the partial fugacity can be written as

$$f_{H_2} = y_{H_2} f^*_{H_2} \tag{16}$$

where f^*_{H2} is the fugacity of hydrogen at the total system pressure (San Marchi et al. 2007). The positive value of *b* means that the fugacity coefficient of hydrogen is always ≥ 1. A plot of Eq. (14) is shown graphically in Figure 3-4.

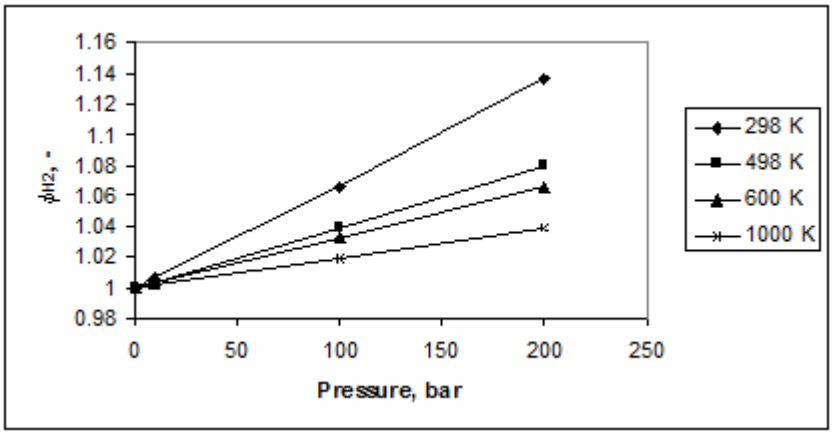

Figure 3-4. Hydrogen fugacity as a function of pressure and temperature

Inspection of the virial coefficient, *b*, for CO_2, CH_4, C_2H_6, C_3H_8 and C_4H_{10}, which are relevant to the separations in this thesis, reveals that *b* is negative up to at least 200°C (CRC Handbook of Chemistry and Physics, 87th Ed., 2006-2007). Thus, the fugacity coefficient of all of these gases should *decrease* with increasing pressure, if the Abel-Noble EOS is assumed to approximate their behaviour. The reader is reminded that the driving force is the difference in fugacities (or partial pressures as a simplification), as described by Eq. (8). The implication,

therefore, is that the driving force for hydrogen separation benefits from real gas behaviour with increasing pressure, whereas the driving force is disadvantaged for CO_2 and hydrocarbons. This would also lead to an apparent increase in *selectivity* as pressure increases, if other material-gas interactions are absent. The coefficient *b* for N_2 is slightly positive above 27°C, but still less than that of H_2 up to 200°C

Thus, membrane models for hydrogen separation that use partial pressure in the calculations may be conservative models that underestimate the purity of the hydrogen product and may slightly overestimate the required membrane area. They would be conservative models compared to those incorporating real gas behaviour.

3.2 Membranes relevant for hydrogen separation

Many materials possess the capability to separate hydrogen from other gases, most of them by the permeation rather than retention of hydrogen. Briefly, these include:

Polymeric membranes

These are the most prevalent membranes in commercial operation (Koros and Mahajan, 2000) and are the most practical and economical to manufacture on a large scale, usually as spiral wound units or hollow asymmetric fibre bundles. Their earliest large scale use, in desalination, arrived after Loeb and Sourirajan (1963) developed the phase inversion technique for forming membranes. This produces anisotropic membranes with an extremely thin selective layer.

Polymeric membranes rely on a sorption-diffusion mechanism for permeation. They are usually made from glassy polymers (such as cellulose acetate and polysulfone), which derive their selectivity by discriminating between penetrants with subtle differences in size. Polymeric membranes are used in the industry to recover hydrogen from hydrocarbon streams, such as refinery off-gases. Examples are Membrane Technology and Research's (USA) hydrogen-permeable membranes which are claimed to recover 90% of the hydrogen at 90-99% purity and Air Product's PRISM® membranes[2].

The problems faced by polymeric membranes include the loss of performance at high temperatures, high pressures and in the presence of highly sorbing (plasticising) components (Koros and Mahajan, 2000). PRISM® membranes, for example, can only operate up to 110°C. High temperatures and plasticising components cause glassy polymers to become rubbery and lose their selectivity. High pressures can cause compaction of the polymer, which reduces permeability, or even the collapse of hollow fibres. Polymer membranes also appear bound to an upper limit in the trade-off between permeability and selectivity (Robeson, 1991), meaning that high purity hydrogen and high recovery cannot always be achieved by polymers. Their current use is mostly for moderate-to-high feed concentrations of hydrogen.

Palladium-based membranes

Palladium-based membranes are highly selective towards hydrogen, because they involve the dissociation of hydrogen on the palladium and diffusion of the proton through the metal as the transport mechanism. Very high hydrogen fluxes of 4.10^{-7} to $1.97.10^{-5}$ mol/m^2.s.Pa (3.2-160 m^3(STP)/m^2.bar.h) have been reported (Bredesen et al, 2004). However, palladium-based

[2] http://www.airproducts.com/Products/Equipment/PRISMMembranes/page08.htm. Last consulted 05.09.2007

membranes must overcome significant challenges before they can be commercially viable on a large scale. The high price of Pd requires that membranes are composed of very thin (1-5 micron) Pd layers that are defect-free, suitable supports are still needed and the membranes are susceptible to poisoning by S- and Cl- containing species, CO, water vapour and strongly-adsorbing hydrocarbons. Furthermore, Pd must be operated at high temperature (300-600°C) to function, incurring an energy and capital penalty unless the feed gas is already at this temperature or the membrane is applied as a high temperature membrane reactor.

Inorganic membranes

Other inorganic membranes such as carbon, glass (Vycor) and silica membranes rely on a molecular sieving effect in small pores (3-4 Å) to separate gases. Amorphous silica membranes have achieved reasonable combinations of permeability and selectivity (Bredesen et al., 2004), but are challenged by sintering at high temperature in the presence of water vapour and are difficult to produce without defects (which reduce separation ability). Vycor membranes have relatively low hydrogen fluxes (10^{-8} mol/m^2.Pa.s, Bredesen et al., 2004). Zeolite membrane show only moderate hydrogen selectivity due to pinholes and voids between zeolite crystals and most zeolite research focuses on the separation of other gases.

Carbon membranes are the subject of this thesis and are introduced in the next section.

4 Carbon membranes – background and theory

Carbon molecular sieve membranes (CMSMs) are prepared by the thermal decomposition, in a controlled chemical environment, of organic compounds that do not melt or soften during carbonization (Koresh and Soffer, 1987). Precursors include thermosetting resin, graphite, coal, pitch and plants and synthetic polymers (Saufi and Ismail, 2004). Synthetic polymers include polyimide and derivatives, polyacrylonitrile, phenolic resin, polyfurfuryl alcohol, polyvinylidene chloride – acrylate terpolymer and phenol formaldehyde. The subject of this thesis is the preparation of CMSMs from cellulose, which is a relatively cheap and abundant raw material, for hydrogen separation. Carbon membranes derived from cellulose have been investigated at the Norwegian University of Science and Technology for some time, primarily for use in CO_2 removal from biogas (Lie, 2005; Lie and Hägg, 2005; Lie and Hägg, 2006).

The structure of CMSMs consists of graphitic layers interspersed with amorphous regions. These regions contain nanopores, on the order of 3-10 Å, which offer a transport route to gases via pore networks. The gases may diffuse through the pores, or they may adsorb on the walls and travel through the pores by a mechanism known as surface flow (Koresh and Soffer, 1987). The networks appear to consist of relatively wide pores that are interrupted by narrow constrictions. The size of the pore constrictions influences the ability of the molecules to pass through the material; small or linear molecules diffuse more easily than relatively larger, bulkier molecules. This is the principle behind molecular sieving, which allows hydrogen to permeate through the carbon membrane while larger molecules such as methane, nitrogen and higher hydrocarbons are largely retained. Larger, more strongly adsorbed molecules may also block the pores for smaller molecules in a phenomenon known as competitive adsorption or selective surface flow. This results in reverse selectivity; the smaller components are retained.

Koresh and Soffer (1987) neatly summarised the benefits of CMSMs compared with polymeric membranes:

- Because they have a different permeation mechanism, CMSMs produce far superior permeability-selectivity combinations than any known polymer membrane.
- Different pyrolysis conditions can be used to tailor the micropore structure for different separation purposes, starting from the same precursor.
- They are far more stable at high temperatures than polymers and may be suited to high-temperature applications (see Table 4-1).
- They are more stable in the presence of organic vapours at high temperatures, organic solvents and non-oxidising acid or base environments.
- They are mechanically stronger and can withstand higher pressure differences for a given wall thickness.

Table 4-1. Thermal stability of carbon membranes in the presence of various gases (Koresh and Soffer, 1987)

Gas	He	H_2	CH_4	CO_2	O_2
Temp. °C	700	>500	500	400	<200

Another advantage of carbon membranes is their ability to be manufactured in any form, due to the processibility of their polymeric starting materials (Barton et al., 1999).

The disadvantages mentioned were:

- Carbon membranes are more brittle and may require special handling.
- Strongly adsorbing organic vapours may block the pore system, requiring a pre-purifier. This may be avoided by operating at higher temperatures.

4.1 Carbon materials: a background

All known carbon materials (except for diamond) form a family of carbons distinguished by their degree of disorder from the single-crystal hexagonal graphite (Figure 4-1) to the most disordered porous carbons (Marsh and Rodriguez-Reinoso, 2006). Even in the latter, however, there is never total disorder.

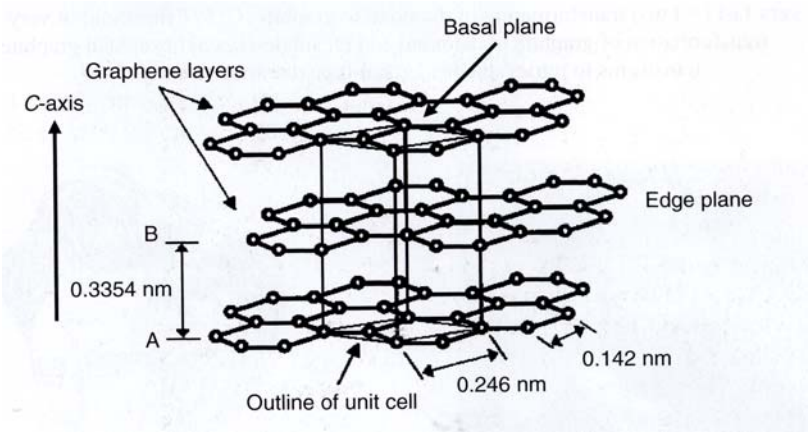

Figure 4-1. The structure of hexagonal graphite (Marsh and Rodriguez-Reinoso, 2006)

Carbon membranes fall into the class of disordered, porous carbons. In order to understand the important factors in their preparation and optimisation, it is necessary to explore the characteristics of the carbon family and their interaction with gaseous penetrants.

Within hexagonal graphite, the layers of hexagonal planes are defined as graphene layers, with a distance of 0.335 nm between the layers and 0.142 nm between bonded carbon atoms. The layers are stacked above each other in an offset ABABAB configuration. Carbons in adjacent layers are bonded not by chemical bonds, but by van der Waals forces. Resonance analysis indicates that the C to C bonding between layers has the characteristic of a one-third double bond. As one moves away from the single-crystal graphite, the random bonding of polycyclic carbon atoms with linear carbon atoms causes the graphene layers to be arranged in a progressive degree of disorder. They become smaller, more defective and abandon the ABABAB packing arrangement until identifiable layers are almost lost, as in glassy carbons. Due to the imperfect stacking of the defective graphene sheets, space, or porosity, is created.

The family of carbons is divided into two important structural groups: those that are graphitic or may become graphitic upon heating beyond 2000°C and those that will never be graphitic, even upon heating. The first group is termed *anisotropic* and *graphitizable*; the second *isotropic* and *non-graphitizable*.

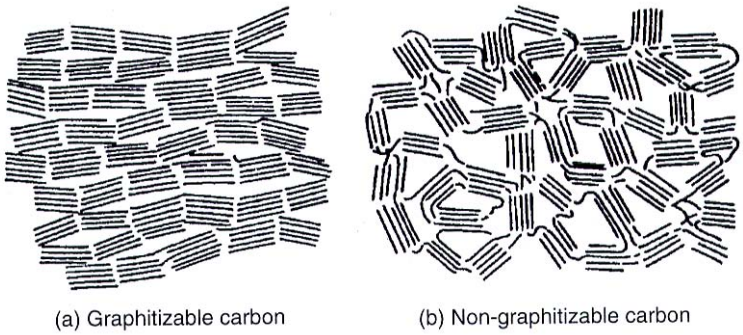

Figure 4-2. Drawings to illustrate the essential differences between (a) graphitizable and (b) non-graphitizable carbons (Franklin, 1950, 1951)

The graphene planes in non-graphitizable carbons cannot rearrange to form a graphitic structure when heated above 2000°C, because so many bonds would need to be broken simultaneously that the activation energy becomes impossibly high. A term often used in literature to describe the low degree of parallelism in carbons is turbostratic, which refers to a structure consisting of graphene planes arranged randomly to each other, like a house of cards that has collapsed in on itself. However, Marsh and Rodriguez-Reinoso argue that this would describe all carbon materials except for AB graphite, including graphitizable carbons, and is of little use. The term is therefore avoided in this thesis.

Carbon molecular sieves are essentially non-graphitizable porous carbons that have been activated. Activation refers to the selective gasification of carbon atoms at high temperatures (*thermal activation*) and the result is the formation of more 'spaces' which have the dimensions of gas molecules. There can be 10^{11} pore openings per mm^2 of activated carbon surface. In fact, activated carbons were aptly described by Marsh and Rodriguez-Reinoso as porosity enclosed by carbon atoms!

A simplified representation of porosity in a solid is shown in Figure 4-3. The diagram and following description is taken from Rouquerol et al. (1994). The first category of pores are those totally isolated from their neighbours, as in region (a), which are described as closed pores. Pores which have a continuous channel of communication with the external surface of the body, like (b) (c) (d) (e) and (f), are described as open pores. Some may be open only at one end, like (b) and (f); they are then described as blind pores. Others may be open at two ends (through pores), like around (e). These pores are responsible for in gas permeation in carbon membranes. Pores may also be classified according to their shape: they may be cylindrical (either open (c) or blind (f)), ink-bottle shaped (b), funnel shaped (d) or slit-shaped. Close to, but different from porosity is the roughness of the external surface, represented around (g).

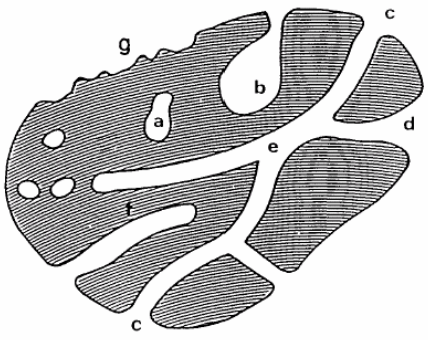

Figure 4-3. Representation of a porous solid (Rouquerol et al., 1994)

The definitions of porosity and adsorption, taken from Marsh and Rodriguez-Reinoso (2006) and used in this thesis, are:

- Porosity within porous solid is space which is accessible to molecules from the gas/vapour and liquid phases
- The adsorbent is the solid porous material, in this case carbon
- The adsorbate is the gas or vapour, or solute from solution, which is adsorbed within the adsorbent
- The adsorption process is when an adsorbate enters into the porosity of the adsorbent.
- Micropores have entrance dimensions <2.0 nm
- Mesopores have entrance dimensions between 2.0 and 50 nm
- Macropores have entrance dimensions >50 nm
- Ultra-microporosity or nanoporosity is often used to describe dimensions less than 0.7 nm, although nanoporosity can be confusing since micro- and mesopores also have nanometre dimensions

It must be noted that, due to the difficulty in determining the exact shape or dimensions of a pore opening, the dimensions above are not precise. They are often defined in terms of an adsorbate molecule and depend on the dimensions and polarity of both the molecule and the pore surface

Adsorption occurs at the interface of a gas and a solid substance, under the operation of surface forces[3]. The strength of the adsorption is related to the change in the chemical potential of the adsorbate molecule as it nears a surface, which is described by the adsorption potential of the wall-molecule interaction (Figure 4-4). A minimum is seen in the potential at a certain distance from the surface, which corresponds to the 'resting' position of an adsorbed molecule. As the molecule approaches the wall from the gas bulk, the force of attraction increases. The force then rises sharply towards a state of repulsion if the molecule approaches closer to the wall than the minimum. The depth of this minimum, or 'well', also corresponds with the strength of the physisorption.

The proximity of pore walls in microporous carbons leads to the overlap of wall adsorption potentials to create a deeper 'well' and, hence, molecules are more strongly adsorbed than on external surfaces. The adsorption potential for a slit-shaped pore with a width of two molecular dimensions is twice that of a flat graphite surface (Rodriguez-Reinoso and Molina-Sabio, 1998), which means that physisorption is a surprisingly strong phenomenon within CMSMs. This is important for both transport mechanisms and the blocking of pores, as will be discussed later in the thesis.

[3] IUPAC Compendium of Chemical Terminology, Electronic version, http://goldbook.iupac.org/A00155.html

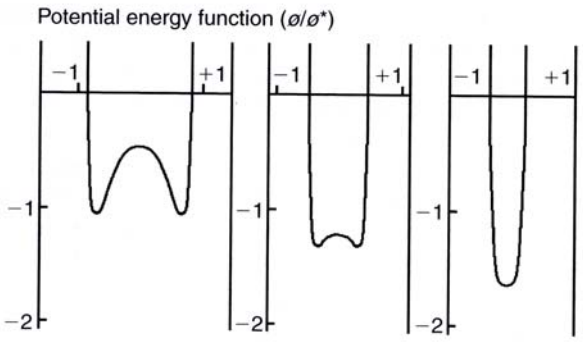

Figure 4-4. Diagrams to illustrate the change in the depth of the potential energy well, for an adsorbate molecule, as the size of a slit-shaped pore decreases (left to right). Marsh and Rodriguez-Reinoso, 2006 who adapted it from Rouquerol et al., 1999

4.2 Synthesis and structure

In order to produce a carbon molecular sieve membrane, one must begin with an even, flawless, thermosetting polymer that will not soften during the pyrolysis process (Koresh and Soffer, 1983). This starting material is termed the precursor. This process involves heating the precursor, often in a series of steps with isothermal dwells or 'soaks', to a final temperature, usually between 500°C and 1000°C. Rodriguez-Reinoso and Molina-Sabio (1998) defined pyrolysis as primary decomposition occurring below 600°C and carbonization as secondary decomposition occurring above 600°C.

The gases and tars liberated upon decomposition depend on the chemical composition of the precursor and can include CO_2, CO, H_2, N_2, NO_x and H_2O. A carbon residue is formed by condensation of polynuclear aromatic compounds and expulsion of side chain groups (Barton et al., 1999). On the macro-scale, the material maintains its shape during pyrolysis, although all dimensions may shrink proportionately (Koresh and Soffer, 1983). During the carbonization process, the remaining carbon atoms of the parent macromolecule move short distances (<1 nm) to positions of greater stability, for example to form 6-membered aromatic compounds (Marsh and Rodriguez-Reinoso, 2006).

Thermosetting polymers form non-graphitising carbons due to the occurrence of crosslinking, which removes the molecular mobility required for rearrangement to a 3D graphitic order. What remains is a non-graphitizable carbon matrix consisting of randomly orientated graphitic regions interspersed with porous regions. These graphitic regions comprise twisted hexagonal carbon layer planes of about 5 nm wide (Barton et al., 1999), occurring singly or in stacks of two to four. The spacing between the layers is typically 0.34-0.8 nm. Functional groups such as C=O may bind to the periphery of the carbon layer boundaries. Due to the random arrangement of the carbon layer stacks, there exists significant pore space between the graphitic regions. These nanoporous networks may also be initiated by the channelling of gases through the material as they are evolved during decomposition (Koresh and Soffer, 1983).

Koresh and Soffer (1980) proposed that carbon molecular sieves possess a network of inhomogeneous pores with slit-like constrictions and showed that these constrictions were between 3.7 and 5.02 Å in thickness for activated TCM 128 carbon fibres. The nanopores contribute 30-70% of the apparent volume of the carbon solid (Koresh and Soffer, 1983).

Constrictions may be formed by the disorganised packing of the graphitic stacks, the attachment of functional groups to the edges of the layer planes and the redeposition of carbon formed by the cracking of volatiles (Barton et al., 1999). Constrictions may also be created by the addition of metallic compounds to the precursor, which is discussed in Section 4.2.6.

Koresh (1993) found, via sorption experiments with non-swelling nitrogen, that the carbon skeleton is actually slightly flexible and that the constrictions can be dilated by adsorbates. The implication of this is that certain components that adsorb close to constrictions, dilating them, may increase the permeability of other gas species.

4.2.1 Surface functional groups

Carbon structures can contain other atoms, known as heteroatoms, such as hydrogen, oxygen, nitrogen and sulphur. Hydrogen is bonded with edge atoms, but oxygen, nitrogen and sulphur can bond both within and at the edges of graphene sheets (Marsh and Rodriguez-Reinoso, 2006). Oxygen influences the properties of the carbons in particular. Due to the electronegativity of oxygen, the surface oxygen complexes have dipole moments and provide sites with high adsorption potentials for polar groups. Carbons are only free from oxygen if heated beyond 950°C under vacuum or hydrogen.

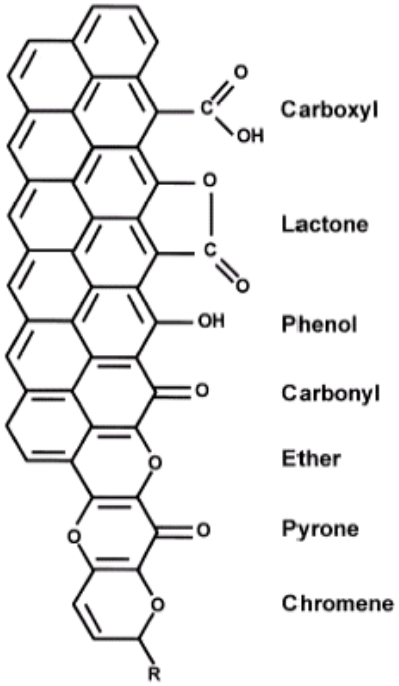

Figure 4-5. Examples of oxygen functional groups on carbon surfaces (Rodriguez-Reinoso and Molina-Sabio, 1998)

4.2.2 Heat treatment temperature

Koresh and Soffer (1980) demonstrated that gradual opening of pores in TCM 128 carbon fibres occurs when degassing between 100 and 700°C, by the removal of surface groups as CO and CO_2. The apparent increase in pore size was more significant up to 400°C; thereafter

only small changes in diameter were seen up to 800°C. Pore 'sintering' was marked above 800°C, although the authors concluded that 'sintering' was already occurring well below this. Total pore closure to nitrogen was achieved at 1200°C. Further pore widening could be achieved by mild air oxidation at 400°C. Analysis of the permeabilities of H_2 and CH_4 showed that they passed a maximum in membranes that were heat-treated at 500-700°C (Koresh and Soffer, 1986) (Figure 4-6).

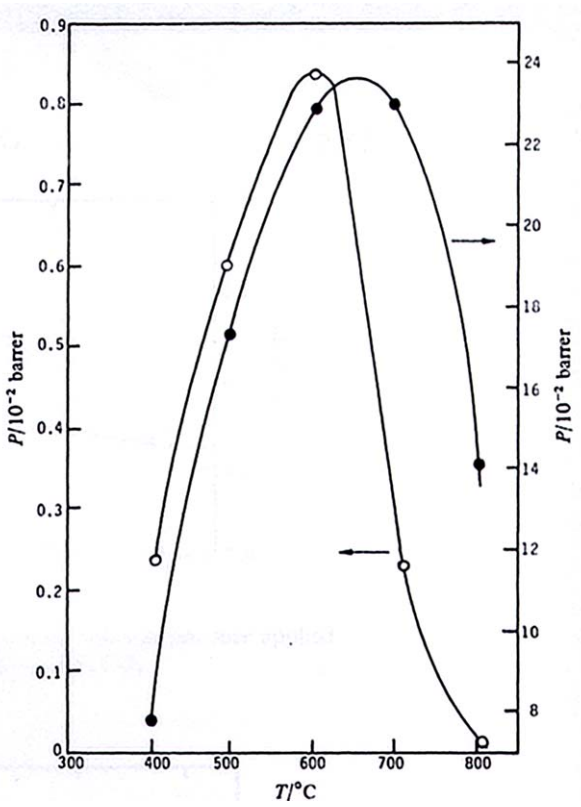

Figure 4-6. Permeability of CH_4 and H_2 in membranes heat treated to various temperatures: ○, CH4; ●, H_2 (Koresh and Soffer, 1986)

Steel and Koros (2003) varied the final pyrolysis temperature of polyimide to determine the effect on structure and separation properties and developed a hypothetical ultramicropore size distribution as a tool to interpret trends. They proposed a shift in pore size distribution (PSD) with temperature, shown in Figure 4-7. Pore sizes denoted A to F represent the sieving sizes for the respective gases. As final pyrolysis temperature is increased, so the PSD shifts to the left.

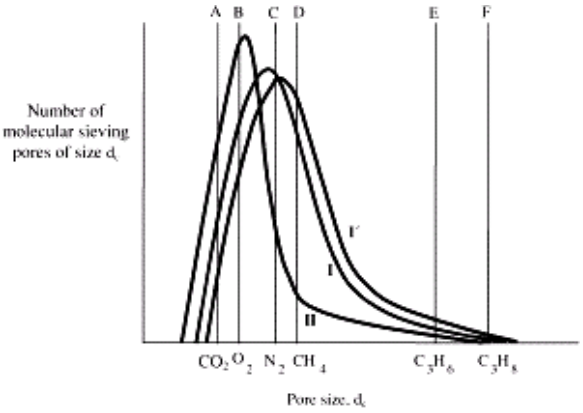

Figure 4-7. Illustration of hypothetical trends in molecular sieving pore size distribution vs. pyrolysis condition as maximum temperature is shifted from 800 °C (curve II) to 550 °C (curve I) to still lower 500 °C (curve I′) pyrolysis case (Koros and Steel, 2003)

Electronic spin resonance (ESR) has been used to measure the presence of "dangling bonds" or free radicals within the carbon lattice, where carbon atoms have been unable to move into a more stable position and the orbitals of the carbon atom are incomplete. A correlation can be seen between the heat treatment temperature of PVDC, the density of free radicals and the specific surface area of non-graphitizible carbons (Lewis and Singer, 1981, Marsh and Wynne-Jones, 1964). As the temperature is increased, the number of free radicals and surface area increases, implying the creation of porosity and free radicals simultaneously. Both properties reached a maximum at approximately 700°C and then decline. These dangling bonds may also provide sites with high adsorption energy and are relevant for adsorbate behaviour and membrane aging, which is introduced later in this thesis.

The IUPAC Compendium of Chemical Terminology defines sintering as the "coalescence of solid particles". In my opinion, the term sintering used by many researchers does not accurately describe the process of pore closing, because the immobility of a non-graphitizable carbon prevents the mass transport or coalescence of carbon. Marsh and Rodriguez-Reinoso (2006) state that pore closing in carbon molecular sieves is due to the increase in cross-linking as individual carbon atoms shift short distances to eliminate dangling bonds in the discontinuous carbon network, left by departing C=O and other functional groups. In my opinion, therefore, it is more sensible to imagine carbon atoms cross-linking at critical constrictions in the network, blocking access to adsorbates, rather than the traditional physical sintering of pores. This was noted by Steel and Koros (2005) when pyrolysing polyimides, who stated that "a simple generalised collapse of all pore dimensions is not occurring at the higher vs. lower temperature". Unlike sintering, the crosslinking process does not produce a continuous solid. Furthermore, this rearrangement of carbon atoms to eliminate dangling bonds should also be active in the lower temperature range. The theory therefore provides one comprehensive mechanism that describes events from the beginning of carbonization to the closure of pores and the final "quasi-equilibrium state" above 2000°C, described by Marsh and Rodriguez-Reinoso. In conclusion, the terms 'pore closure' or 'crosslinking' are more accurate terms to explain permeability loss at higher temperatures and will be used instead of 'sintering' in this thesis.

4.2.3 Thermal soak

Steel and Koros (2003, 2005) found that longer heating times (or *thermal soaks*) at final temperature produced more compact, less permeable carbon membranes. Generally, longer soak times and higher temperatures produced more selective membranes as the pore size distribution shifted downwards. However, at extreme conditions, the loss of small pores which were initially only accessible to smaller gases led to a decrease in selectivity, as an increased fraction of transport is forced to occur within larger, non-selective pores. Longer soak times at 550°C tended to move the carbon's separation properties toward those obtained at 800°C. The work of Bradbury and Shafizadeh (1980) also showed that pyrolysis of cellulose at 450°C for 20 minutes produced a material with similar properties to that obtained at 550°C for 1.5 minutes.

The reorganisation of carbon atoms in the structure (e.g. dangling bond elimination) is an activated process and the approach of the structure towards an 'equilibrium state' therefore depends on both time and temperature. Thus, a trade-off may exist in the commercial production of membranes between these two variables. In the development work in this thesis, it was decided to employ a standard soak time of 2 hours, in order to eliminate one preparation variable. The value of 2 hours was chosen to be consistent with the protocol of Lie (2005), so that comparison of results was possible.

4.2.4 Precursor

At lower carbonization temperatures, CMSMs may contain subdomains where the structure of the polymeric precursor can still be recognised (Sedigh et al. 1998). This subdomain structure determines the differences found between CMSMs derived from different precursors. This depends on the pyrolysis conditions – the longer the carbonization period and the higher the temperature, the less similar the final structure is to that of the precursor.

Koros and Steel (2005) reported that more free volume in the precursor produced more porosity in the final carbon. They compared carbon molecular sieves produced from Matrimid® (a polyimide) and a packing-disrupted 6FDA/BPDA-DAM derived material and found that the oxygen diffusion coefficient was 140% greater in the latter, when pyrolysed at 550°C. The differences between the materials were greater at a final treatment temperature of 550°C than 800°C.

4.2.5 Carbonization environment

Geiszler and Koros (1996) carbonized polyimide under vacuum (<0.1 mmHg) or flowing argon, helium or carbon dioxide. They found that the membranes prepared under an inert flow were more permeable and less selective that those under vacuum, because the heat and mass transfer were better under flowing gas. Carbon dioxide, which is oxidative at 800°C, produced the most open membrane. It was seen that the inert flow rate, which was varied between 1.02 and 10.2 cm/min (superficial velocity), was an important variable, with higher velocities producing more permeable membranes. The effect was higher at 550°C than 800°C. As well as increasing the heat transfer, higher velocities more effectively removed pyrolysis products, which reduced the amount of redeposition on the carbon surface.

They also evaluated the effect of residual oxygen on the membranes. The argon contained 0.3 ppm of oxygen, which could be eliminated by the use of an oxygen trap. Membranes made

without the trap in place were more permeable and less selective, because oxygen oxidised the carbon, producing wider critical constrictions.

4.2.6 Metal Addition

Barsema et al. (2003) attempted to functionalise carbon membranes prepared from polyimide. They added $AgNO_3$ or AgAc to the precursor in the range of 0 to 23 wt% (Ag) and varied the final pyrolysis temperature. It was seen that much of the silver migrated towards the surface to form a layer that reduced permeability and that $AgNO_3$ produced more dispersed, bulk contained clusters than AgAc. The migration of silver to the surface was enhanced by higher final temperatures and longer soaks. Below 600°C, however, Ag was seen to improve permeability and decrease selectivity by acting as a spacer in the pores. High contents of Ag formed very brittle membranes. The researchers concluded that an Ag content of 6 wt%, derived from $AgNO_3$, produced the most stable membranes, with finely dispersed nanoclusters ~50 nm in diameter.

Lie and Hägg (2005) investigated the addition of the oxides of Ca, Mg, Fe(III) and Si and the nitrates of Ag, Cu and Fe to cellulose derived carbon membranes. They found that the nitrates of copper and silver were particularly effective in improving selectivity for the gas pairs O_2/N_2 and CO_2/CH_4. Hydrogen permeabilities were obtained of 1100 Barrer for copper (II) nitrate (CuN) and 1500 Barrer for silver nitrate (AgN). Apart from the spacer effect of the additives, they also proposed that the gases released upon nitrate decomposition were porogens, in that they create pores by tunnelling through the material. Furthermore, H_2 may penetrate the Cu or Ag clusters, as in Pd/Ag and Pd/Cu membranes, increasing the selectivity. Cu was also seen to migrate to the surface, which can create a barrier to gas transport.

From the work of the two groups described above, it was decided to focus on the effect of silver nitrate and copper nitrate addition on H_2 separation performance. The precursors were to be doped with 0-6 wt% of the metal nitrate, calculated on the basis of the salt without the water of crystallization.

The metal nitrates may interact with the cellulose solvent, trifluoroacetic acid (TFA), to produce a soluble metal trifluoroacetate (Lie and Hägg, 2005) and allowing the metals to disperse within the precursor (Equation (17)).

$$TFA\ (aq) + MeN(s) \rightarrow MeTFAc\ (aq) + HNO_3\ (aq) \qquad (17)$$

At the final carbonization temperatures in this work (400-700°C), copper (II) nitrate in a polymer is reduced to copper oxide (Silverstein et al., 2004). The melting point of CuO is 1232°C, so it is unlikely that the material can flow or form clusters in the temperature range and should stay dispersed. Rather than migrating, copper oxide may be left in place as the carbon matrix recedes around it, producing a higher surface concentration of copper. The behaviour of CuTFAc, on the other hand, is unknown. The nitric acid produced in Equation (17) is known to be a stronger hydrolyser of hemicellulose than sulphuric and hydrochloric acid (Rodriguez-Chong et al., 2004). However, its effect on the precursor can be ignored at the low concentrations present in the solution (<0.02 wt%).

Silver nitrate melts at 212°C and decomposes to silver oxide at 444°C. Silver oxide melts at 200°C and decomposes at about 300°C (L'Vov, 1999). Hence,

$$AgNO_3(l) \rightarrow Ag(g) + NO_2 + \tfrac{1}{2} O_2 \qquad \text{(L'Vov, 1999)}$$

The silver vapour condenses simultaneously and transfers the energy of condensation to the reactant. It certainly feasible, then, that silver compounds can migrate to form clusters and surface layers in the pyrolysis range. Furthermore, since silver compounds can migrate, it may be that they can also coalesce in pores, reducing the effective pore size.

Metal additives may also influence the chemistry of pyrolysis. Shafizadeh and Sekiguchi (1983) found that cellulose treated with NaCl and $(NH_4)_2HPO_4$ yielded more char upon pyrolysis than pure cellulose, and had a higher degree of aromaticity. They speculated that the additives increased the condensation and cross-linking reactions and dehydrated the glucose units in the cellulose molecule. Golova and co-workers (mentioned by Shafizadeh, 1979a) reported that even trace inorganic contaminants catalysed extensive degradation of cellulose.

A summary of the possible effects of metal addition are presented in Table 4-2.

Table 4-2. Speculated effects of metal nitrate addition on membrane properties

Phenomenon	**Effect**
Pore spacer	More permeable, less selective
"Cluster in a cage": spaces between metal and carbon	More permeable, less selective
Pore filling	Less permeable, more selective (especially to metal permeating gases like H_2)
Surface metal layer	Less permeable, more selective (especially to metal permeating gases like H_2)
Decomposing nitrate ion evolves porogen gases	More permeable
Metals catalyse degradation	Possibly greater weight loss, more permeable
Embrittlement at high metal concentrations	Defects, poor structural strength

4.3 Synthesis from cellulose

Cellulose is a polysaccharide generated from repeating β-D-gluco-pyranose molecules. Spruce wood pulp served as the source for cellulose in this thesis (supplied by Södra Cell Tofte). The precursor was lignin free and contained 15-20% hemicellulose (see Figure 4-8 for the chemical structures of these compounds).

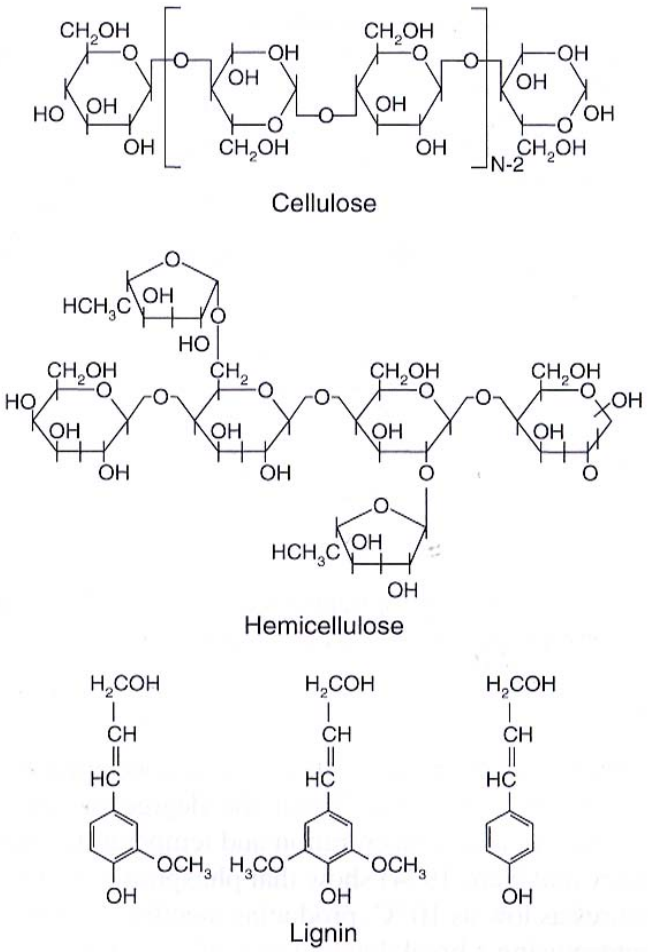

Figure 4-8. Chemical structures of cellulose, lignin and hemicellulose (Jagtoyen and Derbyshire, 1998)

In the case of wood pulp, the number of repeating units in a chain is typically between 300 and 1700 (Klemm et al., 2005). Due to the linearity of the polymer chains and the occurrence of hydrogen bonding because of the large number of –OH groups attached to each repeating unit, cellulose is a partially crystalline polymer. The degree of crystallinity of dissolving pulp is 43-56%, with the size of the crystallites up to 20 nm. Cellulose molecules also clump together in the axial direction to produce fibrils some 100Å long and 30Å thick, held together by hydrogen bonding. This crystallinity deters degradation (Fan et al. 1987). Hemicellulose, one of the other main constituents of plant cell walls, consists of shorter chain polysaccharides. These include glucomannans, which in the case of hardwood pulp contains galactose side chains, and xylans, which contain acetal side chains. The higher degree of branching of these hemicelluloses means that they are not crystalline and can dissolve in water.

4.3.1 Solubility of cellulose and effect of TFA exposure

In order to process cellulose into the films or hollow fibres that constitute membranes, raw cellulose must first be dissolved. Unfortunately, because of the strength of the hydrogen bonding in fibrils, cellulose is insoluble in water and more aggressive solvents are required. Strong acids, strong alkalis, concentrated salt solutions and various complexing agents can disperse or dissolve cellulose (Fan et al. 1987). These include trifluoroacetic acid, sulphuric acid, hydrochloric acid (Morrison and Stewart, 1998), NMMO/water (Klemm et al., 2005), sodium tartrate/ferric chloride/sodium sulfite/sodium hydroxide (CMCS) and ethyldiamine/water (Cadoxen) (Fan et al., 1987).

Trifluoroacetic acid (TFA) was used in this work. TFA is a strong acid that can dissolve cellulose and easily be removed by evaporation. Morrison and Stewart (1998) reported that crystalline cellulose does not undergo extensive hydrolysis within the first 8 days of dissolving in TFA, but after 12-16 days some cleavage of the 1,4-β-linkages occurred. In contrast, non-cellulosic polysaccharides such as hemicellulose, which are not crystalline, were depolymerised in 99vol% TFA at 37°C. They also reported that TFA can be diluted with acetic acid, up to a ratio of 1:9 (v/v), reducing the solution viscosity and making handling less hazardous.

Hydrolysis in a strong acid proceeds by addition of water molecules at the 1,4-β-linkage, producing two chains but preserving the basic chemical structure (Fan et al., 1987). Hydrolysis occurs randomly in the chain and proceeds through the steps:

$$\text{Cellulose} \rightarrow \text{acid complex} \rightarrow \text{oligosaccharides} \rightarrow \text{glucose}$$

Acid complexes may only form once the crystalline structure of the cellulose fibrils is destroyed by dissolution.

Shafizadeh et al (1979a) reported that mild acid hydrolysis of Cottonwood before pyrolysis decreased the char yield (i.e. increased weight loss), because hydrolysis of hemicellulose produces xylose and hydrolysis of cellulose produces glucose derivatives, two tarry components.

Lie and Hägg (2006) investigated the effect of cellulose hydrolysis by 99 vol% TFA on the final carbon membrane performance. They found that longer hydrolysis times improved the separation performance of the eventual CMSM, and concluded that hydrolysis produced intermediates (furan derivatives) and glucose that hasten the degradation route in

carbonization. It is speculated by this author that the delay seen by Lie and Hägg and Morrison and Stewart may be related to the time taken to dissolve the fibrils before hydrolysis can proceed.

4.3.2 Cellulose pyrolysis

Pyrolysis of cellulose and cellulosic materials proceeds through a series of primary and secondary reactions which provide a mixture of gaseous products, tarry condensate and carbonaceous char (Shafizadeh and Sekiguchi, 1983). Shafizadeh and Sekiguchi heated cellulose in nitrogen in the range of 300-500°C for 5 minutes and measured the extent of aromatization (see Table 4-3). They observed a rapid weight loss and the development of aromatic structures between 350 and 400°C. The H/C ratio decreased from 1.5 to 0.7 in the same range. Weight loss was reduced above 400°C, but aromatization continued more rapidly with a decrease of H/C, as condensation and growth of aromatic clusters continued. The total aromatic content increased from 2.8% at 350°C to 15.7% at 500°C. Although the mass of the char was relatively stable, the conclusion was that the chars were far from being graphitized carbon and that secondary reactions forming highly condensed aromatic structures continued. Elsewhere, Shadizadeh and Sekiguchi (1983b) stated that the lower weight loss in 'stable' chars proceeds involves the loss of aliphatic carbons from 28 to 10% and an increase in aromatic carbons from 70 to 90%.

Table 4-3. Residual char yield and its elemental analysis (Shafizadeh and Sekiguchi, 1983)

Char	Yield	Composition			Formula	
	(wt%)	C	H	O(diff)	(Ref. to C6)	H/C
untreated		42.0	6.5	50.7	$C_6H_{10}O_5$*	1.7
300°C for 5 min	89.4	44.0	6.4	49.6	$C_6H_{10.4}O_{5.0}$	1.7
325°C for 5 min	63.3	47.9	6.0	46.1	$C_6H_{9.0}O_{4.3}$	1.5
350°C for 5 min	31.8	59.9	5.2	34.9	$C_6H_{6.2}O_{2.6}$	1.0
400°C for 5 min	16.6	76.5	4.7	18.8	$C_6H_{4.4}O_{1.1}$	0.7
450°C for 5 min	10.5	78.0	4.3	16.9	$C_6H_{3.9}O_{1.0}$	0.6
500°C for 5 min	8.7	80.4	3.6	16.0	$C_6H_{3.2}O_{0.9}$	0.5

*Theoretical value (author's note: theoretical is assumed to mean accepted molecular ratios for cellulose)

Bradbury et al. (1979) proposed first order kinetics for the vacuum pyrolysis of cellulose, which followed a competitive two reaction scheme:

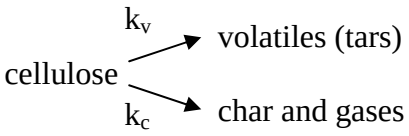

They found that the char was 35 wt% of the char and gas fraction at 314°C. The volatiles referred to condensibles captured in a water-cooled condenser between the furnace and the vacuum pump. Little variation was observed in the volatiles' nature over the pyrolysis range (260-340°C). It was seen that there was a temperature dependent 'activation' period that preceded rapid pyrolysis. It was speculated that this period is related to the cellulose macromolecules proceeding through glass transition and depolymerisation to a degree of polymerisation (DP) of 200, before they can degrade to volatiles, gases and char. This may also explain the effect of hydrolysis by acids such as TFA on weight loss and membrane performance (described in Section 4.3.1) – hydrolysis may 'activate' the cellulose by cleaving the chains to a lower DP.

Shafizadeh et al. (1979a) reported that the tar fraction, which can account for up to 60-81% of the product of cellulose pyrolysis, consists of levoglucosan, furanose and randomly linked oligo- and polysaccharides. They presented the kinetics of tar formation and weight loss, showing that these accelerated above 300°C. The amount and composition of the tar differed greatly between pyrolysis under a vacuum and under flowing nitrogen at atmospheric pressure, with 81% tar recorded for vacuum pyrolysis and 54-60% for nitrogen-swept pyrolysis. The remaining char mass, or carbon, was correspondingly higher for the latter condition. They attributed this difference to the better removal by vacuum of volatile compounds, which can undergo secondary decomposition. They also found that the source of cellulose determines the tar and levoglucosan fraction, with wood-derived paper and pulp producing lower levels of levoglucosan and slightly lower tar (47%). The paper and pulp also contained lignin and hemicellulose.

Since tar is volatile at pyrolysis temperatures, its formation is an important step in weight reduction. An important question is whether some tar undergoes carbonization and contributes to the final carbon structure. Tar molecules are bulky and must also be trapped by sieving restrictions in the pore network during pyrolysis, so one could speculate that they must find, and perhaps create, micro- to mesoporous escape routes. Bradbury et al. (1979) reported that smaller sample sizes produced smaller char fractions and concluded that the residence time of the volatiles in the cellulose during pyrolysis largely influences the extent of char formation. It has also been shown that the pyrolysis of levoglucosan produces some residual char (Shafizadeh and Lai, 1972, Kawamoto et al., 2003).

Kawamoto et al. (2003) argued that the kinetic pathways proposed by Shafizadeh et al. were too simplistic, and suggested that levoglucosan is in fact a critical species in the route to solid carbon products. They proposed that levoglucosan, the major product of pyrolysis, can undergo reversible ring-opening and polymerisation to form polysaccharides, which in turn convert to solid carbonized products. They did not explain the extent of this contribution to the final carbonized mass or why cellulose, itself a polysaccharide, cannot directly form solid products. The formation of liquid products as intermediates also seems consistent with graphitising carbons, not non-graphitising carbons formed from thermosetting polymers like cellulose. What does seem reasonable is that levoglucosan that is trapped in the heating zone (in the sample) for long enough can re-polymerise and form part of the final carbon, in other words, as a side contribution.

Bradbury and Shafizadeh (1980) studied the affect heat treatment temperature (HTT) of cellulose on the surface area, free spin concentrations (using ESR) and the chemisorption of oxygen on the resulting chars. The free spin concentration is a measure of the free radical sites present in the carbon, which are found at edged carbons with unpaired σ electrons and provide sites attractive for the chemisorption of oxygen. It can be seen in Figure 4-9 that the maximum surface area is obtained in cellulose heat treated at 550°C. Curve b clearly shows that the number of free radical sites peaks at 550°C, while the surface area measured with physical adsorption shows a flatter peak between 550°C and 700°C. One could therefore expect the maximum flux for carbon membranes to be in this range. An important cautionary note about this conclusion is that the samples were heat treated for only 1.5 minutes. Bradbury and Shafizadeh observed that cellulose chars prepared at 450°C for 20 minutes had the same residual mass and chemisorption potential as samples prepared at 550°C for 1.5 minutes. At the longer HTT times used in this thesis work (120 minutes), the curves in Figure 4-9 would most likely be shifted to the left.

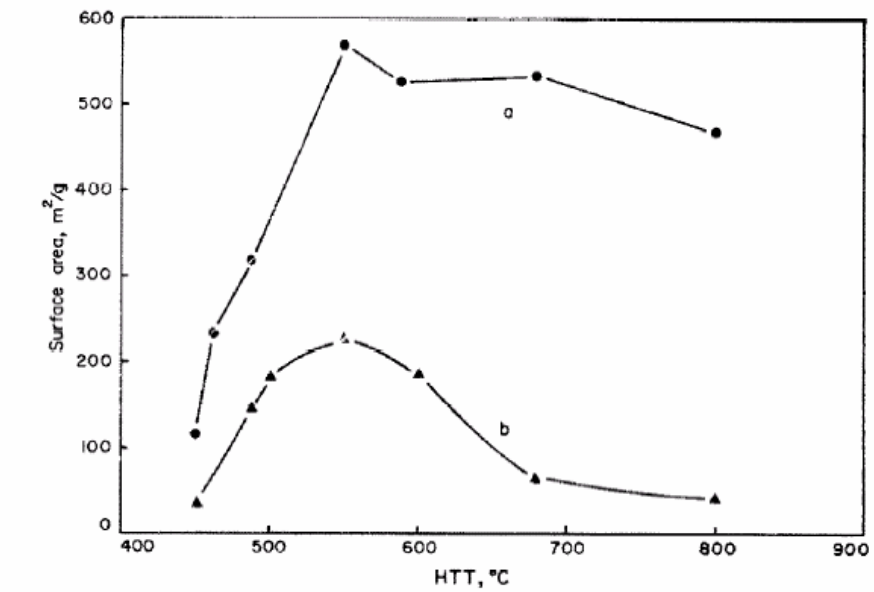

Figure 4-9. Comparison between total surface area calculated from O_2 adsorption at 25°C (curve a) and that occupied by surface oxides calculated from O_2 chemisorption at 230°C (curve b) (Bradbury and Shafizadeh, 1980)

Byrne and Marsh (1995)[4] proposed a route for the carbonization of cellulose, including a new intermediate structure between cellulose and carbon (Figure 4-10). Stage (b) shows the formation of a crosslinked, random structure formed by condensation and functional group elimination. By stage (c), most of the functional groups have been removed and the carbon atoms have begun to stabilise themselves in 5-, 6- and 7-membered rings.

[4] Referenced from Marsh and Rodriguez-Reinoso, 2006

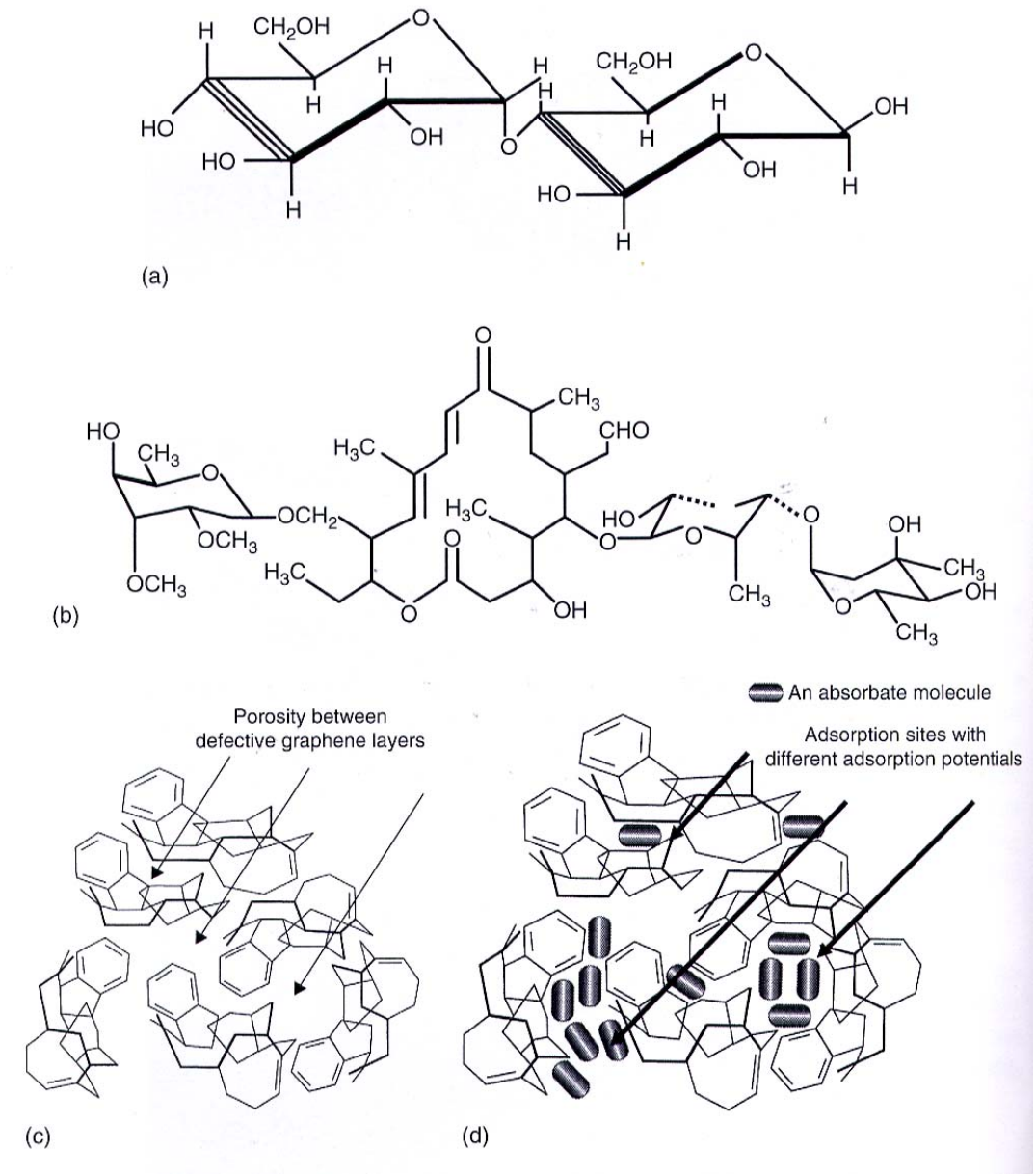

Figure 4-10. (a) Molecular structure of a cellulosic-type precursor. (b) A possible structure intermediate between cellulose and that of a resultant carbon. (c) Possible highly defective carbonaceous structures which, when interconnected, create microporosity. (d) Possible highly defective carbonaceous structures which, when interconnected, create microporosity, this model showing locations of adsorbate molecules (Byrne and Marsh, 1995)

4.4 Transport mechanisms

The mechanism of separation in carbon membranes depends on the pore structure, gas species, mixture composition and operating conditions. These factors determine the degree of interaction between molecules and pores. Briefly, three regimes are important which relate roughly to effective pore diameter.

1. Knudsen diffusion

This is seen in pores of 2-100 nm (Burgraaf and Cot, 1996) and is observed when collisions between molecules and the pore walls become significant. A rigorous method of predicting whether Knudsen diffusion is applicable is to calculate the Knudsen number, N_{Kn}, which is a ratio of the mean free path of a diffusing molecule, λ, and the pore diameter (Geankoplis, 2003). Knudsen diffusion is expected to dominate transport when N_{Kn} is greater than 10.

$$N_{Kn} = \frac{\lambda}{d_p} \qquad (18)$$

λ is temperature dependent; higher temperatures increase the mean free path and cause more collisions. Knudsen diffusion results in low selectivity, for which the following relationship is true:

$$\alpha = \frac{D_A}{D_B} = \sqrt{\frac{M_B}{M_A}} \qquad (19)$$

where, M_i is the molar mass of component *i*. A carbon membrane exhibiting Knudsen selectivity would be considered to be a failed membrane, with too many mesopores. However, open CMSMs which exhibit sieving behaviour for larger molecules (molecular sieving diameter > 0.43nm) may exhibit Knudsen selectivity for smaller molecules, particularly at high temperatures where the effect of adsorption is attenuated (Gilron and Soffer, 2002).

2. Selective surface flow

This mechanism is dominant in membranes with an effective pore diameter of 5-6Å (Rao and Sircar, 1993, 1996), where the competitive adsorption of gases in pores becomes significant. Selectivity comes about through the dominance of more adsorbable gases on the pore walls, such as ethane and other non-ideal gases, which reduce the effective pore volume available to smaller species, such as hydrogen. The adsorbed molecules diffuse over the surface. These membranes may be termed reverse-selective, because normally fast-penetrating, smaller molecules are retained. This mechanism is discussed more thoroughly in Section 4.4.4.

3. Molecular sieving

Molecular sieving, as the name suggests, arises from the hindrance of molecules by constrictions in the pores, according to their size and shape. This mechanism is dominant when the effective pore diameters are on the molecular scale – in the range of 3-5Å. Excellent selectivity and permeability can be achieved simultaneously, making this the desired mechanism in this work. This mechanism is discussed more thoroughly in Section 4.4.1.

4.4.1 Molecular sieving

Koresh and Soffer postulated in 1980 that a kinetic-statistical mechanism must be responsible for the highly specific ability of carbon molecular sieves to discriminate between different molecules. In this model, each constriction contributes to the overall probability of a molecule passing through a layer consisting of *N* constrictions. In terms of kinetic theory, the probability of a molecule passing a constriction is given by

$$p = p_0 \cdot \exp(-E_a / kT) \tag{20}$$

where p_0 is a frequency factor, E_a is the activation energy (related to forcing a molecule to climb up the repulsive segment of its adsorption potential as it approaches a constriction) and T is temperature. The larger the molecule, the greater is E_a (Burggraaf, 1999). The probability of a molecule passing all constrictions, N, in a path is:

$$P_A(N) = {P_{0A}}^N \exp(-NE_A / kT) \tag{21}$$

and the sieving selectivity ratio can be expressed as the ratio of probabilities of two molecules passing through a layer:

$$\frac{P_A}{P_B} = \left(\frac{P_{0A}}{P_{0B}}\right)^N \exp(-[N(E_A - E_B)/kT] \tag{22}$$

Thus, even a small difference in activation energies is multiplied N times and compounded. This explains why molecular sieves with relatively wide pore size distributions can separate molecules with similar sizes so effectively. From Equations (21) and (22), it can be expected that higher temperatures increase the permeability of a molecule through a molecular sieve, and that the permselectivity between two gases is dependent on temperature and their respective activation energies. Furthermore, if B is a larger molecule with a higher E_B, one could expect selectivity to decrease with increasing temperature.

Singh and Koros (1996) extended the analysis of the molecular sieving mechanism by studying the importance of entropic selectivity in diffusion. The diffusivity, D, of a molecule can be expressed as

$$D = D_0 \exp(-{E_D}^\dagger / RT) \tag{23}$$

Where ${E_D}^\dagger$ is the activation energy required to jump past constrictions and D_0 is the pre-exponential diffusion constant. D_0 may also be written as

$$D_0 = e\lambda^2 \frac{kT}{h} \exp\left(\frac{S_d^\dagger}{R}\right) \tag{24}$$

Where λ is the average diffusivity jump length in the medium, ${S_d}^\dagger$ is the activation entropy of diffusion and k and h are Boltzmann's and Planck's constants, respectively. The diffusivity selectivity between two components is therefore

$$\frac{D_A}{D_B} = \exp\left[\frac{(S_{d_A}^\dagger - S_{d_B}^\dagger)}{R}\right] \exp\left[\frac{(E_{d_A}^\dagger - E_{d_B}^\dagger)}{RT}\right] \tag{25}$$

The entropic selectivity arises from the restriction of orientation of a molecular in order for it to execute a jump through a constriction. A cylindrical molecule might not be able to rotate in a plane perpendicular to that of a slit, for example, while a spherical molecule might and hence the bulkier molecule possesses fewer degrees of freedom when passing. Thus, shape and size are important in the sieving mechanism.

According to Steel and Koros (2003), the characteristic dimensions of molecules with respect to carbon sieving is given by their kinetic diameters, as determined by zeolite adsorption ().

Table 4-4. Lennard-Jones kinetic diameters of relevant gases, as determined by zeolite adsorption (Breck, 1975)

Gas	He	H_2	CO_2	Ar	O_2	H_2S	N_2	CH_4	SF_6	C_2H_4	C_3H_8
Diameter, Å	2.60	2.89	3.30	3.40	3.46	3.60	3.64	3.80	5.50	3.9	4.30

Sorption still contributes to transport in molecular sieving, even for 'light molecules', which explains why hydrogen is often seen to permeate faster than helium (Suda and Haraya, 1997).

4.4.2 Effect of pressure on transport

Koresh and Soffer observed in 1986 that the permeabilities of low-boiling gases H_2, He, O_2 and Ar are independent of pressure, whereas the permeabilities of more adsorbable gases such as CH_4, CO_2 and N_2O decreased as pressure increased. Furthermore, this effect of pressure on the permeabilities of the higher-boiling gases decreased as temperature increased. This was explained in terms of the dependence of permeability on the adsorption isotherm for the gas. The reader is invited to revisit Equation (3). Since adsorption isotherms in molecular sieves are usually of type I, we can insert the expression for the Langmuir isotherm ($C = C_0 \cdot b \cdot p/(1+bP)$) into Equation (3), yielding:

$$P = D \cdot C_0 \cdot b/(1+bp)^2 \qquad (26)$$

Where C_0 is the adsorption saturation capacity and b is an interaction parameter. The reduction of the permeability with increasing pressure is clear from Equation (26). The interaction parameters for light gases such as H_2 are small and so their permeabilities are independent of pressure (i.e. they follow Henry's law). Parameter b, or sorption equilibrium constant, follows an Arrhenius relationship, i.e. $b = b_0 \cdot exp(-H_s/RT)$ (Wankat, 1986). Thus, parameter *b* decreases exponentially with temperature and the dependence on pressure of the heavier gases decreases with temperature.

4.4.3 The effect of temperature on transport

The effect of temperature on transport has already been introduced in Section 4.4.1 in Equations (20) - (25). Taking this further, Suda and Haraya (2000) investigated the permeability of gases following a sorption-diffusion mechanism in a carbon molecular sieve. In that case, dC/dp was assumed to follow Henry's law, thus

$$P = D \cdot S \qquad (27)$$

This relationship can further be expressed as

$$P = D_0 \exp\left(\frac{-E_d}{RT}\right) \cdot S_0 \exp\left(\frac{-H_s}{RT}\right) \qquad (28)$$

Here D_0 is the temperature-independent diffusivity constant, S_0 is the sorption constant, E_d is the activation energy required for diffusion to occur and H_s is the heat of sorption. Steel and Koros (2003) described E_d as the energy required for a molecule to execute a jump from one cavity to another, or to overcome the forces of repulsion by the walls at the constriction. The term $S_0 \cdot exp(-H_s/RT)$ would be analogous to the term, $C_0 \cdot b$, in Equation (26), because as the temperature increases so that $b \cdot p$ becomes small relative to 1 in the denominator of Equation 6, the sorption term reduces to that seen in Equation 28.

By rearrangement,

$$P = D_0 S_0 \exp\left(\frac{-(E_s)}{RT}\right) \qquad (29)$$

where $E_s = E_d + H_s$, the activated energy of transport.

Since sorption tends to be an exothermic process (hence H_s has a negative value) and E_d is positive, the effect of temperature is dependant on the relative sizes of E_d and H_s. Thus, the permeability for a gas such as hydrogen, which has a lower tendency to adsorb than carbon dioxide, but a smaller diameter and hence higher diffusivity, could be expected to increase with increasing temperature. CO_2, for which surface flow is large contributor to transport in pores, was observed by Suda and Haraya to increase only slightly. This behaviour is seen in Figure 4-11.

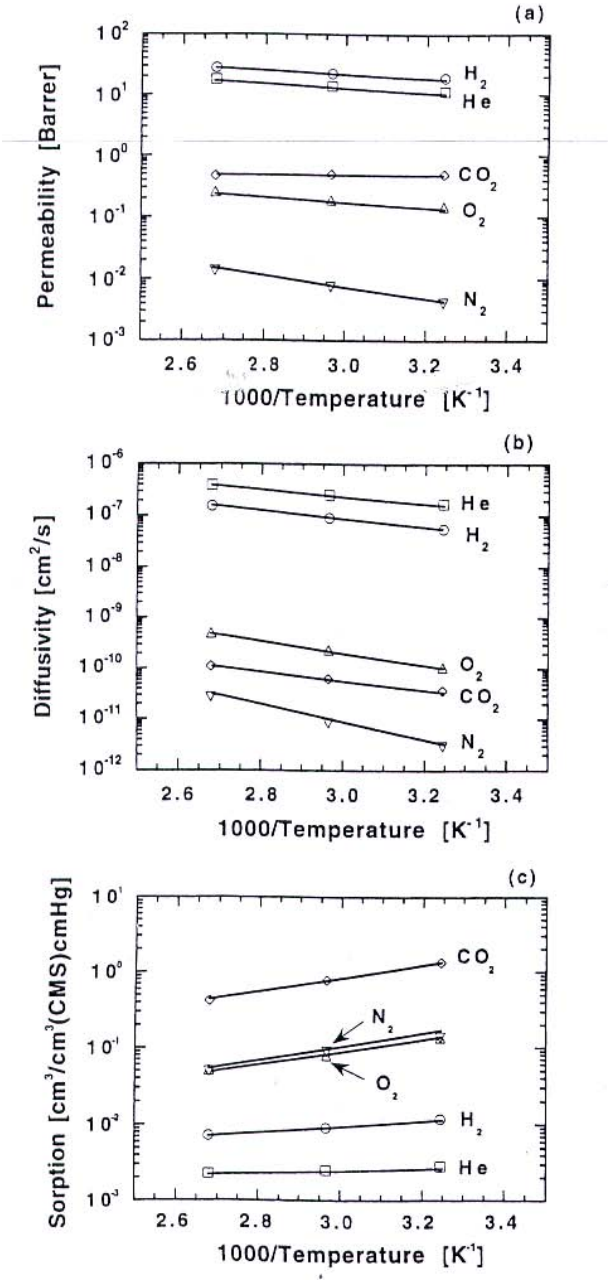

Figure 4-11. Arrhenius plots of (a) permeability (b) diffusivity, and (c) solubility for a CMS membrane prepared by pyrolysis of a Kapton film at 1223 K for 2 hours at a heating rate of 1.33 K/min under Ar flow (Suda and Haraya, 2000)

Productivity in hydrogen separation can therefore be increased by operating at higher than ambient temperatures. The upper temperature would be constrained by process economics, module fabrication issues and alteration of the carbon structure by pyrolysis or pore closure.

The effect temperature has on the selectivity between two gases also depends on the size of E_s. The ratio of permeabilities of a gas at two temperatures, $T_1 > T_2$, is given by

$$\frac{P_{T1}}{P_{T2}} = \frac{P_0 \exp(-E_s / RT_1)}{P_0 \exp(-E_s / RT_2)} \qquad (30)$$

By rearrangement we get

$$\frac{P_{T1}}{P_{T2}} = \exp\left[\frac{E_s(T_1 - T_2)}{RT_1T_2}\right] \qquad (31)$$

Thus, the ratio of permeabilities is dependent on the size of E_s. One can also speculate that, for a given material and adsorbate, the smaller the effective pore size, the larger E_d is relative to H_s. Of course, H_s also increases as pore size decreases and there is more overlap of wall adsorption potentials, but since the molecular sieving dominates below a certain pore size, E_d must be larger. The important implication for Eq. (31) is that, for molecular sieving materials, gases with a larger E_s will experience greater ratios of P_{T1}/P_{T2} and selectivity may decrease. Actual examples of this will be presented from literature in Section 4.6.2 and in this work.

4.4.4 Selective surface flow

Selective surface flow (SSF) is sometimes described as a transport 'mechanism' but it is my opinion that it is more correctly termed a competition phenomenon. More strongly adsorbing species adhere to, and flow or hop along pore walls, and at the same time reduce the available pore space for less strongly adsorbing species. The transport mechanism for molecular sieving and surface flow is still described by Eq. (29). Even hydrogen transport includes a sorption component in ultramicropores, as shown by the work of Suda and Haraya (1997), and is therefore 'flowing' along walls. Although molecular sieving selectivity in the sense of Equation (25) can be quantified by single gas tests, selective surface flow cannot. Single gas tests may imply that hydrogen is faster permeating than butane, for example, until reality is revealed in mixed gas tests. Equation (29) is as equally valid for molecular sieving as for selective surface flow; in other words, there is only one transport mechanism. The competition phenomenon occurs only when the effective pore size is such that molecules adsorbed on opposite walls have less than a molecule diameter between them, i.e. 2-3 molecular diameters.

This assertion is supported by the fact that single gas behaviour is affected by pressure and temperature in the same way for light and more strongly sorbing gases. Increasing the temperature increases permeabilities for both. Increasing the pressure decreases the permeabilities of more strongly sorbing gases, even though this should increase the surface concentration of the gas.

Researchers have attempted to exploit competitive adsorption. Rao and Sircar (1993, 1996) developed an SSF membrane with a very narrow pore size distribution for hydrogen recovery (at the retentate side) from hydrocarbon streams. They observed that activated diffusion was the dominant mechanism and that gas diffusivity can change by several orders of magnitude if the average pore diameter changes by a few Ångstroms. The permselectivity due to selective adsorption is strongly dependent on temperature. In order to obtain reasonable selectivities, the membranes must operate at below ambient temperatures (Centeno and Fuertes, 2002).

Both molecular sieving and selective surface flow may take place in the same membrane. Vieira-Linhares and Seaton (2003) modelled selective surface flow (SSF) in a carbon membrane using critical path analysis, for H_2 and CH_4 transport. They concluded that the gases effectively travel in separate sub-networks in the pore network, with CH_4 only travelling in pores larger than 6.4Å and hydrogen in pores narrower than 6.5Å.

4.5 Aging of membranes

Carbon membranes may experience 'aging', or a change in permeability and selectivity over time when exposed to certain environments. Two mechanisms are particularly important for aging in carbon: chemisorption and physisorption (Dubinin, 1980). Chemisorption is the chemical bonding of a component, such as oxygen, with sites on the carbon surface and tends to be irreversible. Regeneration is usually only possible by heating the carbon to high temperatures (Menedez and Fuertes, 2001), which may concurrently alter the carbon structure. Physisorption is the physical adsorption (through Van der Waals or dispersion forces, permanent dipoles or hydrogen bonding) of a gas on the surface in one or more layers and may be reversible.

Molecules that adsorb to micropore walls in the aging process occupy volume that is usually available for permeation. The usual effect is that the permeabilities of gases are reduced, especially when adsorption of molecules occurs near constrictions in the pore network. Pores may become completely blocked. As the effective diameter of pores decreases, so the sieving effect may be enhanced and selectivities often increase with time.

The purpose of this section is to explain the observed change in separation properties of the carbon membranes in this study with time. This behaviour and suggested strategies to deal with aging are presented in Sections 7 and 9, respectively.

4.5.1 Exposure to oxygen and air

Oxygen chemisorbs at active sites on the carbon surface to form C-O surface complexes, which reduce the available pore volume. Chemisorbed oxygen near pore restrictions would be particularly effective at hindering transport. The C-O groups can only be removed by heating to high temperature (700-1000°C), where they are liberated as CO and CO_2. According to Marsh and Rodriguez-Reinoso (2006), the process of chemisorption can take months to complete, more so if in the presence of water vapour.

Menendez and Fuertes (2001) explored the effect of oxygen, humidification and storage under air, nitrogen and propylene on membranes carbonized from phenolic resin. They found that storage in lab air and dry air led to significant permeance loss (see Figure 4-12) and selectivity increase, even after one day of exposure. Thus, even exposure while transferring the membrane from the furnace to the permeation test rig will result in aging. The decline slowed after 2 days, but was still significant over the first 5 months. Storage under dry air did not prevent aging.

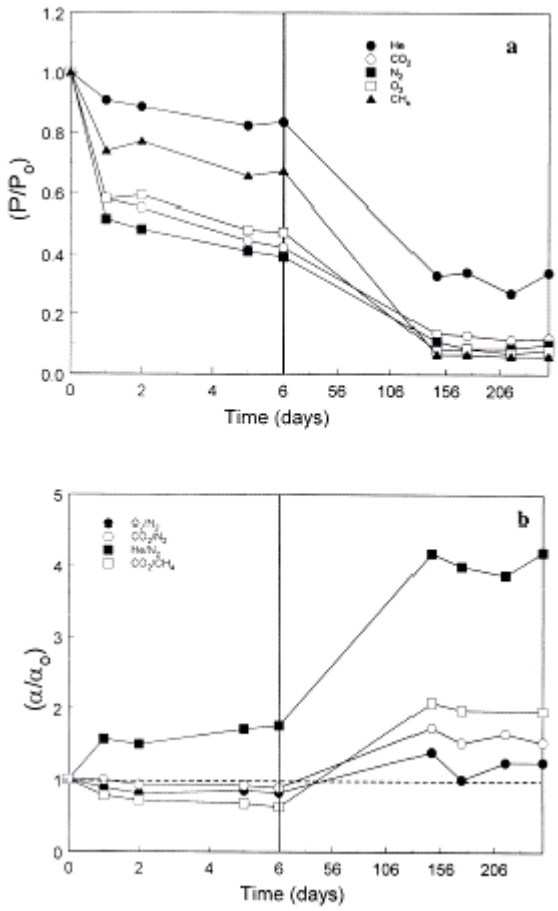

Figure 4-12. Modification with time of (a) the normalised permeance (P/P_0) and (b) the normalised permselectivity (α/α_0) of a carbon membrane stored under a laboratory air environment (Menendez and Fuertes, 2001)

Humidification of the air was seen to slow aging. It was postulated that the water molecules passivate the membrane by adsorbing in the pores and preventing access to chemisorption sites for oxygen. C-O surface groups from the chemisorption of oxygen also exacerbate aging by providing physisorption sites for water molecules (Dubinin, 1980), on what is otherwise a hydrophobic surface (see Section 4.5.2).

Verma and Walker (1992) reported that the treatment of carbon molecular sieves with Cl_2 or H_2 passivated the active sites on the carbon surface, which prevented the chemisorption of oxygen.

Bradbury and Shafizadeh (1980) prepared chars from pure cellulose at HTT's of 400-800°C and observed a maximum in the oxygen chemisorption potential (Figure 4-9) and the free spin concentration (Figure 4-13), which is a measure of the dangling bonds available for chemisorption, at 550°C. As discussed in Section 4.3.2, the short pyrolysis times used by the researchers mean that these curves may be shifted to the right by 100°C or more, compared to carbons that have undergone longer thermal soaks. However, their relevance in pointing out that aging will differ according to HTT is undiminished. Therefore, the positive effect of increasing the surface area (and by implication porosity) on flux may be offset by larger degrees of aging because of the higher concentration of dangling bonds.

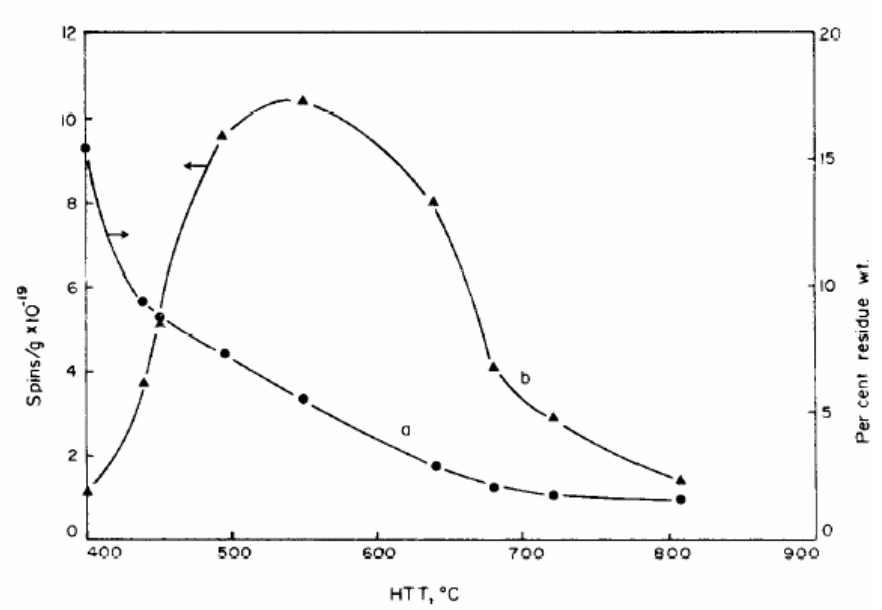

Figure 4-13. Comparison between char residue weight (curve a) and free spin concentration (curve b) as a function of char HTT (Bradbury and Shafizadeh, 1980)

The most likely sites for chemisorption are with free radicals in the carbon lattice. However, another important conclusion from kinetic experiments in the study of Bradbury and Shafizadeh (1980) is that chemisorption can also proceed by the saturation of diene bonds in the carbon structure, which is an activated reaction. The range of activation energies calculated from the experiments indicated that a range of activated sites are available, which may explain the long periods over which aging occurs, as observed by Menendez and Fuertes (2001).

4.5.2 Exposure to water vapour

Carbon surfaces are generally hydrophobic, but oxygen-containing surface groups provide primary sites for the physisorption of water molecules. These adsorbed molecules attract further molecules via hydrogen bonding, producing water clusters within the pores (Dubinin, 1980; Lagorsse et al., 2005a).

These reduce the available pore volume and may eventually lead to pore blocking at high humidity levels (Jones and Koros, 1995a/b). They found in continuous tests with humidified feed that most productivity loss occurred in the first few hours of exposure, as water molecules attached themselves to active sites at critical restrictions in the pores. The initial exposure phase was followed by a more gradual filling of pores. At low humidities (23% RH), significant membrane productivity was maintained, whereas high RH's (85%) resulted in severe decreases in productivity. Jones and Koros (1995b) also found that the effect of water vapour adsorption differed between membranes carbonized at 500 and 550°C, due to the differences in porosity and surface chemistry. Membranes in that study were regenerated to approximately the original permeances by heating to 80°C in a vacuum oven for a period of hours.

Sedigh et al. (1998) tested a reformate mixture ($H_2/CH_4/CO/CO_2$) on a poly(furfurylalcohol) derived CMSM at 293 K, in a continuous feed configuration. They observed a decrease in permeance for all gases over a period of 8 days, the CO_2 and CH_4 permeances dropping to

40% of the original values. It was speculated that traces of water vapour in the feed gases caused the aging and they found that full regeneration was possible at 400°C in an Argon atmosphere.

4.5.3 Exposure to nitrogen

Menendez and Fuertes (2001) investigated the storage under nitrogen of carbon membranes derived from phenolic resin. It was seen that N_2 reduced aging rather than causing it. Some permeation loss was seen, but was ascribed to exposure to air when handling the membranes.

Groszek et al. (2002), however, found that the energy of adsorption for both N_2 and O_2 in carbon molecular sieve fibres were in the range of chemisorption. The reason for the strong adsorption of N_2 was thought to be the "tight fit between the molecules and the walls of the micropore in which they reside". This effect would be increased at constrictions in the micropores.

4.5.4 Exposure to organics

Organic compounds have a very high affinity for carbon surfaces. Furthermore, the weak dispersion interactions between organic molecules and carbon walls responsible for adsorption are also enhanced in narrow micropores, as the adsorption potentials of the opposite walls are superimposed (Dubinin, 1980). At pore restrictions, this superimposition effect is highest and molecules can block the pore.

Jones and Koros (1994b) investigated the effect of exposure to propane, propylene, C6 and higher hydrocarbons, as well as subsequent regeneration. Exposure to air saturated with these organics in a continuous rig resulted in a decrease in O_2 flux with time. The higher organics caused a complete loss of flux. This was slowly restored in some cases by flushing with dry air, whereas heating to 90°C in a vacuum proved ineffective. Exposure to pure propylene followed by dry air was far more effective and some cases enhanced recovery. It was speculated that the propylene had acted as a cleaning agent and had removed other compounds from the carbon surface. They observed no flux decline caused by methane.

Menendez and Fuertes (2001) investigated the effect of storing carbon membranes derived from phenolic resin under propylene. They found that the permeance of gases increased after exposure to propylene. It was speculated that hydrocarbon molecules caused expansion of the carbon pores, by strong adsorption into the slightly flexible carbon matrix. They also prevented access to the pores by oxygen.

Higher hydrocarbons may, therefore, be detrimental for separation performance, even if present in trace amounts.

4.6 Application of carbon membranes for hydrogen separation

A review of the application of carbon molecular sieves in hydrogen separation is presented in this section. The current state of carbon membrane module fabrication is also investigated.

4.6.1 Module fabrication

The carbon molecular sieve material must be able to be formed into a configuration that is robust, hydraulically efficient, of a high packing density (metres squared of membrane per metres cubed of module volume) and low pressure drop, in a commercially practical manner. Attempts at achieving these characteristics include the carbonization of polymer hollow fibres (self-supporting) or carbonization of polymer layers on a support.

The challenge to producing self-supporting fibres on a commercial scale is the elimination of defects. Koresh and Soffer (1983) produced carbon hollow fibres with a diameter of 140 microns and a wall thickness of just 6 microns, which withstood pressure differences (feed to permeate) of up to 10 atm. Carbon membranes Ltd (Israel), a former company that included Soffer, later patented methods for carbonizing bundles of cellulose fibres with far fewer defects (Soffer et al., 1999) and a method of potting fibres into tube sheets (Avraham and Dagan, 1999). Carbon hollow fibres are often dismissed as being too brittle. However, they do have the ability to bend and withstand high pressures. Soffer et al. screened pyrolysed cellulose fibres by passing them through a tube with a curvature radius of 1.5 cm, and measured internal burst pressures of 50 to 120 bar. Tanihara et al. (1999) successfully tested carbon molecular sieve asymmetric hollow fibres for H_2-CH_4 separation at feed pressures of 10-50 bar. Carbon hollow fibres, in summary, are able to withstand operational pressures (perhaps as long as they are not exposed to sudden pressure shocks).

Soffer et al. (1996) described a method of selectively clogging the failed fibres in a bundle, greatly simplifying production and maintenance. Carbon Membranes was able to produce large modules (4 m^2) with a packing density of 2000 m^2/m^3 (Lagorsse et al., 2005b). Soffer and co-workers (1999) further developed methods to carbonize cellulose hollow fibres. They found that the use of a gaseous Lewis acid or ionic salt carbonization catalyst reduced structural defects in the final membranes. They also proposed a carbonization profile, determined mainly by the demands of the catalyst, which involved heating rates <1°C/min and frequent isothermal dwells, to allow time for penetration of the catalyst and escape of pyrolysis products.

The MEMFO group at NTNU purchased a small carbon molecular sieve hollow fibre module in 2000 from Carbon Membranes Ltd, containing 100 fibres 35 cm long and 165 microns in diameter. Intended for CO_2/CH_4 separation, it is rated to 120°C and a maximum pressure of 20 bar (gauge). The module has been used in the group and at the University of Southern Denmark (Odense) for the upgrading of biogas, without failure. Unfortunately, Carbon Membranes Ltd closed down in 2001.

Another, novel configuration for CMSMs was synthesized by Lagorsse et al. (2005b). They produced a honeycomb membrane module by carbonizing corrugated sheets of phenolic resin on a paper support. This module can be manufactured commercially using available methods. A packing density of 2500 m^2/m^3 and a surface area of 10 m^2 were obtained.

4.6.2 Hydrogen from methane and carbon dioxide

Koresh and Soffer (1987) performed an early study on the separation of H_2 from CH_4 in both static and continuous feeds, using a carbon molecular sieve membrane. They tested different feed compositions at temperatures between -80 and 500°C. It was observed that, at 200-500°C,

where they expected the adsorption of CH_4 is negligible, the gases behaved independently in the pore network and the measured mixture permeability followed the relationship described by Equation (32). It was suggested that, as the residence time of the molecules at the constrictions is short, there was no hindrance of H_2 by CH_4. The individual gas permeabilities were, therefore, independent of the gas fractions.

$$P_{Exp} \approx P_{Cal} = P_{H2} \cdot y_{H2} + P_{CH4} \cdot y_{CH4} \quad (32)$$

where P_{Exp} is the measured permeability of the mixture, P_{Cal} is the calculated permeability of the mixture, P_{H2} and P_{CH4} are the measured pure gas permeabilities and y is the molar fraction of the gas.

Although the hydrogen permeabilities were markedly lower in the lower temperature range, it was observed that the single gas permeabilities still appeared to be independent of the feed composition, despite the fact that there would have been significant adsorption of methane in the pores. It was also known that the permeability of CH_4 at 25°C decreases as pressure is increased, as expected for an adsorbing gas (as explained in Section 4.4.2). The authors speculated that the hydrogen and methane must occupy different positions prior to the activated jump through a constriction and therefore did not hinder each other. The carbon membrane, which was described as having a relatively open pore structure, achieved mixed gas hydrogen permeabilities in from 55 to 3220 Barrer in the temperature range of -80°C to 200°C, with a selectivity of approximately 35. Plotting log (permeability) vs 1/T (K) did not produce a straight line.

However, Koresh et al. (1990) also showed that methane molecules can cause a slow barrier build-up over a few constrictions in series at the outer ultra-micropores in a TCM 128 carbon cloth that had been activated, and therefore can hinder other gases from permeating.

Jones and Koros (1994a) investigated the separation of a 50% H_2-50% CH_4 mixture using a polyimide-based carbon molecular sieve membrane. The separation was performed at ambient temperature and pressures up to 825 kPa. Permselectivities of 400-550 and permeances of 100-225 GPU (gas permeance unit, 1 GPU = $2.74 \cdot 10^{-3}$ m^3(STP)/m^2.bar.h) were measured and it was seen that the selectivity and permeance of both H_2 and CH_4 declined with increasing pressure. However, even at high pressures, the performance was much better than polymeric membranes.

Sedigh et al. prepared CMSMs by pyrolysing layers of poly(furfurylalcohol) on ceramic supports at 600°C. These were then used to separate CO_2/CH_4 and $H_2/CH_4/CO/CO_2$ mixtures at various temperatures, in a continuous rig. It was seen that the separation factor with respect to CH_4 was lower in the mixed gas tests than the single gas tests, for all gases. The authors argued that CO_2 is the most strongly adsorbing gas and occupies most of the pore space, hence the decrease in selectivities for the multi-component mixture. The separation factor for H_2/CH_4 in the multi-component mixture was approximately 5, with an H_2 flux of 0.005 cm^3/cm^2.psi.min (4.3×10^{-2} m^3(STP)/m^2.bar.h) at 293 K to 0.02 cm^3/cm^2.psi.min (1.7×10^{-1} m^3(STP)/m^2.bar.h) at 410 K. The CH_4 permeance also increased with temperature, demonstrating activated diffusion, and the selectivity with respect to CH_4 was seen to decrease with temperature in the multi-component mixture. Selectivity increased slightly as the CO_2 content in the binary mixture increased.

Rao and Sircar (1993) developed carbon membranes with relatively large pores (5-5.5 Å) which separate H_2 from hydrocarbons by selective adsorption (selective surface flow). The selectivity of CH_4 over H_2 was low (~2), while more strongly adsorbed hydrocarbons, like ethane and propane, had higher selectivities (10-44.5).

Tanihara et al. (1999) prepared carbon molecular sieve membranes from polyimide at 750°C and applied them to H_2, CO_2 and CH_4 separation at 50-80°C and 10-50 bar. Toluene was also added to the feed mixture to study any possible influence. They showed that the permeability and selectivity of H_2 over the other gases were little affected by pressure or the concentration of toluene. Mixed gas hydrogen permeances of about 4.10^{-4} $cm^3(STP)/cm^2.s.cmHg$ (GPU) and selectivities over methane of about 500 were measured. Significantly, little change in permeation properties was observed over the duration of the tests.

A non-exhaustive Robeson plot of single gas results for H_2/CH_4 separation from the literature is shown in Figure 4-14. This type of plot shows the trade-off between permeability or permeance (permeability divided by active membrane thickness) and selectivity. The observed upperbound for polymeric membranes is also exhibited (Robeson, 1991).

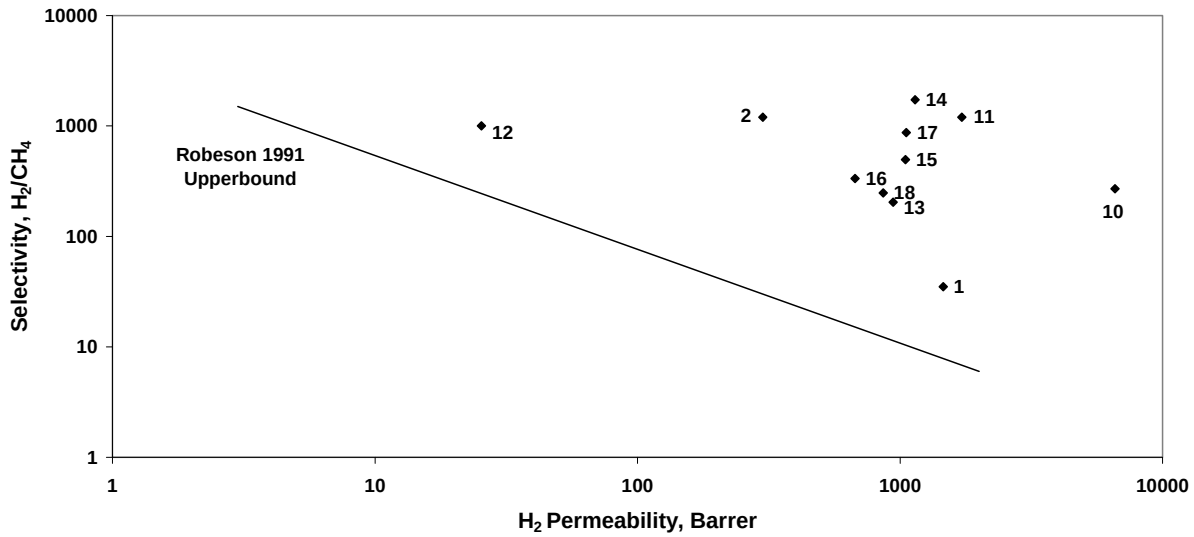

Figure 4-14. Robeson plot for single gas H_2/CH_4 separation with CMSMs. Key to labels in Table 4-5

The permeance of the membrane is often published, especially in the case of hollow fibres, for which the active layer thickness of the asymmetric membrane is difficult to define. In this work, flat films with uniform thickness are prepared, allowing for the straightforward calculation of permeability. Part of the developmental objective of this thesis is to evaluate the various preparation parameters, such as metal addition and carbonization temperature. The resultant performance must be compared on the basis of permeability, which is a material property and independent of the geometry of the membrane. For this reason, only reported permeability-selectivity pairs are presented in Figure 4-14. Permeance data has been listed in Table 4-5

Table 4-5. Reported carbon membrane performances for H_2-CH_4 separation

No.	Membrane	H_2 permeability, Barrer	H_2 permeance, $m^3(STP)/m^2.bar.h$	$\alpha_{H2/CH4}$	Ref.
	Possibly cellulose, 650-750C,				
1	Post-oxidation, Koresh	1460		35	1
2	Cell., 800C, Ar	300		1200	2
3	Phen. Form., 900C		0.01	171	2
4	Polyim. 550C, Vac, Koros		1.26	110	2
5	Polyim. 550C, Ar, Koros		1.90	31	2
6	Polyim. 550C, He, Koros		1.80	6	2
7	Polyim. 550C, CO_2, Koros		1.75	30	2
8	Polyim. 700C, 3.6 min, Kusuki		2.67	132	2
9	Polyim. 850C, 3.6 min, Kusuki		0.48	631	2
10	Polypyrrol., 500C, 1h, Kita	6580		270	2
11	Polypyrrol., 700C, 1h, Kita	1720		1200	2
12	Polypyrrol., 800C, 1h, Kita	25		1000	2
13	HC, 550C,Vac, Lie	941	0.06	204	3
14	HC,CuN, 550C, Vac, Lie	1141	0.05	1725	3
15	HC, FeN, 550C,Vac, Lie	1049	0.04	494	3
16	HC, SiO2, 550C, Vac, Lie	673	0.04	334	3
17	HC, MgO, 550C, Vac, Lie	1055	0.05	871	3
18	HC, CaO, 550C, Vac, Lie	863	0.05	248	3
19	BP-PI,700C,N2,(50C,Mix'd)		1.12	540	4
20	BP-PI,700C,N2,(120C)		4.00	100	4
21	BP-PI,850C,N2,(50C)		0.21	380	4
22	BP-PI,850C,N2,(120C)		0.83	680	4
23	PM-ODA PI,950C,Vac(35C)		0.002	1080	4
24	PM-ODA PI,950C,Vac(250C)		0.22	140	4
25	PM-ODA PI,950C,Vac(0C)		0.00	720	4
26	6F/BP-3MPD PI,500,(Mix'd)		0.26	520	4
27	6F/BP-3MPD PI,500,(Mix'd)		0.29	210	4
28	6F/BP-3MPD PI,550,(Mix'd)		0.59	500	4
29	BP-ODA PI,700C,N2,(He/CH4,65C)		0.67	110	4
30	BP-ODA PI,800C,N2,(He/CH4,65C)		0.10	240	4
31	Phenolic resin,600C,N2,(35C)		0.14	37	4

References: 1) Koresh & Soffer,1987, 2) Saufi & Ismail, 2004, 3) Lie,2005 and 4) Tanihara et al, 1999
Membrane description: *Precursor, additive (if any), final carbonization temp., soak, carb. environment, first author (if known), (perm. test conditions)*

The H_2/CH_4 permselectivity ranged from 6, for very open membranes, to1725 for the CuN-doped cellulose membrane prepared by Lie. Another observation is that the most selective membranes were derived from cellulose (2 and 14).

Less data is available in the literature for H_2/CO_2 separation. A non-exhaustive Robeson plot of carbon membrane performance in H_2/CO_2 separation is shown in Figure 4-15. It is clear that carbon membranes perform worse than the polymer upperbound (Robeson et al., 1994). Carbon membranes would not be the technology of choice unless process conditions excluded polymers, for example in high-temperature applications.

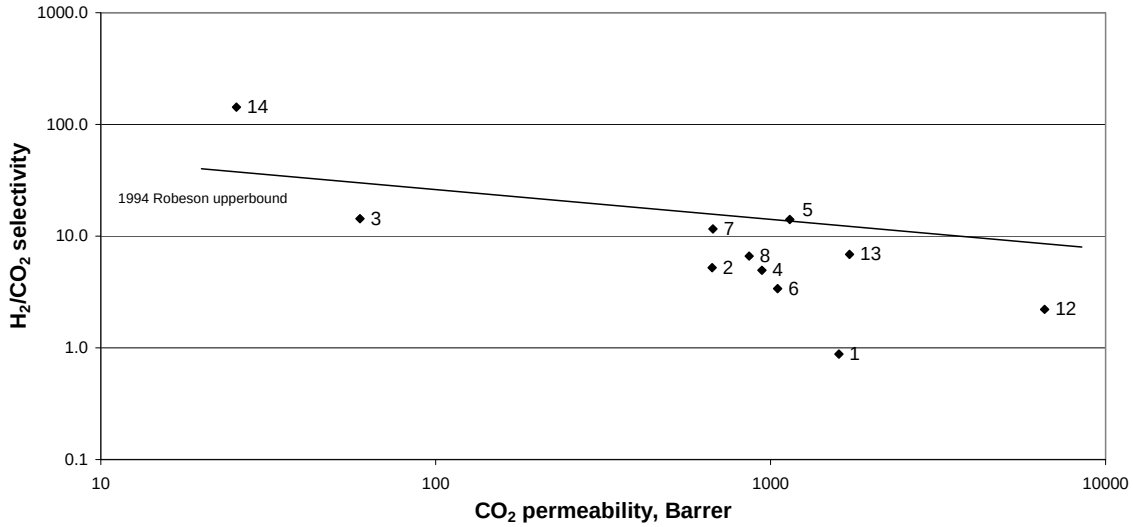

Figure 4-15. Robeson plot for single gas H_2/CO_2 separation with CMSMs. Key to labels in Table 4-6

The H_2/CO_2 selectivity of CMSMs ranges from about 0.9 to 14, with one membrane achieving 143 at a very low permeability (14).

Table 4-6. Reported carbon membrane performances for H_2-CO_2 separation

No.	Membrane	H_2 permeability, Barrer	H_2 permeance, $m^3(STP)/m^2.bar.h$	$\alpha_{H2/CO2}$	Ref.
1	Kapton, 600C, 2h, Suda	1600		0.9	1
2	Kapton, 800C, 2h, Suda	669		5.2	1
3	Kapton, 1000C, 2h, Suda	59.4		14.3	1
4	HC, 550C,Vac, Lie	941	24	5.0	2
5	HC,CuN, 550C, Vac, Lie	1141	18	14.1	2
6	HC, FeN, 550C,Vac, Lie	1049	14	3.4	2
7	HC, SiO2, 550C, Vac, Lie	673	13	11.6	2
8	HC, CaO, 550C, Vac, Lie	863	18	6.6	2
9	Kapton, 600C, 2h		1500	1.3	1
10	Kapton, 800C, 2h		790	4.0	1
11	Phenol Formald., 900C, 1h		5	8.3	1
12	Polypyrrol., 500C, 1h, Kita	6580		2.2	1
13	Polypyrrol., 700C, 1h, Kita	1720		6.9	1
14	Polypyrrol., 800C, 1h, Kita	25		143	1

References: 1) Saufi & Ismail, 2004 and 2) Lie,2005
Membrane description: *Precursor, additive (if any), final carbonization temp., soak, carb. environment, first author (if known), (perm. test conditions)*

Adsorption-selective membranes can also be used to recover hydrogen from carbon dioxide. Rao and Sircar (1993) developed an SSF carbon membrane (5-5.5Å) to selectively permeate CO_2 from an H_2-CO_2 mixture, achieving a selectivity of ~20 at 257 K. They proposed incorporating this membrane into a PSA process to recover H_2 from the PSA off-gas (Sircar et al, 1999).

4.6.3 A discussion of results presented in literature

Following the discussion of factors influencing membrane performance, some comment is required on results presented in the literature. The first weakness in published results is the lack of aging information, which, as demonstrated by Menendez and Fuertes (2001), can

cause an 80% reduction in methane permeability over 5 months. Without the age and knowledge of the susceptibility of the material to aging, one cannot know if the published results are for new (optimistic), somewhat-aged (transitional) or final state membranes and so values cannot be assumed to be applicable for commercial operation. There is a need for a common basis of comparison.

The second major issue is with Robeson plots published for single gas pairs. Not only can one expect lower gas permeances in real operation with mixed gas feeds, due to competition for pore volume, but the values may be totally fictitious if reversed selectivity occurs. For example, a Robeson pairing that implies very high hydrogen productivity may be due to open pores that are actually in the correct range for competitive adsorption and blocking. An example of this occurring was reported by Sedigh et al. (1998), where hydrogen was the fastest permeant in a poly(furfuryl alcohol)-derived carbon membrane in single gas tests, but was slower permeating than CO_2 from an H_2-CO_2-CO-CH_4 mixture.

At best, single gas Robeson plots are a guide, providing partial information about a membrane’s pore size distribution.

5 Characterisation

Lie (2005), Marsh and Rodriguez-Reinoso (2006) and Rouqerol et al. (1994) provide comprehensive reviews of characterisation techniques relevant for carbon membranes. Only those methods used to characterise carbon membranes in this work will be discussed here.

5.1 Stereology

Since stereology involves the direct observation of a cross section of a solid, it should provide more realistic information on structure than indirect methods, such as gas adsorption, which require models for interpretation. Unfortunately, some features, such as ultramicropores, cannot be resolved by even the most powerful imaging techniques (Marsh and Rodriguez-Reinoso, 2006).

5.1.1 Optical microscopy

Optical microscopy is useful for detecting defects in, and characterising the macrostructure of, the carbon films.

5.1.2 Scanning electron microscopy

Scanning electron microscopy (SEM) involves the focussing of a beam of electrons at a sample, and forming the resulting scatter or emission of secondary electrons into a digital image. The wavelength of light is 400-700 nm, whereas the wavelength of electrons is a mere 0.001-0.01 nm. The consequence of this is that the resolution of an optical instrument using electrons to ‘illuminate’ a sample is higher than one using light. Magnification of 1 000 000× can be achieved (Goodhew et al., 2001).

Electrons are generated either thermionically (by heating a tungsten cathode to >2700 K) or by field emission (when a strong electric field is applied to the emitter). The latter must be accomplished at a very high vacuum, but generates a far brighter beam. In this work, a field emission SEM was used. An image is then assembled either from dislodged secondary electrons or by backscatter of the primary electrons.

The most used signal in SEM is that from secondary electrons. Primary electrons in the incident beam may transfer energy to electrons within the sample, causing one or more to escape and travel towards the detector. There is therefore an abundance of secondary electrons and a brighter image. These have low energy and must be accelerated with a further electrical field in order to excite the detector, or scintillator.

Primary electrons may also be deflected from the sample and themselves be detected. The density of backscattered electrons is lower, but the signal is related to the atomic number of the specimen. Thus, backscatter can be used to distinguish between phases with different chemical composition.

5.2 Thermal gravimetric analysis (TGA)

This method involves the heating of the sample under an inert or reactive atmosphere while simultaneously measuring its mass. Weight-loss curves are generated as a function of time and temperature, which are used to plot the pyrolysis behaviour of the precursor as a function of the heating protocol. TGA is also used to determine the non-combustible content (such as metal compounds) of the carbon membranes, by heating in air.

5.3 Mass spectrometry (MS)

Mass spectrometry is the study of matter through the formation of gaseous ions that are characterized by their mass and charge (Murray et al., 2006). MS generally consists of the formation of ions from a source, the separation of ions of different masses and the detection of the number of ions produced (measurement is based on the mass/charge ratio of the ions). The method of separation and measurement of ions varies; the instrument used in this work utilises a quadrupole mass filter. This device is essentially an ionization vacuum gauge equipped with a rod electrode system that separates the ions based on the mass/charge ratio before detecting them with an ion detector[5]. The four rod electrodes produce a high frequency electric quadrupole field between them that rejects ions that do not have a specific mass/charge ratio. Those that do are able to reach the ion detector.

5.4 Gas adsorption

An adsorption isotherm is a plot of equilibrium amounts of adsorbed gas in or on an adsorbent against the relative pressure (p/p_0) of adsorbate. As pressure increases, the smallest pores will be filled with adsorbate, followed by larger pores, until saturation pressure is reached. This pore filling process is related to the progressively weakening adsorption potential of pores as diameter increases (see Figure 4-4).

Gas adsorption can provide information on (Marsh and Rodriguez-Reinoso, 2006):

a) Overall extents of adsorption (adsorption capacity).
b) Pore size distributions (PSDs) of the porosity of carbons.
c) The presence of porosity with entrance dimensions <~0.7 nm diameter.
d) The presence of sites of high adsorption potential, effective at low relative pressures of the adsorptive.
e) The polarity of the surface of the carbon adsorbent (e.g. presence of surface oxygen complexes.

Modern procedures measure extents of adsorption using automatic volumetric methods which are suitable for most solids with surface areas greater than $1 m^2/g$ (Marsh and Rodriguez-Reinoso, 2006).

Nitrogen at 77K is most commonly used in gas adsorption, but due to its molecular dimensions, is only suitable for mesopore characterisation (Rouquerol et al., 1994). At low pore diameters (<0.5 nm), the diffusion of nitrogen is activated and adsorption becomes diffusion-rate controlled. These rates cannot be detected within the time span of one day. However, nitrogen isotherms still dominate the literature of studies of activated carbon. CO_2

[5] Source: Pfeiffer Vacuum Mass Spectrometer Catalog, June 2005

has been the gas of choice for overcoming the activation diffusion limitations experienced by nitrogen, and is suitable for probing pores <0.5 nm.

Nitrogen and carbon dioxide adsorption in porous carbons produce Type I isotherms (see Figure 5-1). These isotherms are typical of porous carbons with mainly microporosity (Marsh and Rodriguez-Reinoso, 2006; Koresh and Soffer, 1986). They are interpreted (linearised) using the Langmuir (Eq. (33)) or Dubinin-Radushkevich – (34)) equations, amongst others. The first is based on physical models of gas adsorption, the latter on the distribution of pore structure and hence adsorption potential. The DR equation is more relevant to adsorption processes than Langmuir.

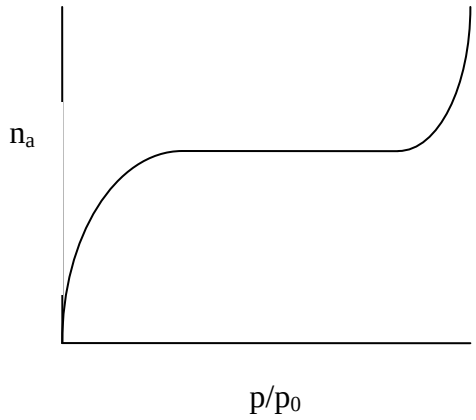

Figure 5-1. Type I isotherm illustration

$$\text{Langmuir} \qquad \frac{p/p^0}{n^a} = \frac{1}{bn_m^a} + \frac{p/p^0}{n_m^a} \qquad (33)$$

where p = equilibrium vapour pressure, p^0 = saturation vapour pressure, n^a =amount adsorbed and $n^a{}_m$ = monolayer capacity.

$$\text{DR} \qquad W = W_0 \exp[(-BT/\beta(\log^2(p^0/p)] \qquad (34)$$

where W is the volume of adsorbate filling micropores and W_0 is the total volume of micropore system.

The above equations predict the monolayer capacity, which is converted to a theoretical surface area via Eq. (35):

$$A_s = n_m^a N_a a_m \qquad (35)$$

where A_s is the surface area, N_a is Avagadro's number ($6.013.10^{23}$ $mole^{-1}$) and a_m is the area effectively occupied by an adsorbed molecule (m^2/molecule). The term *surface area* (m^2/g) is

ubiquitous in the literature and derives from the early interpretation of Langmuir and BET isotherms; that is, that gases cover internal surface area in a monolayer. Later understanding revealed that the monolayer concept in the complex, atomic surfaces in pores is incorrect and that a more realistic interpretation is simply that of *adsorption capacity* (mmol/g) (Marsh and Rodriguez-Reinoso, 2006), since micropore volume filling occurs as well. However, the use of the term surface area has become an intuitively convenient and prevalent description of porous solids. Realistically, though, these values should be interpreted as simply another method of describing adsorption capacity.

The Barret-Joyner-Halenda (BJH) method is usually used in conjunction with the Kelvin equation,

$$r_p = \frac{-2sV_L / RT}{\ln(p / p^0)} \qquad (36)$$

(where s is the surface tension (of N_2) and V_L is the liquid molar volume), to calculate the size distribution of mesopores. The Kelvin equation is based on the principle that capillary condensation occurs in pores with a specific diameter at a certain pressure[6].

5.5 Permeation

Permeation is the *raison d'etre* of membranes and single gas and mixed gas testing provide the ultimate evaluation of membrane performance. Permeation measurement can be carried out in a static dead-end configuration or a continuous set-up with a retentate.

5.5.1 Single gas tests

For the reason of convenience and accuracy, single gas tests are carried out in a static set-up. A vacuum of approximately 0.07 mbar is first drawn on both sides of the membrane. A gas is then charged to the feed side of the membrane at a positive pressure (2 bar is the standard in the MEMFO group) and the permeate side, still under vacuum, is isolated. The permeate pressure is then logged against time and the gradient, *dp/dt*, calculated as the gradient of the resulting graph. The permeability, P_i, is then calculated using:

$$P_i = \frac{dp}{dt} \cdot \frac{T^0}{p^0} \cdot \frac{V_p}{T} \cdot \frac{l}{p_f} \cdot \frac{1}{A_m} \qquad (37)$$

where T^0 and p^0 are at 0°C and 1 bar, V_p is the permeate side volume, T is the permeate temperature, p_f is the feed pressure, l and A_m are the membrane thickness and area, respectively. The assumption behind Eq. (37) is that the permeate pressure is negligible relative to the feed pressure. The feed pressure was always 2 bar or higher in this work and the permeate pressure was typically allowed to rise to 10 mbar or less, meaning that the permeate pressure was less than 0.5% of the feed pressure.

[6] Source: Coulter™ SA3100 surface area analyser manual

5.5.2 Mixed gas tests

Mixed gas tests were also carried out in a static set-up. A feed mixture was applied to the feed side of the membrane and the pressure rise and gas composition on the permeate side recorded (the apparatus and method are described in Section 6.6.3).

In mixed gas tests, the permeate partial pressure should not be neglected because it may be significant relative to the feed partial pressure, especially if the feed partial pressure decreases as the test progresses. For example, a 2 bar feed containing 5mol% H_2-95% CH_4 has a H_2 partial pressure of 0.1 bar. The permeate pressure was typically allowed to rise to 20 mbar or more for practical reasons concerning GC measurement. The highly selective carbon membranes produced an almost pure hydrogen permeate, meaning that the final permeate hydrogen partial pressure was >20% of the feed partial pressure.

The driving force must therefore be linked to the mass balance, when calculating permeabilities. The equation governing transport of a gas from one control volume to another (Figure 5-2), through a membrane, is given by Eq. (6).

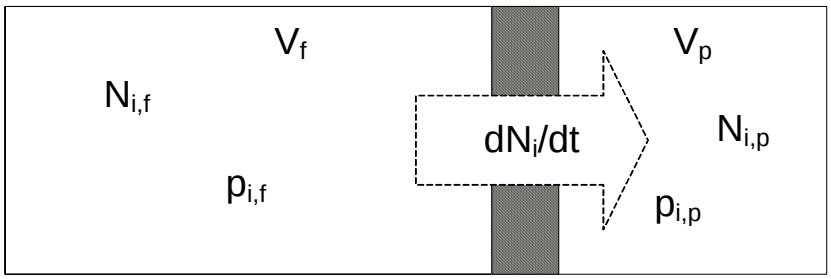

Figure 5-2. Mixed gas static permeation system

In addition, the molar balance for component *i* at any time is given by:

$$N_{i,f}{}^{o} = N_{i,f} + N_{i,p} \qquad (38)$$

Where $N_{i,f}{}^{0}$ is the original number of moles in the feed volume at the start (t = 0). From the ideal gas law, Eq. (38) can also be written as:

$$p_{i,f}{}^{0} \cdot V_f = p_{i,f} \cdot V_f + p_{i,p} \cdot V_p \qquad (39)$$

where V_f is the feed volume and V_p is the permeate volume. Rearranging Eq. (39) to be explicit in terms of $p_{i,f}$ and inserting into Eq. (9) yields:

$$\frac{dN_i}{dt} = \frac{V_p}{R \cdot T} \cdot \frac{dp_{i,p}}{dt} = A \frac{P_i}{l} (p_{i,f}{}^{0} - (1 + \frac{V_p}{V_f}) p_{i,p}) \qquad (40)$$

Rearranging Eq. (40) and integrating from t=0 to t=t_{final} and $p_{i,p}$ = 0 to $p_{i,p}$ = $p_{i,p,\,final}$ yields:

$$P_i = -\frac{l \cdot V_p}{B \cdot A \cdot R \cdot T \cdot t} \cdot \ln(\frac{p_{i,f^0} - B \cdot p_{i,p}}{p_{i,f^0}}) \qquad (41)$$

Where $B = 1+V_p/V_f$. $p_{i,f}^{0}$ is known from the initial condition of the feed. The final $p_{i,p}$ is determined by multiplying the final measured permeate pressure by the fraction of *i* calculated from gas chromatography of the permeate gas.

6 Membrane preparation and experimental procedures

6.1 Experimental program

The experimental program screened preparation variables for their effect on hydrogen permeability and selectivity and investigated the effect of operating conditions on separation behaviour. The variables considered in the program are summarised in Table 6-1.

Because of the difficulties, from an industrial perspective, in dissolving cellulose in benign solvents, alternative wood-derived polysaccharides were also investigated as precursors. As explained in Section 4.3, hemicellulose components have side chains that prevent crystal formation and allow them to dissolve in water. Xylan and galactomannan were included in the experimental program on the basis of their structure and the fact that they are commercially available. Xylan is the raw material for the production of xylitol and galactomannan is a polysaccharide with bulky galactose side groups.

Table 6-1. Screening program parameters

Parameter	Range	Possible effects
Membrane data		
Precursor material	Cellulose, Xylan, galactomannan	Profound effect on final structure, due to differences in carbonization chemistry and polymer chain packing
Metal type	$Cu(NO_3)_2$, $AgNO_3$	Influence on pore structure
Metal amount	0-6wt% (without complexed water)	Influence on pore structure
TFA exposure	0-100 days	Carbonization behaviour
Final carbonization temperature	375-700°C	Pore size distribution and surface structure
Oven type	TZF, HZS	Pore size distribution and surface structure
Carbonization atmosphere	Vacuum, Argon	Pore size distribution and surface structure
Age from carbonization date	1-460 days	Pore constriction, sorption capacity
Operating conditions		
Gas	H_2, CO_2, CH_4, C_2H_6, C_3H_6, N_2	
Components in feed	Single gas, mixed gas	Pore blocking, concentration polarization
Hydrogen content in feed	0-100 mol%	Pore blocking, concentration polarization
Temperature	0-180°C	Arrhenius effect, mixed gas behaviour
Pressure	0-6 bar (limited by equipment)	Mixed gas behavious, effect on *dC/dp* (sorption)

The length of time taken for each gas in the single gas permeation tests was dependent on the permeability of the gas. Straight-line hydrogen and CO_2 permeation plots could usually be obtained within 1 hour and 6 hours, respectively, whereas N_2 and CH_4 required at least 48 hours. At least 12 hours were typically used to evacuate the membrane (to remove adsorbed gas) between tests, and a leak test was performed with a duration as long as the slowest permeating gas in the series. A run with N_2, H_2, CH_4 and CO_2 would typically take 9 days. Since the object was to screen membranes for the effect of preparation parameters, priority was assigned to the gases most important in the chosen industrial cases to make the most effective use of the experimental time available. The first priority was the testing of membranes for the NaturalHy project (i.e. hydrogen from methane). It was also recognised that hydrogen-from-carbon dioxide separation could be important. Therefore, all membranes were screened with hydrogen and methane permeation and some were also tested with CO_2. Usually, those that were considered promising for application and hence likely to be the basis for simulations were tested with nitrogen and mixed gases.

Due to the expected non-linearity of the trends resulting from carbonization temperature and metal addition, 3-4 levels were chosen for each. As will be seen in the Results, the former produces a strong maximum.

6.2 Gases

Argon 5.0 (>99.999%), CH_4 4.0 (>99.99%), H_2 (>99.9%), N_2 5.0 (>99.999%) and CO_2 4.0 (>99.99%) as well as gas mixtures were supplied by AGA AS, Norway.

6.3 Precursor solutions

6.3.1 Cellulose-Hemicellulose

Most solutions were prepared by weighing a sample of hemicellulose-cellulose sheet (Södra Cell Tofte) with a Mettler Toledo AB204-S/FACT balance and placing it in a 50 ml Schott bottle. The precursor was lignin free and contained 15-20% hemicellulose. If called for, an amount of metal nitrate was weighed and added as well. 45 ml of trifluoracetic acid (TFA) was added as the solvent in most cases, unless otherwise indicated. The bottle was then tumbled until the polymer dissolved totally.

Cellulose dissolved readily in trifluoroacetic acid, usually forming a viscous solution within 3 days. The viscosity of the solution decreased steadily thereafter. Upon addition of copper (II) nitrate, small fibres were visible in suspension, even after a week of mixing in the TFA. It may be that the blue solution created by the copper nitrate provided enough contrast to make the white fibres more visible and that these were present in all solutions.

The Teflon® dishes used to cast the precursors were of a uniform depth and diameter. Therefore, the concentration of the cellulose dissolved in TFA determined the dried precursor film thickness. Originally, 1 wt% cellulose solutions were prepared for the membranes carbonized at 550°C. However, it was seen that attempts to carbonize these films at higher temperatures produced carbon films that were too thin to be handled easily in the permeation tests. The concentration of cellulose was then increased to 1.5wt%. This increase was enough to form significantly more robust carbon films.

The claim by Morrison and Stewart (1998) that cellulose could be dissolved in mixtures of acetic acid and TFA (up to ratios of 9:1) was explored (see Section 4.3.1 for discussion). A ratio of 9:1 did not dissolve the cellulose sheet or even cause it to break up after 4 weeks in solution. A 1:1 ratio caused a small amount of the cellulose to dissolve and the cellulose sheet to break up and reform into round flocs, due to the tumbling action of the spinner. The conclusion was that TFA-acetic acid solutions are not suitable for dissolving cellulose.

6.3.2 Xylan from birch wood

Xylan, which is a hemicellulose component, was sourced from Sigma-Aldrich Norway AS. Powder samples were measured and placed in a Schott bottle as described above, but with distilled water as the solvent. It was found that xylan did not dissolve completely at room temperature, even after tumbling for 1 week. However, on heating to 100°C in a microwave oven, it was observed that the xylan dissolved immediately to form a transparent, orange solution. It did not precipitate on cooling back to room temperature.

6.3.3 Galactomannan

Another component of hemicellulose, galactomannan, was also tested for its carbonization potential. Galactomannan from Locust Bean Gum (from *Ceratonia siliqua* seeds) was supplied by Sigma-Aldrich Norway AS. The material, in a powder form, was weighed and placed in a Schott bottle as with the other precursors described here and 45 ml of distilled water added. The material was dissolved in distilled water by mixing on the tumbler.

6.4 Casting and drying

Between 30 and 40 ml of polymer solution was poured slowly (in order to avoid bubbles) into a Teflon dish with a diameter of 95 mm and depth of 8mm, which had first been cleaned with acetone. The dish was placed on a balanced plate in order to maintain an even film thickness. It was then covered with an up-turned glass funnel, the neck of which was loosely covered with aluminium foil. The purpose of this was to reduce the drying rate in order to avoid uneven solvent evaporation and hence produce a smooth film. The secondary purpose was to prevent dust settling on the film. With this procedure, the drying time was approximately 3 days, before the film was robust enough to be prised from the Teflon dish.

In order to remove the remaining solvent dissolved in the polymer, further drying in a vacuum oven (Shel Lab 1410D, Sheldon Manufacturing, Inc, USA) was required. Flat discs with a diameter of 2 cm were punched from the hemicellulose film and placed between aluminium foil sheets. The discs and sheets were further sandwiched between two sheets of glass, to ensure that the discs did not warp while drying in the vacuum oven. The discs were dried for 18 hours at vacuum and 105°C.

6.5 Carbonization

Carbonization was carried out in one of two ovens at the research group. The first was a horizontal *Carbolite® TZF 12/100/900* (Hope Valley, UK) three-zone tube furnace, controlled by a Eurotherm 2408CP temperature regulator (Figure 6-1). The furnace tube was an alumina tube of 80mm ID, delivered by Chemi-Teknik AS, Oslo. The furnace tube was connected by stainless steel end caps to a vacuum pump (RV5 from BOC Edwards, UK), allowing a vacuum of 0.34-0.41 mbar to be drawn during carbonization. The end caps were

sealed using Viton® o-rings and gaskets, together with Molykote® heat-resistant grease. The pressure was measured using a MKS Baratron® 626 pressure transducer. The vacuum line included a coil which passed through a dewar of liquid nitrogen. The purpose of this was to trap volatiles from the pyrolysis process and prevent back-diffusion of oil vapour from the vacuum pump. The films to be pyrolysed were placed on a stainless steel grid (mesh size 3 mm).

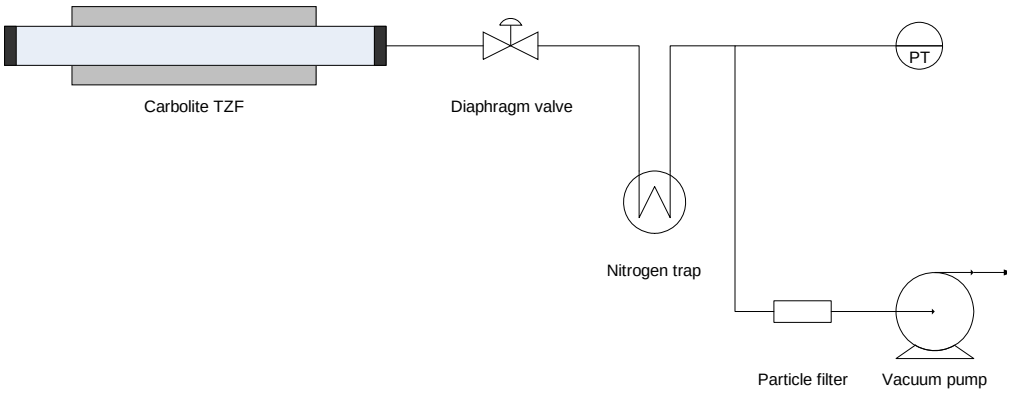

Figure 6-1 TZF furnace set-up

The second furnace was a horizontal *Carbolite® HZS 12/600E* split three-zone tube furnace, also controlled by a Eurotherm 2408CP temperature regulator. The working tube was quartz and was constructed at the glass work-shop in Realfagbygget at the NTNU. The split furnace construction and quartz tube allowed the precursor films to be observed during the carbonization procedure. The ends of the tube were sealed with stainless steel caps secured with clamps; one end connected to a vacuum pump while the other was connected to a flow-controller set-up (Figure 6-2). The films were placed inside the oven on a grooved quartz plate.

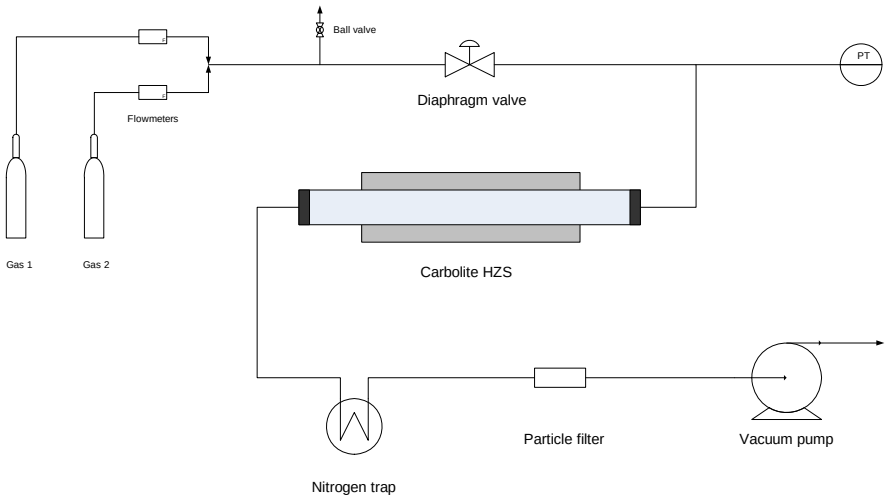

Figure 6-2. HZS furnace set-up

The flow-controller section could be isolated with a diaphragm valve, allowing the furnace to be operated in vacuum mode. Alternatively, the vacuum pump (RV3 from BOC Edwards, UK)

could be disconnected and a gas sweep applied to the furnace tube, via the two MKS Mass-Flo® flow controllers. One controller was rated to 10 standard cubic centimetres per minute (sccm) and the other to 500 sccm. The purpose of these controllers was to allow:

1. Inert sweeps to be applied,
2. sweeps containing low fractions of oxygen, to be used for pore opening procedures and
3. sweeps containing hydrocarbons, to be used in chemical vapour deposition.

The pressure in the furnace was measured using a MKS Baratron® 626 pressure transducer (rated to 10 mbar) and found to be 0.02-0.05 mbar when at full vacuum.

6.5.1 Carbonization heating procedure

The heating procedure (see Figure 6-3), for both vacuum and inert gas flow, followed that used by Lie and Hägg (2005, 2006). This procedure was first proposed by Soffer et al. (1999). Although the latter developed the procedure to facilitate catalysed carbonization, it was found by Lie to produce reliable and defect-free carbon flat sheets and so adopted in this work. The slow rate of heating and dwell times are thought to allow time for mass transfer (such as the removal of absorbed water and evolved pyrolysis products) to occur with setting up warping stresses in the film. Soffer et al. (1999) also found that having dwell times increased the durability of the carbon fibres. It will be shown with thermogravimetric analysis in Section 7.1.2 that the procedure suits the pattern of mass loss under continuous heating.

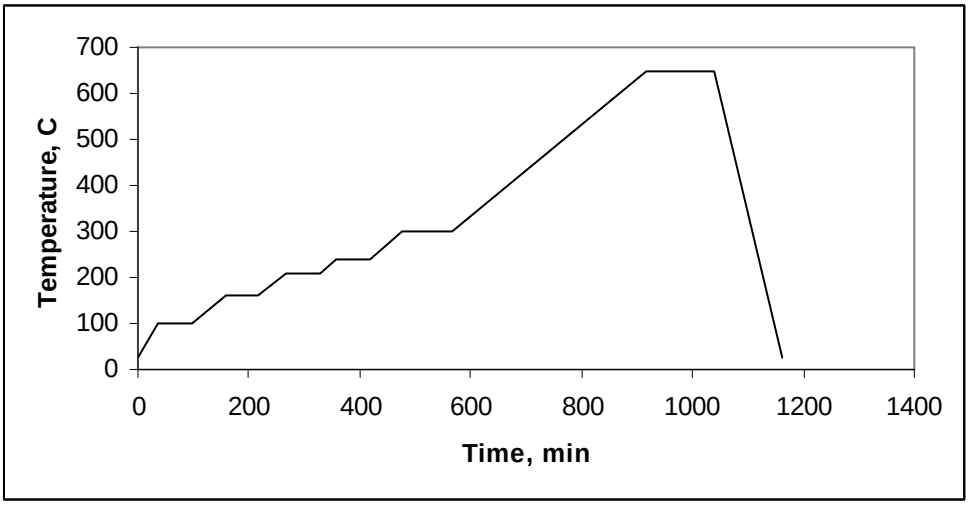

Figure 6-3. Typical carbonization heating profile (for 650°C HTT)

An isothermal dwell of 2 hours is included in the end. It was thought that this would allow time for completion of the first order pyrolysis reactions (as discussed in Section 4.3.2), as well as the elimination of free radical sites by rearrangement of carbon bonds. This is desirable as less free radical sites may result in a lesser degree of aging. As shown by Bradbury and Shafizadeh (1980) (see Section 4.3.2), the concentration of free radical sites decreases after at 550°C, but this is also dependent on the heat treatment time.

6.5.2 Inert gas flow

The HZS split furnace was used to prepare membranes under inert gas flow. The furnace tube and membrane precursors were first evacuated overnight to remove oxygen. Argon 5.0 (>99.999%) was then bled into the tube until the pressure was slightly higher than atmospheric and the outlet on the vacuum side opened. The outlet line from the furnace tube was 2 metre long and the end opposite to the furnace tube was placed into a bucket of water, in order to prevent oxygen from the air diffusing against the flow of argon into the furnace. The flow of argon over the samples was controlled by the MKS flow controller. The gas superficial velocity was varied between 1 and 4 cm/min.

6.6 Permeation tests

6.6.1 Membrane mounting

The membrane was mounted onto the bottom half of a cell, which is shown in Figure 6-5. This was done by first sandwiching the membrane between two doughnut-shaped layers (annuli) of aluminium tape (3M 7940, max. temp. 150°C). Higher temperatures were attained in tests than the stated maximum, but the tape was found afterwards to be intact. The sandwich was then secured on top of the membrane cell frit with a third annulus of aluminium tape (Figure 6-4). Filter paper (S&S 581 Filter paper) was also placed between the membrane and the metal frit of the cell before securing, so as to provide a cushion. Finally, epoxy (Devcon S-208/20845 (max. temp. 93°C) or Huntsman Araldite 2012 (max. temp. 200°C)) or Silicone adhesive (Dow Corning Q3-1566, for tests up to 350°C) was used to seal the edges where the membrane meets the inner annulus and the inner annulus meets the inner edge of the covering annulus.

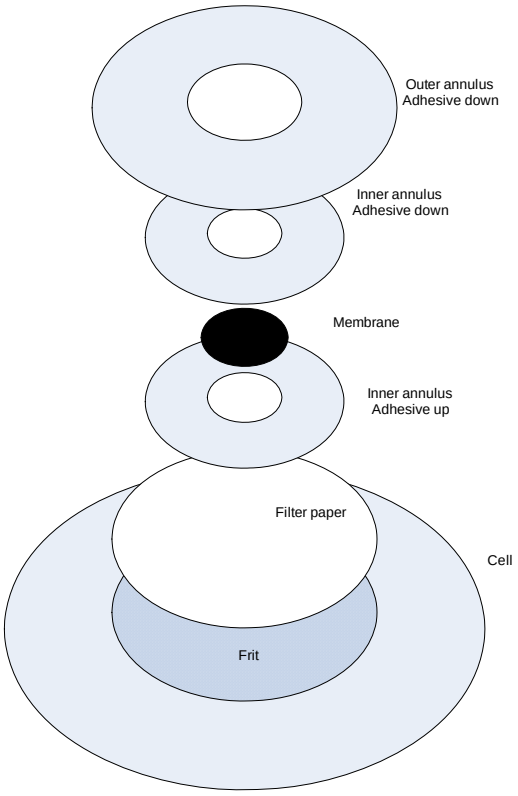

Figure 6-4. Masking the membrane

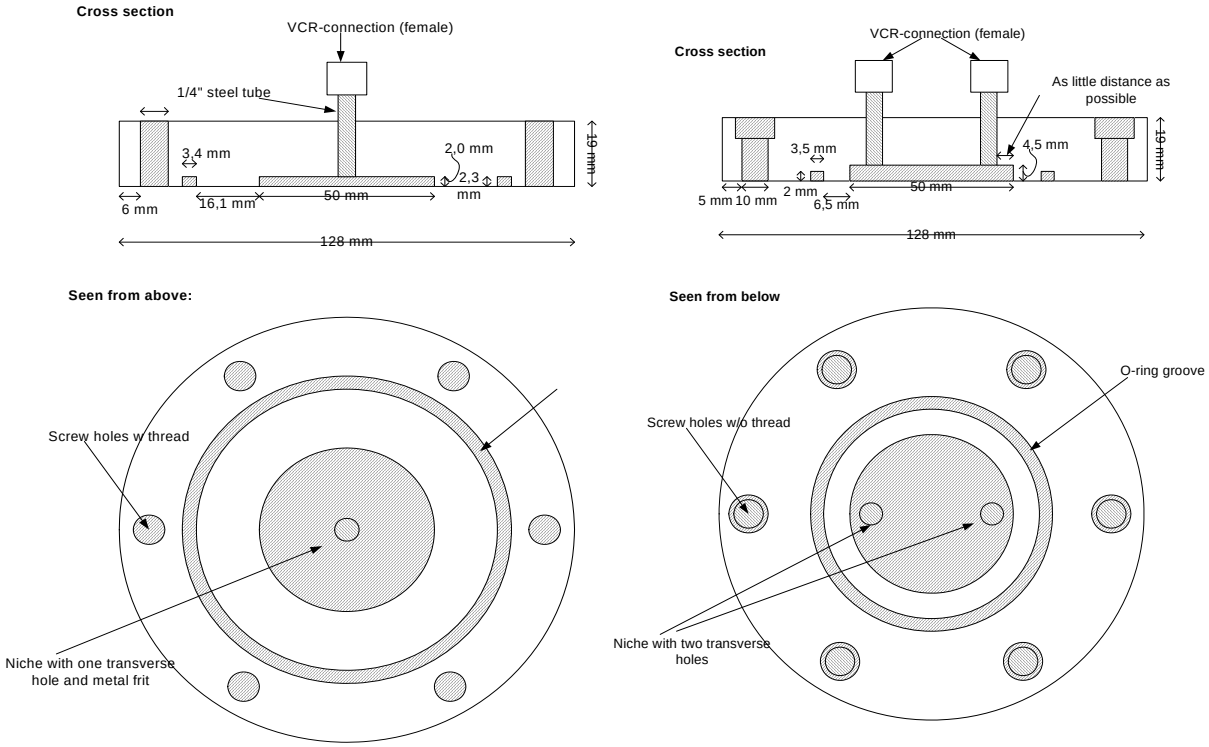

Figure 6-5. Bottom half of membrane cell (left) and top half (right)

6.6.2 Single gas testing

Mixed gas and single gas permeation tests were carried out in the rig shown in Figure 6-6.

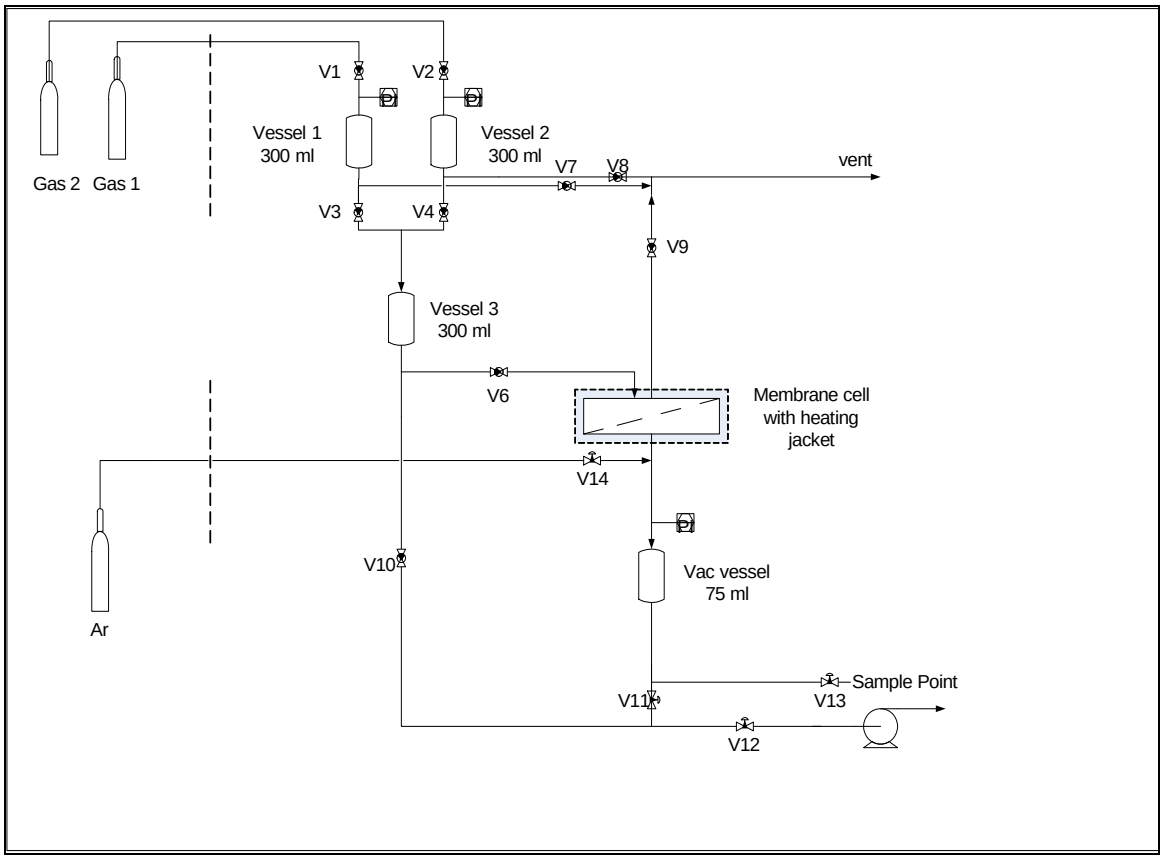

Figure 6-6 Permeation rig flowsheet

The bottom section of the permeation cell, with the mounted membrane, was connected to the vacuum vessel via a VCR connection on a ¼ inch tube. With valves 10 and 13 closed, the permeate side was evacuated with a BOC Edwards vacuum pump (Model RV5) until the pressure decreased to approximately 1 mbar, which indicated an absence of leaks in the membrane mounting. The top half of the cell was then connected to the bottom half with 6 bolts. Sealing between the two halves was obtained with two concentric viton o-rings. A Horst GmBH (Germany) custom shaped heating jacket was then secured around the permeation cell, making sure that nothing of the cell was left exposed. The heating jacket was set to the required test temperature using the integrated Horst HT MC1 temperature regulator.

Valve 11 was closed and valve 10 opened so that the feed side could be evacuated. Once the pressure on the feed side had decreased to 0.07 mbar (abs), valve 10 was closed and valve 11 opened so that evacuation of the permeate side could continue. This was done for a period of at least 16 hours. The purpose of this evacuation was to remove gases that were adsorbed both on the steel walls of the rig and in the membrane itself.

Once evacuation was complete, the feed side was charged via valves 1 or 2 to the desired pressure. Before this was done, valve 6 was closed so that the membrane would be isolated until pressure was reached. Data logging of the time, feed side and permeate side pressures were begun, using LabVIEW™ v6.1 (National Instruments, USA) and valve 6 opened to expose the membrane to the gas. After testing was complete, the leak rate was measured and subtracted for each gas series.

6.6.3 Mixed gas testing

6.6.3.1 Feed preparation

The procedure for static mixed gas tests was similar to that utilised by Koresh and Soffer (1987) for their H_2-CH_4 tests. In that set-up, a single vessel was used to create a mixture of a certain composition by introducing each gas in sequence, at a certain pressure, to a vessel. They found that 30 minutes was sufficient for diffusion mixing to be complete.

The feed side geometry in the permeation rig, shown in Figure 6-6, is more complex than that used by Koresh and Soffer. The procedure for producing a feed gas mixture with the molar fractions y_1 and y_2 and total pressure, P_3, in the rig shown in Figure 6-6, is as follows:

1. The sections around vessels V1, V2 and V3 are evacuated together via Valve 1.
2. Valves V6, V3 and V4 are closed.
3. Vessels 1 and 2 are each charged with a gas to pressures P1 and P2, respectively. These pressures will determine the final gas mixture pressure and composition.
4. Valves V3 and V4 are opened and the gases allowed to mix for at least 5 hours.

The tubes between the vessels and the membrane cell create a distance from the bulk gas that may slow diffusion mixing, so several hours were allowed before starting an experiment.

The molar concentration in the final gas mixture is determined by the initial pressures in each of the individual gas vessels. Due to the significant variation in compressibility factor, Z, with pressure with some of the gases measured, the ideal gas law was not sufficient for calculating the initial number of moles of each gas. This was especially the case with non-ideal gases such as CO_2 at high pressure. Therefore, the virial equation, truncated to two terms, was used to determine the required initial pressures (Smith and Van Ness, pg 78).

$$Z = \frac{PV}{RT} = 1 + \frac{BP}{RT} \qquad (42)$$

The following second virial coefficients, B, were taken from the CRC Handbook of Physics and Chemistry.

Component	H_2	CH_4	CO_2	N_2
B, cm^3/mol	15	-43	-126	-4

By defining the required molar concentrations in the final mixture (y_1 and y_2) and the required pressure, and since the volumes of sections 1, 2 and 3 are known, it is possible to calculate the required initial pressures of each gas in vessels 1 and 2.

This is given by:

$$P_i = \frac{P_T V_T}{V_i} . y_i \Big/ \left(1 - \frac{P_T V_T B_i}{V_i RT} . y_i \right) \qquad (43)$$

Where p_i is the pressure of pure gas i in volume i, V_i is the volume of vessel *i*'s section, V_T is the total volume of vessels and tubing in the feed section and B_i is the second virial coefficient for gas *i*.

6.6.3.2 Permeation rate and permeate composition measurement

Once sufficient feed mixing time had elapsed, Valve 6 in Figure 6-6 was opened to expose the membrane to the feed gas, and the subsequent pressure rise on the permeate side recorded. After at least 20 mbar had been reached (usually 135 mbar), the permeate side was flooded with Argon via Valve 14, to a pressure of 2 bar (abs). This was allowed at least 1 hour for mixing before Valve 13 was opened to bleed gas to an Agilent Technologies 6890N GC system (incorporating one mole sieve and one carbon PLOT column). Once a sample was taken, V13 was closed again. This procedure was repeated four times (the first was generally discarded to avoid previous samples contaminating the line to the GC). The permeate gas concentrations calculated by the GC software (GC ChemStation by Agilent Technologies) were normalised without the Argon value. These mole concentrations were used to distribute the total permeability, calculated from the pressure rise vs. time, between the individual permeants.

Calibration of the GC software was carried out using 93% Ar-6.5% H_2-0.5% CH_4 and 10% N_2-50% H_2-40% CO_2 mixtures provided by AGA AS (Oslo).

6.6.3.3 Continuous feed tests

It was observed that the static (i.e. dead-end feed) tests produced pressure-time graphs with a curvature that was not fully explained by increases in the permeate partial pressures relative to the feed partial pressures (Figure 6-7). Pore blocking by the heavier components was ruled out because gas that flowed on the feed side did not produce a curved *dp/dt* graph, therefore it was concluded that a concentration difference must be developing between the bulk gas in the vessels and the membrane. As a consequence, when ready mixed feeds were available, continuous tests were performed by flowing ready-mixed feed gas from a gas cylinder over the feed side and out through the retentate line. The pressure was fixed with the pressure regulator on the cylinder and the flow rate controlled with Valve 9 in Figure 6-6. The flow rate was measured with a bubble flow meter and maintained above 10 ml/min.

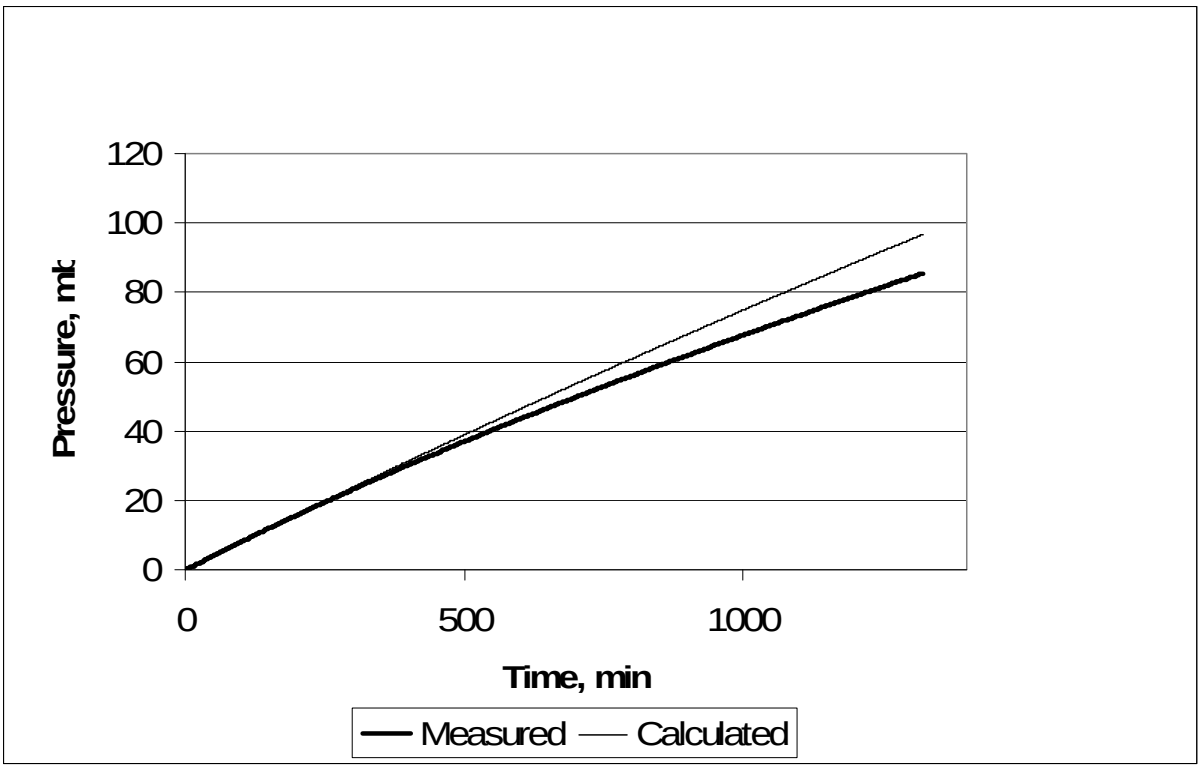

Figure 6-7. Typical curvature in permeate pressure-time graph for a static two-component permeation test (30%H_2-70%CH_4, 2 bar with membrane 4CuN650TZF R3)

When no ready mixed gas was available, continuous flow was approximated by performing a series of static experiments with mixed gas over several days. It was observed in the investigation of the change in the *dp/dt* gradient (Figure 6-7) that the permeability calculated from data in the first hour of a static test was the same as that calculated with the same gas fed continuously. A feed was prepared as described in Section 6.6.3.1 and mixed gas test performed. Once the rate and GC measurements of the permeate gas were completed, Valve 6 was closed in order to isolate some feed gas in contact with the membrane. The rest of the feed system was evacuated and a new feed mixture prepared, at 0.5 bar above the test feed pressure. After at least 5 hours of mixing, V6 was opened. The small volume between V6 and V9 meant that the total pressure was close to that of the newly prepared feed mixture. Valve 9 was then opened slightly and the feed side bled until the pressure decreased by 0.5 bar to the test pressure. This procedure caused fresh gas to flow into the membrane cell and the stale gas previously isolated above the membrane to be vented. The permeate side was cleared to a pressure of 0.07 mbar and a new test begun. The time taken for one cycle (test - feed prep. - mixing - test) was approximately 24 hours.

6.6.4 Temperature control

As discussed in Section 4.4.3, temperature has a marked effect on the transport of gases and can be used to improve separation performance. Membrane cell temperature was regulated by means of a custom-fitted heating jacket and temperature regulator (HT MC1) provided by Horst GmbH, Germany. As the heating jacket controls only the cell's skin temperature, measurements were carried out to calibrate the internal temperature (or membrane temperature) against the regulator's set point (see Appendix B). The time taken for the internal temperature to stabilise after a set-point change was also measured and found to be approximately 8 hours, irrespective of the size of the set-point change.

6.7 Other characterisation methods

6.7.1 Thermogravimetric analysis (TGA)

A Q500 Thermogravimetric Analyser (TA instruments, New Castle, USA) was used to conduct TGA. Samples of about 10 mg were placed in a platinum basket and heated under nitrogen, helium or argon at a rate of 10-20°C/min. Data was processed with TA Instruments Universal Analysis 2000 software. If a mass spectroscope was coupled to the TGA to detect pyrolysis products, argon was used as the sample sweep gas because nitrogen masks carbon monoxide in the MS spectrum.

6.7.2 Mass spectroscopy (MS)

A Thermostar™ gas analysis system (Pfeiffer Vacuum GmbH, Germany) was coupled to the sample gas outlet on the furnace of the TGA. The machine was set-up, and data analysed, with the Quadstar™ TG-MS system software (TSTAR_v7). The MS was synchronised with the TGA and measurement was started via the TGA user interface.

6.7.3 Gas adsorption

A Coulter™ SA3100 Surface Area Analyser, employing a volumetric method to determine the amount of gas adsorbed, was used to characterise porosity. No equipment with the ability to run CO_2 adsorption was available and only N_2 adsorption was performed, which is suitable only for mesopore characterisation.

The sample was placed in a glass tube and outgassed at 300°C for 30 minutes. The tube was then transferred to the analysis port and the nitrogen adsorption analysis begun. A dewar of liquid nitrogen at 77K served as the coolant.

The BET adsorption isotherm was selected for calculating mesopore surface area and the mesopore size distribution was calculated with the BJH method.

6.7.4 Membrane area measurement

Once permeation tests were completed, the membrane and aluminium tape mounting was cut from the membrane cell and the feed-side membrane surface scanned. The image was analysed with Scion Image (Scion Corp., MD, USA) to determine the permeation area.

6.7.5 Membrane thickness

Thickness was initially determined with a Mitutoyo 2109F thickness gauge (Mitutoyo Corp., Kanagawa, Japan). Although the gauge has a resolution of 1 micron, there was significant variation in measured values when the flat sheets were slightly warped. With the purchase of a Carl Zeiss Axio Imager upright microscope (Carl Zeiss MicroImaging GmbH, Germany)

later in the PhD program, images could be used to measure the thickness in a more precise manner. At least 4 discs from the same precursor film were carbonized for each batch. Images were obtained of random samplings of at least two of the discs.

6.7.6 Stereology

6.7.6.1 Optical imaging

Images of the surfaces and cross-sections of the carbon membranes were obtained using a Carl Zeiss Axio Imager upright microscope (Carl Zeiss MicroImaging GmbH, Germany). Images were captured using a DeltaPix Infinity X camera and software (DeltaPix, Denmark).

6.7.6.2 SEM

FE-SEM images were obtained with a ZEISS Supra-55 VP Field Emission Scanning Microscope (LV FE-SEM), manufactured by Carl Zeiss NTS GmbH, Germany. Backscatter and secondary electron images were obtained using an acceleration potential of 5 keV.

7 Results and discussion

A naming convention for the membranes has been adopted in this thesis. The amount and type of additive (CuN, AgN or PureHC for none) appears first, followed by the final carbonization temperature, oven type (TZF or HZS), and what sweep was used. For example, 4CuN650TZF had 4 wt% copper (II) nitrate (calculated without the waters of crystallization) added to the precursor and was carbonized at 650°C in oven TZF, without sweep (i.e. under vacuum). If more than one batch was prepared, then a batch designation is added (e.g. B3). If several distinct runs were executed with air exposure in between, then the run number is also noted (e.g. R3).

7.1 Carbonization

Carbonization of the cellulose precursors produced flat sheets that appeared uniform to the naked eye. Generally, flat sheets had a glassy side and a matt side reminiscent of graphite. At a magnification of 40X, it could be seen that this difference is due to the corrugations on the surface of the matt side (Figure 7-1), caused by ridges on the surface of the Teflon casting dish. These ridges appear to have been preserved through the carbonization process and the final carbon is a shrunken replica of the precursor. The films had thicknesses ranging from about 20-80 microns.

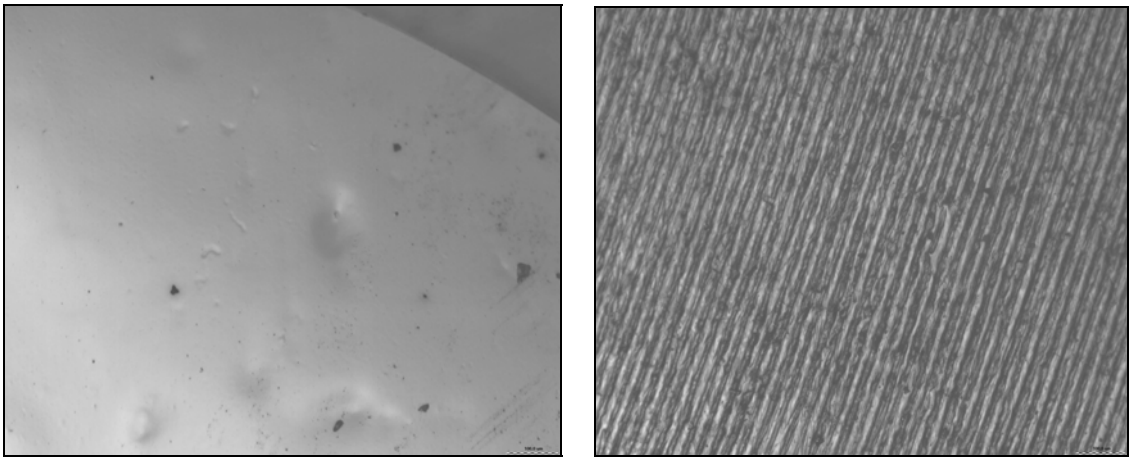

Figure 7-1 Magnified images (40X) of the glassy (left) and matt (right) sides of a typical flat sheet carbon membrane (cellulose with 4 wt% copper (II) nitrate, carbonized at 650°C under vacuum)

Magnified images of the cross-sections of the flat sheet membranes (e.g. Figure 7-2) show that, at a scale of 100 microns, the thickness of the membranes is uniform.

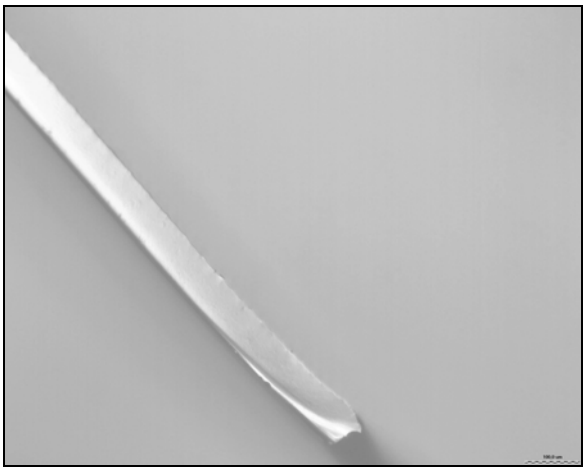

Figure 7-2 Magnified image of the cross section of a carbon flat sheet membrane (cellulose with 4 wt% copper (II) nitrate, carbonized at 650°C under vacuum)

SEM analysis shows the entire film to be dense, at least at a magnification of 300 000× (Figure 7-3). There is also evidence in this example of a distinct thin layer at the surface, possibly formed by faster drying of the surface layer of the polymer precursor in the casting process.

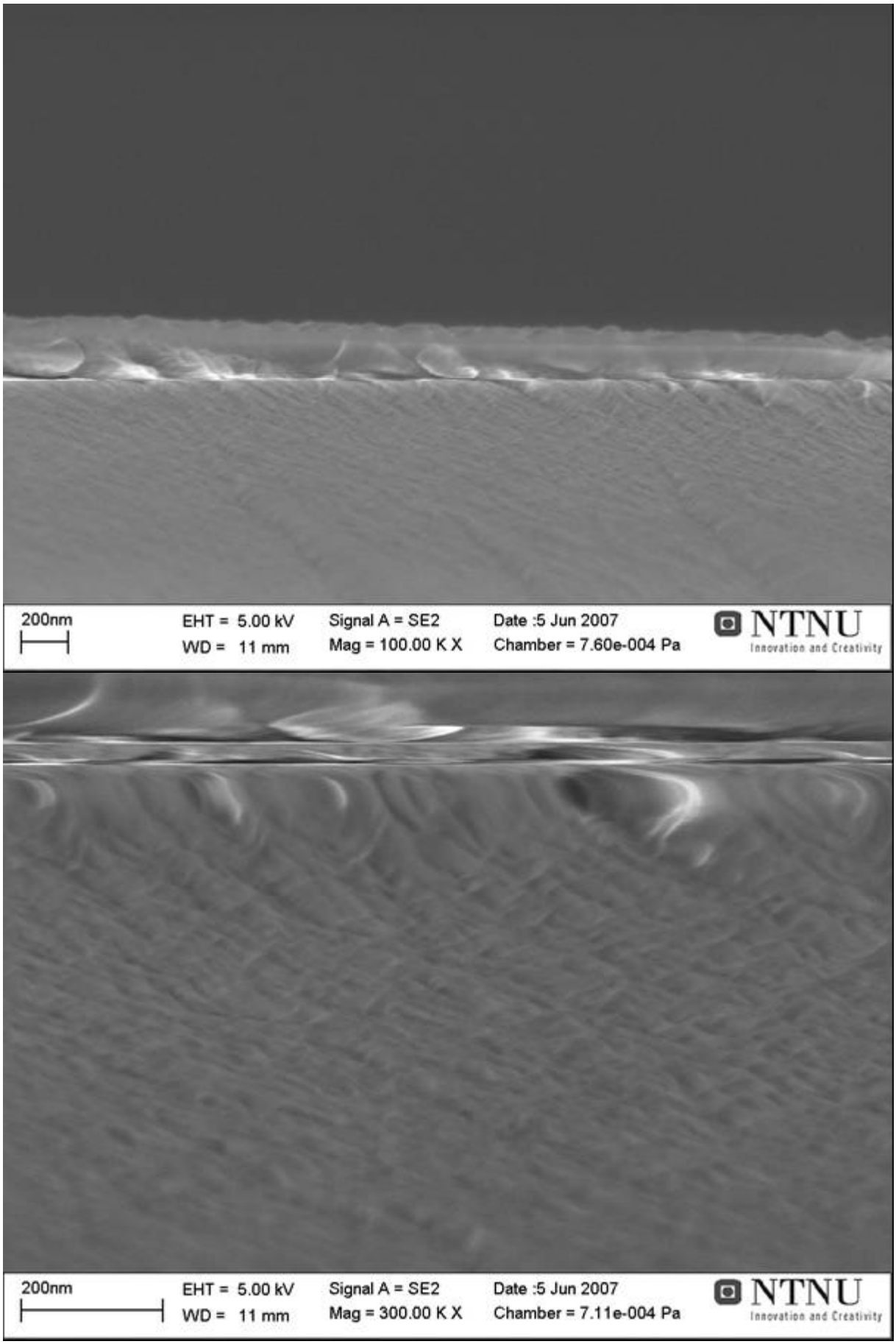

Figure 7-3. FE-SEM images (secondary electron) of a pure cellulose film carbonised at 700°C in oven TZF

7.1.1 Carbonization of hemicelluloses

Drying the xylan-water solution in a Teflon® dish, in the same manner as the cellulose precursor, produced a red-brown film that was slightly flexible. The solution was not as viscous as the cellulose precursor, which raises doubts about the suitability of xylan for spinning hollow fibres. Pyrolysis did yield carbon films, however. Furthermore, the retention of the shape of the precursor film showed that xylan behaved like a thermosetting polymer. However, the experiment was unsuccessful because excessive bubbling in of the material caused an uneven, brittle carbon film to be formed. Galactomannan, derived from locust bean gum, formed a paste in water but did not dissolve totally, even when heated. Suspended solids were present after 2 months of tumbling. Carbonization yielded a brittle, spongy film that was unsuitable as a membrane.

Therefore, hemicellulose does not appear suitable as a precursor. The cellulose precursors used in this work, however, contain 15-20% hemicellulose. The cellulose, therefore, must stabilise the hemicellulose in carbonization. On the other hand, the existence of isolated collapsed bubbles in some of the un-doped cellulose-hemicellulose-derived carbon films might be caused by the hemicellulose fraction.

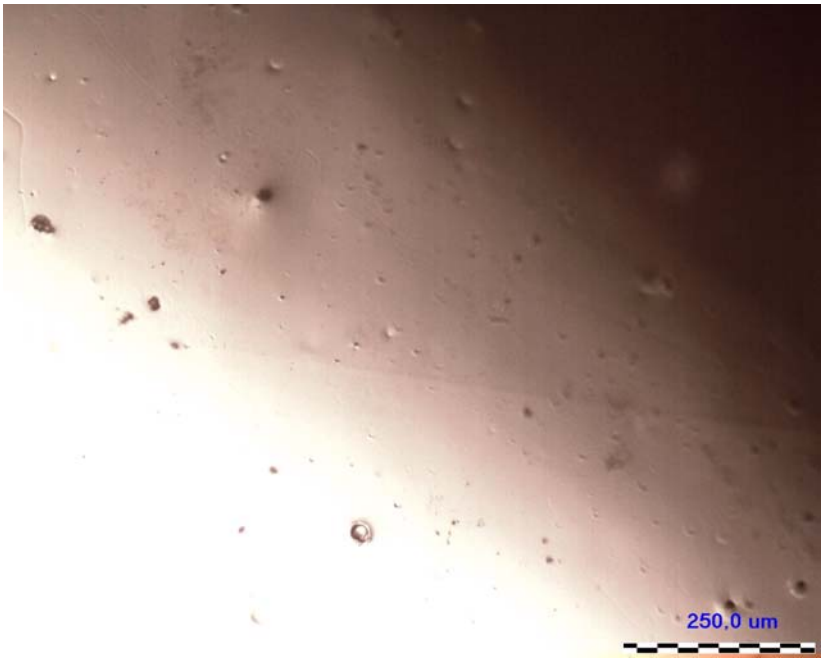

Figure 7-4. Image of pure carbon membrane PureHC650HZS showing small bubbles on surface (magnification 10×)

7.1.2 Thermal gravimetric analysis of cellulose carbonization

The weight loss of the cellulose precursors as a function of temperature was measured in a thermal gravimetric analysis (TGA) instrument. It can be seen in Figure 7-5 that carbonization of raw cellulose (i.e. cellulose not exposed to TFA) begins at approximately 255°C and most of the weight loss occurs below approximately 340°C. The difference between the onset point and endpoint is only 12°C. Weight loss continued at a slower rate up to and beyond 900°C.

Some evaporation of adsorbed water is also seen below 100°C. From this graph, one can conclude that the protocol proposed by Soffer et al. (1999) and used in this work is suitable for cellulose carbonization, because the dwells coincide with the range of highest weight loss (see Figure 6-3). As explained in Section 6.5.1, dwells are necessary to reduce stresses in the film as it decomposes.

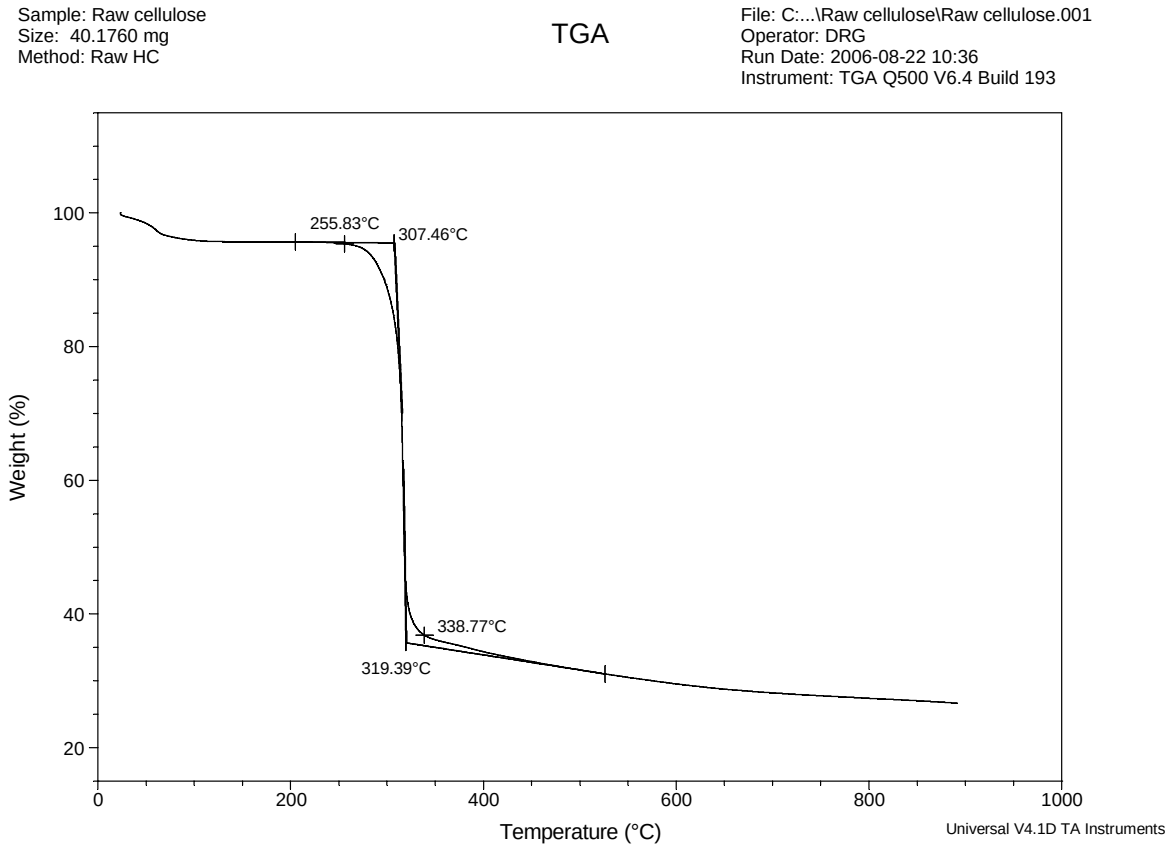

Figure 7-5 Weight loss of raw cellulose as a function of temperature

The evolution of pyrolysis gases is shown against the sample weight loss, in Figure 7-6. The onset of weight loss coincides with the increase in water, hydrogen and carbon dioxide. A nitrogen dioxide peak, from the decomposition of the $Cu(NO_3)_2$ to CuO, O_2 and NO_2, appears between 200 and 400°C. It will be shown in Section 7.1.5 that this is the expected range for copper (II) oxide decomposition and indicates that copper does not form a salt with the trifluoroacetate ion of TFA. Whereas CO_2 evolution peaks in the temperature segment with the highest weight loss, hydrogen evolution rose steadily throughout carbonization. This is consistent with the conversion of aromatic sheets to graphene structures. Four distinct water peaks are present. The first, complete by about 140°C, corresponds to the evaporation of absorbed water from the polymer and removal of the waters of crystallization in the copper (II) nitrate. The following three are found within the main weight loss segment and are produced by the decomposition and aromatization processes, as -OH groups in the cellulose chain are eliminated. CO_2 and H_2O liberation was seen to rise again towards 800°C, perhaps as the more strongly bonded oxygens within the graphene heteroatom groups, like chromenes and pyrones, are ejected. The ion current signal for CO, which is also a decomposition product, was masked by a declining residual ambient nitrogen signal in the furnace. The derivative of

this signal with temperature, however, showed CO evolution occurring between 200 and 300°C.

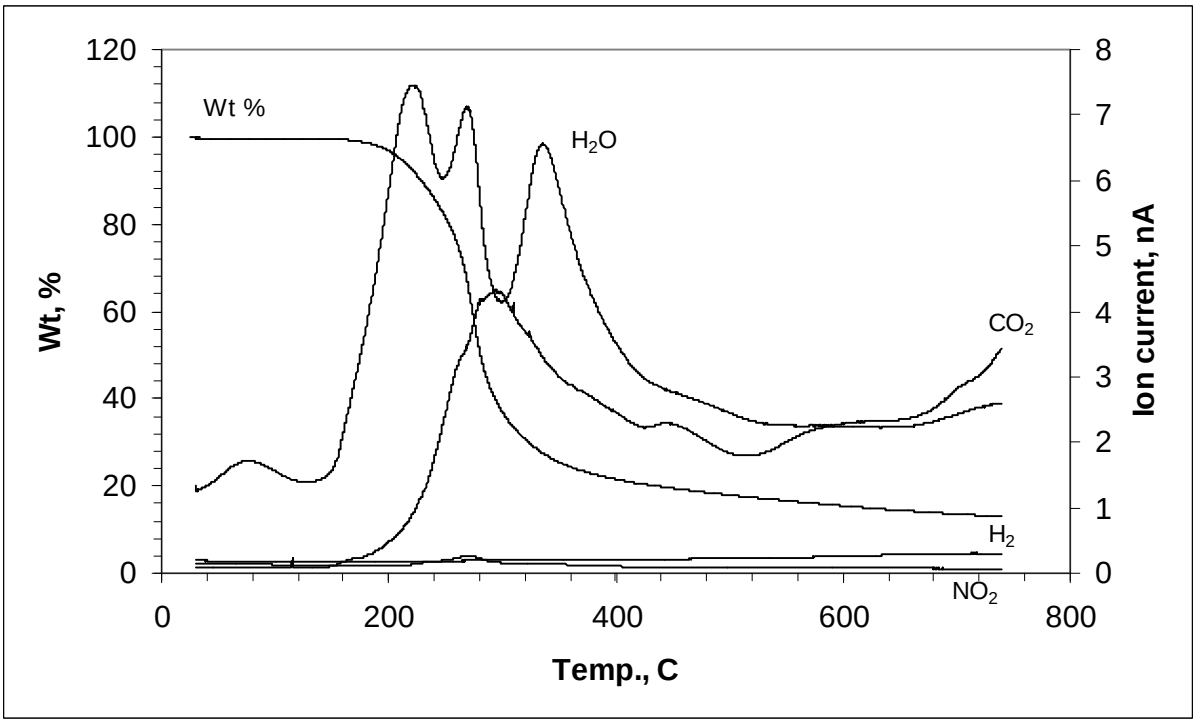

Figure 7-6. TGA and MS signals of the carbonization of a cellulose precursor doped with 4wt% copper(II) nitrate

7.1.3 Porosity

Without carbon dioxide-equipped adsorption analysers, it was not possible to probe the porosity below 3 nm. Nitrogen adsorption of raw cellulose carbonized at 650°C in the HZS oven under vacuum yielded the pore size distribution in
Figure 7-8. There is little macroporosity and most pore volume is in the mesoporous range and lower. Volume appears to peak below 3 nm. More information is obtained from permeation tests, where the kinetic diameters of gases give an indication of the critical pore constrictions (see Section 4.4.1 for detail on kinetic diameters). An example is shown in Figure 7-7. Permeation tests with SF_6, ethane or propane showed that none of these gases permeated to a significant degree, and in some cases methane permeation was not detectible. The critical sieving dimensions of these cellulose-derived membranes probably lie in the range of 3.8-5.5 Å.

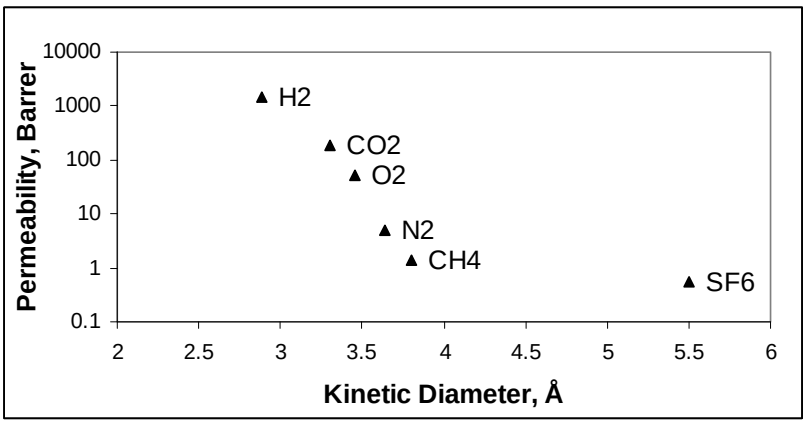

Figure 7-7. Permeability at 25°C vs. kinetic diameter (4AgN550TZF)

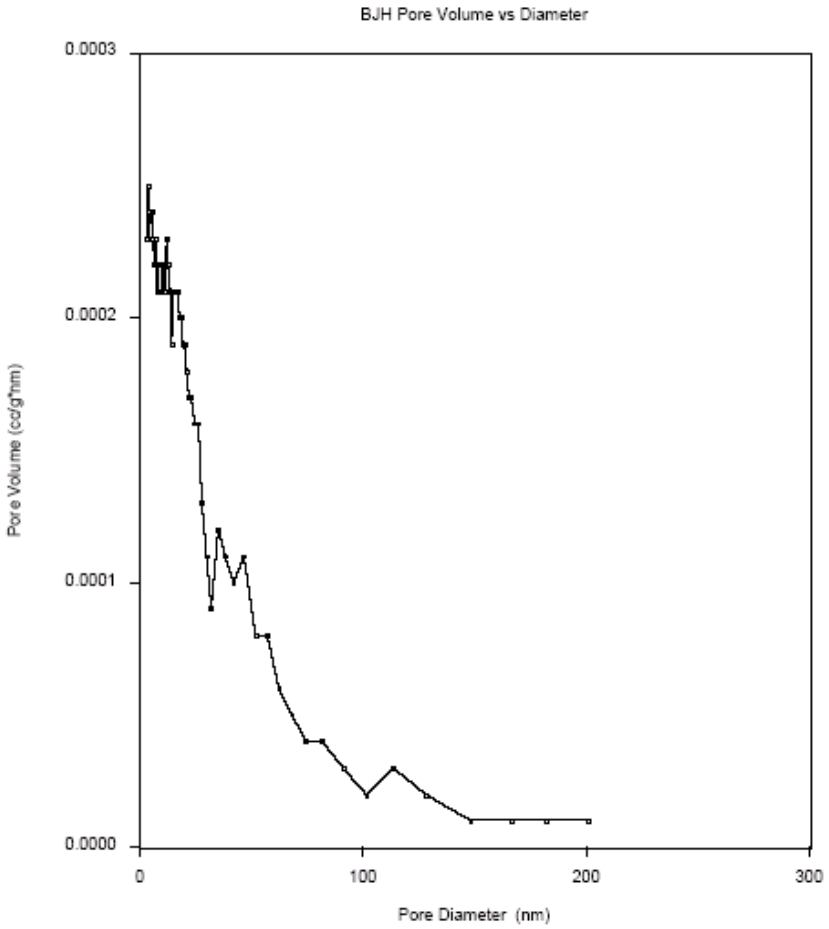

Figure 7-8. Pore size distribution of raw cellulose-derive carbon (650°C, HZS) determined by N_2 adsorption

7.1.4 Effect of TFA exposure

As discussed in Section 4.3.1, trifluoroacetic acid cleaves 1,4-β-linkages in the cellulose chain. The reaction rate is low, according to Morrison and Stewart (1998), with significant cleavage occurring after 12 days of exposure to TFA.

The effect of this depolymerisation on the carbonization behaviour of the cellulose was investigated by preparing a 1.5wt% cellulose solution and performing TGA on samples withdrawn from the solution as time progressed. The samples, approximately 10 mg, were heated at 10°C/min from room temperature to 800°C under nitrogen flow. Before carbonization, the samples were dried on a Teflon surface and then placed in a vacuum oven at 105°C for 18 hours. The TGA curves are shown in Figure 7-9, with the exposure time given as the slope label.

The samples dissolved in TFA started to decompose approximately 50°C lower than the raw cellulose (0 days). Surprisingly, even 2 days of exposure caused a significant decrease in the decomposition temperature, implying that depolymerisation occurs soon after exposure. Furthermore, the decomposition curve for raw cellulose is sharper, whereas the decomposition curve for TFA-exposed cellulose is more gradual and the onset of decomposition earlier. It also appears that longer exposure times caused greater weight loss, although the curves at 97 and 34 days do not follow this trend. It can be speculated that there is a difference between the curves at 6 and 8 days exposure, which would fit with the findings of Morrison and Stewart (1998) and Lie and Hägg (2006). Surprisingly, the final weight loss of the raw cellulose is larger than that of the TFA-exposed cellulose.

It is proposed that the TFA does cause depolymerisation to lighter intermediates, so that decomposition and/or tar evaporation occur at lower temperatures, but that this does not affect the material that will remain as pure carbon. Random cleavage of glucosidic bonds may create a distribution of polymer chain lengths, down to tarry compounds. This could explain the more gradual weight loss seen in the decomposition segment of TFA-treated cellulose, because the range of chain lengths would have a range of boiling points. This is consistent with proposal by Bradbury et al. (1979), discussed in Section 4.3.2, that cellulose must first be ‘activated’ by depolymerisation to a DP of 200 before rapid thermal degradation can occur. Inspection of the degradation curves for TFA-exposed cellulose in Figure 7-9 reveals a kink between 300 and 350°C, or about 40% weight loss, that is absent in the raw cellulose curve. Bradbury et al. found that volatiles (like levoglucosan) are the dominant products of cellulose pyrolysis at 260-340°C and Shafizadeh and Sekiguchi (1982) showed that aromaticisation occurs rapidly above 350°C. Therefore, the kinks seen in the curves may mark the end of the volatile production regime and the beginning of the carbon and gaseous product formation stage. Indeed, the final water evolution peak is seen at about 300-430°C in Figure 7-6, peaking at 340°C. This suggests a difference between material likely to become volatiles and material likely to become carbon and gases, with TFA only affecting the former.

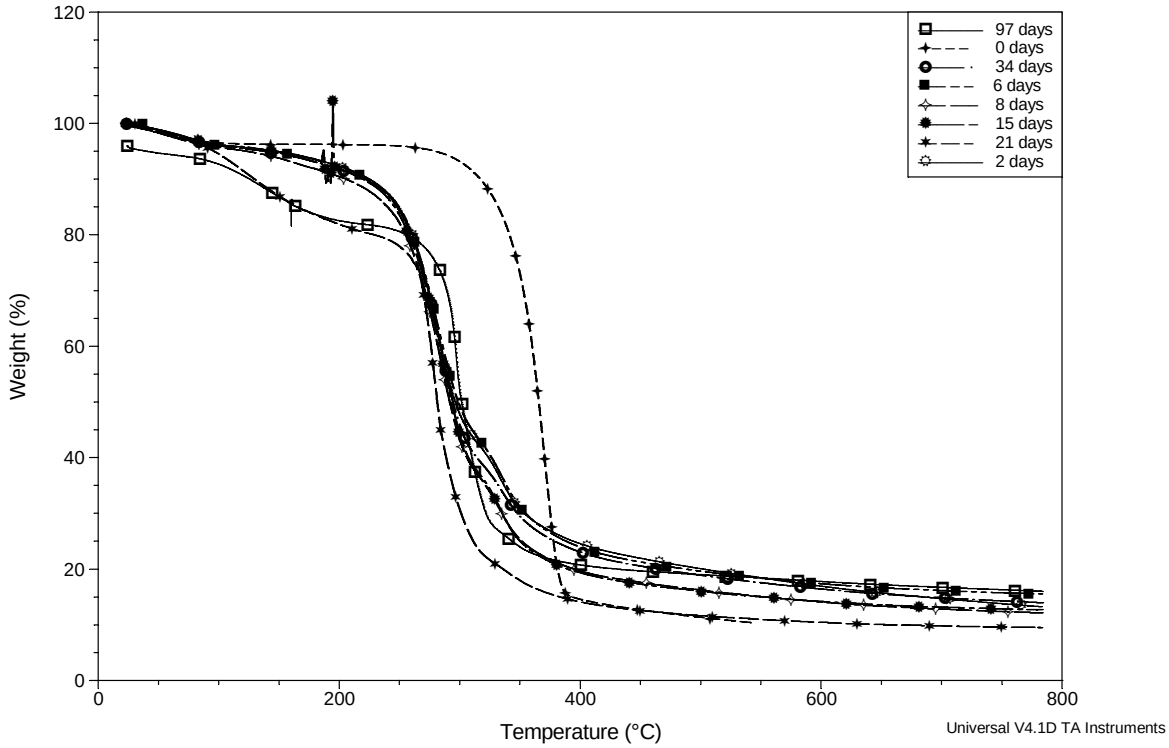

Figure 7-9. The effect of trifluoroacetic acid exposure time on precursor decomposition.

7.1.5 Metal additive state

SEM images showed distinct clusters of the metal compounds embedded throughout the carbon material (Figure 7-10 and Figure 7-11). Back-scatter images reveal the clusters to have heavier nuclei than the surrounding carbon, confirming that they are the respective silver or copper compounds.

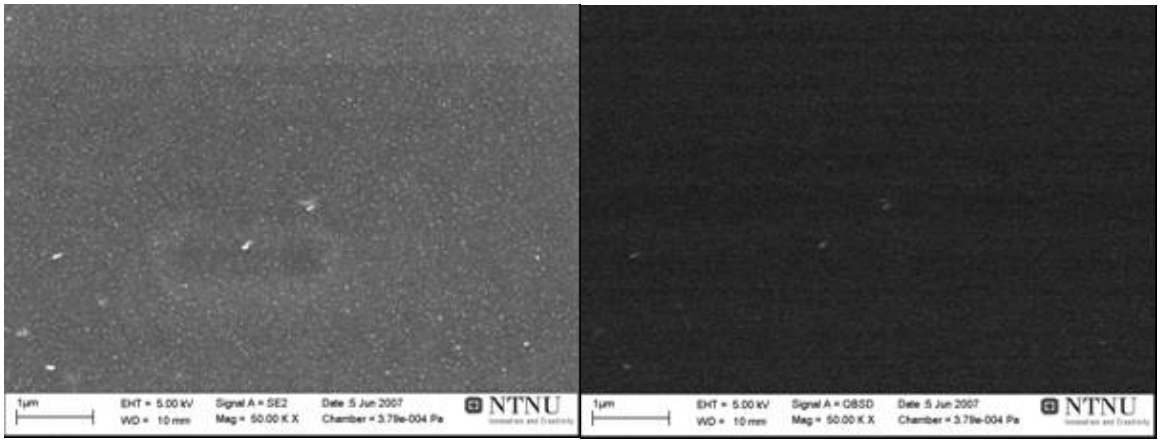

Figure 7-10. SEM images of silver clusters in 4AgN650TZF (30 hr soak): Secondary electron (left) and back-scatter (right). 50 000×magnification

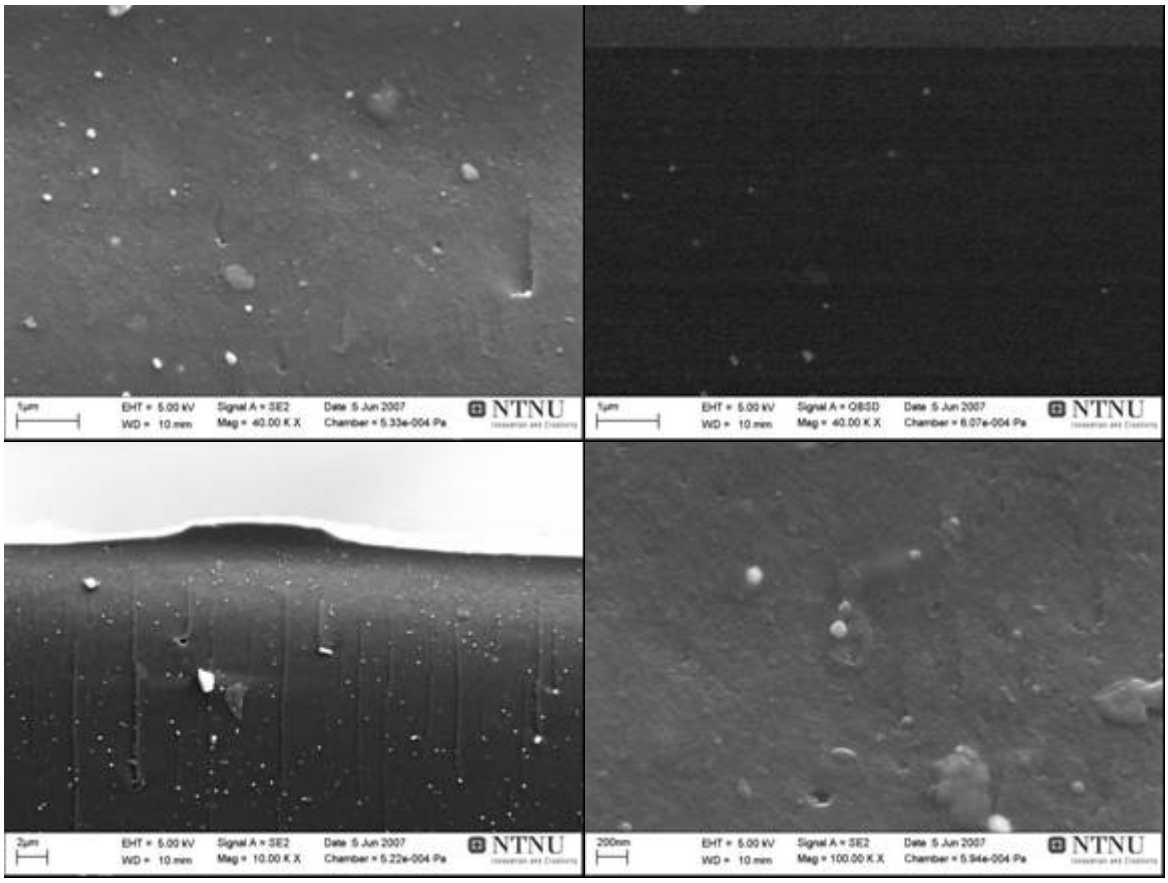

Figure 7-11. SEM images of copper-containing clusters in 4CuN650HZS: Secondary electron (top left) and back-scatter (top right), 40 000×magnification. Secondary electron, 10 000×magnification (bottom left); 100 000×magnification (bottom right)

It is assumed here that metal nitrates precipitate as the TFA evaporates during drying. These would then undergo thermal decomposition during carbonization. The TGA thermogram for $Cu(NO_3)_2.3H_2O$ is shown in Figure 7-12 and the mass of the sample at the end of each weight loss interval in Table 7-1.

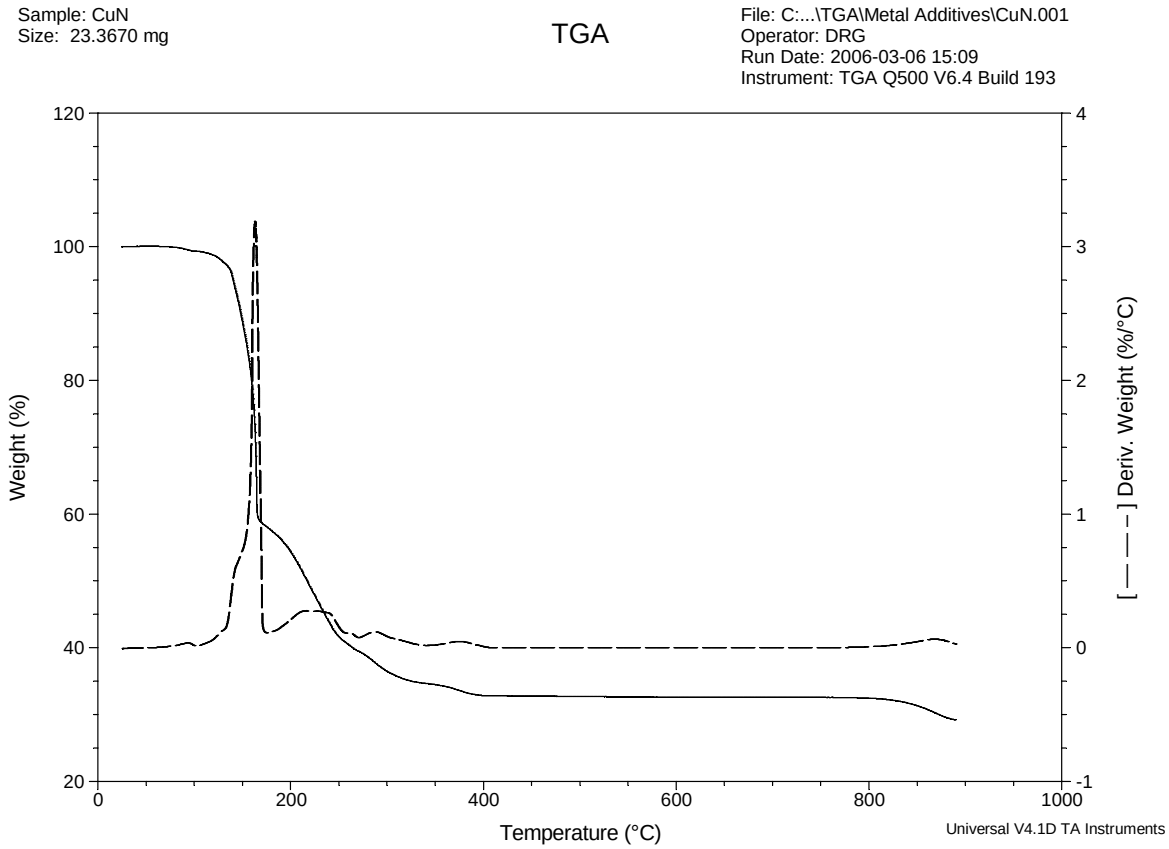

Figure 7-12 Thermal decomposition of $Cu(NO_3)_2.3H_2O$ in Argon

The mass at 400-800°C is 33% of the original sample, corresponding to the formation of CuO. As the carbonization temperatures in this doctoral work were in the range of 550-700°C, it is therefore assumed that Cu existed as CuO in all of these membranes. This is in agreement with the findings of Silverstein et al (2004).

Table 7-1. Comparison of measured mass intervals with Cu species molar masses

Molecular masses			**TGA data**		
Species	Mw, g/mol	% mass of $Cu(NO_3)_2.3H_2O$	Temp., C	Mass, mg	% mass of sample
$Cu(NO_3)_2.3H_2O$	241.5	100%	27	23.37	100%
$Cu(NO_2)_2$	155.6	64%	165	13.95	60%
			249	9.627	41%
			329	8.269	35%
CuO	79.6	33%	400	7.676	33%
Cu	63.6	26%	884	6.841	29%

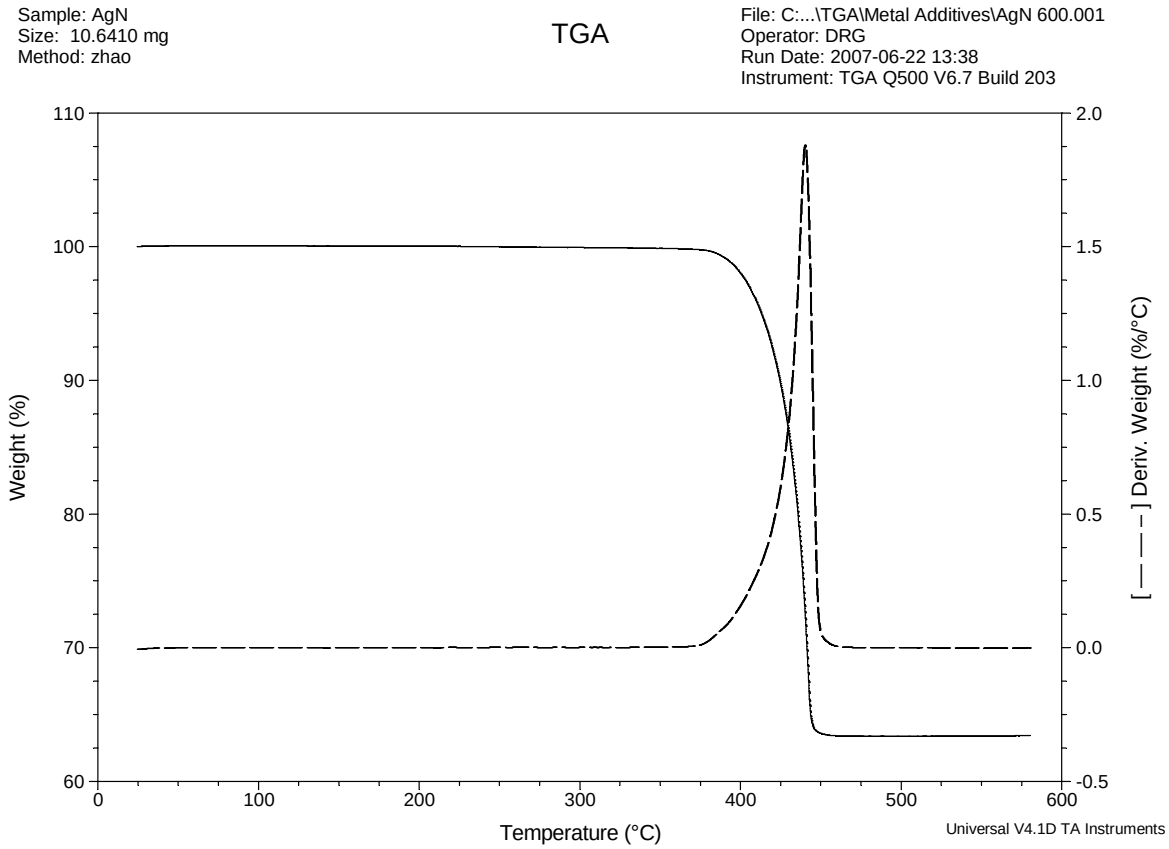

Figure 7-13 Thermal decomposition of $AgNO_3$ in Argon, showing onset point

From the graph above and Table 7-2 below, it is clear that pure silver nitrate decomposes via silver oxide to form silver, and remains in that form in the carbonization range in this work. The decomposition of Ag_2O can be violent and a closed aluminium pan was required to prevent material leaving the platinum basket. Silver needles were observed to cover the aluminium pan, so the silver must evaporate during the reaction and condense on the aluminium surface.

Table 7-2. Comparison of measured mass intervals with Ag species molar masses

Molecular masses			**TGA data**	
Species	Mw, g/mol	% mass of $AgNO_3$	Temp., C	% mass of sample
AgNO3	169.9	100%	25	100%
Ag	107.9	64%	450	64%

The time that the membrane was held at the final temperature, or soak time, was not included as an experimental variable in the program. This was due to lack of time and the knowledge that increasing the soak time tends to produce the same effect as increasing the final temperature (see discussion in Section 4.2.3). However, soak time may also influence the behaviour of silver nitrate, which, along with its decomposition product, Ag_2O, is mobile in the pyrolysis range.

A cellulose precursor, containing 4 wt% $AgNO_3$, was pyrolysed at 650°C under vacuum in the TZF oven. Two batches from the same precursor film were carbonised; the first with a

soak of 30 hrs and the second with a soak of the standard 2 hrs. As expected, the membrane with the longer soak time had a lower porosity and therefore lower permeabilities.

Table 7-3. Effect of soak time on membrane performance (measured at 25°C)

Membrane	P_{H2}, Barrer	P_{CO2}, Barrer	$\alpha_{H2/CO2}$
4AgN650TZF, 2hrs	798	58	14
4AgN650TZF, 30hrs	34	0.6	56

An unexpected result, however, was the difference in the distribution of silver. The membrane prepared with 2 hrs soak was covered with a silver layer, as were some of the previous membranes doped with 4 wt% silver nitrate. The membrane soaked for 30 hrs, however, appeared to be free of silver. Magnified images of the two membranes are shown in Figure 7-14.

a)

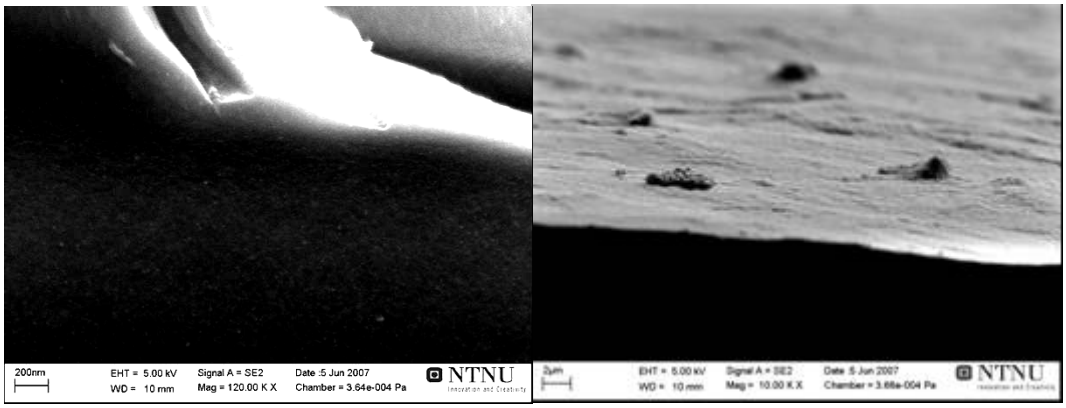

b)

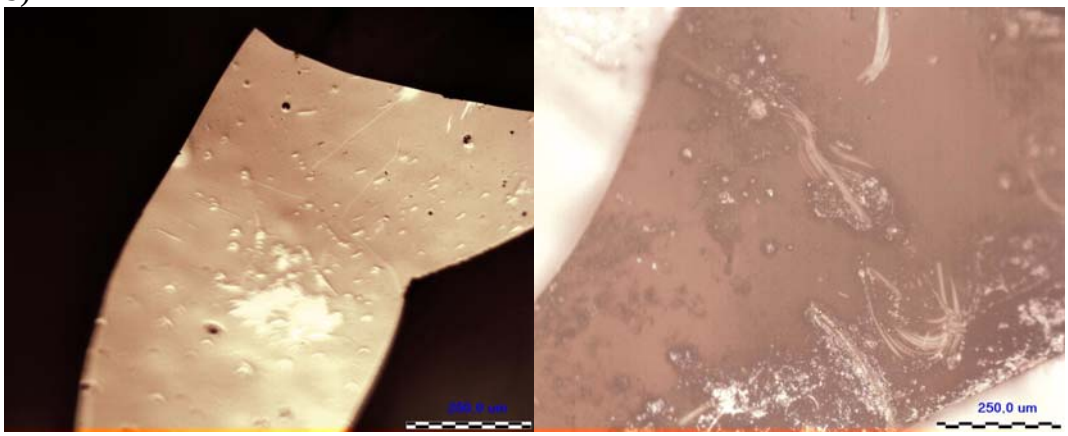

Figure 7-14. a) FE-SEM Photograph of 4AgN650TZF, 2hrs(left, 120 000× magnification) and 4AgN650TZF, 30 hrs (right, 10 000× magnification); b) Micrographs (10× magnification) of 4AgN650TZF, 2hrs (left) and 4AgN650TZF, 30 hrs (right)

The SEM image shows the 200 nm, dense layer of silver on the surface of the 2hr soak film. The microscope images (b) contrast the silver coverage of the surface of the 2hr film with the limited spattering of silver on the 30 hr soak film.

The silver nitrate was not seen to concentrate at the surface of the precursor. It can be concluded that, not only does silver migrate to the surface during carbonization, but it also evaporates from the material. The longer soak time for the 30 hr sample allowed most of the surface silver to evaporate.

Surface layers of Cu or CuO were sometimes seen, for example on the 6CuN650TZF membrane shown in Figure 7-15, but were not as common or defined as the silver layers.

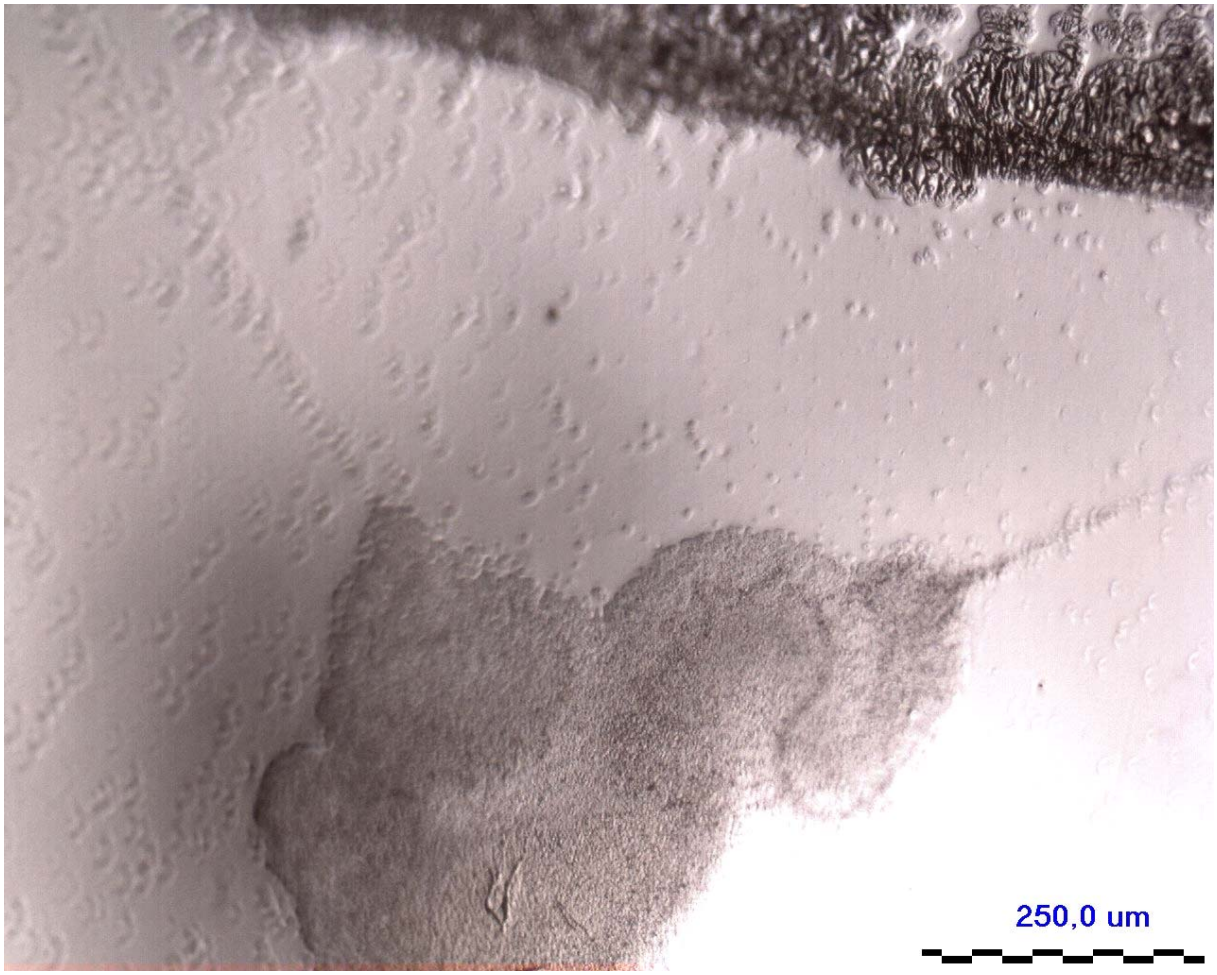

Figure 7-15. Micrographs (10× magnification) of 6CuN650TZF

7.1.6 Carbonization environment

As described in Section 6.5, two ovens were available to prepare membranes, designated TZF and HZS. TZF operates under vacuum only whereas HZS is able to operate under vacuum or inert gas flow. It is seen in Figure 7-16 and Figure 7-17 that these three environments produced significantly different membranes:

- The most H_2-permeable membranes were produced in the TZF oven.
- Vacuum pyrolysis in the HZS oven produced membranes with far lower permeabilities and higher selectivities, indicating lower porosity and a smaller apparent pore size.
- Operating the HZS oven with an inert flow produced membranes with similar hydrogen permeabilities and selectivities to the TZF furnace.

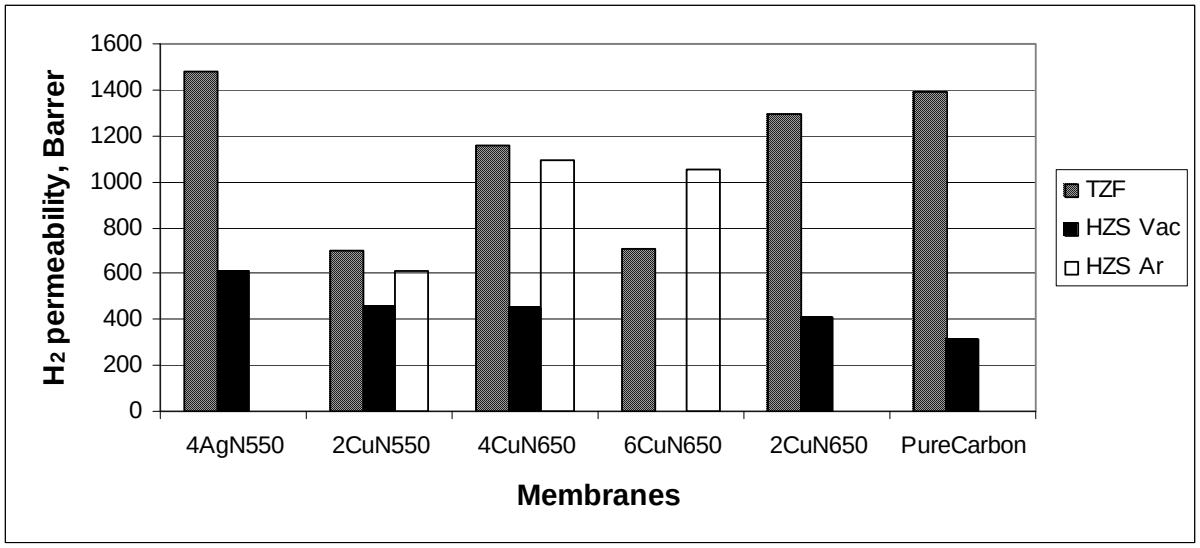

Figure 7-16. Comparison of membrane permeabilities from different carbonization environments (measured at 25°C)

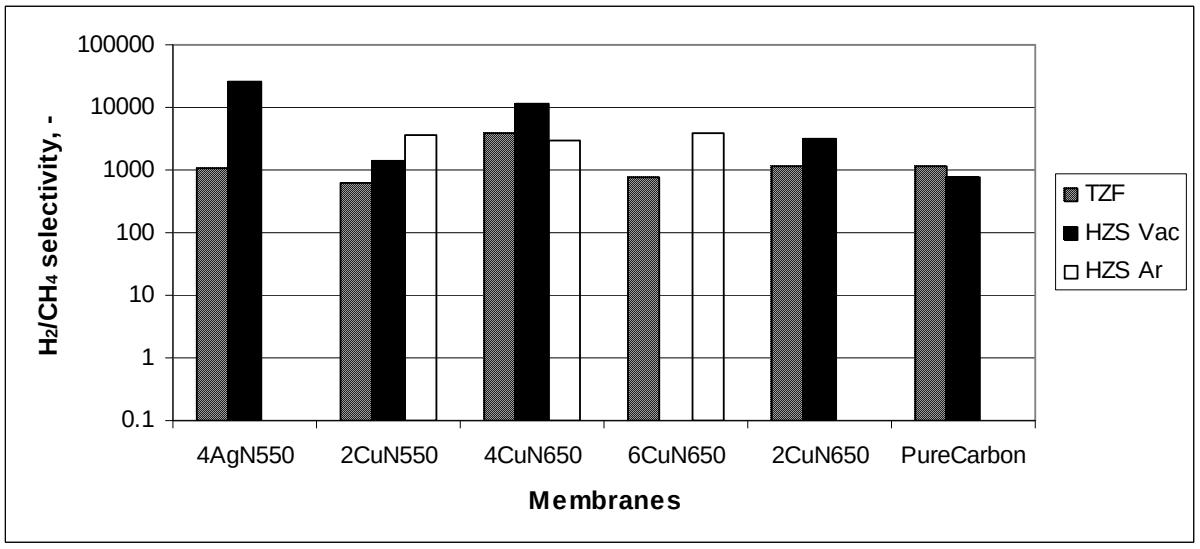

Figure 7-17. Comparison of membrane permselectivities from different carbonization environments (measured at 25°C)

Geiszler and Koros (1996) concluded that inert flows increased the heat transfer to the membranes and were more effective at removing pyrolysis products, which produced more open membranes. This would explain the difference in results between vacuum and Ar flow in HZS. Another mechanism is required to explain the difference between vacuum results between the two ovens. The quartz HZS tube cools faster after completing soak than the ceramic TZF tube, meaning that membranes spend a longer time at elevated temperatures in the TZF furnace. This was discounted as the cause, however, by TGA experiments which were programmed to follow the exact oven temperature-time profiles (Figure 7-18). These showed identical weight loss for the different cooling times. This conclusion was verified by programming the HZS furnace to cool at the same rate as the TZF furnace for membranes from the same precursor batch, which still produced a tighter membrane in HZS (membranes 4CuN650 HZS Vac and 4CuN650 TZF in Figure 7-16)[7].

[7] Recognition and thanks are due to former M.Sc student Tomas Aanonsen for the work undertaken in investigating the effect of temperature profiles.

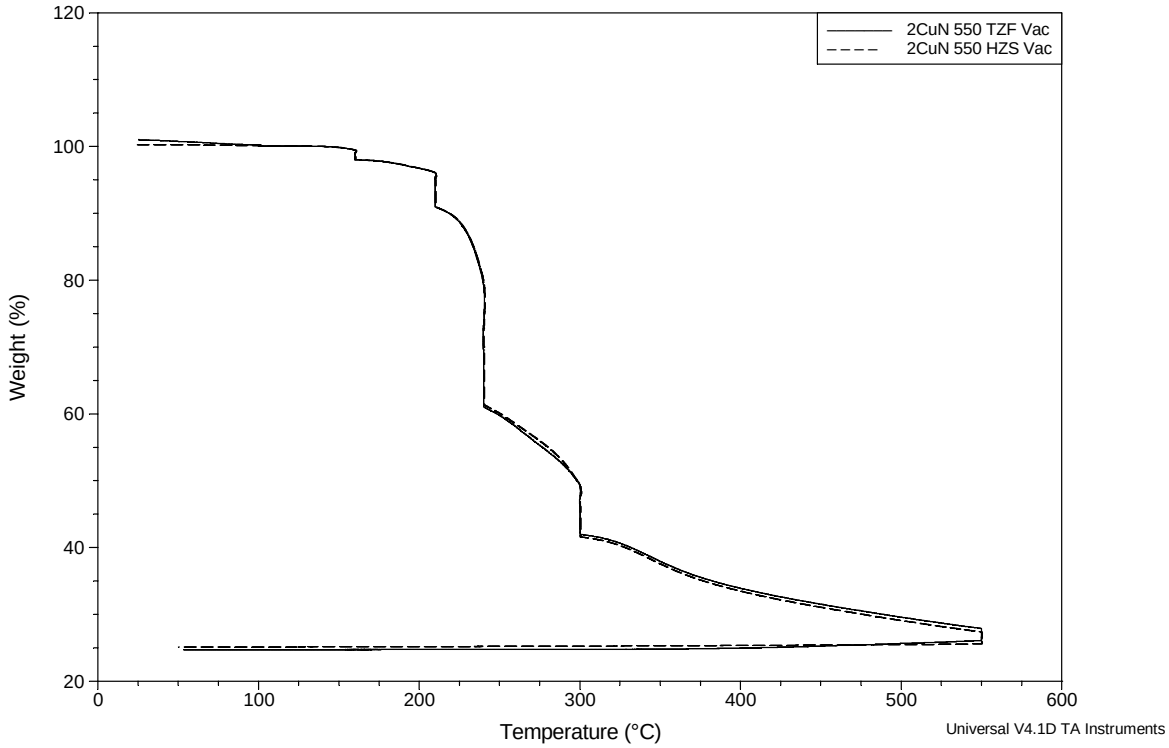

Figure 7-18. Comparison of TGA time-temperature profiles for HZS and TZF ovens, HTT 550°C

The likely explanation is that the lowest absolute pressure in the TZF furnace tube (0.34-0.41 mbar) is higher than in the HZS oven (0.02-0.05 mbar), due to a difference in vacuum pump effectiveness. This implies that the oxygen partial pressure is approximately 0.07-0.09 mbar during pyrolysis in the TZF tube, but only 0.004-0.011 mbar in the HZS. As discussed by Geiszler and Koros (1996), the presence of even 0.3 ppm of oxygen in an inert gas can cause oxidation of the pores and, therefore, create a more open membrane. 0.3 ppm oxygen in 1 bar argon flow is equivalent to a partial pressure of 0.0003 mbar, which is much lower than the levels present in the furnaces. It is accurate to say, then, that the membranes produced in both furnaces are influenced by oxidation, but that the effect is much more significant in the TZF furnace.

7.2 Summary of CMSM performance with single gas feeds

The results for the many membranes that were tested are summarised in this section. The values are for tests performed with 2 bar feed and at 25-30°C. Where possible, the values are shown for membranes that were tested within 1 month of being carbonized, to reduce the influence of aging. Some membranes were so tight that the permeation of methane could not be detected, or was equal to the leak rate of the apparatus. In these cases, the selectivity was practically infinite. To display these membranes on the Robeson plots, they were arbitrarily assigned a selectivity of 10^6.

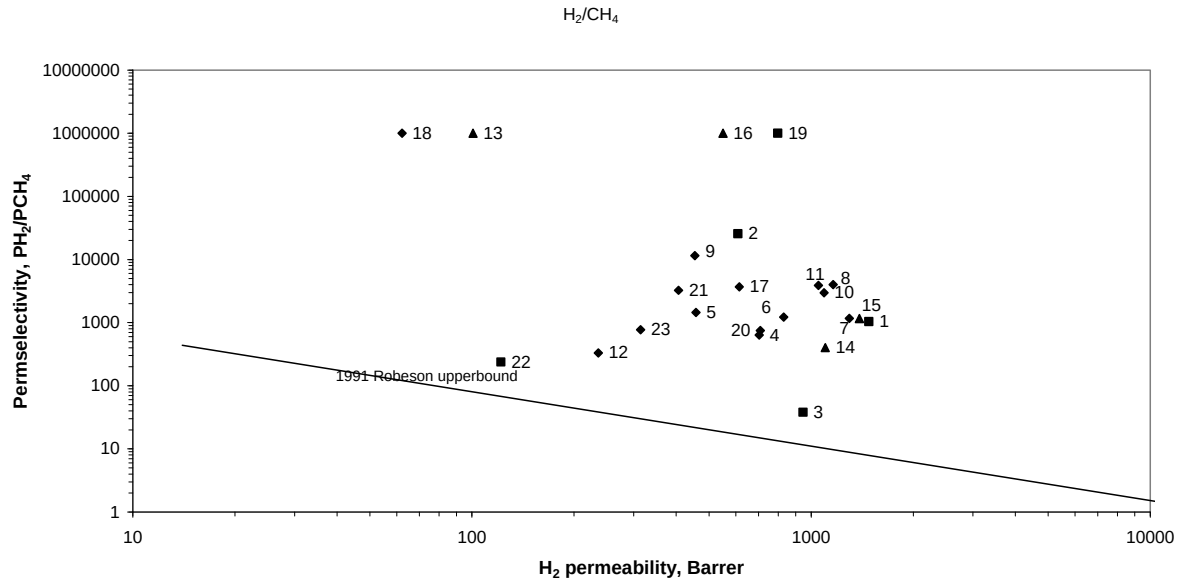

Figure 7-19. Robeson plot for single gas H_2/CH_4 pairs, measured at 25°C (■: silver nitrate ◆: copper (II) nitrate▲:no additive, see Table 7-4 for label key)

The carbon membranes are excellent for the separation of hydrogen from methane. All of those tested in this program exceeded the 1991 Robeson upperbound performance for polymers.

Table 7-4. Data for H_2/CH_4 Robeson plot

No	Designation	Carb. temp, °C	Oven	Additive	Wt% (precursor)	Weight loss, %	Age, days	H_2 perm., Barrer	Selectivity, PH_2/PCH_4
1	3.8AgN550TZFM1	550	TZF	AgN	3.8	78.4%	28	1480	1038
2	3.8AgN550HZSM2	550	HZS	AgN	3.8	67.9%	5	608	25628
3	6AgN550TZF	550	TZF	AgN	6	79.2%	10	947	38
4	2CuN550TZF	550	TZF	CuN	2	78.9%	17	703	636
5	2CuN550HZS	550	HZS	CuN	2	78.6%	19	458	1444
6	4CuN550TZFJ	550	TZF	CuN	4	73.3%	456	1130	1227
7	2CuN650TZF	650	TZF	CuN	2	85.2%	3	1296	1169
8	4CuN650TZFB3	650	TZF	CuN	4	83.7%	29	1161	4007
9	4CuN650HZS	650	HZS	CuN	4	83.7%	1	454	11544
10	4CuN650HZSAr	650	HZS, Ar	CuN	4	78.5%	5	1092	2969
11	6CuN650HZSAr	650	HZS, Ar	CuN	6	79.4%	10	1051	3894
12	4CuN700TZF	700	TZF	CuN	4	83.3%	100	236	331
13	Pure400TZF	400	TZF	-	-	80.5%	1	101	V. large
14	Pure550TZF	550	TZF	-	-	83.8%	1	1101	402
15	Pure650TZF	650	TZF	-	-	84.6%	1	1388	1157
16	Pure700TZF	700	TZF	-	-	84.8%	1	549	V. large
17	2CuN550HZSAr	550	HZS, Ar	CuN	2	85.4%	11	614	3690
18	4CuN400TZF	400	TZF	CuN	4	79.6%	1	62	V. large
19	4AgN650TZF	650	TZF	AgN	4	84.3%	1	798	V. large
20	6CuN650TZF	650	TZF	CuN	6	-	7	708	750
21	2Cun650HZS	650	HZS	CuN	4	80.8%	2.00	407	3242
22	3.8AgN375HZS	375	HZS	AgN	4	60.9%	22	122	238
23	Pure650HZS	650	HZS	-	-	81.2%	2	314	773

Few of the carbon membranes performed better than the Robeson upperbound for H_2-CO_2 separation. Membranes produced in the HZS oven (4, 5, 15 and 16) did perform better than

the polymer upperbound, attesting to the narrow effective pore size of the molecular sieves. TZF membranes that were not doped with metal (7-10) generally performed the worst.

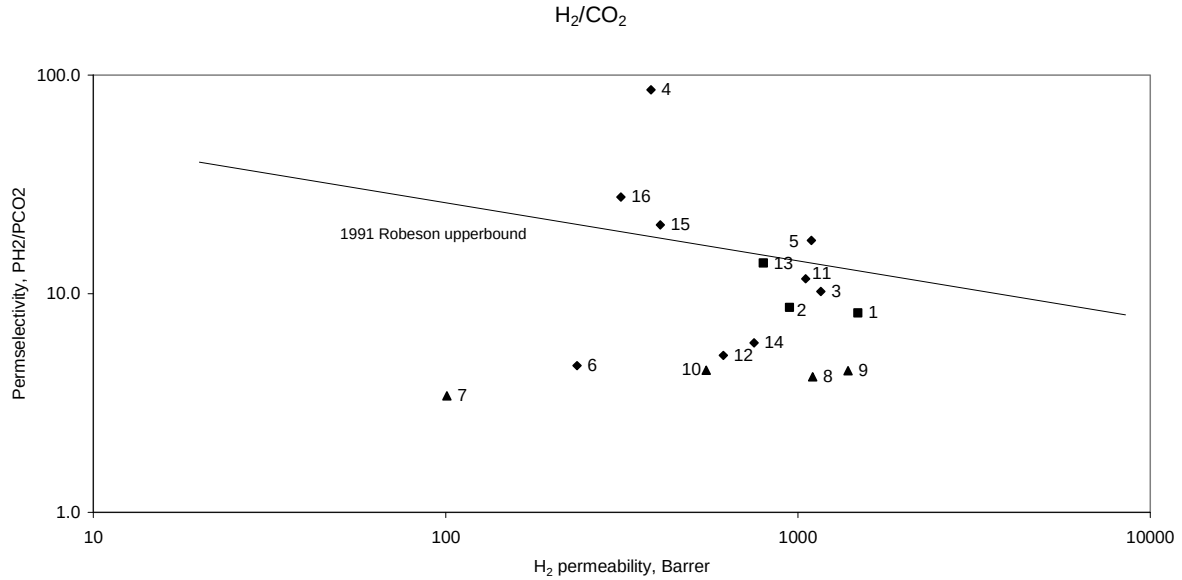

Figure 7-20. Robeson plot for single gas H_2/CO_2 pairs, measured at 25°C (■: silver nitrate ◆: copper (II) nitrate▲:no additive, see Table 7-5 for label key)

Table 7-5. Data for H_2/CO_2 Robeson plot

No.	Designation	Carb. temp, °C	Oven	Additive	Wt% (in precursor)	Age, days	H_2 perm., Barrer	Selectivity, $PH2/PCO_2$
1	3.8AgN550TZFM1	550	TZF	AgN	3.8	28	1480	8.2
2	6AgN550TZF	550	TZF	AgN	6	10	947	8.6
3	4CuN650TZFB3	650	TZF	CuN	4	29	1161	10.2
4	4CuN650HZS	650	HZS	CuN	4	19	383	85.5
5	4CuN650HZSAr	650	HZS, Ar	CuN	4	5	1092	17.5
6	4CuN700TZF	700	TZF	CuN	4	100	236	4.7
7	Pure400TZF	400	TZF	-	-	1	101	1.7
8	Pure550TZF	550	TZF	-	-	1	1101	4.2
9	Pure650TZF	650	TZF	-	-	1	1388	4.4
10	Pure700TZF	700	TZF	-	-	1	549	4.5
11	6CuN650HZSAr	650	HZS, Ar	CuN	6	10	1051	11.7
12	2CuN550HZSAr	550	HZS, Ar	CuN	2	11	614	5.2
13	4AgN650TZF	650	TZF	AgN	4	1	798	14
14	6CuN650TZF	650	TZF	CuN	6	7	750	6
15	2Cun650HZS	650	HZS	CuN	4	2	407	21
16	Pure650HZS	650	HZS	-	-	2	314	28

The membranes tested for H_2-N_2 separation all performed better than the 1991 polymeric upperbound.

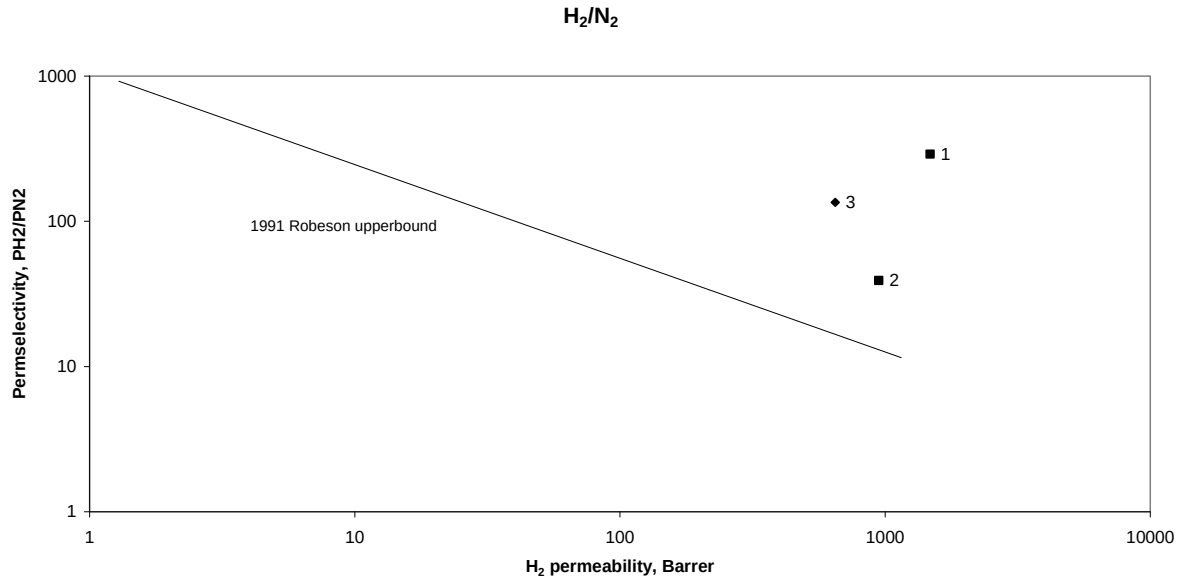

Figure 7-21. Robeson plot for single gas H_2/N_2 pairs, measured at 25°C (■: silver nitrate ◆: copper (II) nitrate, see Table 7-6 for label key)

Table 7-6. Data for H_2/N_2 Robeson plot

No.	Designation	Carb. temp, °C	Oven	Additive	Wt% (in precursor)	Age, days	H_2 perm., Barrer	Selectivity, PH_2/PN_2
1	3.8AgN550TZFM1	550	TZF	AgN	3.8	28	1480	290
2	6AgN550TZF	550	TZF	AgN	6	10	947	39
3	4CuN650TZFB3	650	TZF	CuN	4	231	649	135

7.2.1 Initial assessment of metal additives

Once sufficient membranes had been made to compare the effect of the metal nitrates, it was observed that there was no clear advantage to doping with silver nitrate over copper nitrate. This is seen in the previous Robeson plots. Given the relative prices of these components (13.31 $/ounce or ~428 000 $/ton for silver vs. 7282.5 $/ton for copper[8]), copper nitrate doping is more likely to be commercialised. The experimental focus therefore turned to copper nitrate addition.

The Robeson plots provide a good overview of the performance of the membranes made and tested in this program. However, it is difficult to extract the influence of the individual variables from them. This will be done in the remainder of Section 7. Firstly, though, the uncertainty in results and impact of aging must be discussed, because these can overwhelm the effect of the membrane preparation parameters.

7.2.2 Analysis of uncertainty

Uncertainty in the calculated permeabilities in this work results from the propagation of error in the factors of Eq.'s (37) and (41). The experimental random error (relative standard deviation %) is summarised in Table 7-7. Lie (2005) also calculated the coefficient of

[8] http://newsvote.bbc.co.uk/2/shared/fds/hi/business/market_data/commodities/default.stm on 09/06/07

variation in apparatus permeate-side volume to be 2.6%, which would introduce systematic rather than random error into the permeability.

Table 7-7. Relative error (standard deviations) in experimental work

Factor	Coefficient of variation (SD%)	Reference/calc. method
Feed pressure (transducer)	0.09	Manufacturer
Permeate pressure (transducer)	0.25	Manufacturer
Permeate temperature during test	0.60 (298±2 K)	Cabinet thermometer
Membrane area, average SD	1.3	Repeat measurements, pooled SD
Membrane thickness, average SD	3.3	Repeat measurements, pooled SD

The standard deviations in area and thickness measurement were pooled over the data sets. Random error propagation in an equation of form

$$y = \frac{ab}{c} \tag{44}$$

where a, b and c are experimental variables, may be calculated by summing the squares of the relative standard deviations of each variable and obtaining the square root (Skoog, West and Holler, 1996):

$$\frac{s_y}{y} = \sqrt{\left(\frac{s_a}{a}\right)^2 + \left(\frac{s_b}{b}\right)^2 + \left(\frac{s_c}{c}\right)^2} \tag{45}$$

According to this formula, the coefficient of variation associated with pure gas permeability is 3.6%. Most of the random error in the single gas tests was introduced by the standard deviation in membrane thickness. The uncertainty in the measured molar concentrations of the permeate gases introduced further error in the mixed gas calculations, but this is dealt with in the relevant sections.

7.3 Aging of membranes

The membranes had been stored in a desiccator or exposed to laboratory air between experimental runs. Several membranes were retested over a period of time and all exhibited signs of aging, in the form of permeability decreases (see Figure 7-22).

- This occurred for all degrees of metal addition, carbonization procedures and ovens used.
- Permeability decreased as much as 80% in some cases.
- The permeabilities for AgN membranes carbonized at 550°C did not appear to stabilise, even after 300 days, whereas those in 650°C membranes tended to bottom out.
- The original hydrogen permeability of a membrane was not recovered by evacuation or heating to 150ºC (the limit tested), once aging had occurred.

It was suggested in Section 4.5.1 that the final pyrolysis temperature may influence the aging behaviour, because the final temperature affects the number of dangling bonds in the material. In Figure 7-22, it can be seen that the aging curves for AgN membranes prepared at 550°C are steeper than those of the 650°C membranes, which supports this suggestion (though the

metals are different). From an aging point of view, therefore, membranes prepared at 650°C are more robust.

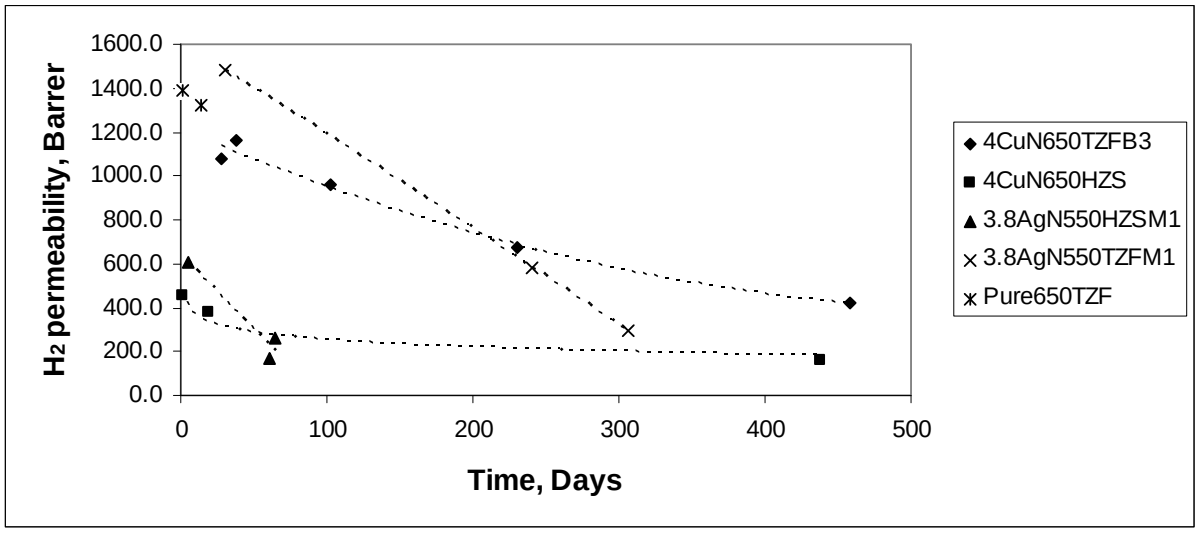

Figure 7-22. Decreasing hydrogen permeability of membranes as a function of age. Conditions: single gas, 2 bar, 25°C

The behaviour of permselectivity with time is different to that of permeability (Figure 7-23) and also appears to depend on the oven used. The H_2/CH_4 selectivity increased for the 4CuNHZSM1 membrane (prepared in the HZS oven), perhaps because the smaller effective pore size was more affected by oxygen group addition, whereas the TZF membranes experienced a slight decline in selectivity over this range. The value for membrane 4CuN650TZFB3 at 100 days appears to be an outlier, error perhaps being introduced by a leak in the permeation rig during that test.

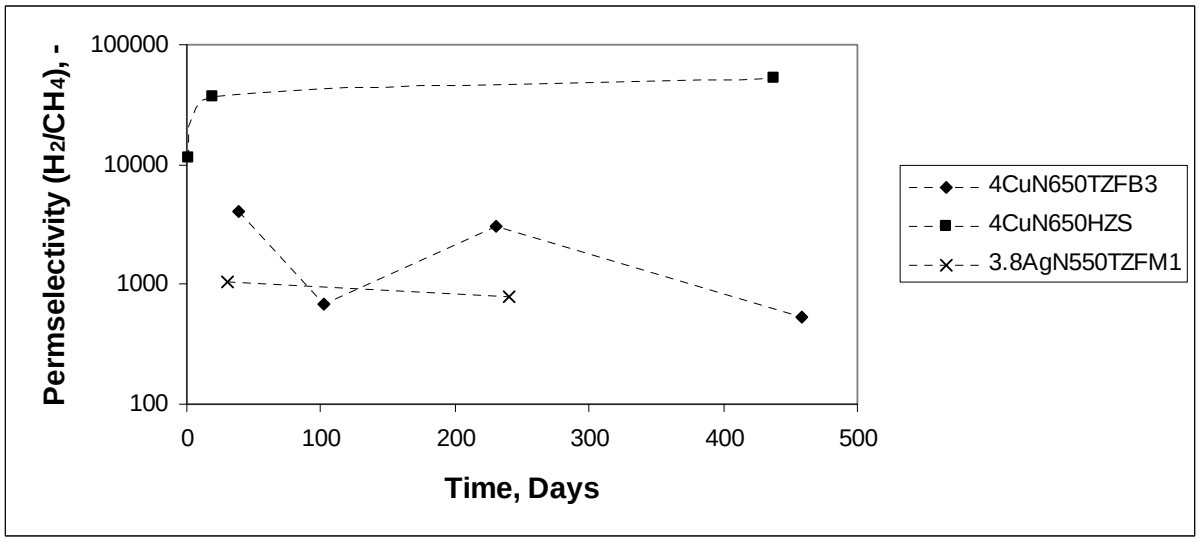

Figure 7-23. Changing hydrogen selectivity of membranes as a function of age. Conditions: single gas, 2 bar, 25°C

There seemed to be little aging *during* experiments, when the membrane was not exposed to air. A 4%CuN membrane (designated 4CuN650TZFB3) was exposed to H_2, CH_4, N_2, CO_2, C_2H_8, C_3H_8 and i-C_4H_{10} at temperatures between 25°C and 90°C over three months without aging. The results for this membrane are presented in Section 7.8.1.

It was observed in some cases that the permeability of a membrane that had been stored in air increased slightly after the first test in a specific run, perhaps due to the evacuation of physisorbed gases and water between tests. The hydrogen permeability for 4CuN650TZFB3 at 460 days increased by 17% to the value presented in Figure 7-23 after heating to 90°C and evacuating overnight.

The statement that the effect of aging can mask other variables is supported by Figure 7-24. Here, hydrogen permeability has been plotted against age for two groups. The first is for all membranes made in the TZF oven at 650°C, containing 0-6% CuN (CuN650TZF). The second series consists of all membranes prepared in the HZS oven under vacuum, with any metal additive and at 550°C or 650°C. Both series produce monotonic aging curves.

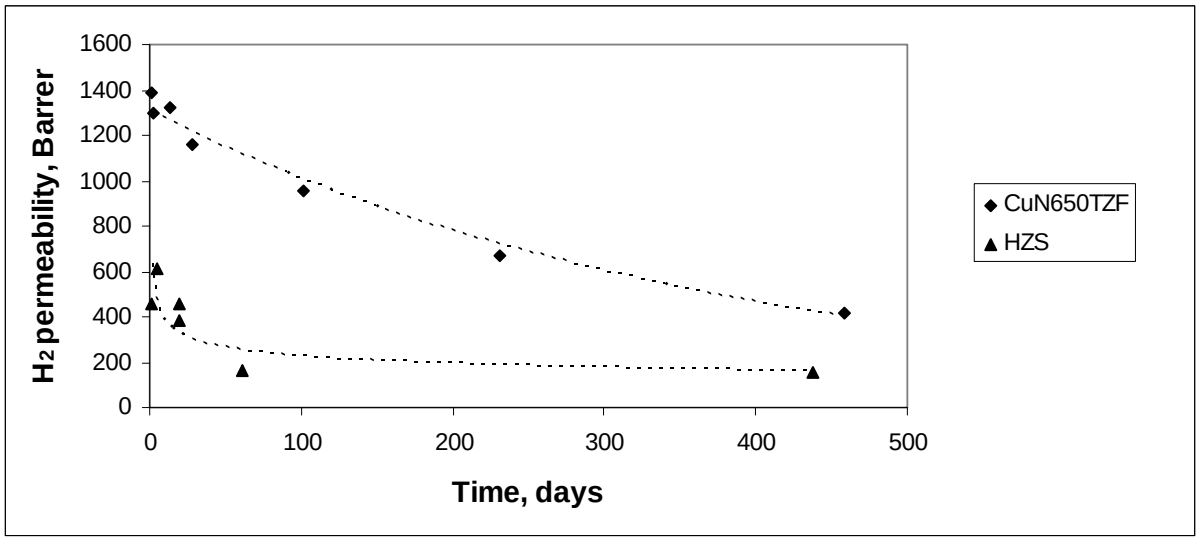

Figure 7-24. Decreasing hydrogen selectivity of membranes as a function of age. Conditions: single gas, 2 bar, 25°C

7.4 Heat treatment temperature

When the ages of the membranes were similar, it was possible to elucidate the effect of the final carbonization temperature in the protocol on the permeation properties. Figure 7-25 shows how the hydrogen and carbon dioxide permeabilities vary with final temperature, for a series of membranes that were stamped from the same precursor film. This eliminated other factors such as TFA exposure time, cellulose source inhomogeneity and contamination. The membranes were allowed 1 day's exposure to laboratory air (since even short exposures are known to cause aging, it was decided to standardize contact time rather than attempt to avoid it). The graph shows a maximum permeability between 550 and 650°C for both gases, with the inferred peak being close to 650°C. Permeability is very low up to 400°C, as pore creation is still occurring. It can be seen in the TGA curves of cellulose carbonization (such as Figure 7-9) that the majority of the weight loss has already occurred by this temperature, yet the porosity responsible for permeation is apparently still low. There is further, but more subdued, weight loss between 400°C and 600°C and this, together with rearrangement of the pore structure, contributes to a dramatic rise in permeability over this range. This weight loss is shown in Figure 7-26. The closure of pores as carbon atoms rearrange to eliminate dangling bonds dominates beyond 650°C, so that an increase of only 50°C in the final temperature greatly reduced the hydrogen and carbon dioxide permeabilities.

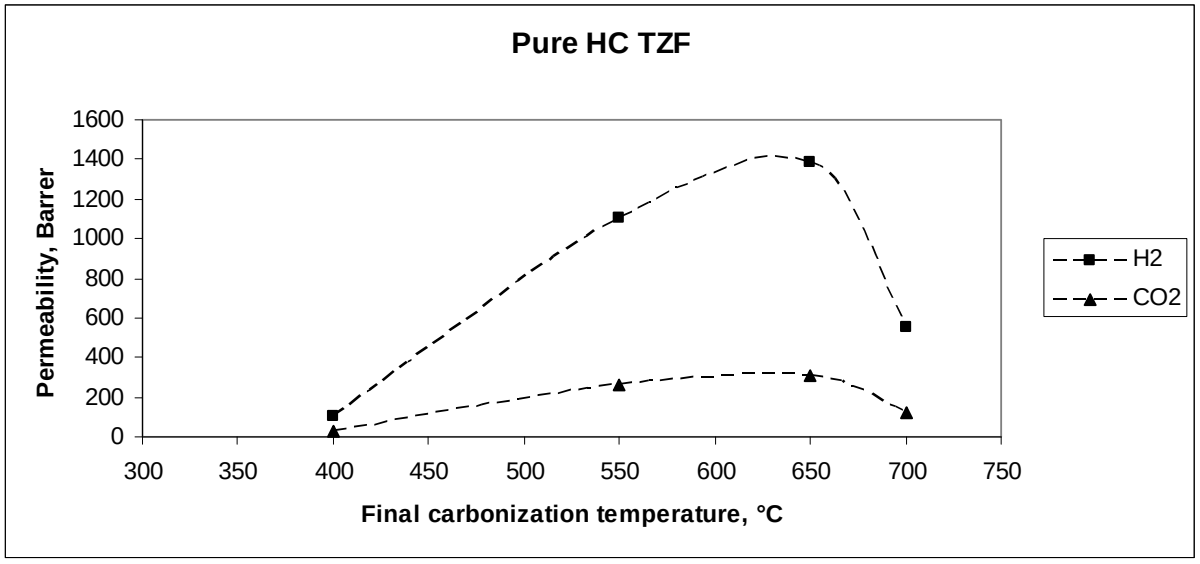

Figure 7-25. Hydrogen and carbon dioxide permeability plotted against final carbonization temperature, measured at 25°C. Pure carbon (no metal additives), produced in TZF oven under vacuum (PureHC TZF)

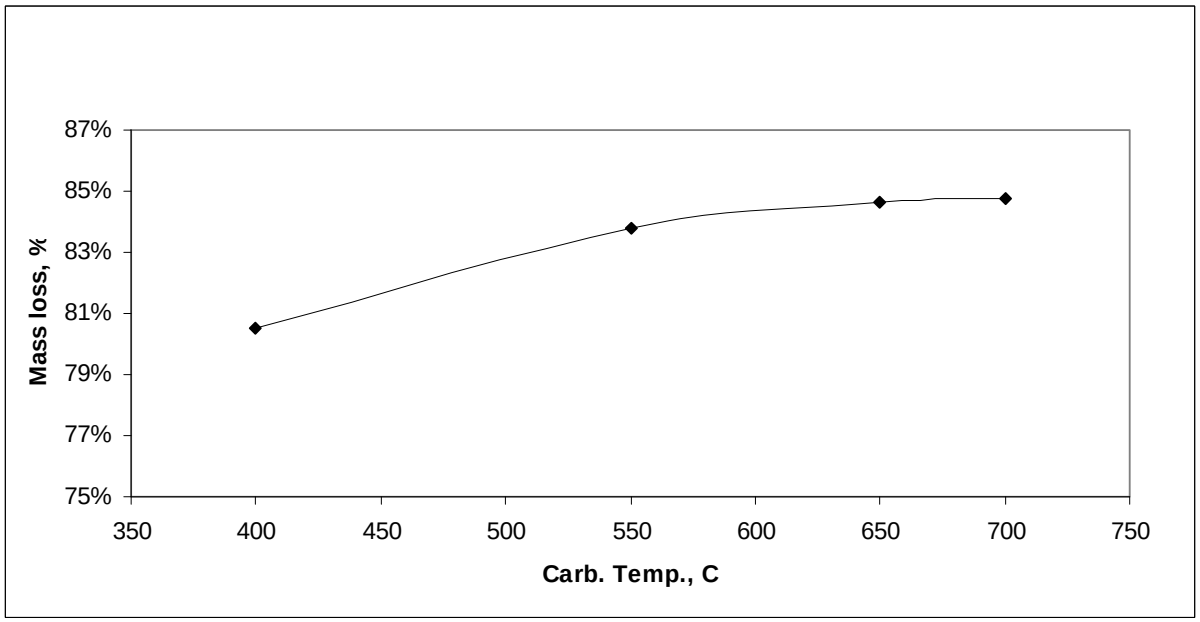

Figure 7-26. Weight loss plotted against final carbonization temperature. Pure carbon (no metal additives), produced in TZF oven under vacuum (PureHC TZF)

The effect of final carbonization temperature was also plotted for membranes that had had 4 wt% copper (II) nitrate added to the precursor (Figure 7-27). The external factors for this series were not controlled as tightly as for the pure carbon series and the membranes were created from different precursor batches and tested after different aging times. Nevertheless, a similar trend is seen, with hydrogen and CO_2 permeability peaking between 550 and 650°C.

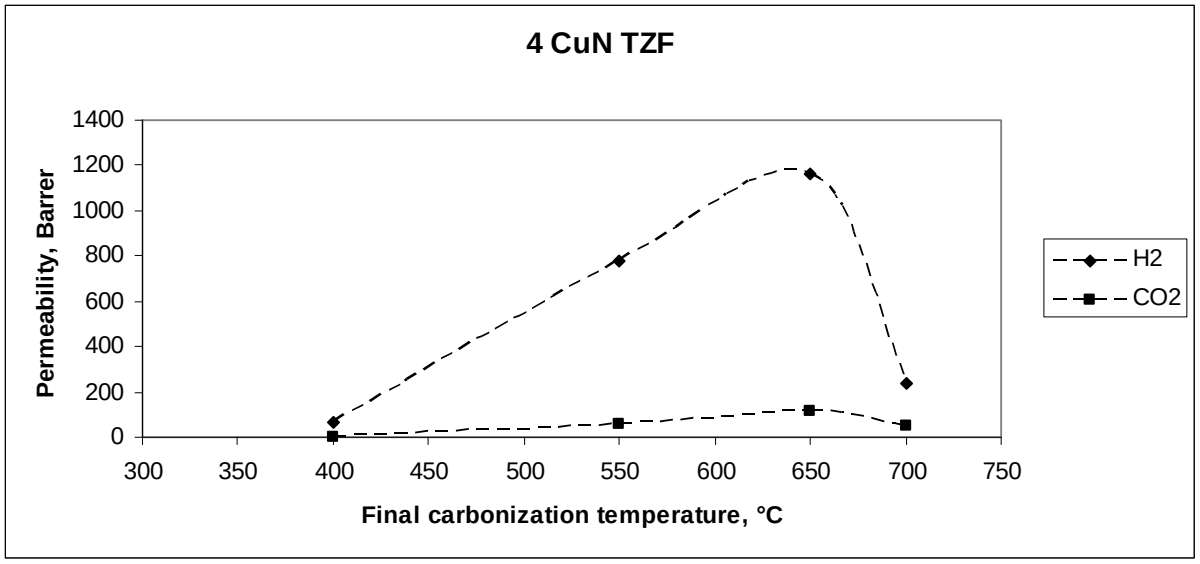

Figure 7-27. Hydrogen and CO_2 permeabilities plotted against final carbonization temperature, measured at 25°C. 4wt% copper nitrate added to precursor, produced in TZF oven under vacuum. CO_2 value at 550°C measured by Jon Arvid Lie (Lie, 2005)

The permselectivity of the membranes for hydrogen vs. carbon dioxide is presented in Figure 7-28. The selectivity of the pure cellulose membrane increased from approximately 2 at 400°C to 4 at 550°C, and remained constant to 700°C. This surprising result implies that the ratio of porosity available to hydrogen vs. carbon dioxide was similar from 550°C to 700°C, even though the permeabilities decreased. The selectivity of the copper nitrate-doped membrane was higher than for the pure carbon membrane, decreasing as the final temperature increased. The copper oxide therefore constricted the pores and increased selectivity.

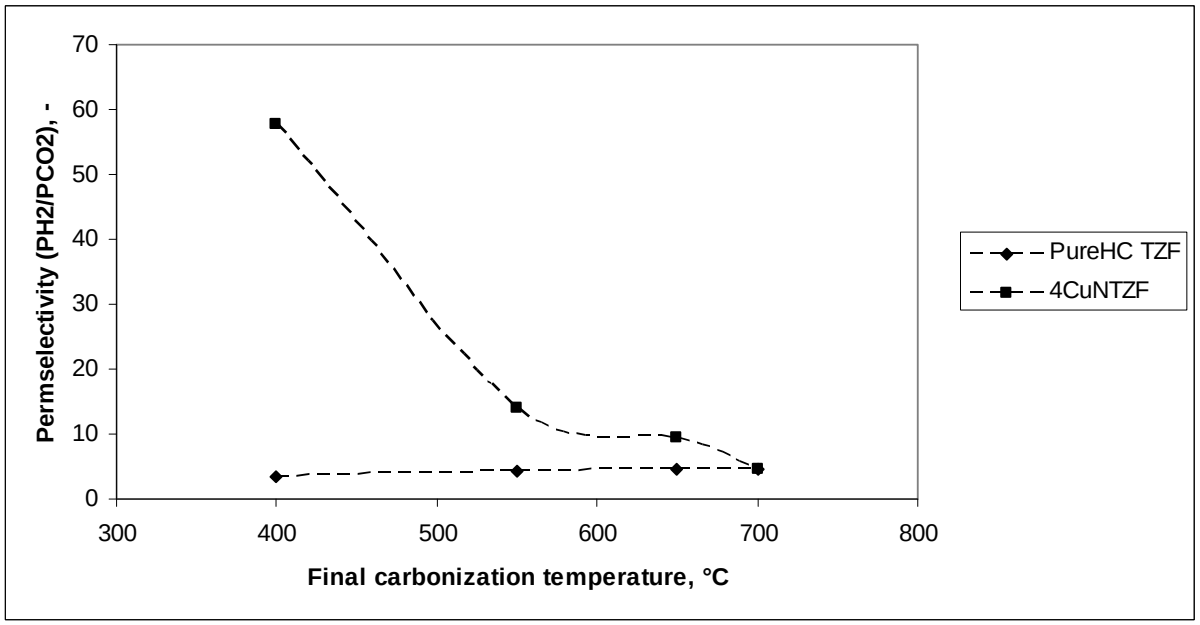

Figure 7-28. Hydrogen/carbon dioxide SG selectivity plotted against final carbonization temperature, measured at 25°C

The methane permeability peaks at a lower temperature (Figure 7-29), because the pore rearrangement at higher temperatures that benefited hydrogen and carbon dioxide also constricted pores that were initially accessible to methane.

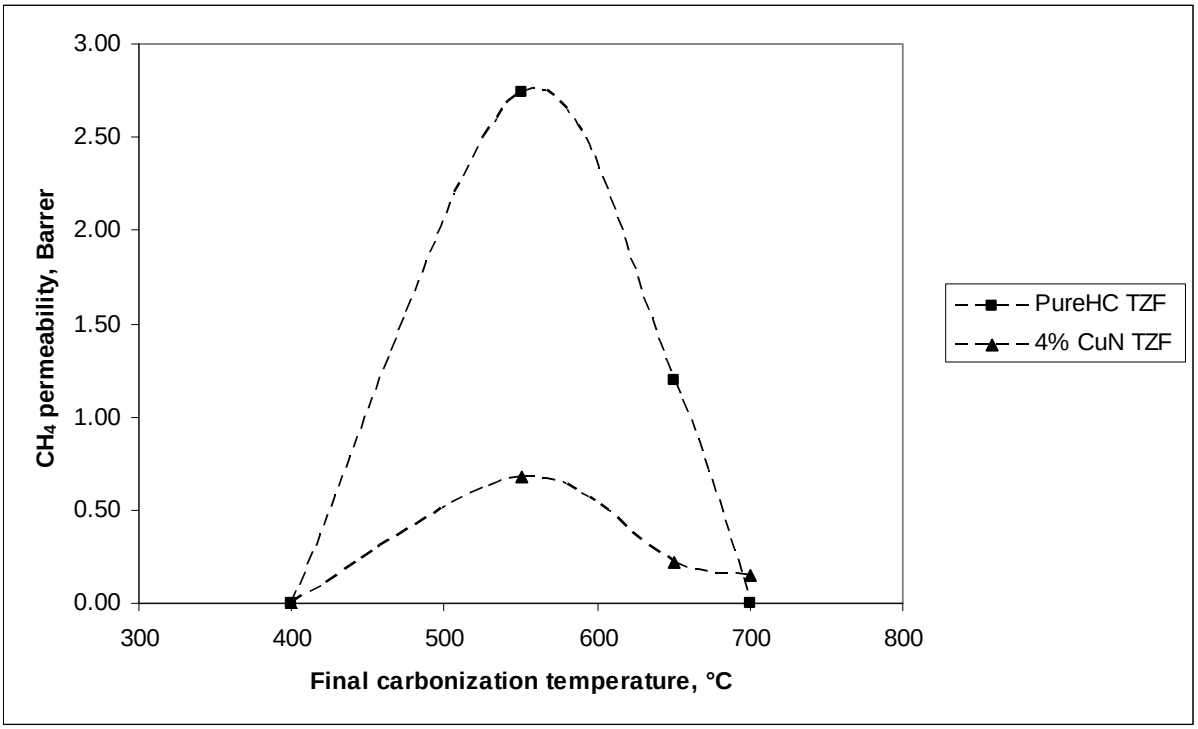

Figure 7-29. Methane permeability (25°C) plotted against final carbonization temperature for pure carbon and carbon with 4wt% copper nitrate added to precursor, produced in TZF oven under vacuum

It was difficult to calculate the low methane permeability for the 400°C and 700°C membranes. Normally, the leak rate was subtracted from the rate of pressure rise (*dp/dt*), but at the high and low temperatures the methane *dp/dt* was close to or even less than the measured leak rate. The permeability was set to zero in these cases.

Table 7-8. H_2/CH_4 SG selectivity vs. final carbonization temp (25°C)

	Final carbonization temperature, °C			
	400	550	650	700
Pure HC TZF	V. large	402	1157	V. large
4CuN TZF	V. large	1227	4007	1550

Generally, these trends are in agreement with the findings of Koresh and Soffer (1986), which is discussed in Section 4.2.2. They also found that hydrogen permeability peaked between 600 and 700°C and that CH_4 peaked somewhat lower, between 500 and 600°C. This behaviour is consistent with the pore distribution shift proposed by Steel and Koros (2003), which is also discussed in Section 4.2.2. It implies a redistribution of porosity from a wider, more random distribution to a narrower, more homogenous distribution at higher temperature, because more porosity apparently becomes available to hydrogen but not methane (Figure 7-30).

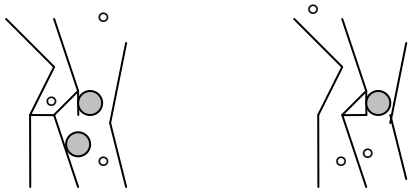

Figure 7-30. Creation of more homogenous porosity at higher temperatures. ○: H_2, ●: Methane

7.5 Metal nitrate addition

In the previous section, it was shown that the 4wt% copper nitrate-doped membranes were more selective than pure carbon ones. The analysis is extended in this section to all of the membranes doped with silver or copper nitrate. There is some scatter in the graphs of permeability vs. metal salt wt%, but the general trend was that the permeability decreased as metal salt was added to the precursor (see Figure 7-31 to Figure 7-33). One exception to this is the range prepared in the HZS furnace under vacuum, which saw an increase in H_2 permeability, indicating a spacer effect in the very tight membranes.

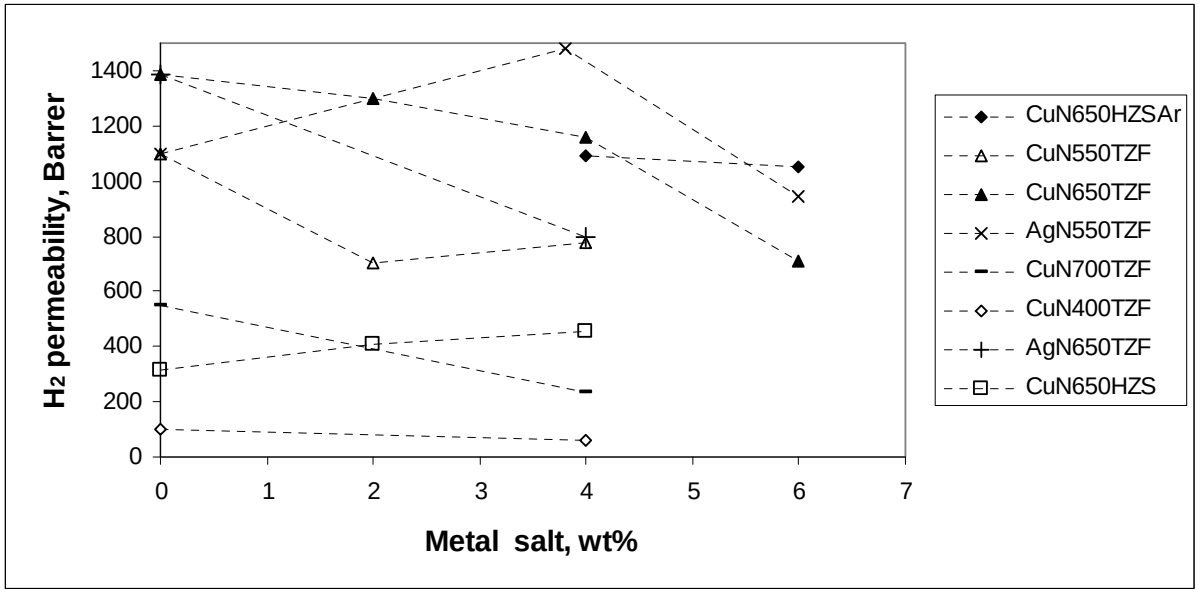

Figure 7-31. H_2 permeability vs metal nitrate wt% of cellulose precursor, measured at 25°C

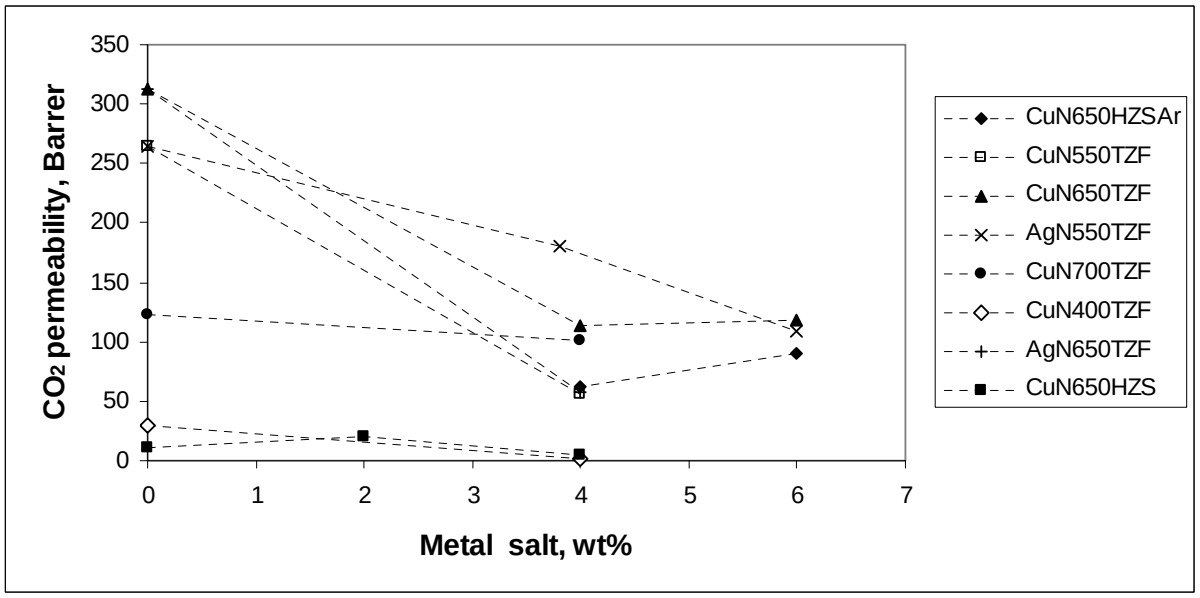

Figure 7-32. CO_2 permeability vs metal nitrate wt% of cellulose precursor, measured at 25°C

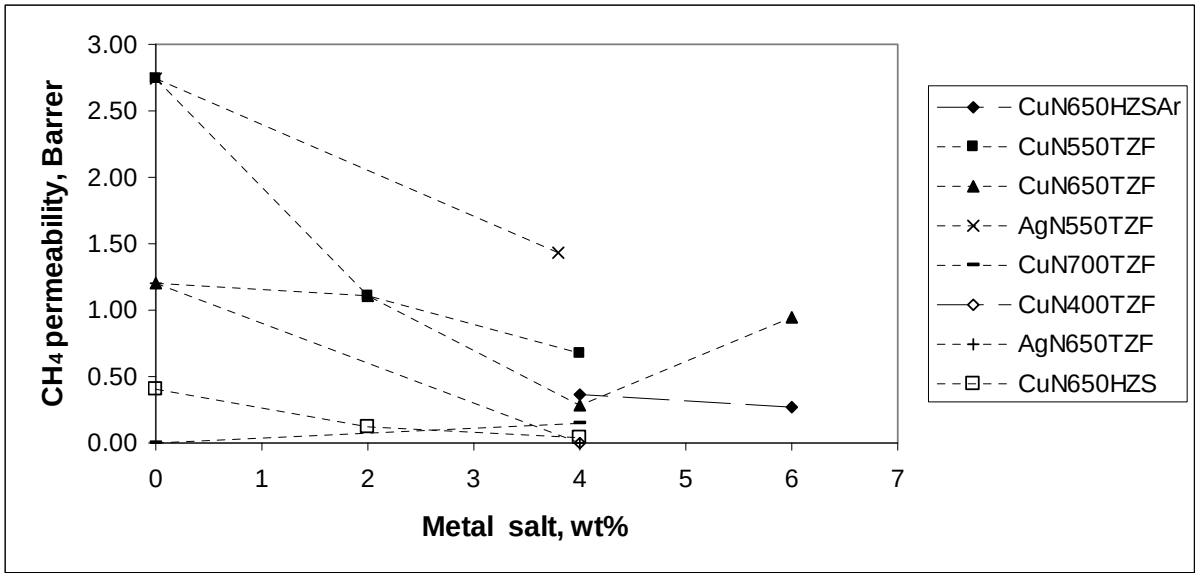

Figure 7-33. CH_4 permeability vs metal nitrate wt% of cellulose precursor, measured at 25°C (6AgN550TZF appears to be an outlier and is excluded)

The behaviour seen above is consistent with pore constriction by deposition of the metal species in the pores. There is little evidence of the metal nitrates acting as porogens in the TZF and HZSAr series (in that case one would expect an increase in permeability for all gases). The decrease in permeability for components can cause the selectivity to shift in either direction. The change in selectivity, $\Delta\alpha$, can be represented by

$$\Delta\alpha_{A/B} = \frac{\Delta P_A}{\Delta P_B} \qquad (46)$$

If component A is retarded more than B by the increase in metal doping, then selectivity will decrease, and vice versa. This phenomenon depends on the pore size distribution of the material as well as the components. Generally, the H_2/CH_4 selectivity of membranes increased with metal addition (Figure 7-34). The H_2/CO_2 selectivity increased from 0-4% and decreased from 4-6% (Figure 7-35).

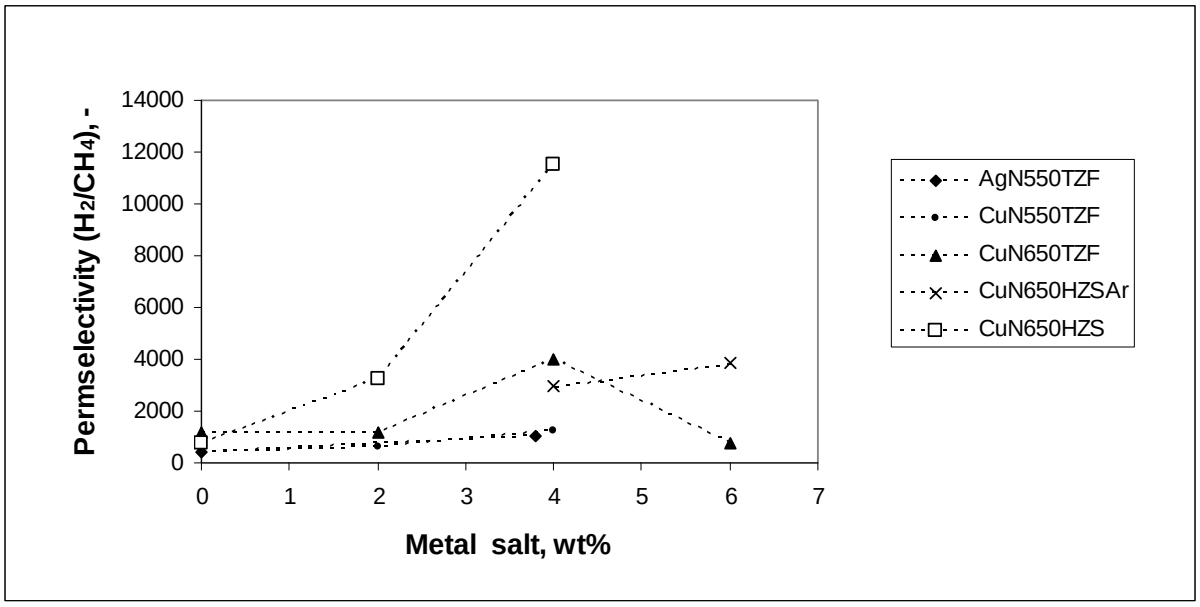

Figure 7-34. H_2/CH_4 permselectivity vs metal nitrate wt% of cellulose precursor, measured at 25°C (6AgN550TZF appears to be an outlier)

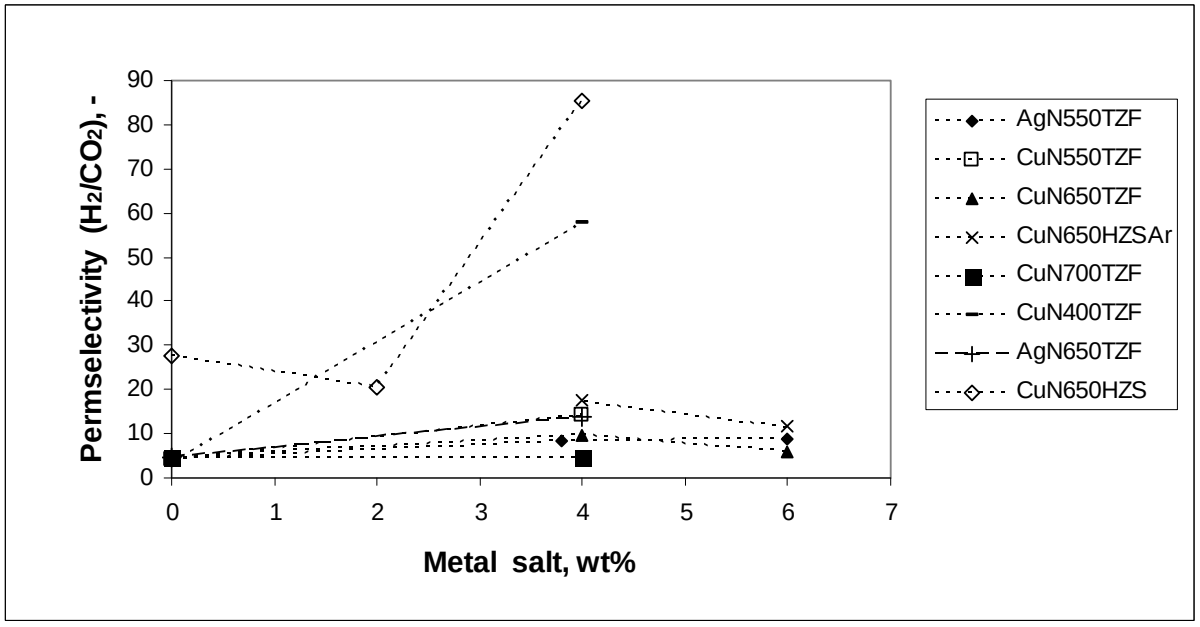

Figure 7-35. H_2/CO_2 permselectivity vs. metal nitrate wt% of cellulose precursor, measured at 25°C

Unfortunately, there is a degree of correlation between the metal wt% of the membrane and the age of the membrane when tested (Figure 7-36). This is because it was thought, in the early stages of the experimental work, that storing the membranes in a desiccator was sufficient protection against aging and the delay between preparation and testing tended to be longer. Many of the membranes with higher metal wt% were made in the beginning as well, hence the correlation. Although most of the membranes were younger than 20 days when tested, it is now known that even this length of exposure causes significant decrease in permeability, due to rapid initial oxygen chemisorption. Some of the trend in Figure 7-31 to Figure 7-33, therefore, must be attributed to aging. Nevertheless, when members of a membrane series have approximately the same age (in AgN650TZF, CuN550TZF,

CuN650TZF, CuN400TZF), those with greater metal contents still have lower hydrogen permeabilities.

It is also certain that metal addition affects the selectivity, despite there being some similarity in the trends of metal% vs. age and H_2/CH_4 selectivity vs. age. The H_2/CH_4 selectivity increases more strongly as a function of additive wt% than with the aging effect alone (refer to Figure 7-22). The CuN400TZF, Ag650TZF and CuN550TZF series showed a large increase in H_2/CO_2 selectivity as metal addition increased, even though the membranes were the same age.

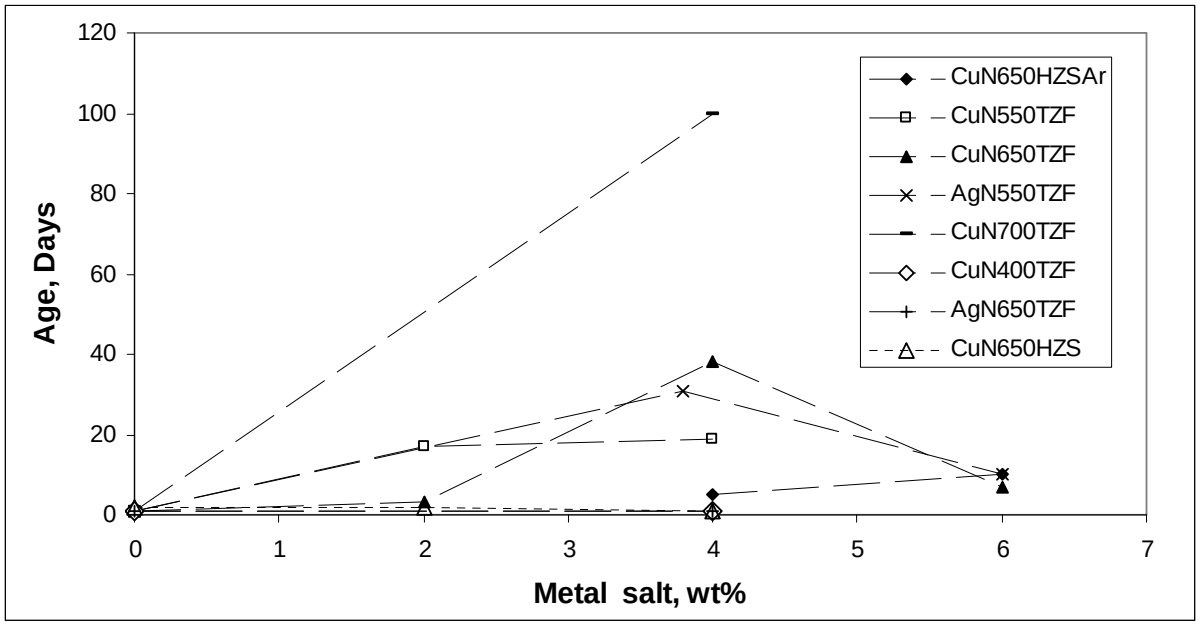

Figure 7-36. Metal salt wt% vs. age of membrane when tested

The optimum metal loading is dependent on the application, since there appears to be a trade-off between permeability and selectivity. H_2-CH_4 applications may favour no loading and high permeability, especially when the separation is easy and the highest selectivity is unnecessary. H_2-CO_2 separation is best served by membranes with about 4% CuN loading, to increase selectivity.

7.6 Single gas vs. mixed gas tests

One of the dangers of characterising carbon membranes by single gas Robeson plots is that reverse selectivity will not be identified. This was explained in Section 4.6.3. However, none of the membranes tested with mixed gases demonstrated competitive adsorption to the extent that selectivities were reversed – all of them functioned as molecular sieves. There was, however, evidence that the competitive adsorption by heavier gases reduced the permeability of hydrogen. A table comparing single gas and mixed gas permeabilities is shown below (Table 7-9). A reduction in permeability was also seen for CO_2 and CH_4. This could be due to the mutual hindrance of CO_2 and CH_4 in the natural gas mixture and CO_2-N_2 in the 50% H_2-40% CO_2-10% N_2 mixture. Surprisingly, methane also appeared to be hindered by hydrogen at 25°C but not 90°C.

Table 7-9. Single gas vs. mixed gas results for the same membranes.

Membrane	Gas	Temp, °C	Gas mixture	Single gas perm, Barrer	Mixed gas perm, Barrer	%Change
6CuN650HZSAr	H_2	24	H_2-CH_4	1051	943	-10%
2CuN650TZF	H_2	25	H_2-CH_4	1296	700	-46%
4.3AgN550TZF	H_2	25	H_2-CH_4	320	135	-58%
4CuN650TZFB3 R2	H_2	24	H_2-CH_4	673	636	-5%
	H_2	60	H_2-CH_4	930	854	-8%
	H_2	90	H_2-CH_4	1087	999	-8%
	CO_2	90	50H_2-40CO_2-10N_2	105	77	-26%
	CO_2	25	30H_2-70 NG*	27	22	-16%
	CO_2	90	30H_2-70 NG*	105	84	-20%
	CH_4	25	H_2-CH_4	0.22	0.04	-82%
	CH_4	90	H_2-CH_4	1.09	1.01	-7%

*NG = natural gas mixture, containing approximately 82 mol% CH_4, 10 mol% C_2H_6, 4.5 mol% C_3H_8, 2 mol% CO_2, 1.5 mol% N_2 and 0.2 mol% i-C_4H_{10}

7.7 Effect of operating temperature and pressure

Some of the membranes made were subjected to permeation tests with varied temperature and pressure. The general behaviour is introduced in this section, with examples from a sample spread of membranes, whereas the details of specific application tests (i.e. extended runs with representative feeds) are presented in the Section 7.8. Conclusions were:

- Temperature was observed, in all the single gas cases, to increase the permeabilities of gases and decrease H_2 selectivities, behaviour consistent with the theory presented in Section 4.4.3.
- Pressure had little or no effect on hydrogen or carbon dioxide permeability in single gas tests.
- Some pressure effect was seen in the mixed gas tests, where increased pressure appeared to increase the hindrance of hydrogen permeability by the more condensible gases.

The effect of higher temperature on the materials used to mount the membranes on the permeation cell was checked. Apart from some discoloration of the epoxy or Araldite® and aluminium, there was no evidence of shrinkage or failure of these materials. The area of a membrane sealed with Araldite® was measured before and after it had been heated to 150°C (for results shown in Figure 7-37) and was found to be identical, indicating that the Araldite® did not creep.

7.7.1 Single gas tests

An example is shown of a cellulose membrane doped with 4% copper (II) nitrate and carbonized under Ar flow (~1cm/min), which was tested with H_2, CO_2 and CH_4 (Figure 7-37). Pressure had little effect on the hydrogen permeability in the range of 2-6 bar, whereas temperature had a significant effect.

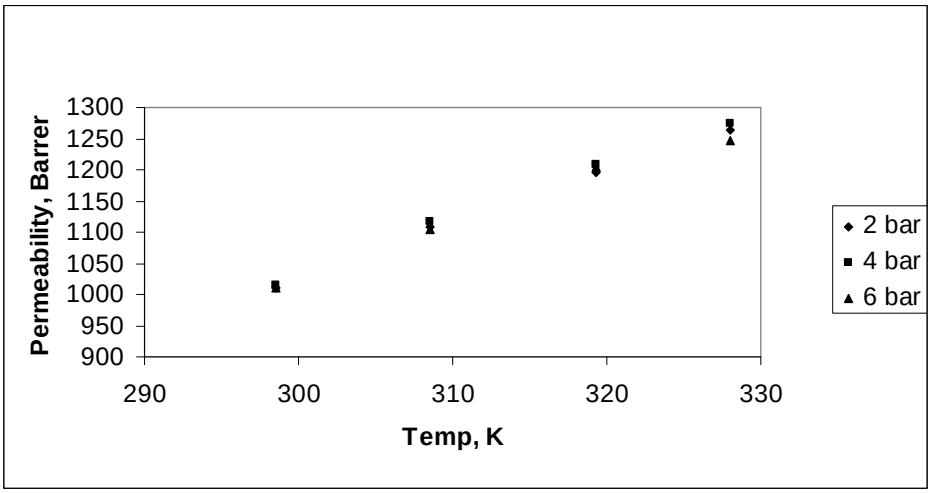

Figure 7-37. The influence of pressure and temperature on hydrogen permeability (4CuN650HZSAr)

The permeabilities of CO_2 and CH_4 were also insensitive to pressure in the range of 2-6 bar. A summary of results for pressure variation is shown in Table 7-10.

Table 7-10. Influence of feed pressure on CO_2 and CH_4 permeability for two different membranes

Test/membrane	Gas	Pressure, bar	Temperature, °C	Permeability, Barrer
4CuN650TZFB3 R3	CH_4	2	90	1.1
		6	90	1.2
	CO_2	2	25	26.7
		6	25	26.5
		2	90	105.1
		6	90	99.3
	N_2	6	90	1.5
4CuN650HZSAr	CO_2	4	25	42.8
		6	25	42.7

The apparent transport activation energy, E_s, and P_0 (of $P=P_0\ exp(-E_s/RT)$, see Eq. (29)) were calculated for the tests where temperature was varied. There is a lot of scatter in the values (Table 7-11). What *is* apparent is that the activation energies follow the order $E_s(H_2)<(E_s)CO_2<E_s(CH_4)$. There also appears to be a relationship between the activation energies and the pyrolysis ovens used. Generally, E_s (H_2) was higher for the 'tighter' membranes pyrolysed under vacuum in the HZS oven. Activation energies, therefore, are an indicator of the apparent pore size of carbon membranes, consistent with the theory that diffusion activation energy stems from the probability of a molecule passing a constriction (Eq. (20)). As expected, a rough linear trend is seen between the permeability of a gas at 25°C and the gas's activation energy, because both are dependent on pore size distribution (Figure 7-38). Aging was also observed to increase the transport activation energy, as pore size is reduced by chemisorption.

Table 7-11. Kinetic parameters for gas permeation ($P=P_0 \exp(-E_s/RT)$)

Membrane	Gas	Perm. at 25°C, Barrer	E_s, kJ/mol	P_0, Barrer
4CuN650TZFB3M3	H_2	673	8.0	16020
	CO_2	27	20.1	78042
	CH_4	0.22	24.3	3372
4CuN650HZSAr	H_2	1092	6.1	12014
3.8AgN550HZSM2	H_2	608	15.7	342148
	CH_4	0.02	56.1	$2 \cdot 10^8$
3.8AgN550HZSM1	H_2	166	12.6	43304
3.8AgN550TZFM3	H_2	295	18.4	502733
3.8AgN550TZFM2	H_2	582	13.7	148896
	CH_4*	0.73	65.5	$1.33 \cdot 10^{11}$
2CuN650TZF	H_2	1296	3.8	5961
	CH_4	1.11	18.2	1717
Pure650TZF	H_2	1325	4.3	8075

*Significant scatter in data

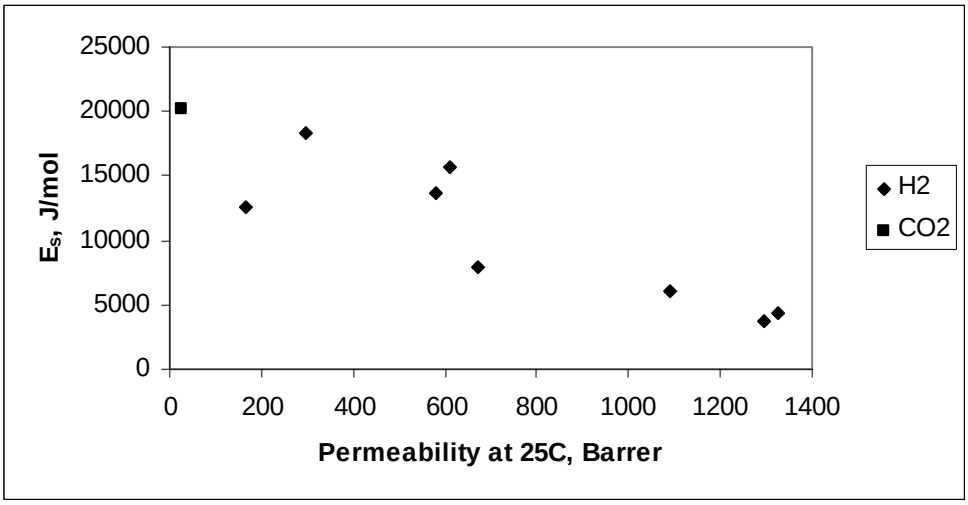

Figure 7-38. Plot of permeability at 25°C and 2 bar vs E_s

Higher test temperature did not only benefit hydrogen. According to Eq. (31), the larger E_s is, the larger the effect temperature will have on permeability. This is seen in Figure 7-42 and Figure 7-43, where the permeabilities of CO_2 and CH_4 increased more than that of H_2. It was observed in all the temperature tests that the selectivity to hydrogen decreased. There is therefore a trade-off between membrane productivity and selectivity that must be considered when designing processes.

In another example, a membrane produced from pure cellulose and pyrolysed under vacuum in oven TZF at 650°C was tested with H_2 and CO_2 from 25°C up to 150°C. The curves exhibited Arrhenius behaviour (Figure 7-39). In this temperature interval, the permeability of hydrogen increased from 1325 to 2255 Barrer, but the selectivity halved (Figure 7-40).

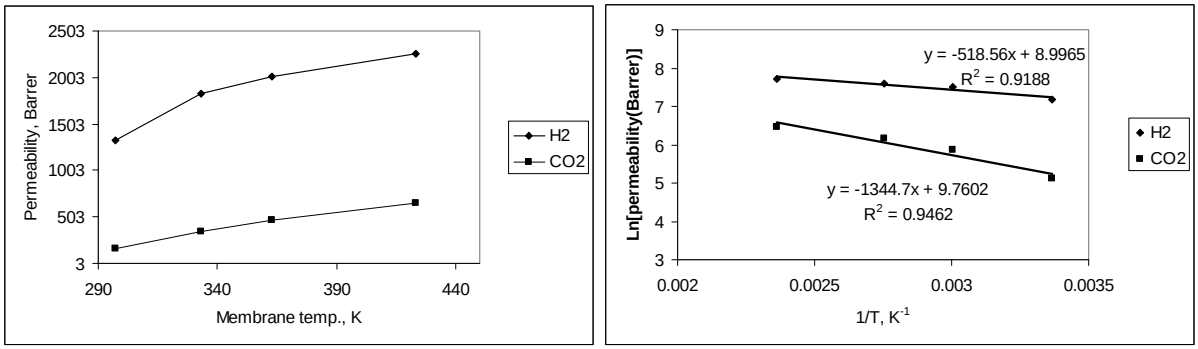

Figure 7-39. Effect of operating temperature on H_2 and CO_2 permeability. Pure carbon membrane (HCPure650TZF)

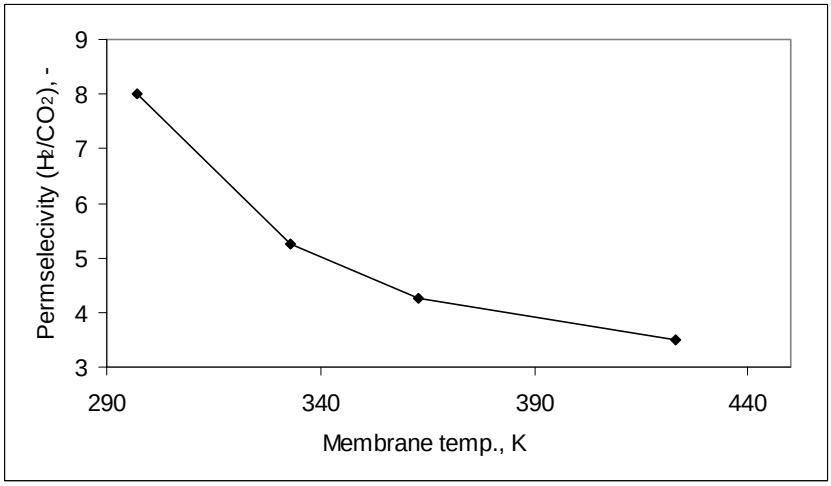

Figure 7-40. Effect of operating temperature on H_2/CO_2 permselectivity. Pure carbon membrane (HCPure650TZF)

7.7.2 Mixed gas tests

Pressure was seen to affect the permeance of hydrogen slightly in mixed gas tests with methane, most likely as a result of competitive adsorption from methane, since single gas hydrogen permeability was shown to be independent of pressure. An example with a membrane prepared from cellulose doped with 2wt% copper (II) nitrate and pyrolysed under vacuum in TZF is presented in Figure 7-41. Further examples are to be seen in Figure 7-43, Figure 7-44 and Figure 7-45.

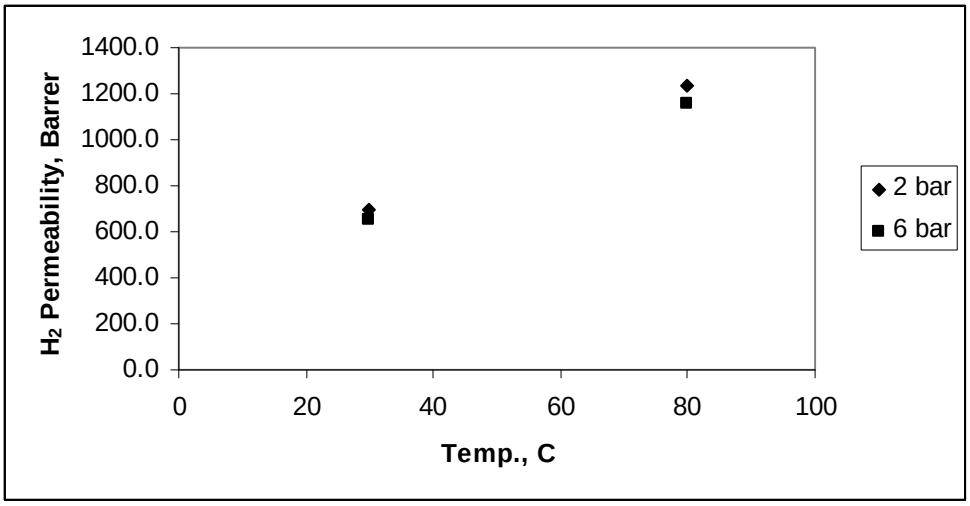

Figure 7-41. Hydrogen permeability for a 30mol%H_2-70mol%CH_4 mixture. Membrane: 2CuN650TZF

Temperature increased the permeabilities of all the gases tested, although the selectivity of hydrogen over other gases generally decreased. The permeability of hydrogen increased significantly in all cases. For example, in Figure 7-41, the permeability almost doubled. The percentage increase was more than that for single gas permeability over the same temperature range, hinting at the simultaneous reduction of the competitive adsorption of methane.

7.8 Realistic gas mixture tests

The application of carbon membranes was simulated by running mixed gas tests with gases that approximated true feeds. Usually, single gas feeds were tested first, followed by mixtures of the principle gases (usually binary feeds), and finally with more representative mixtures.

The applications considered in this work were:

1. Recovery of hydrogen from a natural gas mixture. The principle gases are H_2 and CH_4, with smaller fractions of C_2H_n, C_3H_n, C_4H_n, CO_2 and N_2.
2. Recovery of hydrogen from refinery off-gases. The principle gases are H_2 and CH_4, with varying fractions of C_2H_n, C_3H_n and C_4H_n.
3. Separation of hydrogen from CO_2. The principle gases are H_2, CO_2 and N_2, but small amounts of CO and H_2S are also present.

7.8.1 Tests with 4CuN650TZF

The 4% copper (II) nitrate membrane designated 4CuN650TZF B3 was selected for simulated application testing because:

- The membrane achieved an excellent performance for H_2-CH_4 and reasonable performance for H_2-N_2 and H_2-CO_2 separation (see Section 7.2).
- The membrane's aging history was relatively detailed and reasonable performance was still achieved after 7 months of air exposure.

The membrane was tested using mixed H_2-CH_4, H_2-simulated natural gas (N_2, CO_2, C1-C4), and simulated water gas shift (H_2, CO_2, N_2) feeds at different temperatures and pressures.

Membranes from the same batch were tested 28 (R1), 102 (R2) and 231 (R3) days after pyrolysis. The second and third run included H_2-CH_4 mixed gas tests. The third run, which lasted approximately 3 months, also included simulated natural gas (N_2, CO_2, C1-C4), and simulated water-gas-shift (H_2, CO_2, N_2) feeds.

Figure 7-42 shows the sieving ability of the membrane in run 3, with permeability being strongly dependent on molecule kinetic diameter. Table 7-12 presents the single gas results for all the runs.

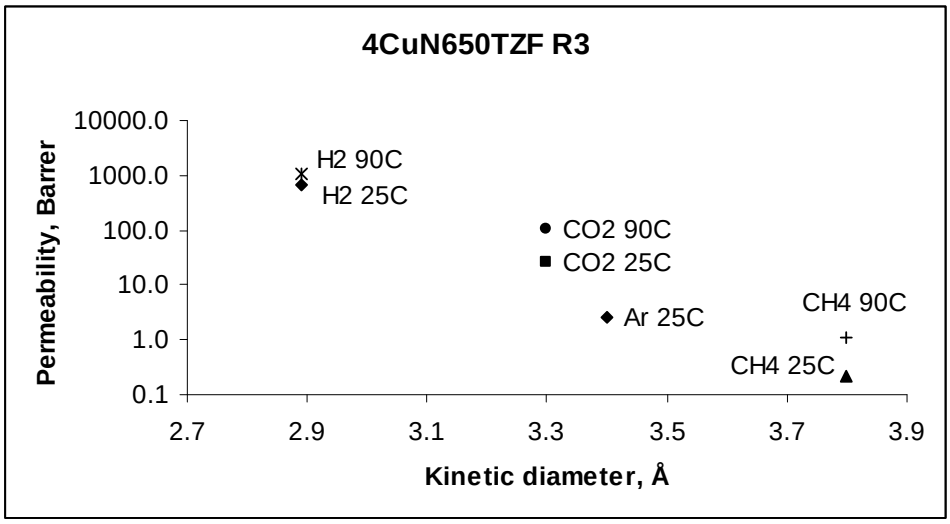

Figure 7-42. Single gas permeabilities at 2 bar

The H_2 and CO_2 permeability at 25°C decreased with membrane age, whereas no trend was discernable with methane. The methane permeability measured in Run 2 appears too high and may have included a large leak contribution. P_{H2}/P_{CH4} decreased between runs 1 and 3, contrary to the expected consequence of aging. The membrane was very selective and permeable, with respect to hydrogen, implying that the membrane possessed pores with a narrow size distribution that lay below the sieving diameter for methane. Aging may have restricted pores that were previously accessible to hydrogen, and to a lesser, extent, carbon dioxide. Thus, the permeability of hydrogen and carbon dioxide would have decreased disproportionately more than that of methane, resulting in a decrease in selectivity. The selectivity for H_2 over CO_2 increased with aging.

Table 7-12. Pure gas history for 4CuN650TZF (R3)

Run	Gas, *i*	Temperature, °C	Pressure, Bar	Permeability, Barrer	P_i/P_{CH4}	$P_i/_{PCO2}$
R1	H_2	25	2	1161.1	4007	10
		25	2	1076.8	3717	9
	CO_2	25	2	113.4	392	
	CH_4	25	2	0.3		
R2	H_2	25	2	956.7	680	
	CH_4	25	2	1.4		
R3	H_2	25	2	672.8	3042	25
		25	2	658.4	2977	25
		25	2	649.0	2950	24
		25	6	662.4	2995	25
		60	2	930.3	-	-
		60	6	961.4	-	-
		90	2	1087.2	1000	10
		90	6	1110.3	940	11
	CO_2	25	2	26.7	121	
		25	6	26.5	120	
		90	2	105.1	97	
		90	6	99.3	84	
	CH_4	25	2	0.2		
		90	2	1.1		
		90	6	1.2		
	Ar	30	2	2.5		

From Figure 7-42, Figure 7-43 and Table 7-12 it can be seen that the H_2, CO_2 and CH_4 permeabilities increased with increased temperature. Methane's permeability increased disproportionately more than those of CO_2 and H_2, and the permeability of CO_2 increased disproportionately more than that of H_2. Therefore, P_{H2}/P_{CH4}, P_{H2}/P_{CO2} and P_{CO2}/P_{CH4} decreased as temperature increased. This is in accordance with Equations (21) and (22) and is in agreement with published results for other carbon membranes (see Section 4.6.2). No significant difference was observed between the results for 2 and 6 bar feed pressures.

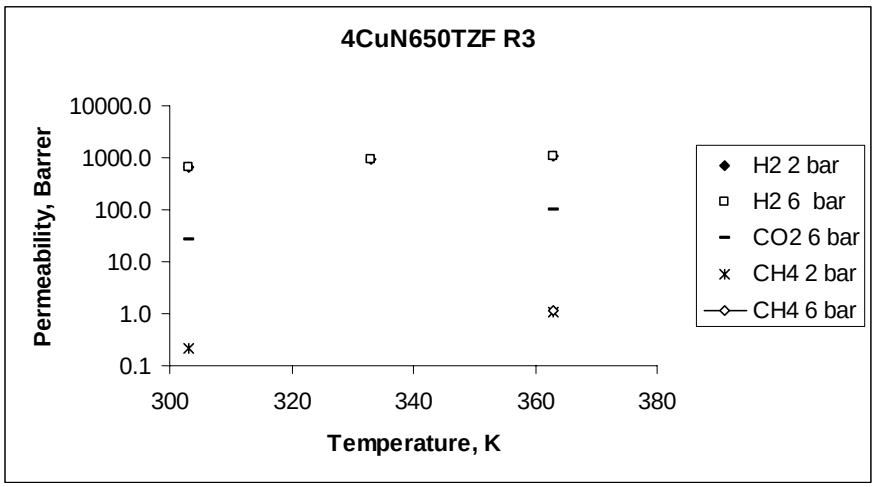

Figure 7-43. Effect of temperature on single gas permeabilities in 4CuN650TZF (R3) (values for hydrogen at 2 and 6 bar coincide).

No serious aging of the membrane was seen during tests, with respect to hydrogen permeability. The final hydrogen permeability for 2 bar and 25°C in Table 7-12 was measured after the mixed gas runs, 97 days later, and showed little difference from the first hydrogen test.

7.8.1.1 Hydrogen-methane mixtures

Both ready-prepared (10% H_2 and 30% H_2 mixtures supplied by AGA AS) and mixed in-situ (5% H_2) feeds were used in these tests. The temperature of the membrane was varied from 25-90°C and the pressure was switched between 2 and 4 bar. The results of the run are shown in Table 7-13 and Figure 7-44 to Figure 7-47. The final column in Table 7-13 shows the measured mixed gas hydrogen permeability divided by the single gas methane permeability. This is to serve as a check against the measured mixed gas selectivity, because the measured mixed gas methane permeability is uncertain. The mixed gas selectivity is much higher at 25°C than in pure gas tests, but approaches the pure gas selectivity at 90°C. This could be due to:

1. Slight adsorption of hydrogen at pore restrictions hindering CH_4 transport at 25°C. Adsorption is attenuated at 90°C and selectivity approaches pure gas values. Methane concentration in the flushed gas increased by an order of magnitude from 25°C to 90°C, whereas H_2 only increased by about 50%.
2. The methane concentration at 25°C (<100 molppm) being out of range for the calibration gas, which has a methane concentration of ~500 molppm. Uncertainty in GC accuracy should also be greater at this low concentration since measurement involves integration of very flat peaks.

The coefficients of variation for H_2 and CH_4 permeability in this series of tests are 3.6% and 8.4% respectively, which is not enough to explain the high selectivity at 25°C. The precision of the measured H_2 permeate concentration in mixed gas tests was good because H_2 accounted for close to 100% of the permeated gas, so the uncertainty is similar to the single gas tests.

Table 7-13. Results for H_2-CH_4 mixed gas runs with 4CuN650TZF

Membrane	Feed mol%H_2	Temp, °C	Press., bar	Single gas H_2 perm, Barrer[1]	Single gas H_2 selectivity	Mixed gas H_2 perm, barrer	Mixed gas selectivity	MG H_2 Perm/SG CH_4 Perm[2]
4CuN650TZF (R2)	10	25	2	957	680	644	600	458
4CuN650TZF (R3)	6	25	2	673	3042	613	18389	2773
	10	25	2	673	3042	609	13432	2755
	10	25	6	673	2995	545	39602	2463
	10	25	6	673	2995	551	32041	2492
	10	25	6	673	2995	592	-	2679
	30	25	2	673	3042	636	15883	2878
	30	25	6	673	2995	554	7681	2506
	10	60	6	961	-	905	-	-
	10	60	6	961	-	905	-	-
	10	60	6	961	-	854	6773	-
	5	90	2	1087	1000	1152	1610	1060
	10	90	2	1087	1000	999	984	919
	10	90	6	1087	1000	975	1143	825
	30	90	2	1087	1000	1047	1086	963
	30	90	6	1087	1000	1015	1095	860
	10	90	6	1087	1000	999	-	846

[1]Single gas permeabilities for 2 bar feed
[2]Mixed gas H_2 permeability divided by the single gas CH_4 at the same feed pressure and temperature

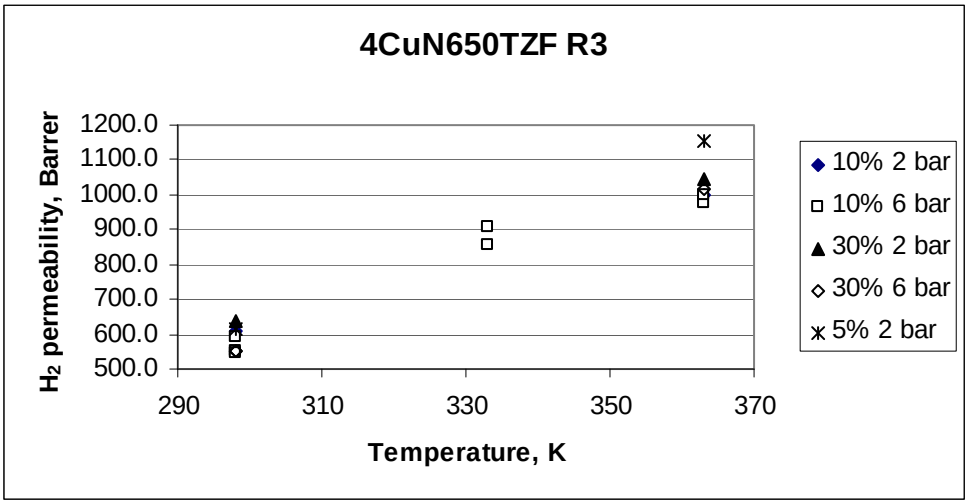

Figure 7-44. Temperature and pressure dependence of hydrogen permeability in the second mixed gas run for membrane 4CuN650TZF (R3)

Hydrogen permeability increased strongly with temperature (Figure 7-44). This may be attributed to a decrease in methane adsorption in the pores, as well as an increase in hydrogen intrinsic permeability (see single gas values in Table 7-12). Also consistent with the former phenomenon is that the hydrogen permeability decreased slightly with increasing pressure (Figure 7-45), which could increase the amount of adsorbed methane.

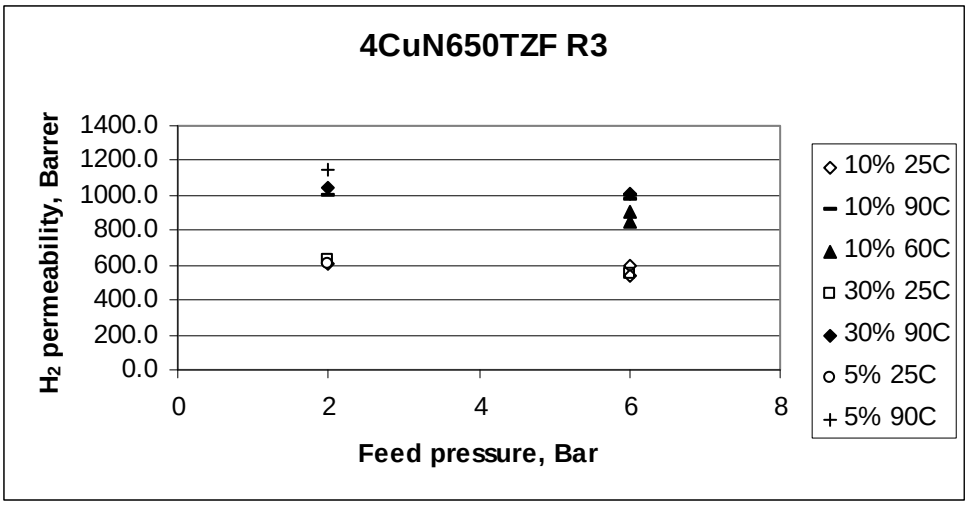

Figure 7-45. Effect of feed pressure on H_2 permeability for membrane 4CuN650TZF (R3)

Figure 7-46 shows feed hydrogen partial pressure plotted against hydrogen permeability for all of the mixed gas tests. No dependence on hydrogen partial pressure was observed.

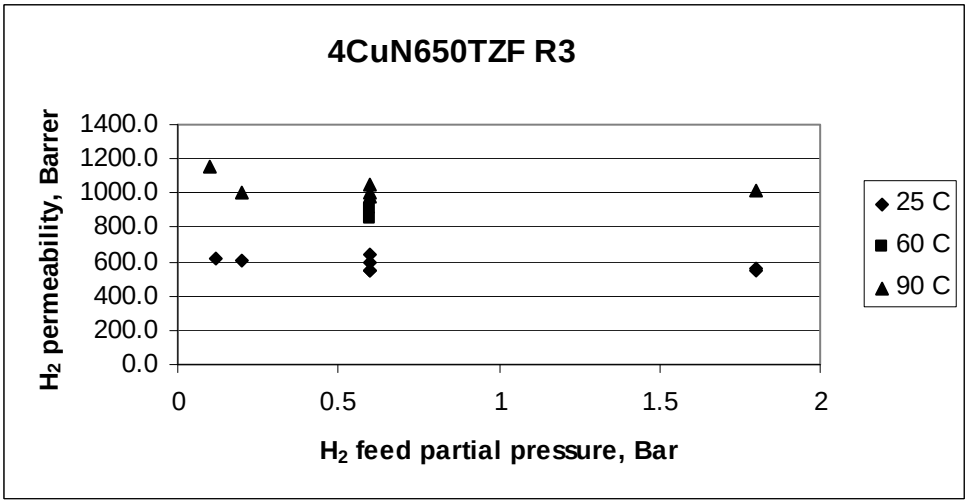

Figure 7-46. Effect of hydrogen partial pressure in feed on H_2 permeability for membrane 4CuN650TZF (R3)

Figure 7-47 shows the selectivity of the membrane as a function of temperature. Although the selectivity at 297 K may be too high, it is clear that the permselectivity decreased as temperature was increased.

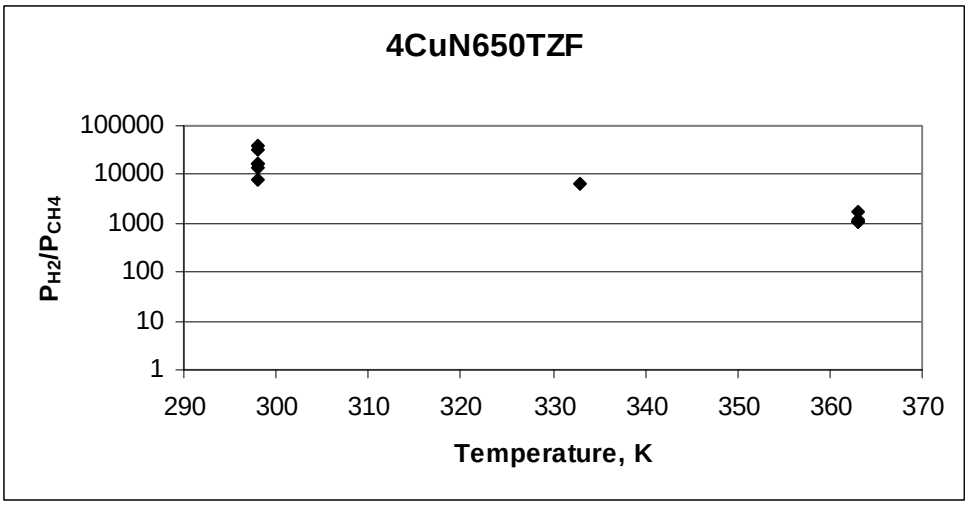

Figure 7-47. Effect of temperature on permselectivity for membrane 4CuN650TZF (R3)

7.8.1.2 Recovery from a simulated natural gas mixture

Mixed gas tests were conducted with a simulated natural gas (NG) feed, provided by AGA AS. The composition is given in Table 7-14. A feed mixture was prepared in situ with a H_2:NG ratio of 30:70 (vol:vol). Tests were conducted at 6 bar and 25°C or 90°C over 320 hours, following the approximated continuous flow method described in Section 6.6.3.3. The H_2-NG mixture was in contact with the membrane for this entire period (Figure 7-48). First, two tests were recorded at 90°C, in case ethane, propane or butane blocked the membrane pores at ambient temperature. Once it was established that this did not happen at 90°C, the temperature was reduced to ~25°C and a series of tests conducted until the permeabilities stabilised. It was observed that the hydrogen permeability decreased from 586 Barrer to a steady value of about 480 Barrer, after 100 hours at 25°C. The membrane temperature was then raised to 90°C and three tests performed to check stability. Ethane, propane and butane were not observed in the permeate.

Table 7-14. Simulated natural gas composition

Gas	i-Butane	N_2	CO_2	Propane	Ethane	Methane
Mole %	**0.254**	**1.5**	**2**	**4.52**	**10**	**81.7**

From these results it can be concluded that some pore blocking by the heavier hydrocarbons occurs, particularly in the first 24 hours. However, the permeability eventually stabilises and hence this membrane appears suitable for the recovery of hydrogen from natural gas or refinery off-gases. The time taken for the permeability to decline could be explained by the slow, activated diffusion of the heavier gases into pores where they can adsorb and hinder hydrogen transport (see discussion in Section 5.4). However, from the good H_2/CH_4 permselectivity and the absence of total pore blocking, it appears that most of the pores are ultramicroporous and inaccessible to the hydrocarbons.

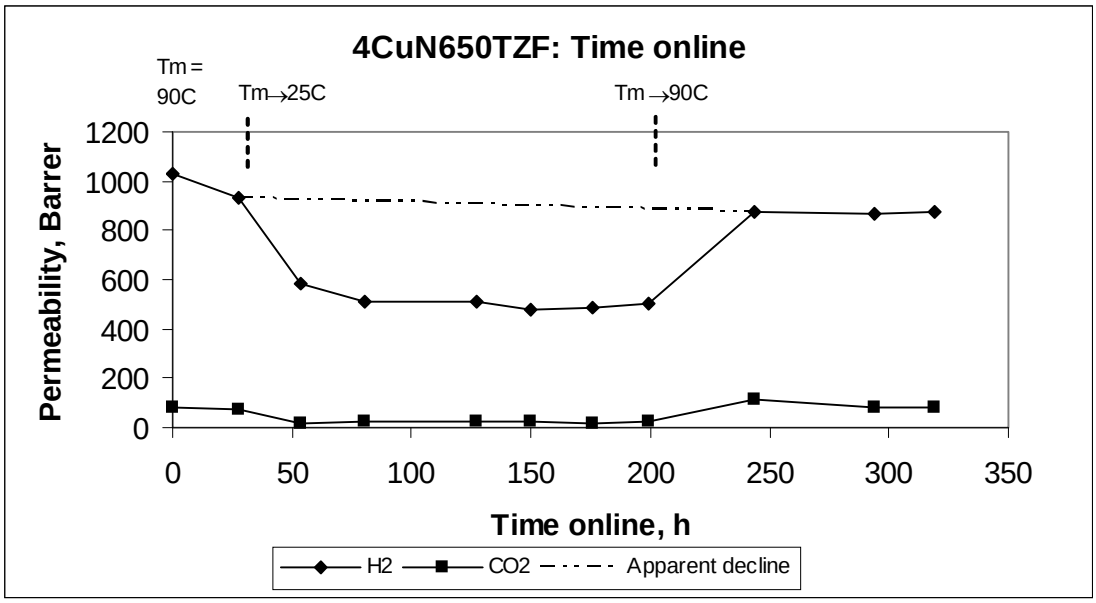

Figure 7-48. Medium-term testing with simulated natural gas – H_2 and CO_2 permeabilities

A closer inspection of the CO_2 and CH_4 permeabilities reveals possible pore dilation by CO_2, C_2H_6, C_3H_8 or i-C_4H_{10} (Figure 7-48 and Figure 7-49), as described by Menendez and Fuertes (2001) and discussed in Section 4.5.4. A slow increase in permeability can be seen for both gases, but particularly for CH_4 at 25°C. The methane permeability at 244 hours is far higher than that at 50 hours, when methane was not detectible in the permeate gas. The larger gases with greater activation energies will be more benefited by slight pore dilation and should show a larger variation than hydrogen. This is supported by the findings of Rao and Sircar (see Section 4.4.4). The permeabilities follow a declining trend after being heated to 90°C, perhaps as the dilating gas slowly desorbs at the higher temperature.

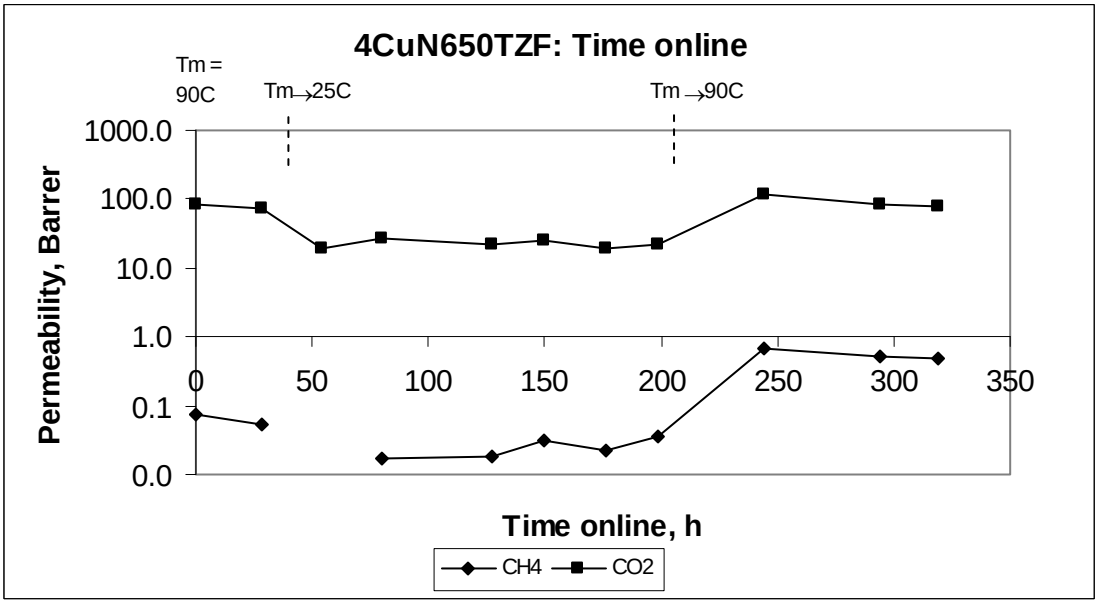

Figure 7-49. Medium-term testing with simulated natural gas – CO_2 and CH_4 permeabilities

Very high permselectivities were calculated for hydrogen over methane. The permselectivity of hydrogen over carbon dioxide was stable, with average values of 11 at 90°C and 23 at 25°C. Again, the larger gases benefited more than hydrogen from the temperature increase.

Practically speaking, this is not an issue for hydrogen separation from methane, since the permselectivity is still very high. If H_2/CO2 selectivity is to be maximised, then operation at ambient temperature is recommended.

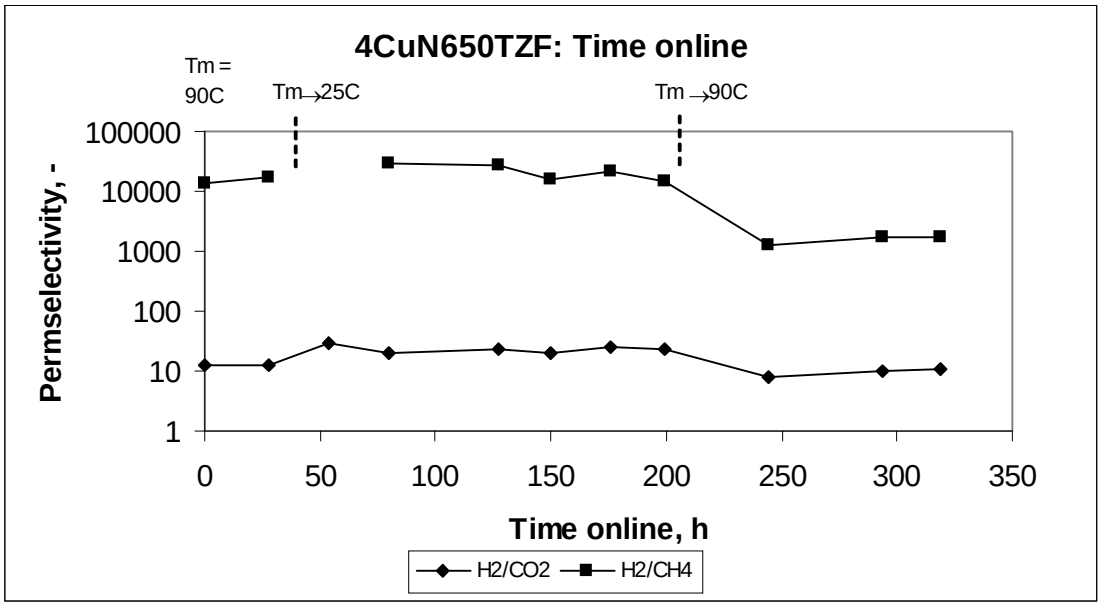

Figure 7-50. Medium-term testing with simulated natural gas – H_2/CO_2 and H_2/CH_4 permselectivities

The coefficients of variation for H_2, CO_2 and CH_4 permeability in this series of tests are 3.6% 29.2 and 34.9% respectively.

7.8.1.3 Recovery from a simulated water gas shift mixture

Tests were performed with an AGA AS ready-prepared mixture containing 50 mol% H_2, 40 mol% CO_2 and 10 mol% N_2, at 6 bar, 60°C and 90°C. The tests were conducted with continuous feed flow. Results are presented in Table 7-15.

Table 7-15. Membrane performance with simulated water gas shift mixture

	H_2 permeability, Barrer	CO_2 permeability, Barrer	Permselectivity
60°C test	644	43	15
90°C test	841	77	11
Rel. SD	3.6%	14.5%	

These values are consistent with those obtained for single gas tests (Table 7-12) and with the simulated natural gas feeds. The mixture compositions did not appear to affect the permselectivity.

7.8.2 Tests with 2CuN650HZS

A tighter membrane that was carbonized in the HZS oven under vacuum was also tested with the 50 H_2-40 CO_2-10 N_2 mixture, as these membranes offer better H_2/CO_2 selectivity than the more porous membranes produced in the TZF oven. The results are shown in Table 7-16 for a membrane doped with 2 wt% copper (II) nitrate, which was tested up to 180°C. At the high temperatures, permeation rates were high, test times short, and mixing of the Ar flush gas and permeates less efficient, leading to larger standard deviations in the results.

Table 7-16. Single gas and mixed gas results for 2CuN650HZS

	H_2 permeability, Barrer	**CO_2 permeability, Barrer**	**Permselectivity**
Single gas, 4 bar, 25°C	406.8	19.7	20.65
Mixed gas, 6 bar feed			
25°C	271	16	17
90°C	924	47	20
90°C repeat	936	41	23
180°C	1501	181	8
Rel. SD	4.2%	38.0%	

Both gas permeabilities increased with temperature, but H_2 did not produce a straight line Arrhenius plot. Also, permeability increased from 26°C to 90°C before decreasing again at 180°C. It can be speculated that CO_2 hindered H_2 in the narrow pores at 25°C, which would explain the large difference between the single gas and mixed gas H_2 permeability. The CO_2 adsorption effect was attenuated at 90°C and H_2 increased more than predicted by Arrhenius behaviour. Selectivity then decreased at 180°C because E_s for CO_2 is larger, following the discussion in Section 4.4.3.

8 Conclusions for experimental work

The experimental program determined the following:

8.1 Preparation

1. The carbonization temperature is the most important parameter when designing cellulose-derived molecular sieves. Six hundred and fifty degrees Celsius appears to be the optimum final temperature when the soak time is two hours, irrespective of metal loading.
2. Adding metal nitrates increases the selectivity of hydrogen over other gases, but at the expense of permeability.
3. Aging, or pore size changes resulting from exposure to oxygen and air, is a significant problem. However, little aging was seen during permeation tests when the membranes were isolated from air.
4. The membrane properties are strongly dependent on the carbonization furnace, which is an issue for reproducibility. The amount of oxygen present during carbonization appears to be crucial. Other researchers may prepare membranes with the same carbonization protocol, but obtain significantly different performance due to furnace differences.
5. Effective membranes were prepared under inert flow – a procedure that is practical for large-scale production.

8.2 General performance

1. Carbon molecular sieves derived from cellulose are able to separate hydrogen from methane, nitrogen and higher hydrocarbons with a high degree of selectivity and productivity, in a combination that is better than the 1991 Robeson upperbound for polymers.
2. CMSMs are capable of separating hydrogen and carbon dioxide, but the ‘open’ membranes that were carbonised in the TZF performed worse than the 1994 Robeson upperbound.
3. Membranes prepared in the HZS oven, particularly those under vacuum, break through the upperbound for H_2/CO_2 separation.
4. Separation performance is poorer in mixed gas tests than single gas. Nevertheless, the cellulose-derived membranes continue to separate effectively as molecular sieves (there is no reverse selectivity) and the pores are not blocked by heavier gases in mixed feeds.

8.3 Application and membrane choice

1. Increasing the operating temperature produces an exponential increase in productivity, but decreases the hydrogen selectivity.
2. Pressure had little effect on separation in the range of 2-6 bar.
3. Excellent permeability for H_2/CH_4 separation was obtained with the pure carbon membrane prepared at 650°C in the TZF oven. In this case, single gas selectivity was about 1100.
4. If higher selectivity is required, 4wt% copper (II) nitrate doping can increase this to more than 4000.

5. Applications requiring high H_2/CO_2 selectivity are best served by membranes prepared at 650°C in the HZS oven (to minimise oxidation) and with 4-6% CuN added to the precursor.
6. Aging of the membrane dominates performance and must be accounted for when designing a process unit or comparing experimental results.

9 Future work

The membranes in this work have been proved capable of separating gas mixtures without pore blocking. However, a strategy must be developed to reconcile the design of processes with the aging of carbon membranes. A process cannot simply be designed based on the performance of a young carbon membrane, because the decrease in productivity over time can be as much as 80% (Section 7.3). The strategies to tackle this issue could be:

- Preventative: blanketing of the module with an inert such as nitrogen
- Adaptive: adding new modules, increasing the driving force or increasing operating temperature as productivity declines
- Conservative: Designing the process based on the steady state, fully-aged performance
- Regenerative: Periodically applying an electrical current to the membrane to regenerate performance (Lie and Hägg, 2006)

It is clear from the above that more information is needed on aging, not least the behaviour in a particular application. Also, deeper understanding of the relationship between aging and preparation parameters such as metal type, metal content and pyrolysis conditions would be invaluable. Most critical is to obtain aging data from long-term, continuous piloting with real mixtures and conditions.

Future work should also investigate the effect of higher pressures (up to at least 40 bar) on separation performance and structural integrity. The maximum pressure tested in the program was 6 bar, because of equipment limitations and the weakness of flat films compared to hollow-fibres. However, it will be seen in Part II that most applications are at higher pressures than this.

PART II Process modelling and techno-economic evaluation

10 Process development

Three applications for carbon membranes have been studied in this work. They are:

1. Recovery of hydrogen from a hydrogen-natural gas mixture in a distribution network
2. Recovery of hydrogen from a refinery off-gas
3. Separation of hydrogen from carbon dioxide and nitrogen in pre-combustion in a power plant

These are discussed in full detail in Sections 11-13. However, the tools used in the process design will first be described in this section.

10.1 Membrane model

A membrane module was needed that could be integrated into Hysys®, the process simulation package used at this department. The criteria decided upon were that the module had to be user-friendly, since it would be used by people within the group as well as students outside MEMFO[9], quick to solve so as not to cause long plant simulation times, and reasonably accurate with multi-component mixtures. The module was not intended to model transport through the membrane or calculate mass transfer coefficients. Rather, the user of the module should be able to input overall mass transfer coefficients that were measured or already calculated in a way that accounts for configuration-related effects. This allows flexibility in terms of the processing of permeance data as well as cutting down processing time. The resulting membrane module was called ChemBrane.

The model handles three membrane configurations – 1) co-current (plug-flow both shell and bore sides), 2) perfectly-mixed (plug-flow on the feed side, perfectly mixed on the permeate side) and 3) counter-current (plug-flow on both sides). ChemBrane can operate with vacuum and/or sweep operation.

The purpose of the module is to calculate the permeate and retentate for a system with any number of components, given the overall mass transfer coefficient (or, in the simplest case, permeances) of the components and the membrane area. Any number of modules can be included, allowing complex process configurations. The pressure drop along the feed side of the membrane is incorporated through the user supplying the feed and retentate pressures independently. A log-mean-average of these values was used when calculating the partial pressures in Equation (9). As explained in Section 3.1.1, where the behaviour of real gases was discussed, the use of partial pressures in a membrane model is a conservative approach since non-ideal gas behaviour (i.e. the use of fugacities) would benefit hydrogen separation.

Two versions of the counter-current model were programmed. The first used the 4th order Runga-Kutta method for solving for the flux along the membrane length and iteration over the permeate flows to converge to a solution. For more detail on the model, see Appendix B. The

[9] MEMFO: Membrane research group at NTNU

second version used a successive stages model with successive permeate approximation (Coker et al., 1998). Both methods produced similar results, but the latter was found to be more robust with respect to convergence when component driving forces were very small.

10.2 Simulation and costing

Simulation of the processes was done with Aspen Hysys® 2004.2. Chembrane modules were integrated and able to interface with the Adjust function, enabling the manipulation of membrane area or operating pressure to achieve given product recoveries or purities. The process designs were then transferred to Aspen's Icarus Process Evaluator, which is a costing program.

Predicting the cost of carbon membrane modules is difficult because of the lack of commercial precedent. Polymeric hollow-fibre membranes are assumed to cost roughly \$20-50/m^2 (Ho and Sirkar, 1992). The cost of carbon membranes is far more uncertain. Koros and Mahajan (2006) stated that it is reasonable to expect carbon, glass, zeolite and other inorganic membranes to cost between one- and three-orders of magnitude more per unit of membrane area compared to polymeric membranes. This would make the range a rather daunting \$200-50 000/m^2. The problem of predicting module costs can be approached from several angles, including:

Calculating the raw cellulose cost

The cost of cellulose is approximately \$520 per air dried ton[10]. However, the precursor is only a small fraction of the module cost, the rest being manufacturing. Assuming self-supported 16 micron thick hollow-fibres like those provided by Carbon Membranes Ltd, the cost of cellulose per m^2 of fibre is calculated as shown in Table 10-1. The cost of metal additives is neglected in this calculation.

Table 10-1. Carbon hollow-fibre: cellulose cost

Hollow-fibre diameter, m	165×10^{-6}
Equivalent fibre length in 1 m^2, m	1929
Volume carbon per m^2, m^3	16×10^{-6}
Density of porous carbon, kg/m^3	1125 †
Mass carbon /m^2, kg	0.018
Carbonization weight loss, wt %	80
Mass cellulose/m^2, kg	0.09
Cost cellulose, \$/m^2	0.05

†Density of graphite ~2250 kg/m^3 (Marsh and Rodriguez-Reinoso, 2006 pg 14). Porosity assumed to be 50%

This method provides little information about the eventual module cost.

Comparison with analogous equipment

Aspen's Icarus Process Evaluator has the ability to cost a heat exchanger with a carbon steel shell and graphite tubing. However, only the active area and 'tube' length can be entered, so the result must be treated as no more than an indication. An exchanger with 500 m^2 of graphite area in the form of 2 m long tubes (the minimum length that could be entered) was calculated to cost \$281 700 (uninstalled). This is approximately \$560/m^2.

[10]See www.foex.fi for spot prices

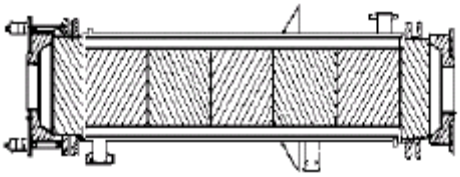

Figure 10-1. Carbon steel – graphite heat exchanger (Aspen Icarus Process Evaluator Guide)

Assembling a cost from analogous manufacturing steps

Another approach would be to assume that the cellulosic hollow-fibre precursors cost \$20-50/m^2 and calculate additional costs for carbonization and module fabrication. The assumption is that cost of cellulose precursor hollow fibres is similar to conventional hollow-fibre membranes polymers such as cellulose acetate is reasonable, provided a practical solvent is found for the spinning of cellulose fibres.

A suggested route for the formation of carbon hollow fibre modules is presented in Figure 10-2. Firsty, the fibres must be spun, dried and carbonized. A commercial precedent exists for these steps in the form of carbonizing PAN, Rayon or pitch spun fibres at 2400°C or more to produce graphitic carbon fibres (Sauder et al., 2004). This ubiquitous material is produced in large amounts and can be found in bicycle frames to aircraft. One source states the cost of commercial grade carbon fibres as being \$8-10/lb (\$17.6-22/kg) (Oak Ridge National Laboratory, 2006). This cost would encompass the first four steps in Figure 10-2, the cost of the PAN and profit. An approach could be to add the cost of the carbon fibre per m^2 (to cover up to pyrolysis) to the cost a polymer hollow fibre module per m^2, to represent the entire process. This treats the polymer module cost as only being for module shell and assembly. Using a density of 1750 kg/m^2 for carbon fibre of 165 microns in diameter and \$22/kg to calculate the carbon fibre cost/m^2 gives \$2/m^2. This is an insignificant increase on the initial \$20-50/m^2 to yield \$22-52/m^2.

The difficulty of assembling a module with fragile carbon hollow fibres is of course not reflected in this figure, but it is still nowhere near the lowest suggested cost of \$200/m^2. Also not reflected is any effort spent inspecting the fibres for defects and subsequent attempts at plugging.

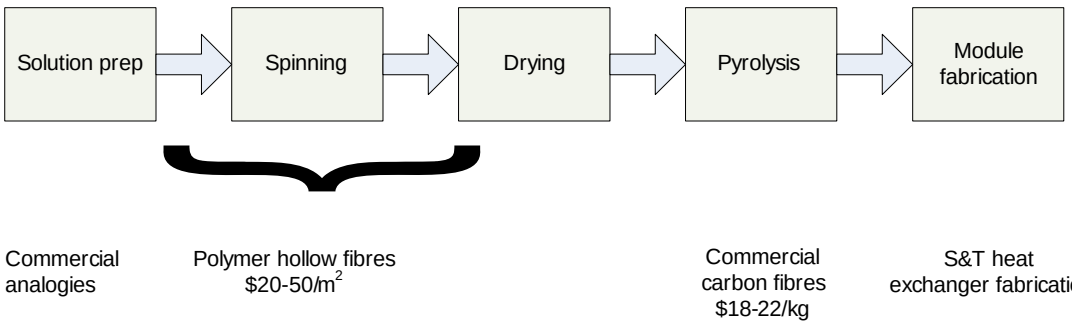

Figure 10-2. Production of cellulose carbon fibres

Adding carbon fibre cost to steel module cost

If we are to assume a module membrane area of 500 m^2, a length of 1 m and a fibre bundle diameter of 0.2 m (calculated by assuming a triangular pitch arrangement and a fibre spacing of 0.2 mm), we could calculate the cost of materials. A carbon steel shell of the same dimensions and with 100% extra weight allowance for internals and nozzles would cost $4500 (Aspen Icarus Process Evaluator). The cost of the hollow fibres, using the value of $\$2/m^2$ calculated above, would be $1000. The materials would then cost $5500 in total or $\$11/m^2$. Even if 80% of the fibres were discarded due to defects, the material costs would only be $\$19/m^2$.

The above attempts to calculate a module cost from materials produces low values in the same range as polymer hollow fibre modules. It can be concluded that the materials would contribute a small fraction of the total cost and the majority is due to the man-hours or mechanisation of the assembly process, other operating costs, profit and payback of capital. These are difficult to predict. However, a cost of $\$200\text{-}500/m^2$, which is the minimum suggested by Koros and Mahajan, and 10 times the material costs, seems pessimistic. A range of $\$50\text{-}500/m^2$ has therefore been used in the economic studies.

11 Case 1: H_2 from natural gas in a mixed distribution network

The transition to a full hydrogen distribution system may be a lengthy and costly exercise; hence a transitional approach using existing natural gas (NG) networks in Europe to transmit mixtures of hydrogen and NG is being investigated. In an EU 6th FWP project, NaturalHy, consisting of 39 European partners, the aims are to test all critical components in a mixed network by adding hydrogen to existing natural gas networks. This consortium includes network operators, hydrogen producers, specialist practitioners and academic researchers. The effect of hydrogen on technical components of the pipeline, reliability, safety and pipeline integrity as well as the possibility to separate out hydrogen for the end user, are being tested.

Critical to the success of the project is the feasible separation of the hydrogen for end-use components requiring relatively pure hydrogen, such as fuel cells. Palladium membranes are commonly seen as the bench mark membrane technology for the recovery of hydrogen from feed streams with a low (<30 vol%) hydrogen concentration. In order for these membranes to function efficiently, the entire gas feed stream must be heated to temperatures higher than 350°C, incurring a capital and energy penalty.

11.1 The design basis

A hypothetical natural gas distribution network is shown in Figure 11-1 (provided by the NaturalHy programme). There are effectively two pressure levels where hydrogen would be withdrawn – 40-80 bar (medium pressure) and less than 8 bar (low pressure). The maximum pressure that the cellulose-derived carbon fibres can withstand is currently unknown. Tanihara et al. (1999) successfully tested asymmetrical carbon hollow fibres at pressures up to 50 bar, so it is assumed for the sake of this exercise that cellulose-derived carbon membranes can also be applied in the 40 bar segment of the pipeline. The suggested range of hydrogen concentration, at the point of injection, was 5-30 mol%.

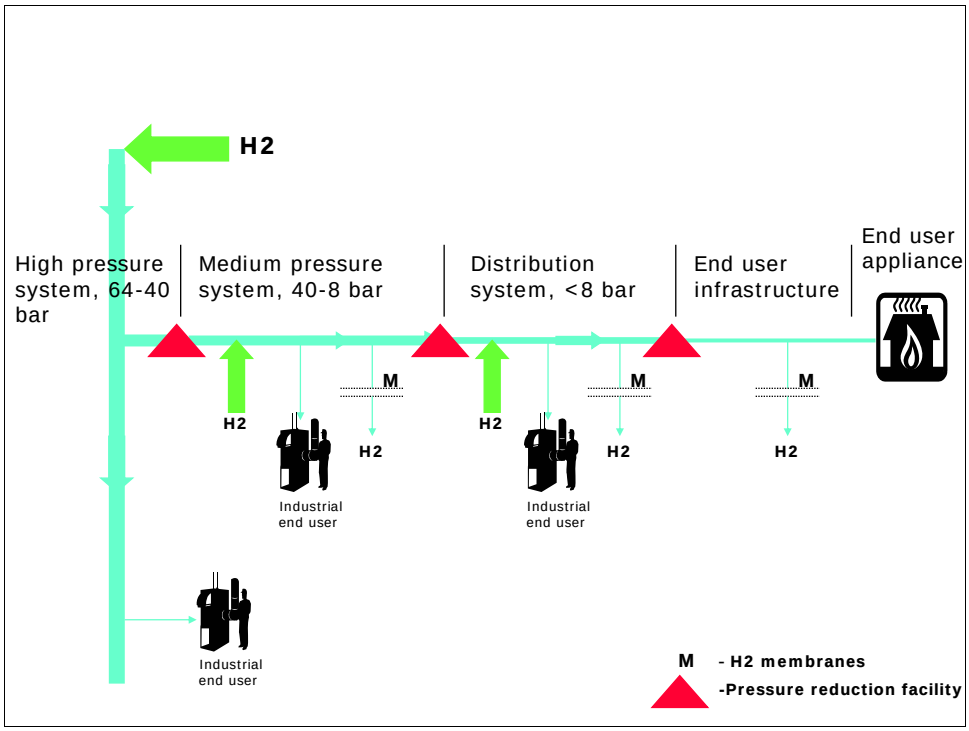

Figure 11-1. The natural gas distribution network showing end-users and pipeline segment pressures (Ref: NaturalHy)

The composition of natural gas differs according to the source. A gas mixture representing natural gas was already available at the department from another project and, since the composition is similar to confidential assays provided by GasUnie (Netherlands), one of the project partners, it was chosen for experiments and as the design basis. The composition is presented in Table 11-1. The location is assumed to be the Netherlands, with yearly average temperatures ranging from 1-22°C (www.bbc.co.uk/weather/world/city_guides/). However, it was assumed for the sake of simulations that the gas feed to battery limits was 25°C, which was the lowest temperature applied in the experiments. Lower temperatures and no feed preheating would decrease hydrogen permeability, but this was not accounted for.

Table 11-1. Representative natural gas composition.

Gas	i-Butane	N_2	CO_2	Propane	Ethane	Methane
Mole %	0.254	1.5	2	4.52	10	81.7

The product specification depends on the end-use. PEM fuel cells were assumed to be the base case and the NaturalHy project set the following purity targets:

Table 11-2. Product purity targets

Total CH_4, C_2H_4, C_2H_6	5%
C_6H_6	750 ppm
CO	0.1-0.2 ppm
SO_2	0.2 ppm
H_2S	0.1-0.2 ppm
HCHO	5-10ppm
HCOOH	20-100ppm
NH_3	0.3ppm
CH_3COCH_3	250-500ppm

Since the specs did not mention CO_2 or N_2, it was assumed for this analysis that the total impurity fraction, including CO_2 and N_2, should be <5 mol%. Proposed production ranges were:

1. Domestic use: 5-50 Nm^3/h
2. Moderate scale e.g. hospital fuel cell: 100-500 Nm^3/h
3. Industrial use: 700-2000 Nm^3/h

Delivery pressure would be 1.5 bar (abs), sufficient for PEM fuel cells.

11.2 The simulations and sensitivity analysis

The process design depends on the following variables:

Hard-to-manipulate variables:

1. The mole fraction of hydrogen in the pipeline, y_{H2pipe}
2. The pressure of the pipeline gas
3. The hydrogen flow rate in the pipeline relative to the end use requirement, F_{H2use}/F_{H2pipe}. This determines the required recovery; the closer the ratio to 1, the closer recovery must be to 100%. The ratio also sets the difference between the partial pressure of hydrogen in the feed and retentate of the membrane and hence the driving force for separation. The lower the ratio F_{H2use}/F_{H2pipe}, the easier the separation from a driving force point of view. From a pressure drop perspective, there are limits to the size of the gas stream that can be sent through a finite-sized module.
4. The price of the membrane unit

Easy-to-manipulate variables:

1. Membrane temperature. Heating can be accomplished by combusting gas, preferably from the retentate to reduce the loss of hydrogen from the network
2. Membrane area to achieve recovery
3. Feed and permeate pressure. As will be explained in the next section, the higher the ratio p_{feed}/p_{perm}, the purer the product, but at the expense of more gas compression
4. Membrane configuration. If purity is not met by one stage, more stages in cascade or recycle loops can be implemented.

If we assume initially that the purity can be met with one stage, the possible configuration is shown in Figure 11-2.

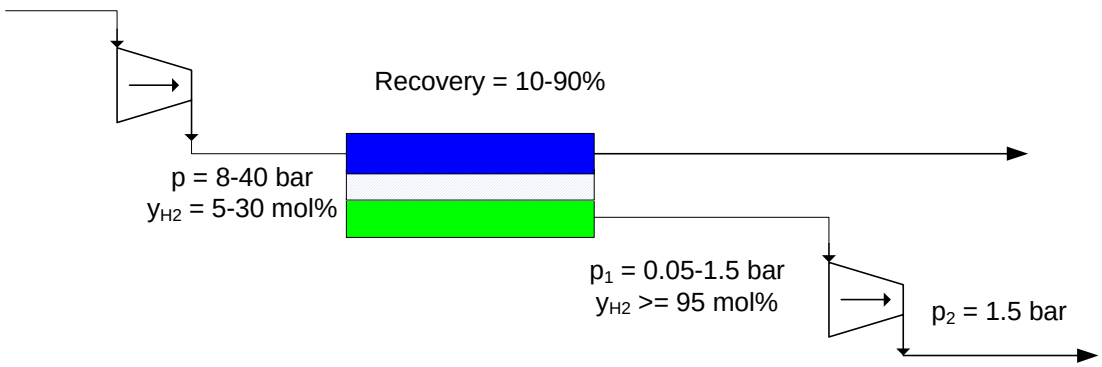

Figure 11-2. Configuration of a single stage membrane unit

The gas permeabilities were taken from the experiments with membrane 4CuN650TZFB3 (Section 7.8.1). The membrane area was assumed to be in the form of hollow-fibres with a wall thickness of 16 micrometers. The thickness of the dense selective layer in the asymmetric fibre wall was taken to be 1 micrometer, a typical value observed in the cellulosic carbon hollow fibres spun at MEMFO. Since C_2-C_4 hydrocarbons are significantly slower permeating and in lower concentrations in natural gas, they were assigned permeances of 0. N_2 was not detected in the permeate during experiments, but should permeate faster than CH_4 and so was assigned its single gas value. Single gas permeabilities were also used for methane, because very low CH_4 concentrations were detected in the mixed gas permeate and the calculated permeabilities are uncertain; the use of single gas values should therefore be conservative in terms of selectivity.

Table 11-3. Gas transport data. Repeat values from H_2-NG runs in Section 7.8.1 averaged for H_2 and CO_2

Gas	H_2	i-Butane	N_2[1]	CO_2	Propane	Ethane	Methane[1]
Permeability 25°C, Barrer	514	0	1.5	26	0	0	0.2
Permeability 90°C, Barrer	909	0	1.5	80	0	0	1.0
Permeance 25°C, m^3(STP) /m^2.bar.h	1.4	0	0.004	0.07	0	0	0.00055
Permeance 90°C, m^3(STP) /m^2.bar.h	2.5	0	0.004	0.20	0	0	0.00270

[1]Single gas values used because mixed gas values uncertain or gas not detected in permeate

The mixed gas tests showed that pressure affects the separation only slightly in the range 2-6 bar. There is no data for higher pressures due to equipment limitations, so the simplification must be made that permeabilities are independent of pressure.

The many variables in these processes (feed pressure, permeate pressure, temperature, hydrogen feed fraction and hydrogen recovery) make the results data set large. Furthermore, the large number of simulations required to cover the variable space are time consuming. As a simplification, feed compression was not considered so that separation occurred at pipeline or off-gas stream pressure. The assumption was also made that the feed mixture can be approximated by hydrogen and methane only, with all other components lumped with methane. Methane permeability is larger than those of the larger hydrocarbons, so this assumption is conservative with respect to eventual product hydrogen purity. Although CO_2 is much more permeable than methane, it is only 2 mol% of the natural gas fraction. The reduction of the stream to a binary mixture then allowed the separation to be solved using the analytical solution provided in Mulder (1997, pg. 496) for binary gas separation under cross-flow conditions.

A Microsoft® Office Excel spreadsheet was then developed that could simultaneously generate and analyse many cases. The spreadsheet calculates, for each case, the area required for separation and the mass balance. The costs of the two main equipment items – the membrane and the compressor – were estimated from the cost per unit area of the former and the calculated power of the latter. The equation for adiabatic compression,

$$-W_s = \frac{\gamma}{\gamma - 1} RT_1 \left[\left(\frac{p_2}{p_1} \right)^{\frac{\gamma-1}{\gamma}} - 1 \right] \qquad (47)$$

was used to calculate compression duty. Here, W_s is the shaft work of the compressor (kJ/mol) and $\gamma = c_p/c_v$. The graphical method of costing compressors provided by Peters and Timmerhaus (2003) was fitted to a log function that could be entered into the spreadsheet. The compressor material was assumed to be stainless steel (for hydrogen use). An operating cost estimate was then made using the parameters in Table 11-4.

Table 11-4. Economic factors for Excel-based performance analysis

Factor	
Installation factor for purchased equipment	4
Annual operating time	8000 hours
Fixed costs	
Capital charge	15% of installed capital cost
Module replacement frequency	Every 5 years
Maintenance	2% of installed capital cost, excluding module replacement
Insurance	1% of installed capital cost
Variable cost	
Electrical power	€0.035/kWh [a]
Natural gas price	$7/MMBTU [b]
€:$ euro exchange rate	1.3

a) http://www.engineerlive.com/european-process-engineer/environmental-solutions/2113/debating-the-true-cost-of-wind-power-electricity.thtml
b) http://www.wtrg.com/daily/oilandgasspot.html

The TABLE() function in Excel was then used to generate the membrane area, mass balance, energy consumption and operating cost simultaneously over the recovery (10-90%) or temperature, and permeate pressure ranges. The permeate pressure that produced the lowest specific operating cost (€/kg H_2 separated) and met the purity specification for a certain recovery was selected and the corresponding membrane area and energy consumption recorded.

The objective function subject to minimisation was:

$$\textit{Annual Specific separation cost} = (C_{\textit{capital charge}} + C_{\textit{Module replacement cost/yr}} + C_{\textit{maintenance}} + C_{\textit{insurance}} + C_{\textit{electricity consumption}} + C_{\textit{natural gas combusted/yr}})/\textit{Mass } H_2 \textit{ recovered per year}$$

Capital charge was calculated as 15% of the total installed cost of equipment, per year. Module replacement cost was taken as a 20% of the module purchased cost, per year, based on the replacement frequency.

11.3 Results

The costs calculated by the spreadsheet and those derived from simulations in Hysys will differ slightly because 1) Chembrane can operate in counter-current mode, which produces higher average driving forces and purer product and 2) 15% of the natural gas is ethane and propane, which permeate very little relative to methane. Lumping ethane and propane with methane will therefore overestimate the amount of methane in the permeate. However, the spreadsheet approximation is a useful way to map the system. The difference between Excel and Hysys results is checked in Section 11.5.

The results for the feed boundary cases are shown in the following graphs. The end use was assumed to be a hospital fuel cell requiring 100 Nm^3 H_2/h. The following can be observed in these cases:

- The lowest costs are obtained for low recovery from a feed of 40 bar and 30% H_2. The last two factors provide a higher driving force, leading to smaller membrane area and higher permeate pressure. As recovery increases, so the driving force decreases per unit of recovery and the membrane area required increases per unit of recovery.
- Purity decreases with increasing recovery and decreasing feed H_2 concentration. In the separation at 25°C, purity was met in all the optimum cases. At 90°C, the selectivity of the membrane is lower and the minimum purity could not be achieved at high recoveries for the 5 mol% hydrogen feed.
- The optimum permeate pressure decreased as recovery increased and as feed pressure or hydrogen concentration decreased. The steps seen in some of the pressure graphs are due to the 5 kPa interval used to generate the results.
- The cost of the membrane influences the optimum permeate pressure. If the membrane costs more, the optimum moves towards lower permeate pressures to increase the driving force and reduce the necessary membrane area.

Overall, the conclusion is that the choice of permeate pressure is influenced by all the variables and any unit will be adapted according to conditions in the field. There is no single cost of separation for a carbon molecular sieve unit, even if the cost/m^2 of membrane is fixed.

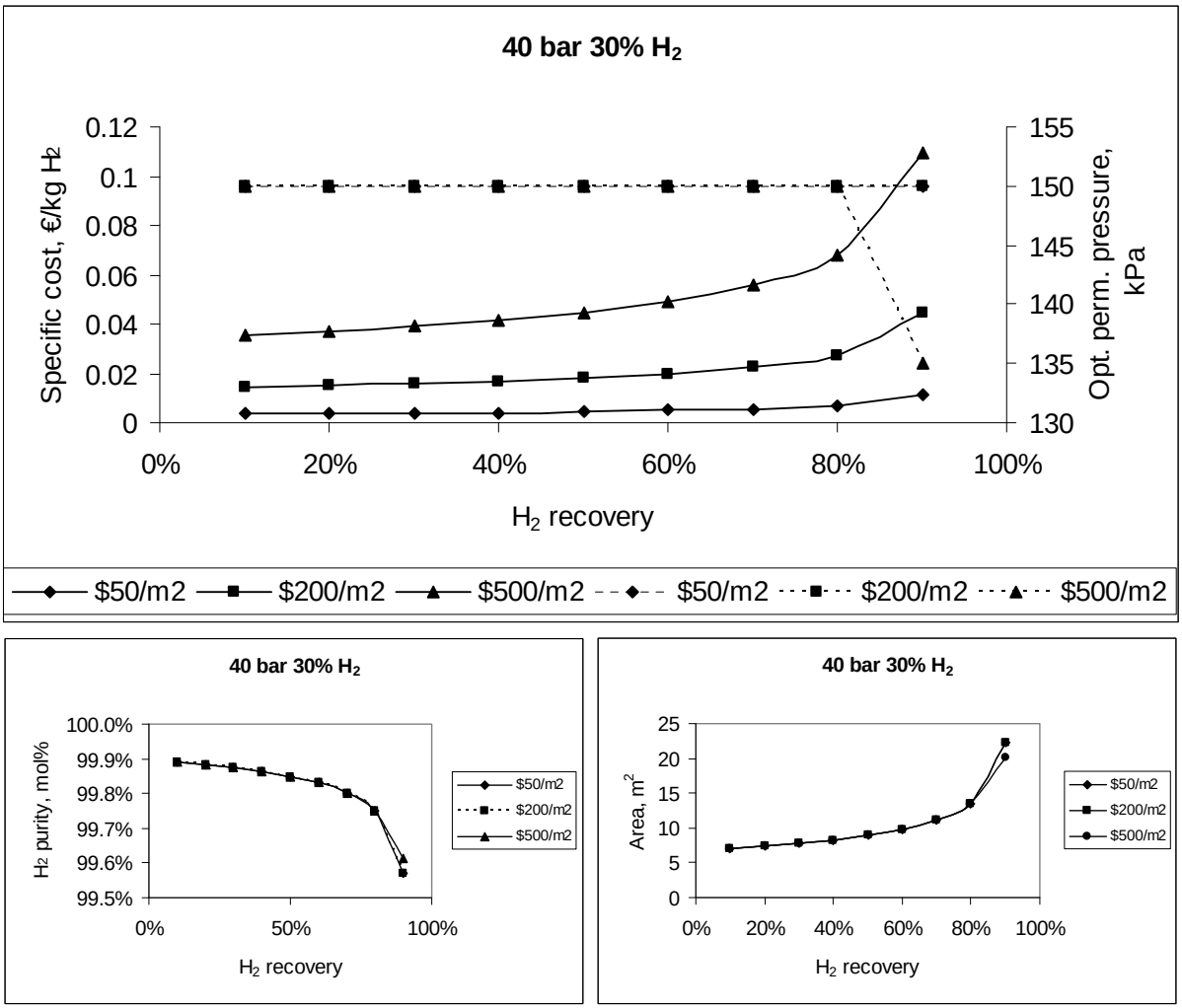

Figure 11-3. 40 bar feed pressure, 30% H_2 at 25°C. Top: Specific costs (—) and optimum permeate pressure (- - -); bottom: H_2 purity (left) and membrane area (right). H_2 partial pressure is high and permeate pressure is held constant at 1.5 bar over most of the recovery range. Purity is high, but decreases slightly, while area and cost follow the same upward trend

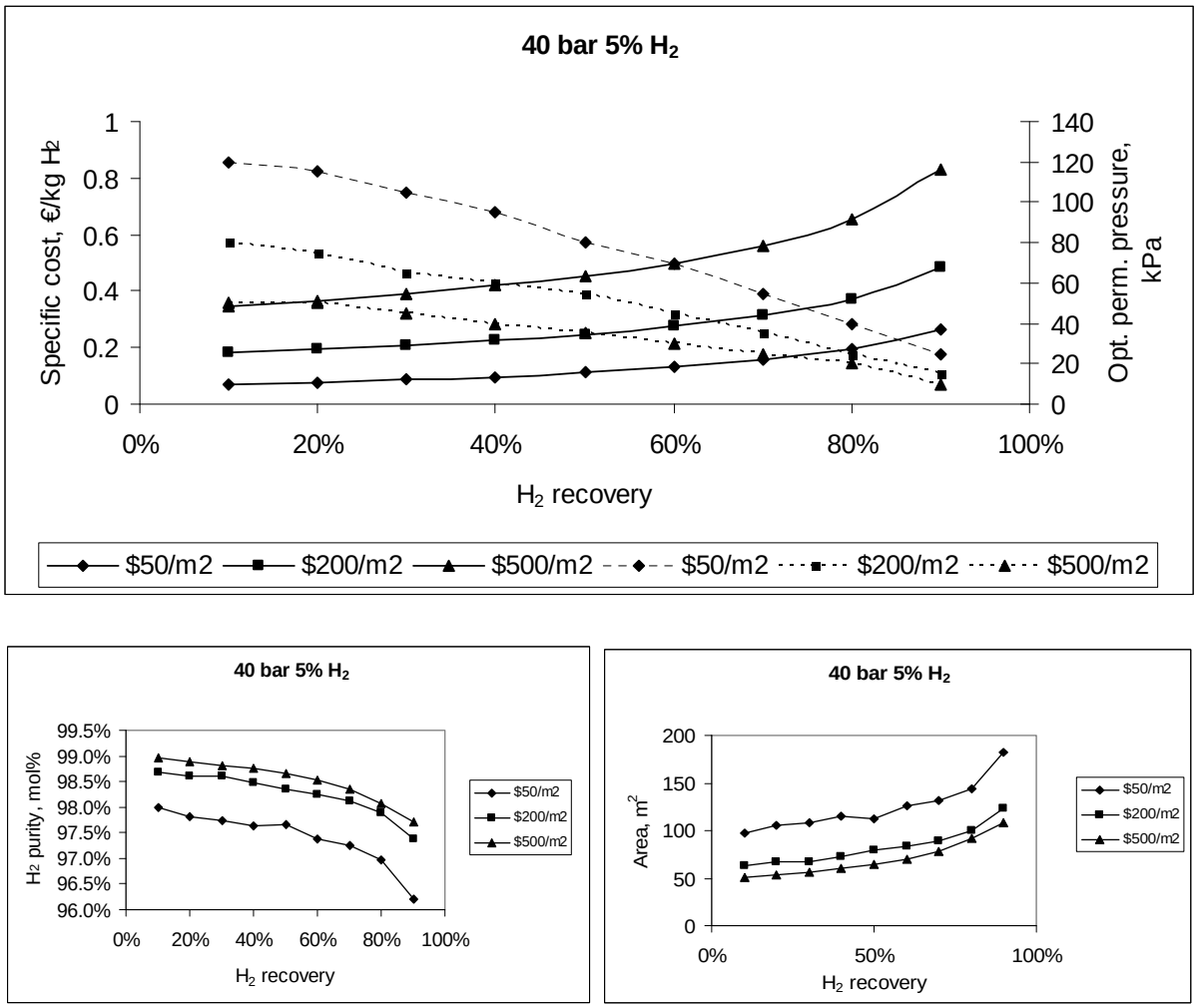

Figure 11-4. 40 bar feed pressure, 5% H_2 at 25°C. Top: Specific costs (—) and optimum permeate pressure (- - -); bottom: H_2 purity (left) and membrane area (right). H_2 partial pressure is less than previous case and driving force influences cost. As recovery increases, so permeate pressure and purity decrease. Area and specific cost increase exponentially

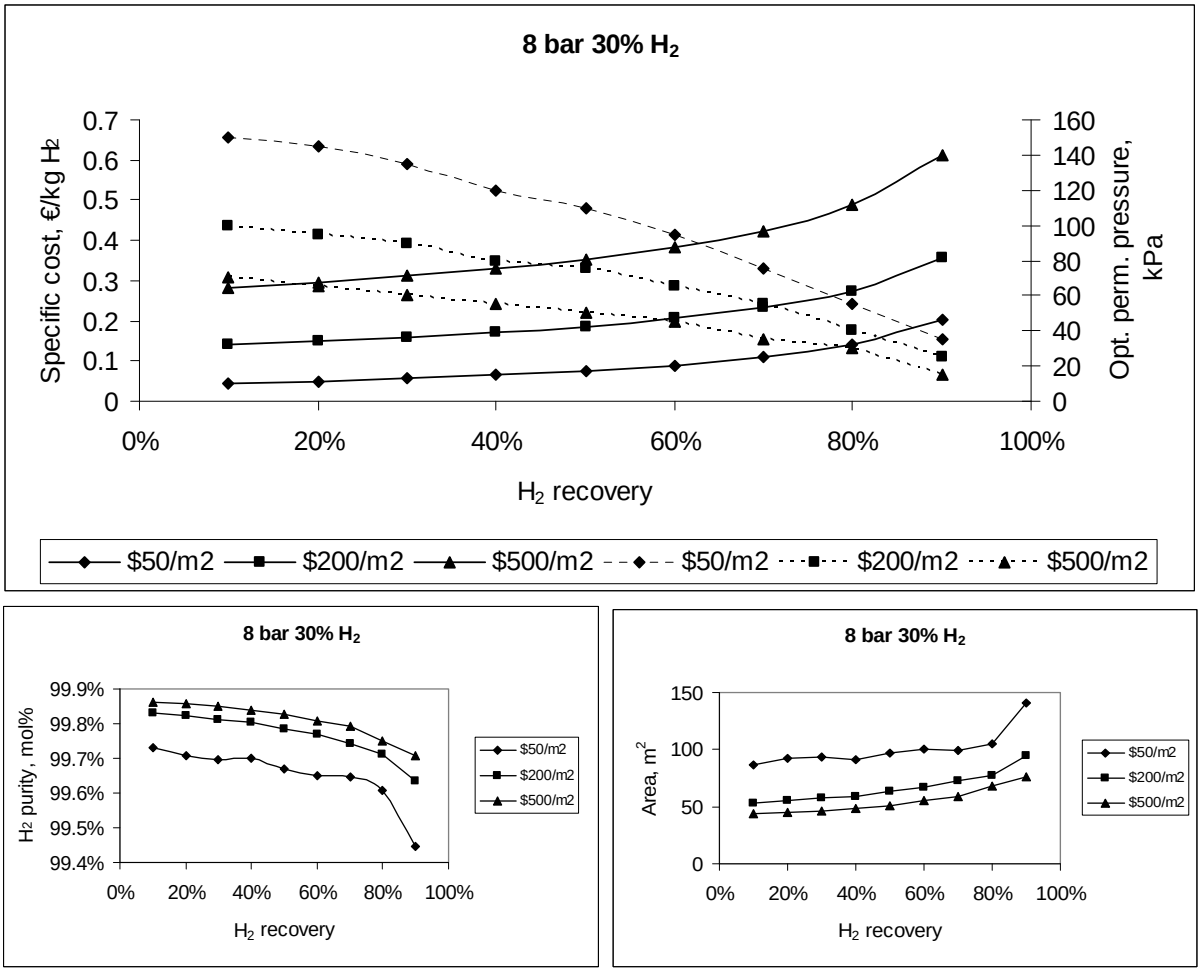

Figure 11-5. 8 bar feed pressure, 30% H_2 at 25°C. Top: Specific costs (—) and optimum permeate pressure (- - -); bottom: H_2 purity (left) and membrane area (right). H_2 partial pressure is less than previous case and driving force influences cost. Permeate pressure is lower than 1.5 bar. As recovery increases, so permeate pressure and purity decrease. Area and specific cost increase exponentially

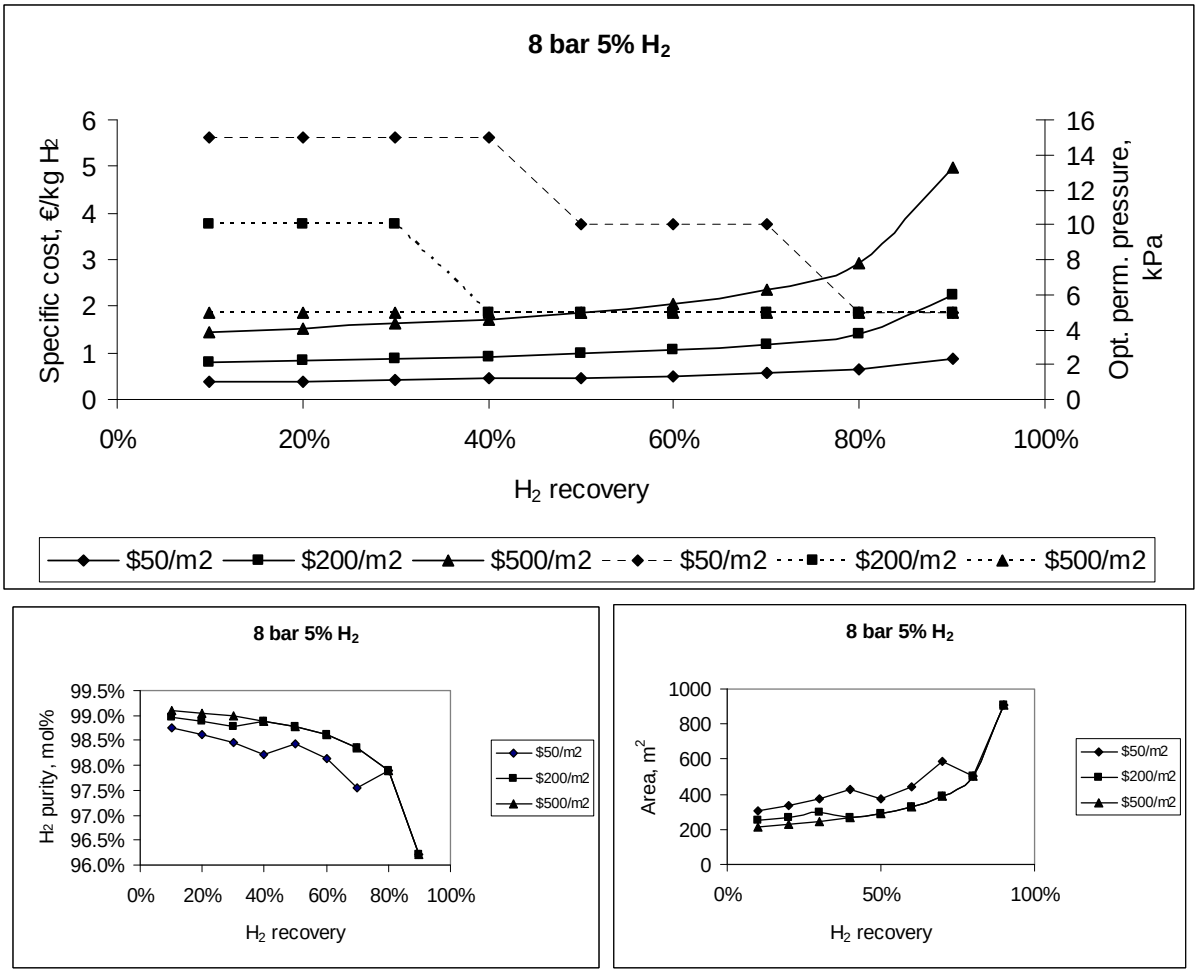

Figure 11-6. 8 bar feed pressure, 5% H_2 at 25°C. Top: Specific costs (—) and optimum permeate pressure (- - -); bottom: H_2 purity (left) and membrane area (right). H_2 partial pressure is lowest and membrane area influences costs. Permeate pressure is v. low to meet purity and reduce membrane cost

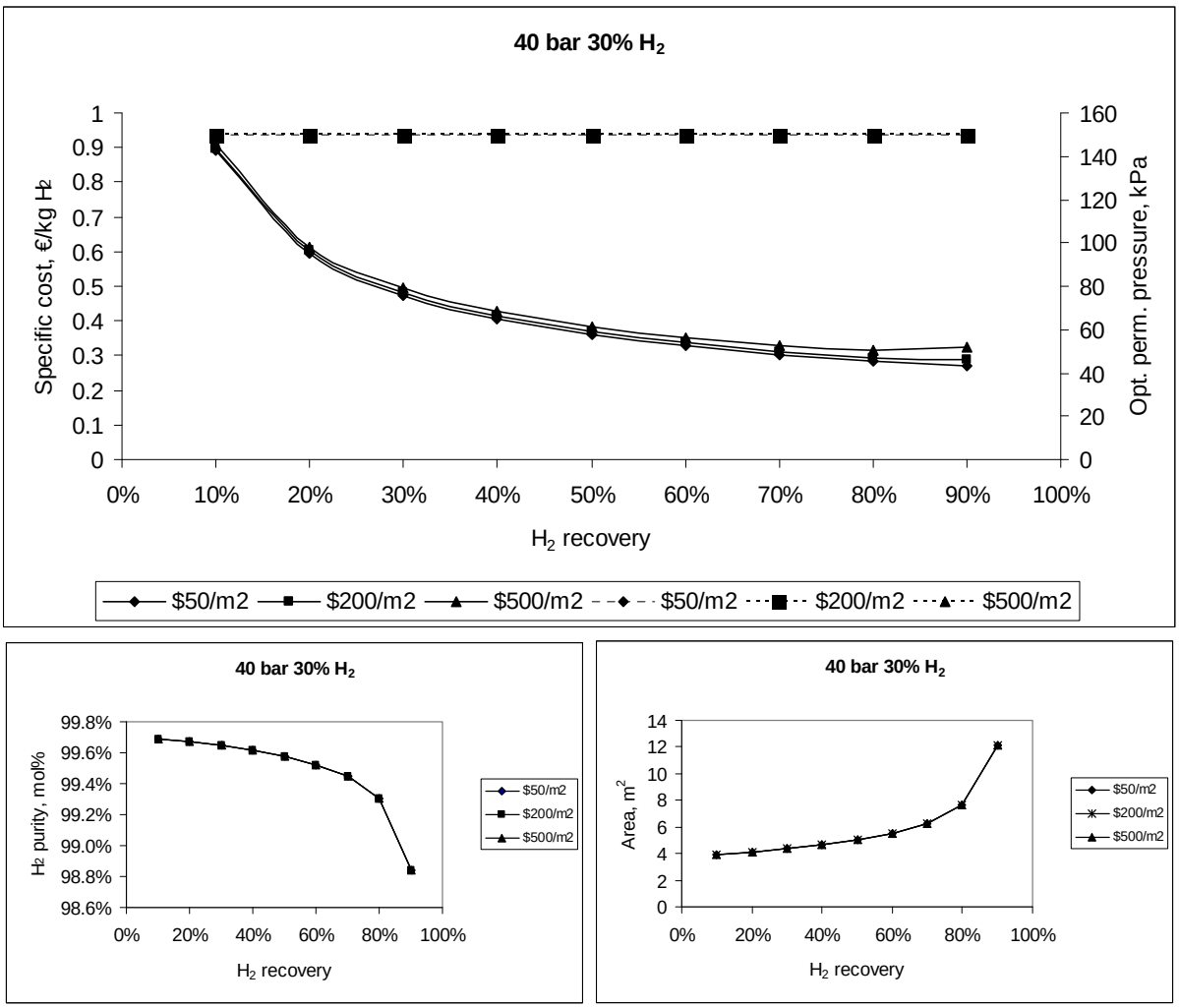

Figure 11-7. 40 bar feed pressure, 30% H_2 at 90°C. Top: Specific costs (—) and optimum permeate pressure (- - -); bottom: H_2 purity (left) and membrane area (right). Driving force and permeances are high, membrane area influences cost little; consequently no differentiation between module cost curves. Cost is higher at low recovery because entire feed is heated for lower relative product

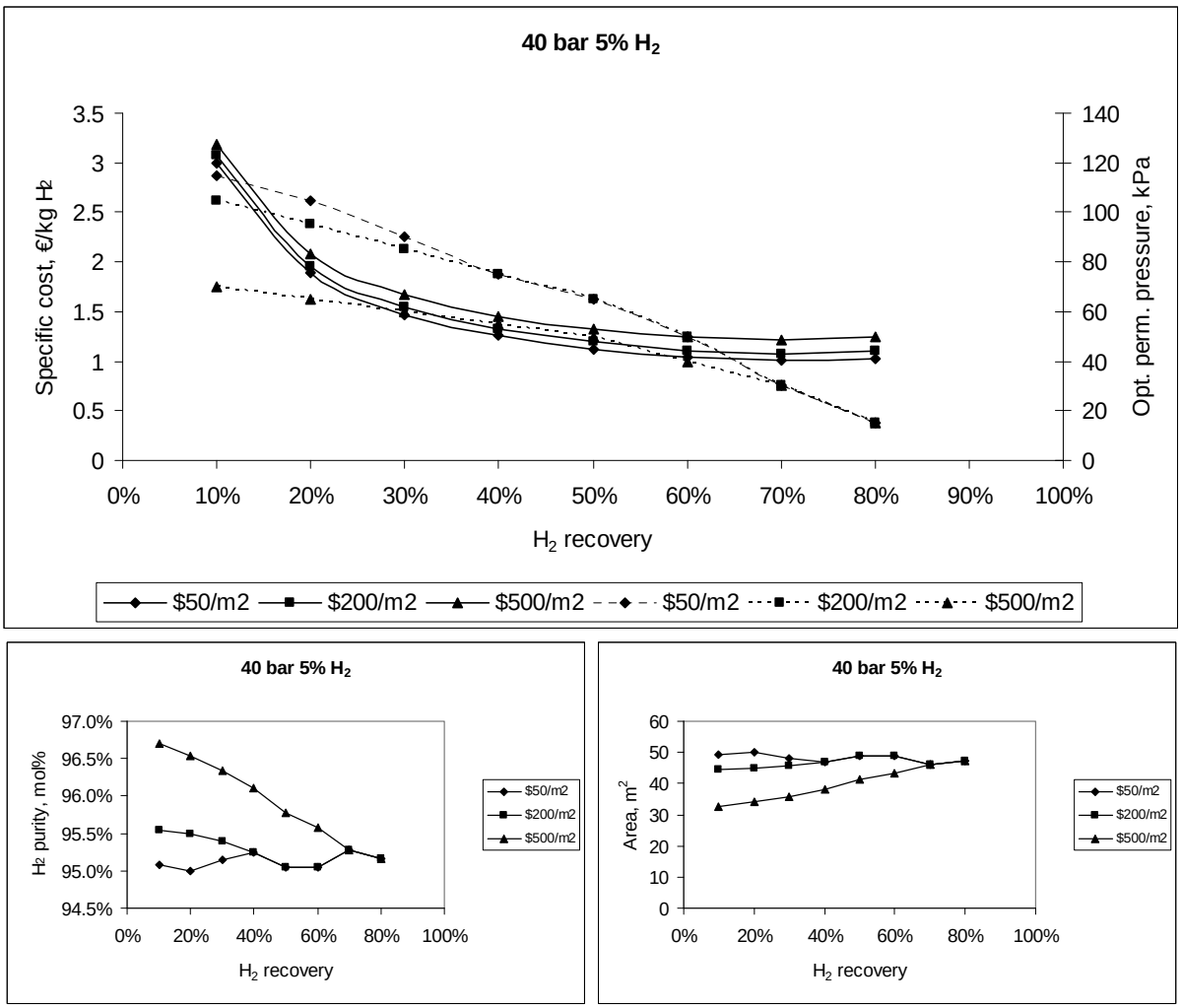

Figure 11-8. 40 bar feed pressure, 5% H_2 at 90°C. Top: Specific costs (—) and optimum permeate pressure (- - -); bottom: H_2 purity (left) and membrane area (right). Permeances are high and driving force moderate, so little differentiation between module cost curves. Selectivity of membrane becomes influential, leading to low permeate pressures. Cost is higher at low recovery because entire feed is heated for lower relative product

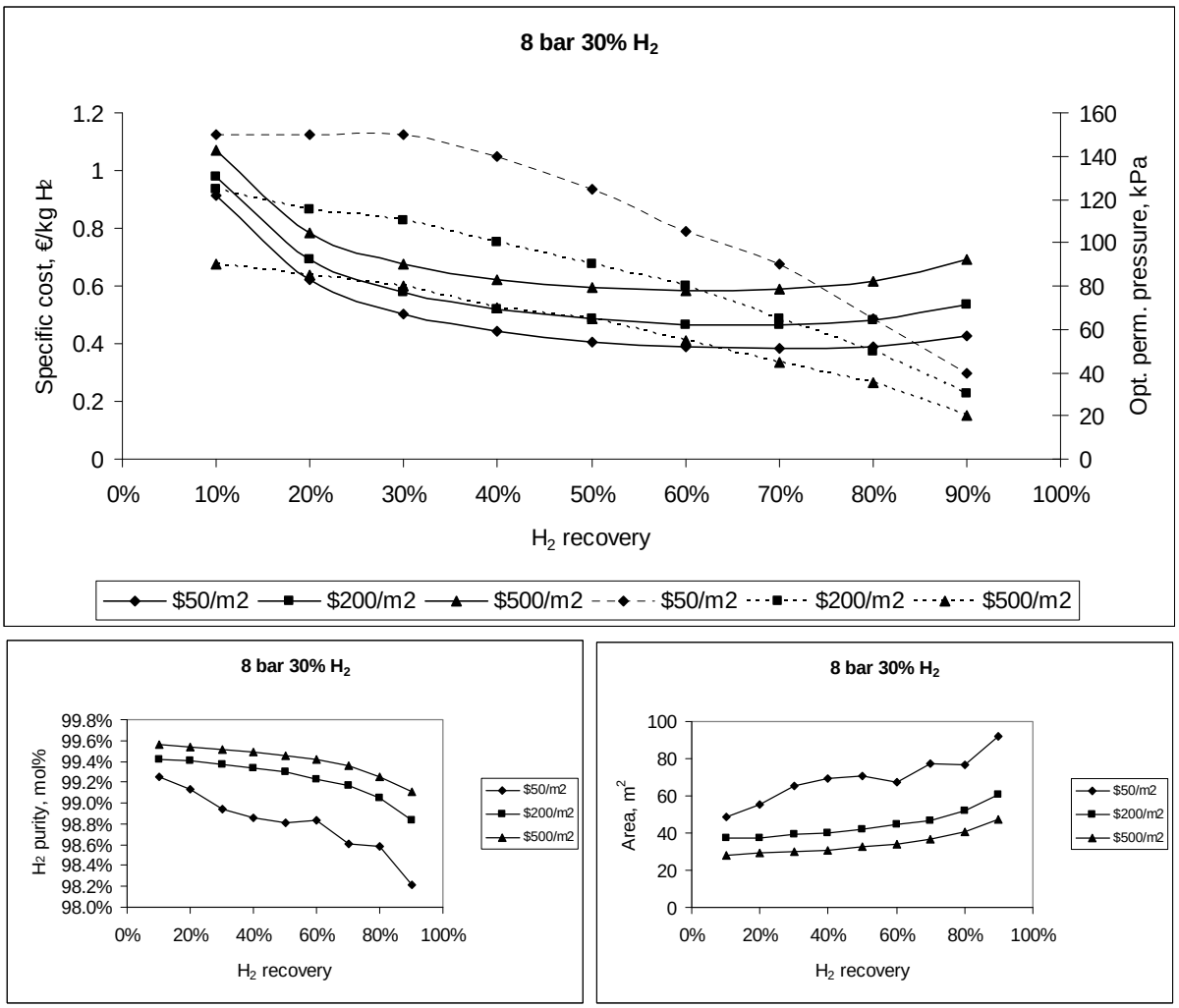

Figure 11-9. 8 bar feed pressure, 30% H_2 at 90°C. Top: Specific costs (—) and optimum permeate pressure (- - -); bottom: H_2 purity (left) and membrane area (right). Driving force and selectivity are influential leading to lower permeate pressures. Membrane area is also a significant factor, causing differentiation between module cost curves. Low driving force at high recovery increases cost

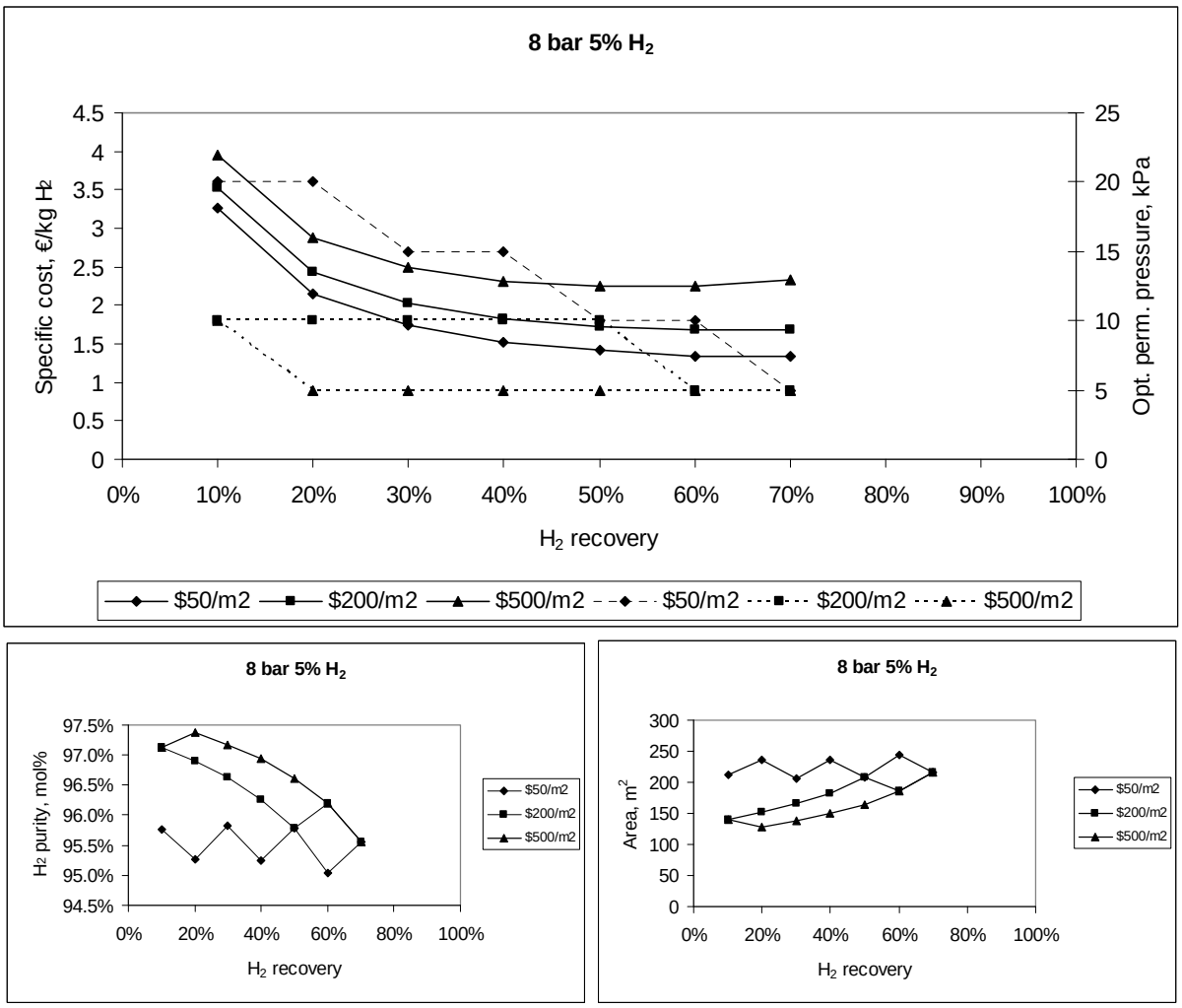

Figure 11-10. 8 bar feed pressure, 5% H_2 at 90°C. Top: Specific costs (—) and optimum permeate pressure (- - -); bottom: H_2 purity (left) and membrane area (right). Driving force and selectivity are influential leading to lower permeate pressures. Membrane area is also a significant factor, causing differentiation between module cost curves.

11.4 Comparison of operating temperatures

An important question is whether heating the feed reduces operating cost. The extra costs for a fired heater (and the associated gas combustion) are offset by the higher permeation rate and lower membrane area. A comparison of temperature levels is shown in the graphs in Figure 11-11. The curves show the specific operating costs for operation at 25 and 90°C for a module cost of \$200/m^2 and a 'break-even cost'. The break-even cost is the cost of a module at which the highest recovery with one stage results in the same specific recovery cost for both 25°C and 90°C operation. The highest recovery is 90% in most cases. The higher the cost of the membrane, the greater is the benefit of increasing the permeation rate with temperature. Similarly, the lower the driving force, the greater is the benefit of heating. If the feed is 40 bar with 30% H_2, there is no benefit to heating to 90°C until the membrane cost is \$4000/m^2. At 40 bar with 5% H_2, this value drops to \$2000/m^2. The lowest driving force is provided by the 8 bar, 5% H_2 feed. Here, heating is advantageous when the membrane module cost is \$500/m^2. The conclusion, therefore, is that there is no benefit to heating the feed for the module cost range.

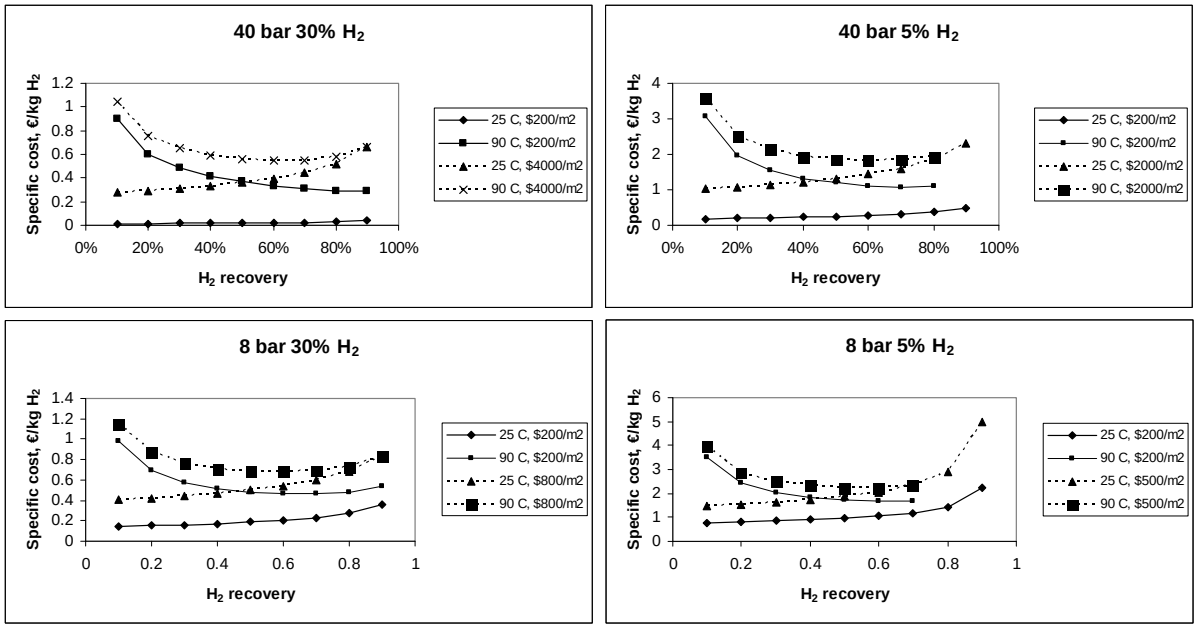

Figure 11-11. Comparison of heating effect for different feed cases. Cost of the membrane included as a parameter

The economy of scale inherent in the compressor cost and fired heater mean that the application size will influence the specific cost of separation. This influence was tested for the 8 bar, 30% H_2 feed, where the economy of scale effect of these two equipment items should be clear. It can be seen in Figure 11-12 that economy of scale is important with respect to the heater. In fact, it was discovered by plotting Aspen Icarus Process Evaluator cost results vs. fired heater duty that the cost is a close fit to the power law,

$$\text{Purchase cost} = 7943.\text{Duty (kW)}^{0.473} \qquad (48)$$

The membrane module cost is proportional to area, by definition. The cost of the compressor follows the following relationship, as fitted to the cost graph of Peters and Timmerhaus (2003):

$$\text{Purchase cost} = 891.\text{Duty (kW)}^{0.9315}.F_s \qquad (49)$$

Here, F_s is the material of construction factor, which is 2.5 for stainless steel. The index is close to 1 and the effect of economy of scale is slight. Thus, without any fired heater, the size of the separation unit was not very important in the 25°C case. On the other hand, the size of the heater unit is significant.

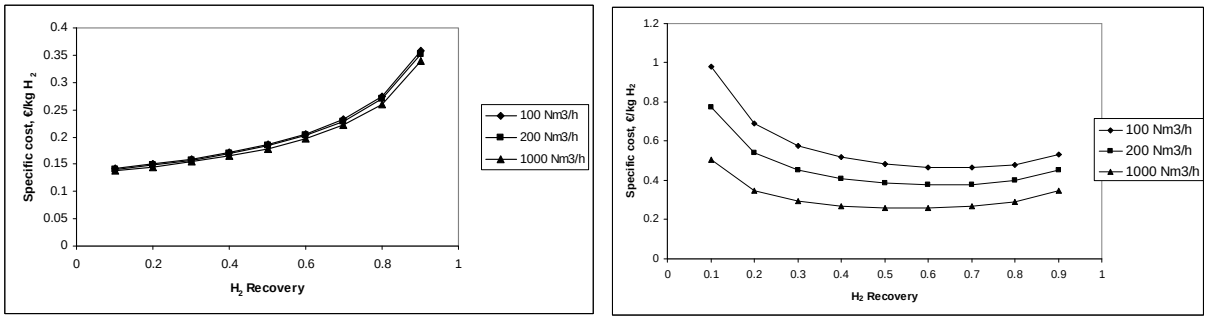

Figure 11-12. Influence of scale of end-use hydrogen requirement (given as a parameter) on specific separation cost. Feed at 25°C (left) and 90°C (right). Membrane module cost = $200/m^2

11.5 Validation of Excel results with Hysys

The preceding analysis was performed with a spreadsheet based on several simplifications of the process. The optimum permeate pressure-recovery series determined from the spreadsheet were fed into ChemBrane via Hysys and the resultant membrane area and specific separation cost were compared. This was done for the major boundary cases for the CMSM at 25°C: 1) 40 bar, 30% H_2, which provides the highest hydrogen partial pressure and 2) 8 bar, 5% H_2, which provides the lowest. The results are shown in Figure 11-13.

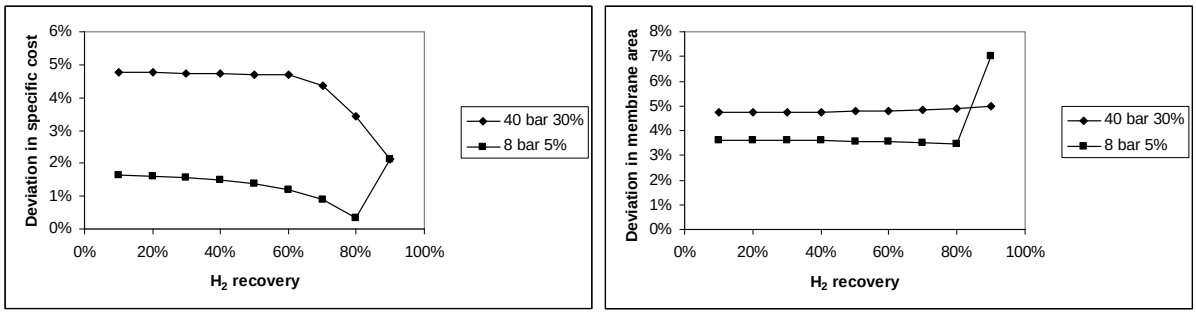

Figure 11-13. Comparison of results for optimum cases from Hysys and Excel

The specific cost and membrane area are never more than 5% higher in the case of the spreadsheet results, except for 90% recovery in the 8 bar case, where there is an unexplained jump in deviation. Considering that this study is only a preliminary techno-economic evaluation of the process, and typically subject to ±30% error, the difference between models does not change the conclusions in this section.

11.6 Comparison with a commercial polymer

The performance of a UBE Industries Ltd. polyimide membrane (Kaldis et al., 2000) was analysed for the purpose of comparison. The permeances of the membrane are shown in Table 11-5. The hydrogen permeance of the polymer membrane is approximately half that of the CMSM at 25°C, but has a H_2/CH_4 selectivity an order of magnitude lower.

Table 11-5. Polyimide membrane permeances (adapted from Kaldis et al., 2000)

Component	Permeability, $m^3(STP)/m^2 \cdot bar \cdot h$	Activation energy, E_p (kJ/mol)
H_2	$7.9 \cdot 10^{-1}$	13.9
CO_2	$2.0 \cdot 10^{-2}$	12.3
CH_4	$1.0 \cdot 10^{-2}$	9.30
C_2H_6	$1.8 \cdot 10^{-3}$	7.70

A typical cost for polymeric membranes of $\$20/m^2$ was as assumed for the polyimide module. Despite this low cost, separation was more economic with the carbon molecular sieve at higher recoveries. This is because the permeate pressure must be lower for the polyimide to produce hydrogen of 95 mol% purity, whereas the CMSM does not need permeate recompression for the full range of recovery. The polyimide process is cheaper for recovery below 40%. This is seen in Figure 11-14, which shows the separation performance of one polyimide stage at 25°C.

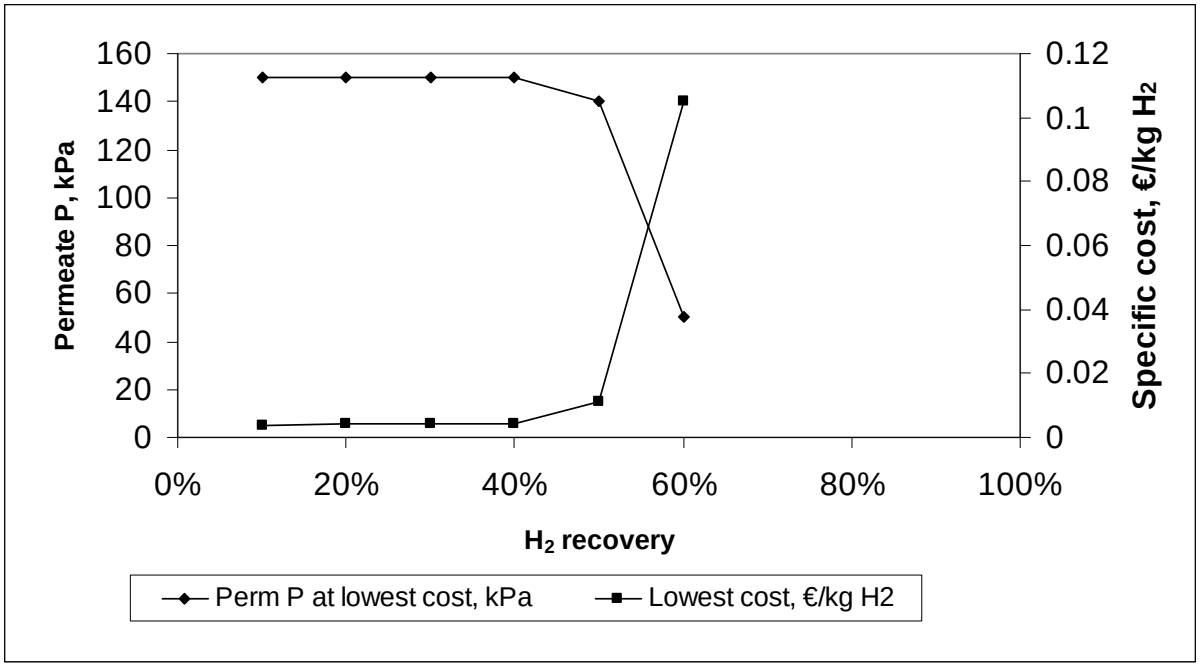

Figure 11-14. Optimum costs and permeate pressures for polyimide separation of a 40 bar, 30% H_2 feed (T=25°C). Purity specification not met above 60% recovery

This spec cannot be met at all for recoveries higher than 60% and the product must be purified in a further membrane stage. If the hydrogen content in the feed is less than 20 mol%, then 95 mol% purity cannot be achieved in one stage for any recovery.

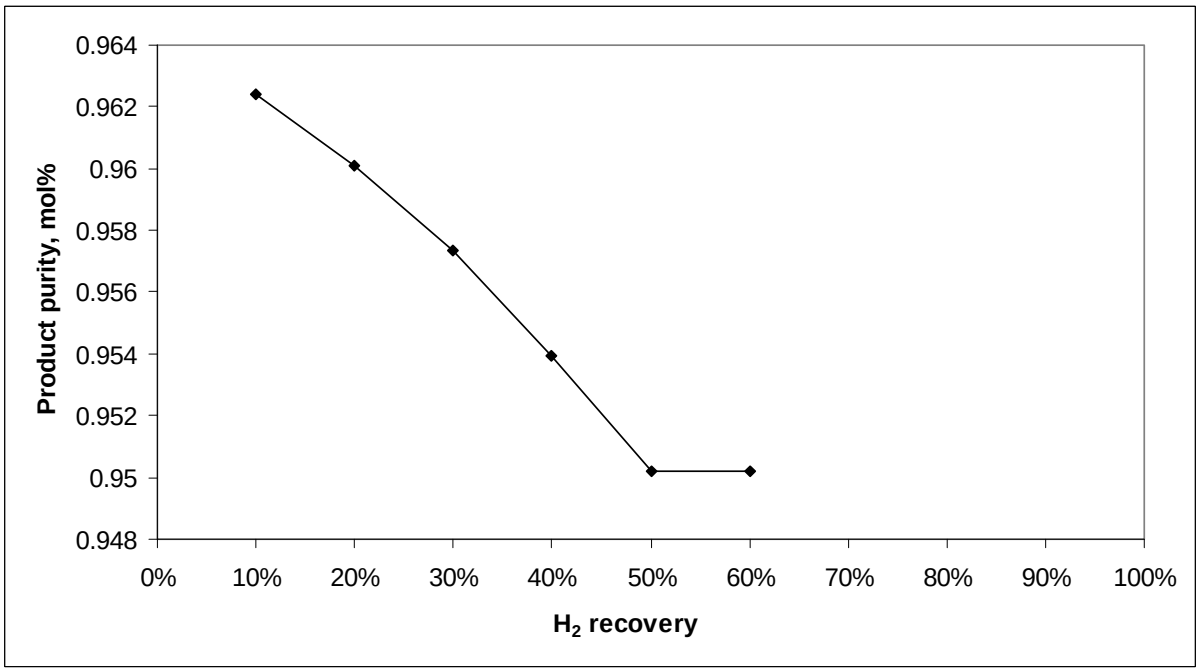

Figure 11-15. H_2 purities at optimum costs for separation of a 40 bar, 30% H_2 feed (T=25°C)

In order to purify feeds with less than 20% hydrogen, two stages are required, where the permeate of the first stage is purified in the second (Figure 11-16).

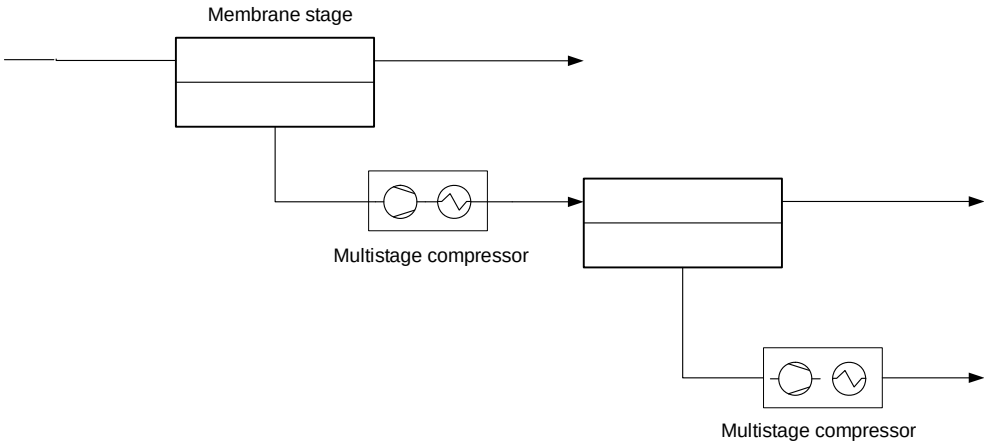

Figure 11-16. Two stage polyimide membrane process

The permeate pressures of both stages were set equal to simplify the sensitivity study, whereas the feed pressure (compressor outlet) for the second stage was varied to find the lowest cost. It was found that 400 kPa provided this. Since the product amount is fixed (~4.5 kmol/h for a hospital fuel cell), the feed size will vary according to the overall recovery (or usage ratio, $F_{H2product}/F_{H2feed}$). This relationship is seen in Equation (50).

$$F_{feed} = F_{product} \cdot y_{H2,product} / (R_T \cdot y_{H2,feed}) \qquad (50)$$

where R is recovery. R_T is the product of the two stage recoveries, i.e.

$$R_T = R_1 \cdot R_2 \qquad (51)$$

And hence, for stage 2, the size of the feed stream is determined by

$$F_{feed,\ stage\ 2} = F_{feed} \cdot y_{H2,feed} \cdot R_1 / y_{H2,\ feed\ stage\ 2} \qquad (52)$$

The relationship between R_1 and R_2 has a large impact on the cost and energy consumption of the process, because the larger R_1, the larger the compression duty for the same amount of product. The goal is therefore to minimise the recovery in the first stage and still meet the requirements of Eq. (51) and the purity specification. It was found that setting $R_1 = 1.05 \cdot R_T$ satisfied these conditions.

It was also found that heating the stream was not beneficial, mostly because the polymer membrane is cheap and area savings were not as influential. The performance at 25°C is shown for a 40 bar, 5% H_2 feed in Figure 11-17 and Figure 11-18. The performance of the CMSM at 25°C and 90°C for the same feed is shown in Figure 11-19. Higher recoveries demanded lower permeate pressures to meet the purity spec. The cost of separation ranged from €0.3-1.0/kg H_2 produced and the purity was maintained at about 95% by progressively lowering the permeate pressure.

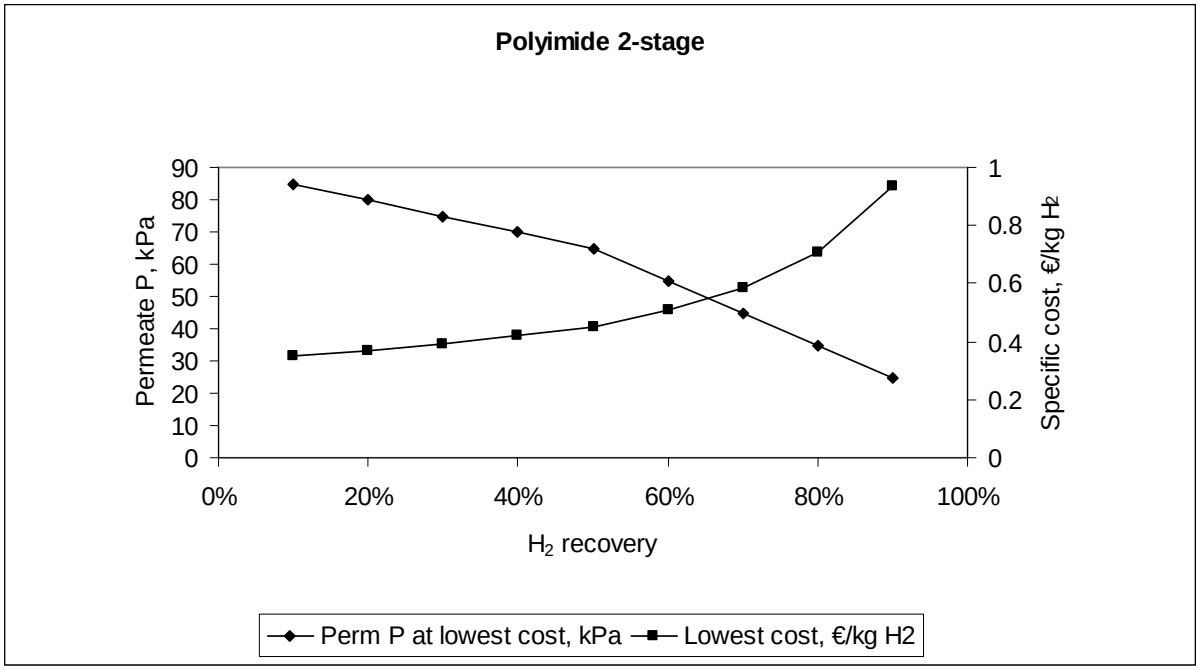

Figure 11-17. Peformance of a 2-stage polyimide process for 40 bar feed, 5% H_2

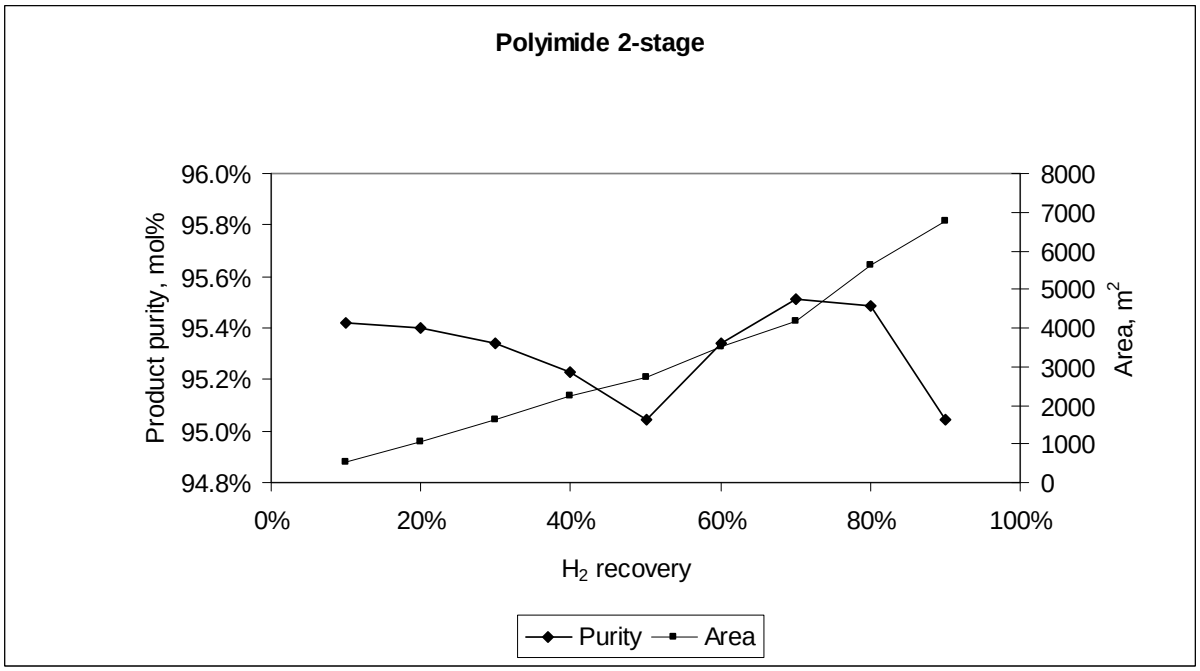

Figure 11-18. Product purity from a 2-stage polyimide process for 40 bar feed, 5% H_2. Increase in purity after 50% due to reduced perm. press.

The carbon molecular sieves (Figure 11-19) achieved costs of €0.014-0.045/kg H_2 at 25°C and €0.29-0.90/kg H_2 at 90°C. These values are for an assumed module price of \$200/m^2. The CMSMs, especially in the case of 25°C, achieve much higher product purity (see Figure 11-6). The curve for the CMSM process at 90°C is upturned at the lower recovery range because the entire feed stream must be heated for a relatively small amount of product.

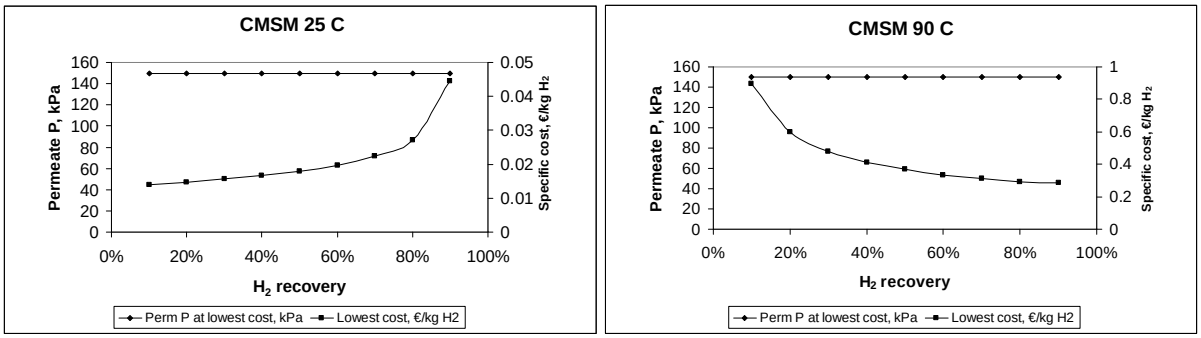

Figure 11-19. Performance of CMSMs for 40 bar feed, 30% H_2 (Mod. cost = \$200/m^2)

When the hydrogen partial pressure of the feed is reduced, the CMSM is still competitive and produces higher purity hydrogen (Figure 11-20). The two-stage process cost, depicted on the left in the figure, is as expensive as the CMSM (25°C), assuming \$200/m^2 for the CMSM.

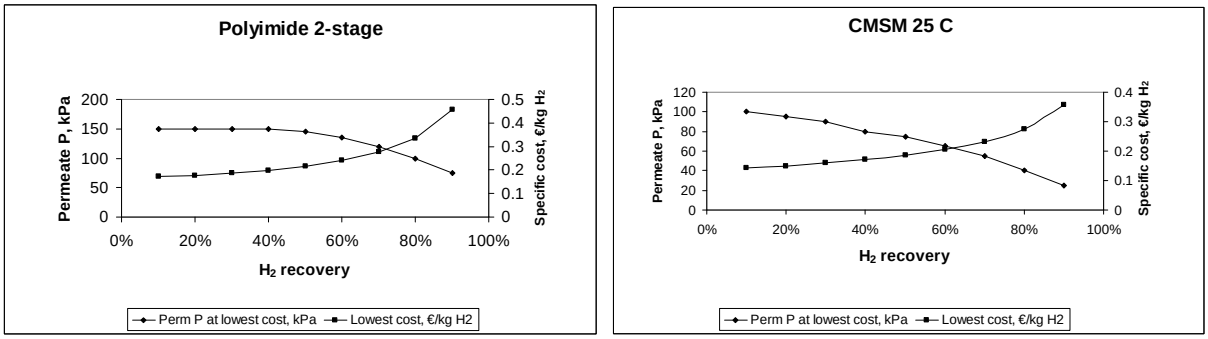

Figure 11-20. Comparison of membranes for 8 bar feed, 30% H_2 (CMSM Mod. cost = \$200/m^2)

For a feed of 8 bar, 5% H_2, the 2-stage polyimide process is slightly cheaper because the membrane area requirement is large due to the low driving force.

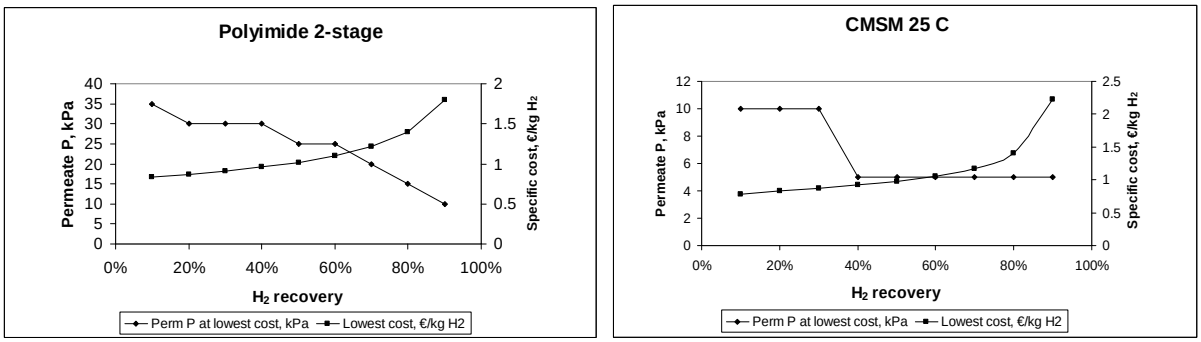

Figure 11-21. Comparison of membranes for 8 bar feed, 5% H_2 (CMSM Mod. cost = \$200/m^2)

The estimation of specific cost is subject to many assumptions, not least of all the cost of the modules. Another point of comparison is the energy consumption per mole of hydrogen, shown in Figure 11-22 and Figure 11-23. These are thermal equivalent values, obtained by converting electrical consumption to thermal by multiplying by 3 (representing an energy conversion process with 33% efficiency) and adding any heating duty. Bearing in mind that the lower heating value (LHV) of hydrogen is 242 kJ/mol, the energy consumption of the polyimide 1-stage process is low. With 2 stages, however, the extra interstage compression causes the energy consumption to be a significant fraction of the LHV of H_2.

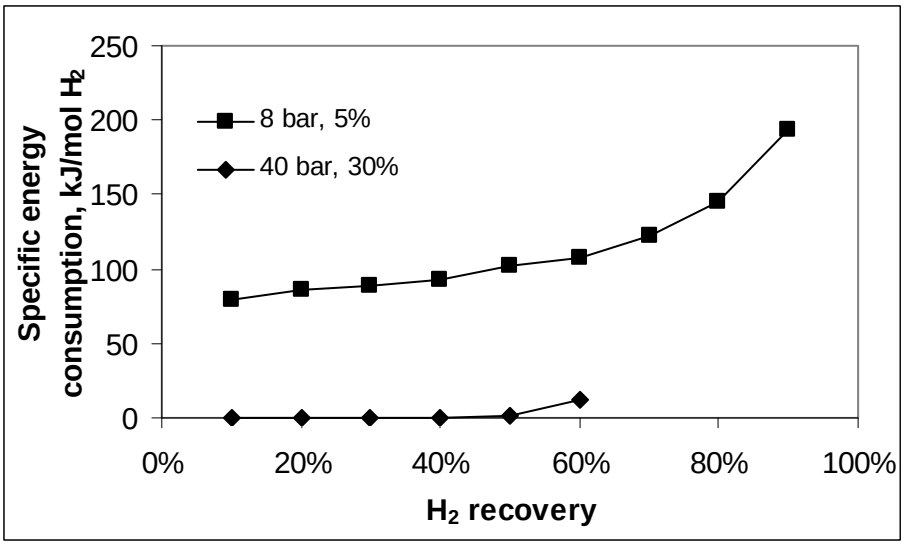

Figure 11-22. Energy consumed per mole of hydrogen produced. Polyimide membrane

The energy consumption for the CMSM (25°C) process is lower for both 30% and 5% H_2 feed cases, because less permeate recompression is required. This is a result of the higher selectivity of the membrane – separation can be achieved in one stage and permeate pressures are higher.

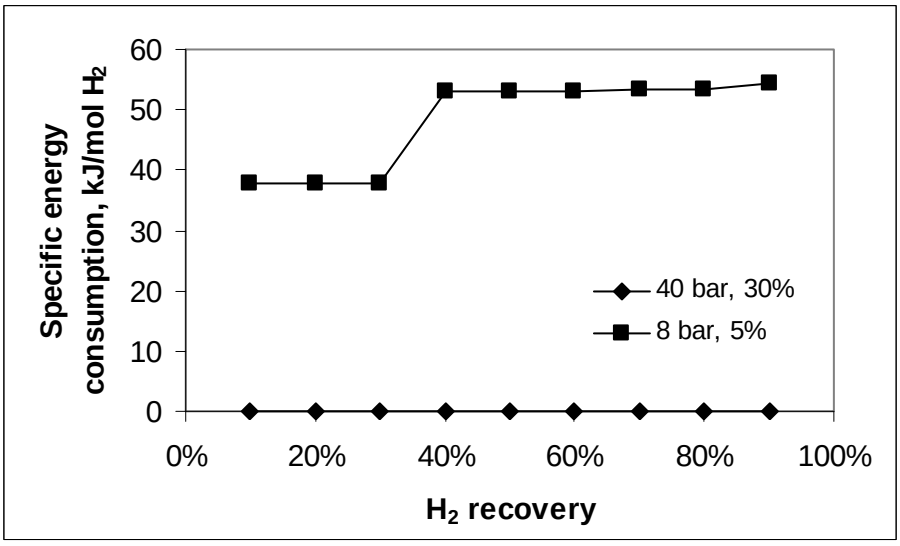

Figure 11-23. Energy consumed per mole of hydrogen produced. CMSM membrane at 25°C

The energy consumed in the CMSM (90°C) cases is significantly higher because natural gas is combusted to heat the feed stream. The process is not energy efficient. This problem could be partially solved by installing a feed-retentate heat exchanger to recover some energy, but the small temperature range (90°C - 25°C) and the minimum temperature approach for gas-gas exchangers (typically 20°C) limit the potential saving.

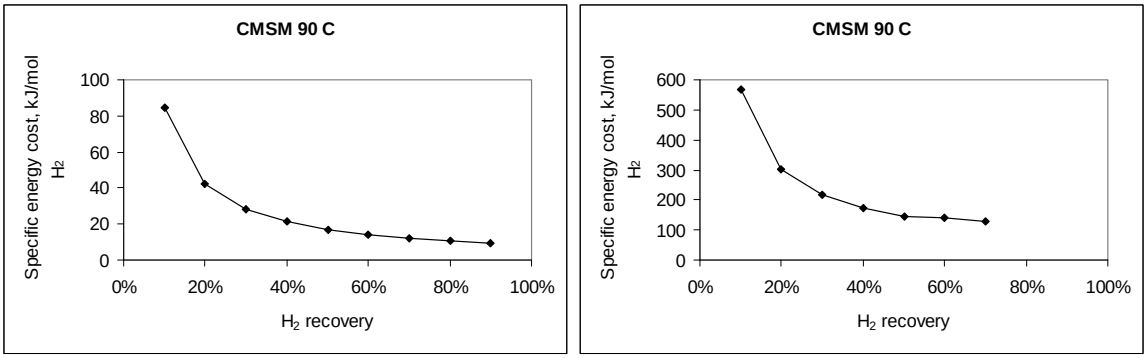

Figure 11-24. Energy consumed per mole of hydrogen produced, for 40 bar, 30% H_2 (left) and 8bar, 5% feed (right). CMSM membrane at 90°C

11.7 Conclusions

- The first, and simplest conclusion, is that carbon molecular sieves are able to separate hydrogen from streams with as low as 5 mol% hydrogen, at the required purity, in one stage.
- The energy consumption of CMSM processes is generally lower than that of polyimide membrane processes.
- The performance and optimum process parameters depend on the feed conditions and the cost of a CMSM module. The latter was found to be a dominant variable.
- It is generally cheaper to run at lower recoveries; in other words, to feed enough to the membrane unit so that the end use requirement is met by a low fraction of the hydrogen in the feed. This is obviously not possible for all users. Those at the end of the pipeline are forced to squeeze out the last bit of hydrogen and so operate at high recoveries.
- In the studied cost range ($50-500/$m^2$), CMSMs are competitive with the polyimide membrane and produce purer hydrogen.

This competitiveness also depends on the hydrogen permeance of the CMSM. The values in this study were taken from the mixed gas data experiments using a 4% CuN membrane carbonized at 650°C (4CuN650TZF) because of the reliability of the mixed gas data. If the permeance of the material can be increased, which is possible given the results with other membranes, then CMSM processes will be even more attractive.

Finally, the small carbon membrane areas required to effect the separation mean that these modules will have a small footprint, with modules of less than 250 litres able to service a hospital fuel cell from streams with 5% hydrogen.

12 Case 2: H_2 from refinery gases

The demand for hydrogen is growing in refineries due to stricter product specifications and a decline in the quality of crude for processing (Pacalowska et al, 1996). Refinery waste gases, containing hydrogen and lower hydrocarbons, provide an opportunity for hydrogen recovery with membranes. Typical hydrogen values are shown in Table 12-1.

Table 12-1. Typical hydrogen content of various off-gases (Pacalowska et al, 1996)

Off-gas source	Typical hydrogen concentration, vol%
Naphtha reformer	65-90
Hydroprocessing	
High pressure	75-90
Low pressure	50-75
Fluid catalytic cracking	10-20
Toluene hydrodealkylation	50-60
Ethylene manufacture	70-90
Methanol manufacture	70-90

Polymeric membranes, such as Air Products' Prism Separator membranes, are already in commercial operation for this purpose, but generally for streams with high hydrogen content. Air Liquide's polyaramide MEDAL membranes achieve H_2/CH_4 selectivities of >400 but with relatively low fluxes, whereas MEDAL polyimide membranes are used for high productivity, moderate purity applications[11].

Other common hydrogen recovery technologies are Pressure Swing Adsorption (PSA) and cryogenic processes. Table 12-2 shows a comparison of the three technologies.

Table 12-2. Hydrogen recovery technologies. Membranes referred to here are polymeric (Pacalowska et al., 1996)

Technology	Membrane	Adsorption	Cryogenics
Hydrogen prod. Purity, %	<95	99.9+	95-99
Typical hydrogen recovery, %	<90	75-90	90-98
Hydrogen prod. pressure	<< Feed pressure	Feed pressure	Variable
Byproduct availability	No	No	No
Feed pressure, bara	16-126	11-56	16-36

From the previous study on CMSM application in distribution networks, it is apparent that CMSM processes are competitive against commercial polyimide membranes over a range of feed conditions. If 'free' energy is available from the refinery in the form of low quality steam (100°C), high temperature feed (e.g. direct from a HP separator in a hydrocracking unit) or fuel gas, then CMSMs may be even more viable at high temperature (>100°C) because permeances are high. Another advantage that carbon membranes have over polymeric membranes is that H_2S, which is sometimes present in refinery streams, should be rejected by molecular sieving carbons since the kinetic sieving diameter of H_2S is 3.6Å (similar to N_2). The carbon membrane should tolerate H_2S and thus there would be no need for feed pre-treatment unless irreversible sorption occurs. Conversely, H_2S is a fast-permeating gas in polymers and will contaminate the hydrogen product.

Rao and Sircar (1993, 1996) have also published extensively on a selective surface flow membrane (SSF™) they have developed, in which more readily adsorbed molecules are

[11] Source: http://www.medal.airliquide.com/en/membranes/hydrogen/ammonia.asp

transported and hydrogen is retained. This has the advantage that the product, hydrogen, is delivered at the higher pressure. However, the selectivities are low for H_2/CH_4 (~2) and the membrane appears limited to hydrogen enrichment in hybrid applications.

12.1 Design basis

Kaldis et al. (2000) provided typical compositions and conditions of small-medium refinery streams available for hydrogen recovery. Three of these, which represent the range of H_2 content, were chosen for simulation and are shown in Table 12-3.

Table 12-3. Typical refinery gas streams (Kaldis et al. 2000)

	Naptha hydrotreater	**Mild hydrocracking**	**Gas oil desulphurisation**
Gas composition mol%			
H_2	90.0	32.4	79.9
Methane	5.2	23.1	14.4
Ethane	1.8	17.3	3.9
C_3, C_4+	3.0	18.0	1.8
H_2S	-	9.2	-
Flowrate, Nm^3/h	500	8000	2315
Temp. °C	35	40	40
Pressure, bar g	40	12	25

Although the temperatures are given as 35-40°C in the basis, the actual source of the stream may be at much higher temperatures. An example would be purge hydrogen from the high pressure (HP) separator in a hydrocracking unit (see Figure 12-1). Hydrocracking reactors operate in the region of 350-400°C (Speight and èOzèum, 2002).

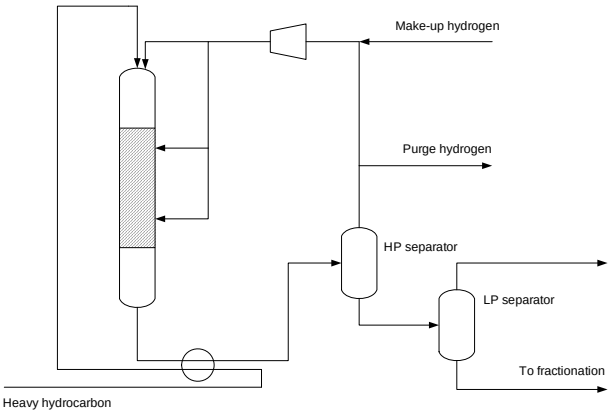

Figure 12-1. Typical hydrocracking unit

Permeation tests have been conducted successfully up to 180°C (Section 7.8.2), showing that CMSM membranes easily tolerate high temperature operation. However, mixed gas tests with hydrocarbon feeds have only been tested up to 90°C. For the sake of this study, it will be assumed that the temperature-permeation relationship observed over the range 25-90°C, for membrane 4CuN650TZFB3-R3, is valid up to 200°C. The Arrhenius parameters derived

from this study are shown in Table 12-4. The membrane was assumed to be in the form of hollow fibres with a wall thickness of 16 microns and a dense layer of 1 micron.

Table 12-4. Arrhenius parameters for permeabilities in CMSM (4CuN650TZF-R3)

Component	Es, kJ/mol	P_0, Barrer	Source
H_2	8.0	14820	H_2-CH_4 tests
CH_4	24.3	3372	Single gas tests

According to Kaldis et al. (2000), the polyimide membrane can operate up to 100°C. The influence of temperature on the two membranes is shown in Figure 12-2. The permeance increases for both as temperature is raised, but the selectivity decreases for the carbon molecular sieve membrane and increases for the polyimide membrane. The latter's behaviour is probably due to the decrease in solubility of methane in the polymer as the temperature increases. The performance of the polyimide is better in all respects at the 100°C and so modelling of the polyimide process was performed at that temperature. The operating temperature was varied in the CMSM study.

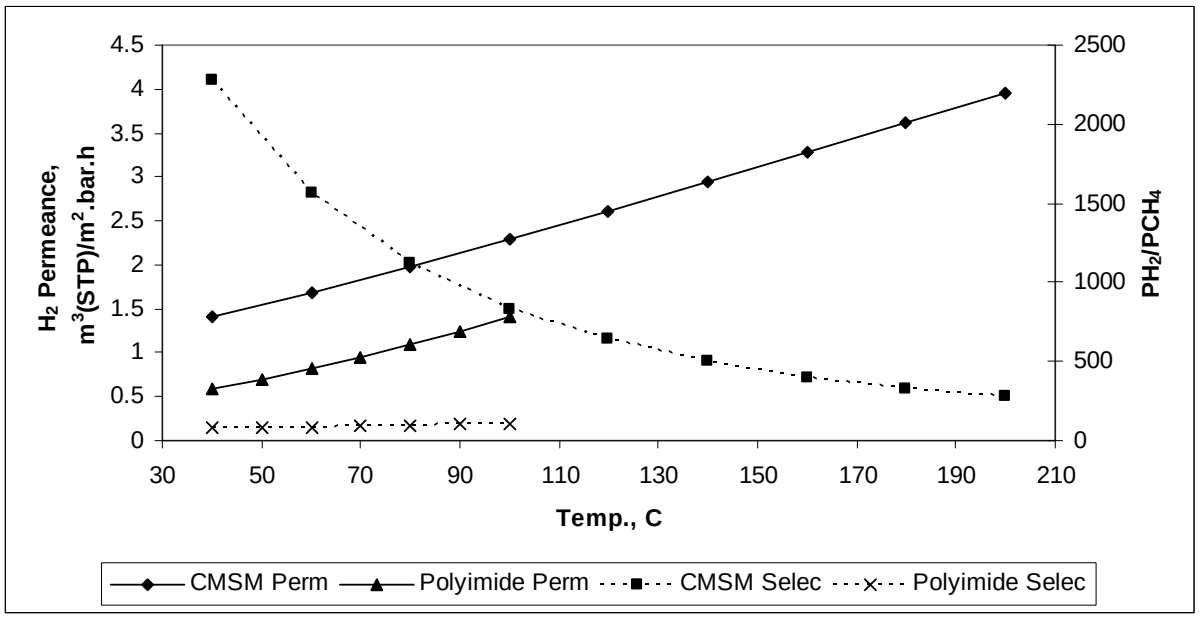

Figure 12-2. Influence of temperature on membrane performance

The delivery pressure from the membrane unit depends on the hydrogen consumer. The most common technology for hydrogen purification in refineries is Pressure Swing Adsorption, which delivers the hydrogen at approximately feed pressure. For comparison, the delivery pressure for the simulation cases in this study was therefore set to the feed pressure.

Since 95% is considered a 'typical' purity achievable with polymeric membranes (Table 12-2), the lower purity limit for carbon membranes in the hydrocracking and desulphurization cases was also set to 95 mol%. Since the hydrogen content in the Naphtha hydrotreating off-gas is already high (90%), the minimum product purity was specified as 99 mol%.

12.2 The simulations and sensitivity analysis

The higher hydrocarbons were first lumped with the methane, for the purpose of exploring the variable space in the Excel spreadsheet introduced in the previous section. This is a conservative approach. Thereafter, the more rigorous Hysys model was used to verify the main results with all of the components present.

As in the previous study, the permeate pressure was altered to achieve the lowest possible operating cost, while still meeting the minimum hydrogen product purity. Often, the purity at the optimum operating cost was higher than the minimum.

12.3 Naphtha hydrotreater

The performances of the CMSMs are shown in Figure 12-3 to Figure 12-5 for different module costs. This case is characterised by the high partial pressure of hydrogen in the membrane feed. The membrane areas are small (10-60 m^2) and the costs of separation appear low (€0.02-0.09/kg H_2). The major cost contributor is the recompression of the permeate back up to 40 bar, therefore, there is little difference between membranes that cost \$50/m^2 or \$500/m^2. The permeate pressure is also relatively high. As expected, higher recovery caused the cost of separation to increase. Increasing the operating temperature lowered the cost of separation as membrane area decreased and also allowed the permeate to be at a higher pressure. Although increasing the temperature and recovery reduced the permeate purity, the specification was easily met in all the cases. In a few instances (see graphs for \$50/m^2 case), the minimum purity was approached at higher temperatures and the permeate pressure accordingly decreased by a set increment (which was more than necessary). This caused a jump in purity and sharper drop in membrane area.

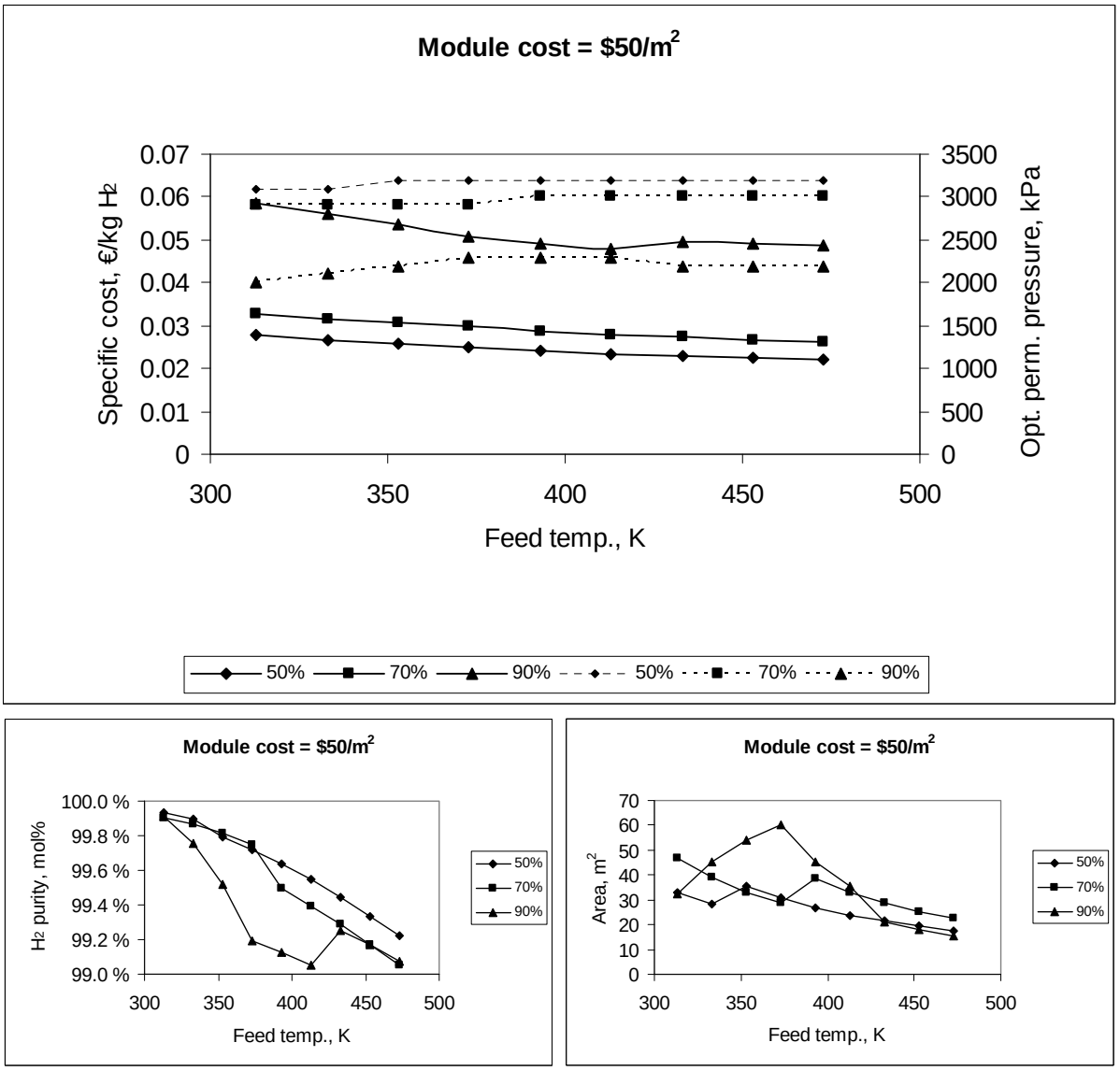

Figure 12-3. Results for the Naphtha case, CMSM module cost = $50/m^2. Top: Specific costs (—) and optimum permeate pressure (- - -). H_2 recovery included as a parameter. As temp. increases permeate pressure can increase because mem. area decreases. Above 400 K, purity spec is reached for 90% rec. and permeate pressure decreases slightly

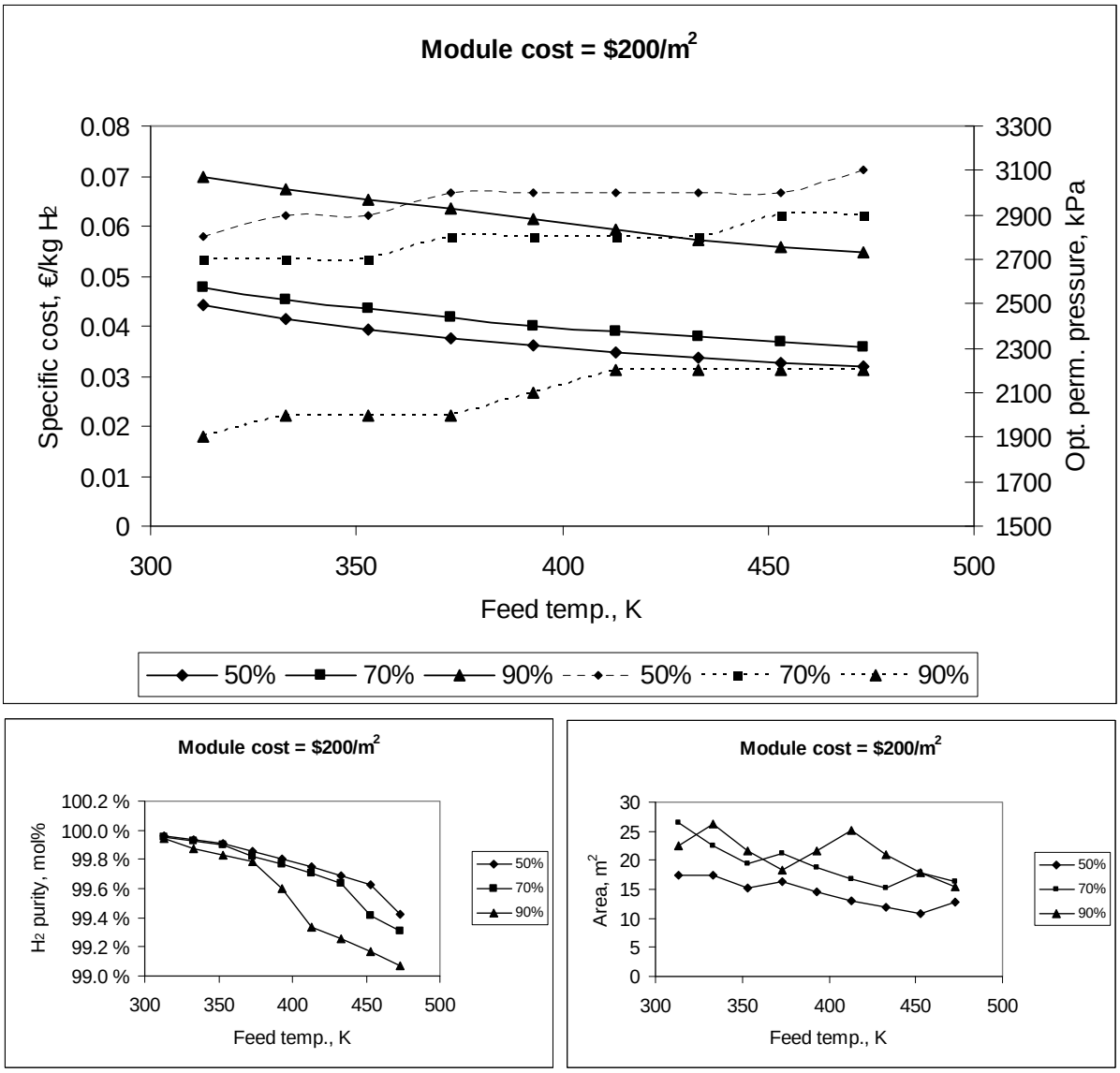

Figure 12-4. Results for the Naphtha case, CMSM module cost = $200/m^2. Top: Specific costs (—) and optimum permeate pressure (- - -). H_2 recovery included as a parameter. Mem. cost more influential than previous case and permeate pressure lower to decrease mem. area

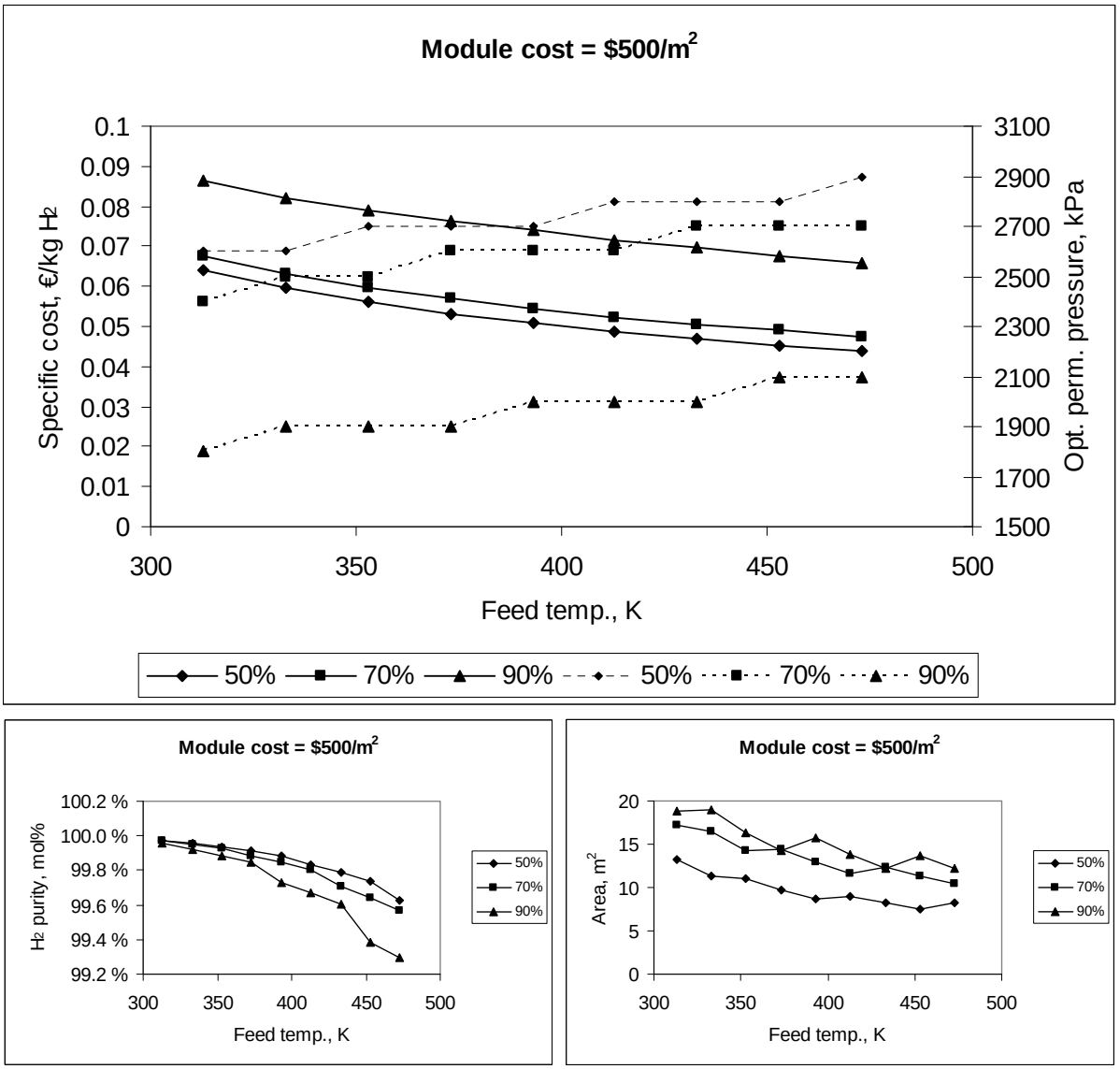

Figure 12-5. Results for the Naphtha case, CMSM module cost = $500/m^2. Top: Specific costs (—) and optimum permeate pressure (- - -). H_2 recovery included as a parameter. Mem. cost more influential than previous cases and permeate pressure lower to decrease mem. area

The performance of the polyimide membrane is shown in Figure 12-6. The permeate pressure was generally controlled by the required product purity and so is lower than for the CMSMs. Due to the negligible membrane cost, the polyimide separation cost is similar to that for the CMSM cases. The main difference is that the hydrogen product purity is higher with the carbon membranes.

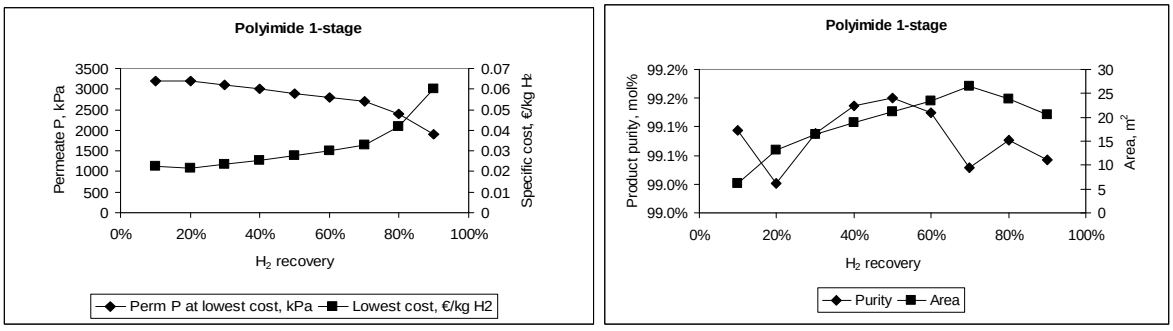

Figure 12-6. Polyimide performance for Naphtha hydrotreating case. Influence of recovery at 100°C

Unsurprisingly, the energy consumption in both processes is similar since recompression occurs from roughly the same pressure (Figure 12-7).

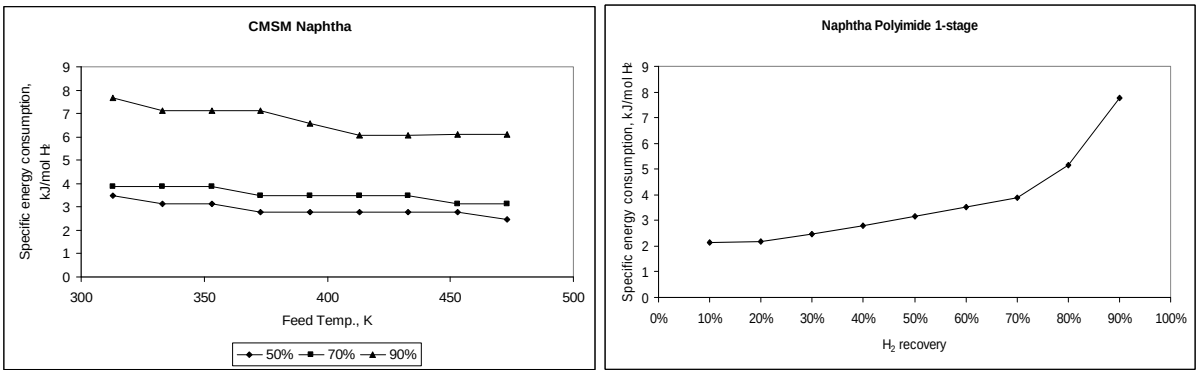

Figure 12-7. Energy consumption per mol H_2 produced in CMSM (left) and Polyimide (right) processes. Recovery shown as a parameter for the CMSM process

In this application, there is no clear winner. A polyimide membrane may be more robust and present less risk, but does not produce ultra-pure hydrogen as the carbons do. Furthermore, should the feed stream temperature be higher than that tolerated by the polyimide, then this would be in the CMSMs favour.

12.4 Hydrocracking

The feed in this application has both lower pressure (12 bar) and lower hydrogen content (32.4 mol%) than the previous case. The result is that the CMSM membrane area and cost have a significant influence on the optimum cost, membrane area and permeate pressure (Figure 12-8 to Figure 12-10). The permeate pressure was lower relative to the feed pressure than in the previous case, in order to reduce the membrane area. As with the last case, increasing the operating temperature improved the separation economics. The cost of separation varied between €0.15-0.55/kg H_2 produced, depending on the assumed cost of module and the recovery. The minimum product hydrogen purity was met easily in all cases.

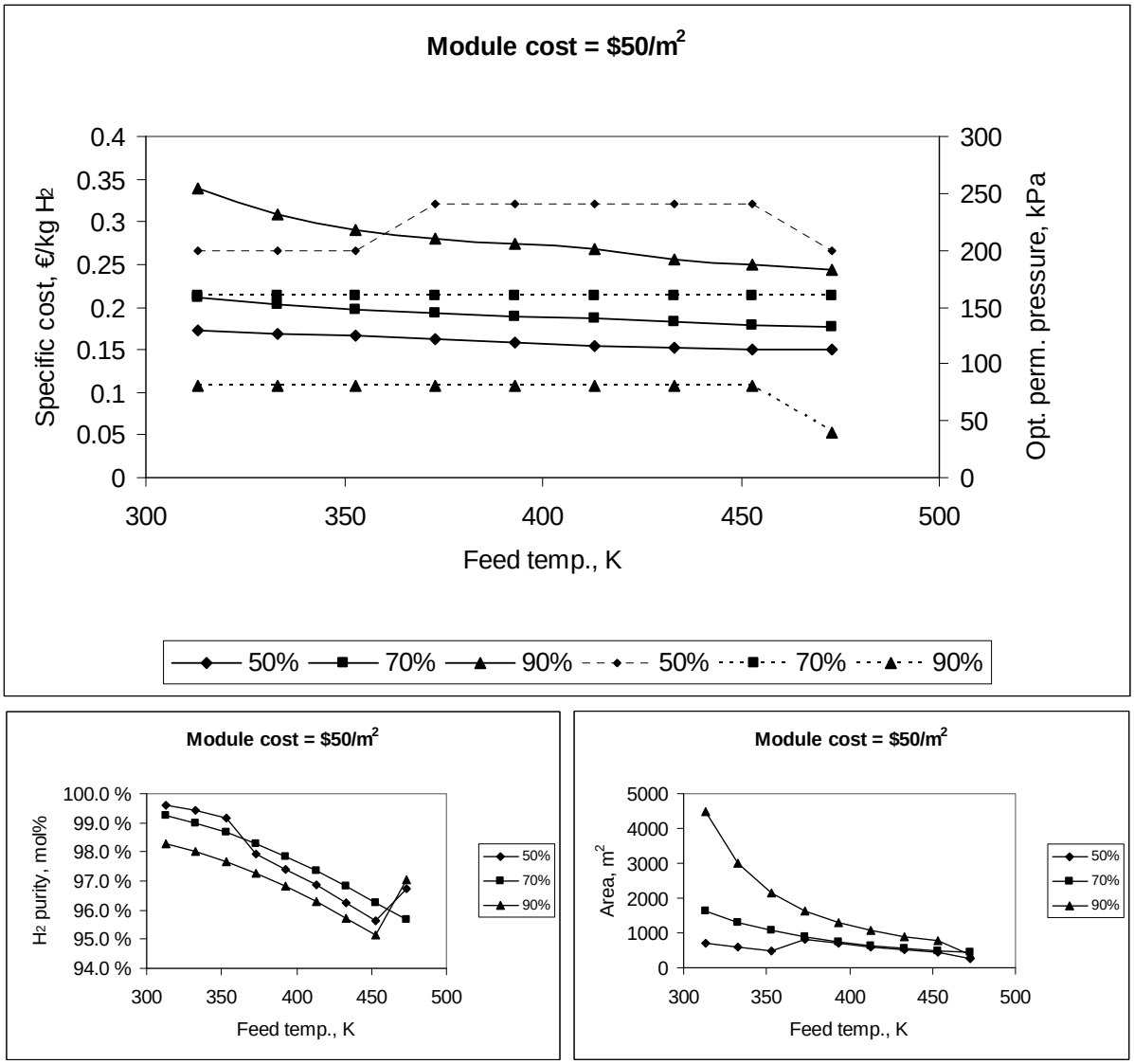

Figure 12-8. Results for the Hydrocracking case, CMSM module cost = $50/m^2. Top: Specific costs (—) and optimum permeate pressure (- - -). H_2 recovery included as a parameter. Permeate pressure steady over most of recovery range but decreases at high recovery to achieve purity spec.

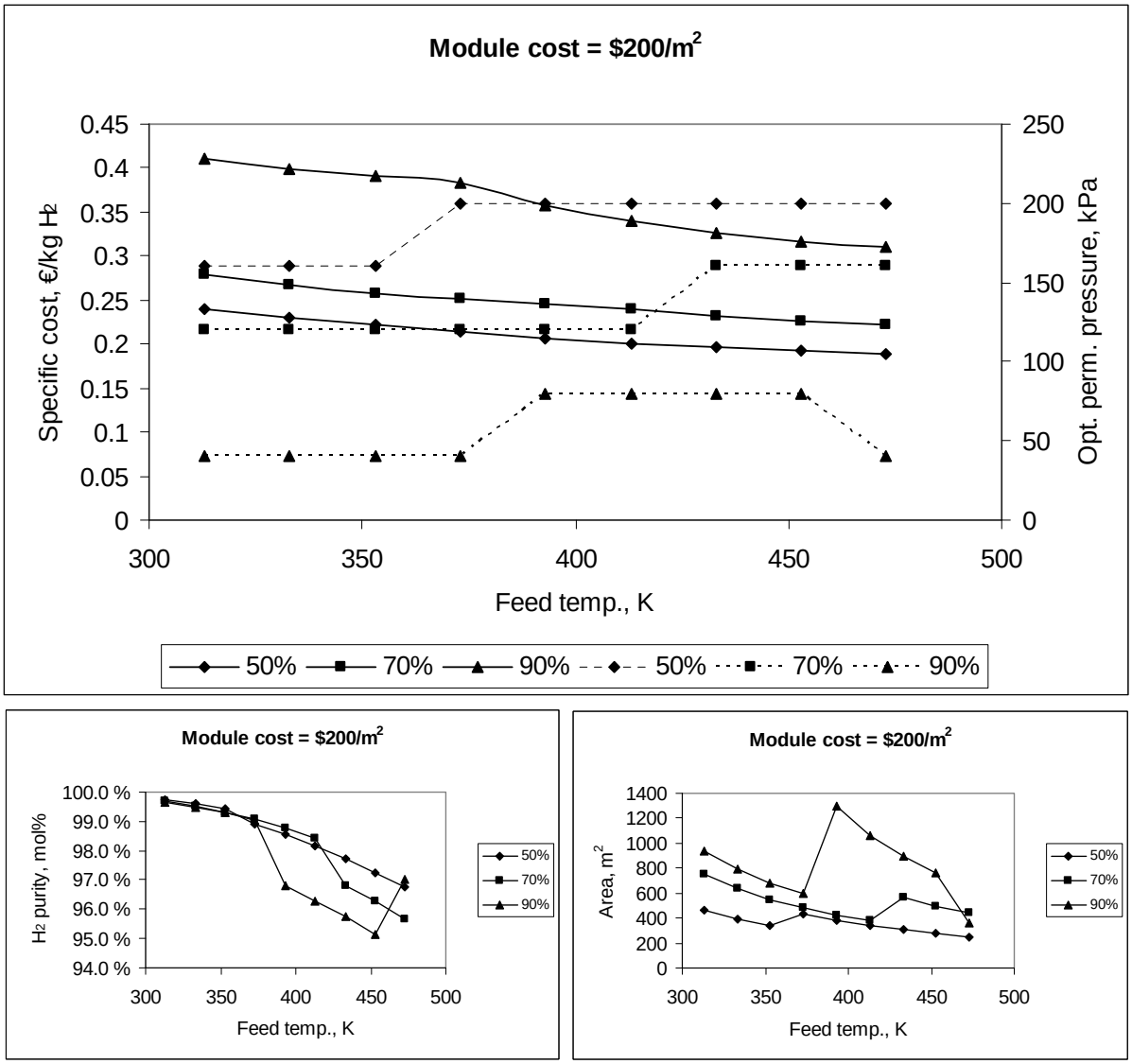

Figure 12-9. Results for the Hydrocracking case, CMSM module cost = $200/m^2. Top: Specific costs (—) and optimum permeate pressure (- - -). H_2 recovery included as a parameter. Permeate pressures lower than previous case in response to membrane cost. Increase in permeate press. for 90% rec at 400 K causes jump in membrane area. Perm. press. decreases again after 450 K as selectivity too low

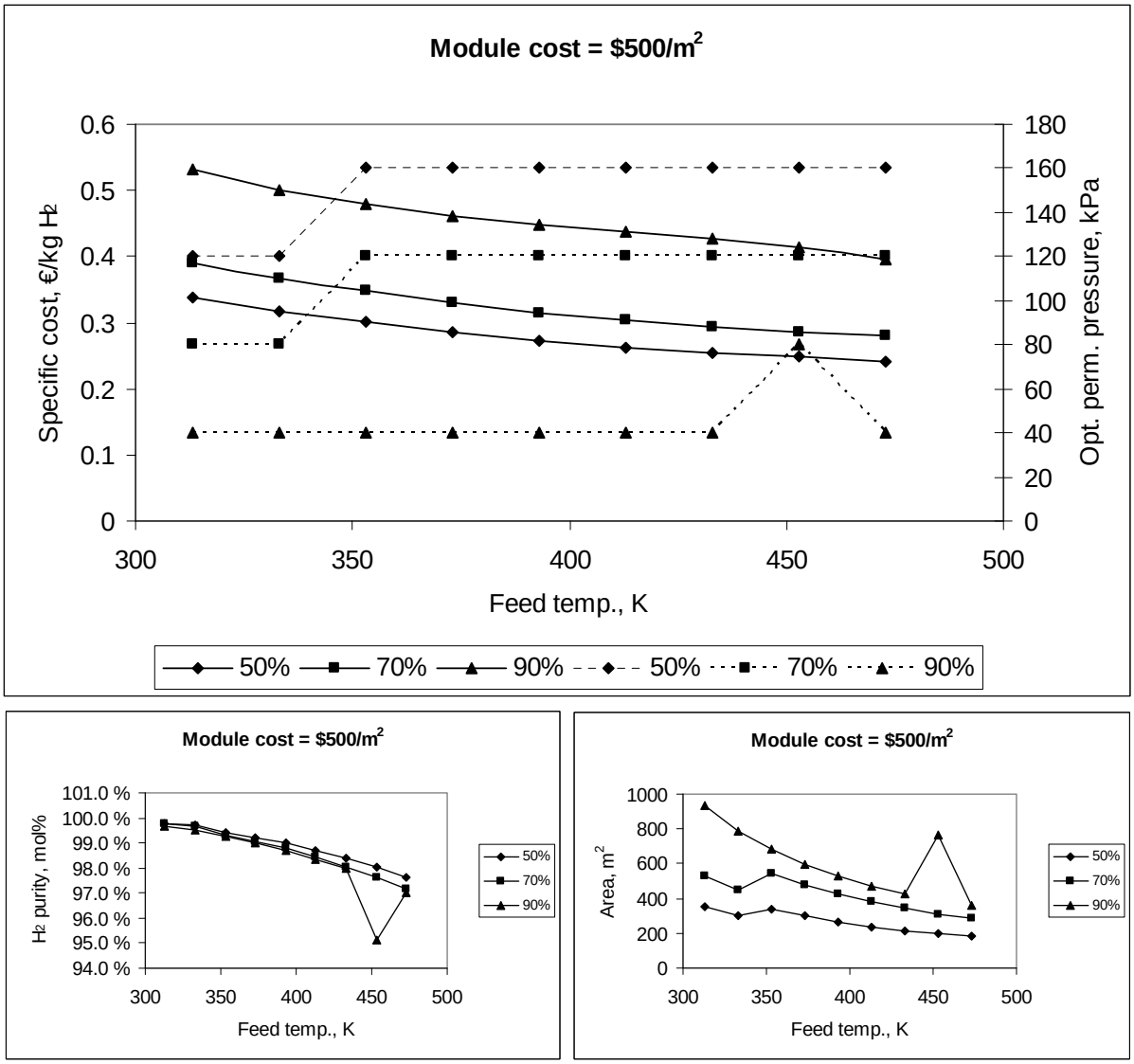

Figure 12-10. Results for the Hydrocracking case, CMSM module cost = $500/m^2. Top: Specific costs (—) and optimum permeate pressure (- - -). H_2 recovery included as a parameter. At 450 K, increased permeance allows permeate press. to increase as mem. area decreases, but purity not met at 473 K at this perm. press. so it moves to lower level

A one-stage polyimide process (Figure 12-11), on the other hand, can only recover up to 80% of the hydrogen at the required purity and a two-stage process is required to achieve 90% recovery (Figure 12-12). The permeate from stage 1 was compressed to 12 bar. The permeate pressure is generally lower than in the CMSM processes in order to obtain this purity specification. Because the polyimide module cost is so much lower than the CMSM module cost, however, the separation costs are similar.

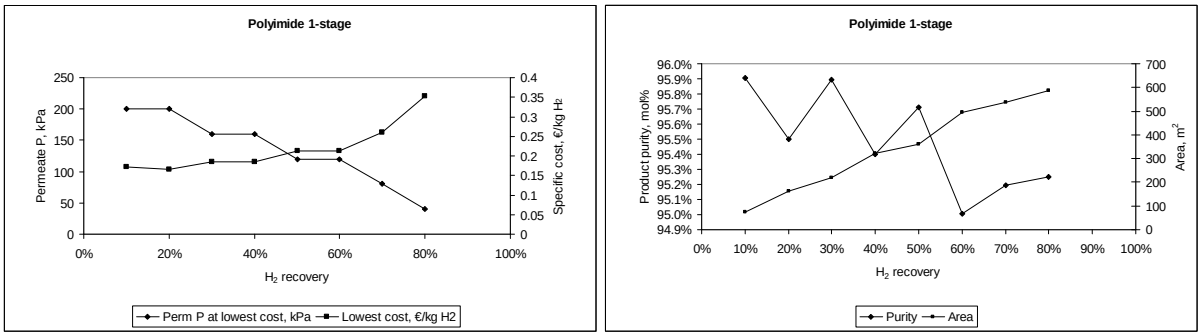

Figure 12-11. One-stage polyimide process for mild hydrocracking case

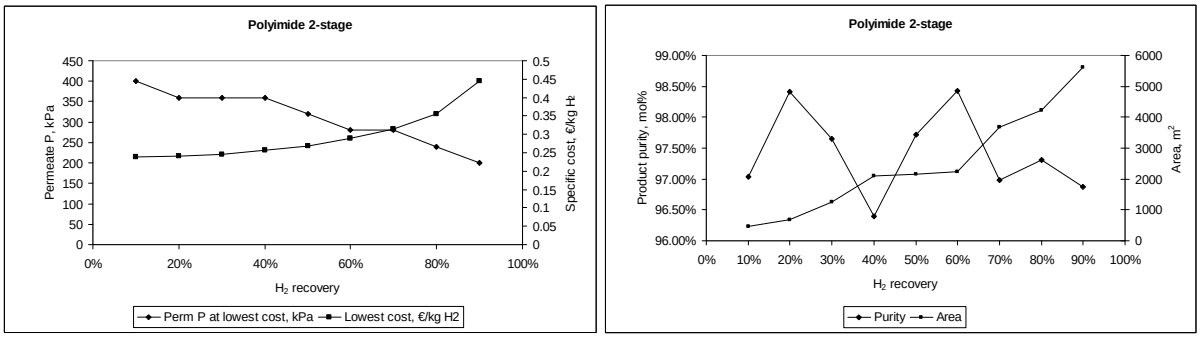

Figure 12-12. Two-stage polyimide process for mild hydrocracking case

From an energy consumption perspective, the CMSMs perform better. At the highest respective operating temperatures and in the 50-90% recovery range, the CMSMs consumed 25-40 kJ/mol H_2 recovered whereas the polyimide process consumed 30-55 kJ/mol H_2.

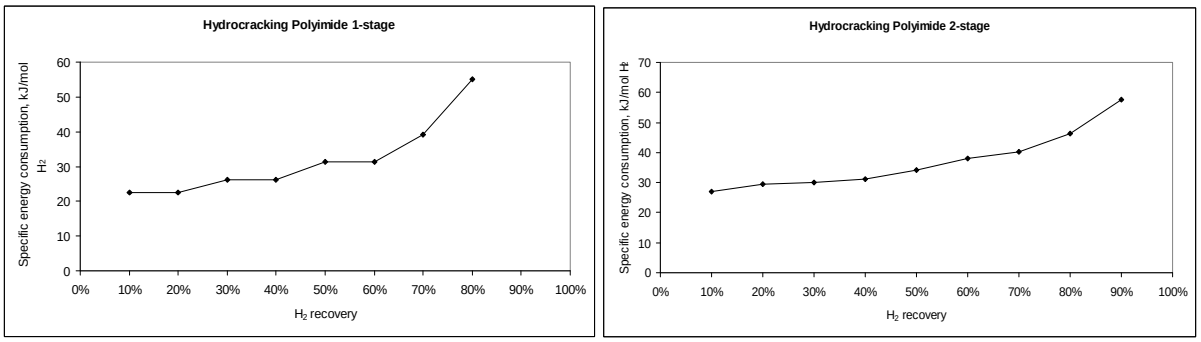

Figure 12-13. Energy consumption per mol H_2 produced in polyimide 1-stage (left) and polyimide 2-stage (right) processes.

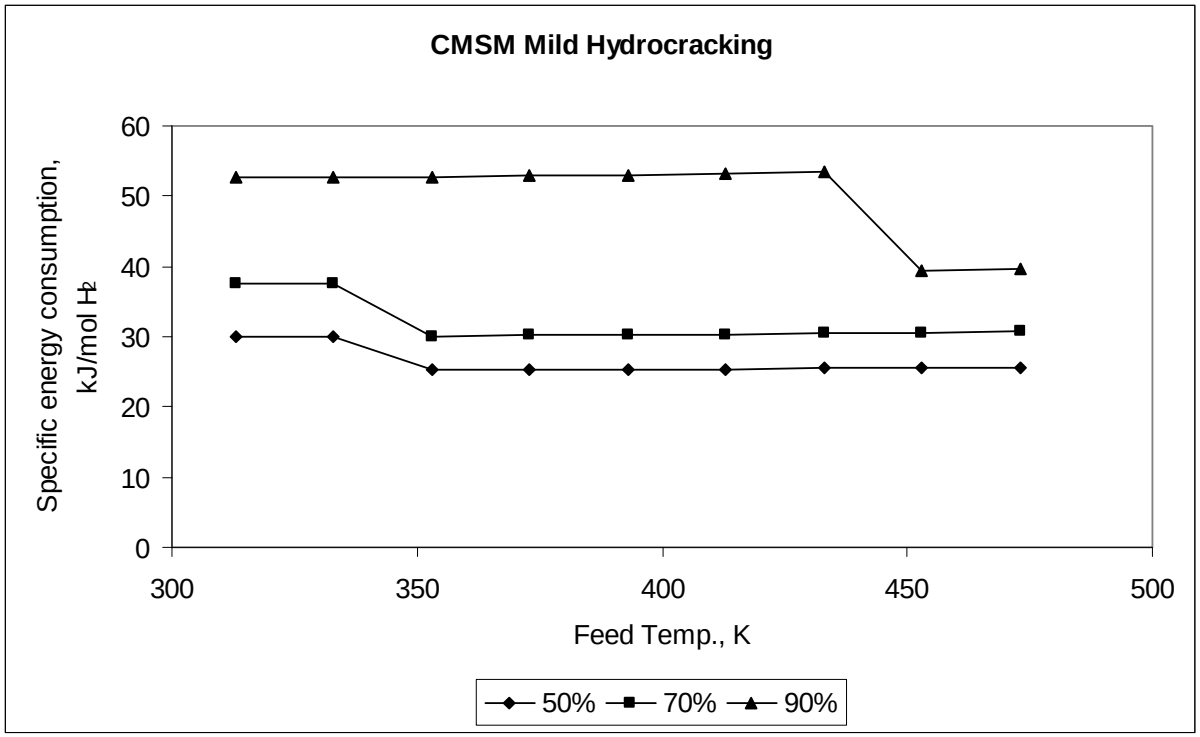

Figure 12-14. Energy consumption per mol H_2 produced in CMSM Hydrocracking process

12.5 Gas oil desulphurization

The off-gas from gas oil desulphurization contains much hydrogen (80 mol%) and is at a moderate pressure (25 bar) and, thus, the membrane processes exhibit behaviour somewhere in between that of the last two cases. The permeate pressure does not vary by much between the assumed module cost cases, implying that the membrane area is not as important as in the Hydrocracking case. Conversely, the separation cost does change with assumed module cost, meaning that the membrane size is not negligible as in the Naphtha case. Required product purity was met easily and hence was rarely a controlling factor in optimisation of the permeate pressure (Figure 12-15 to Figure 12-17).

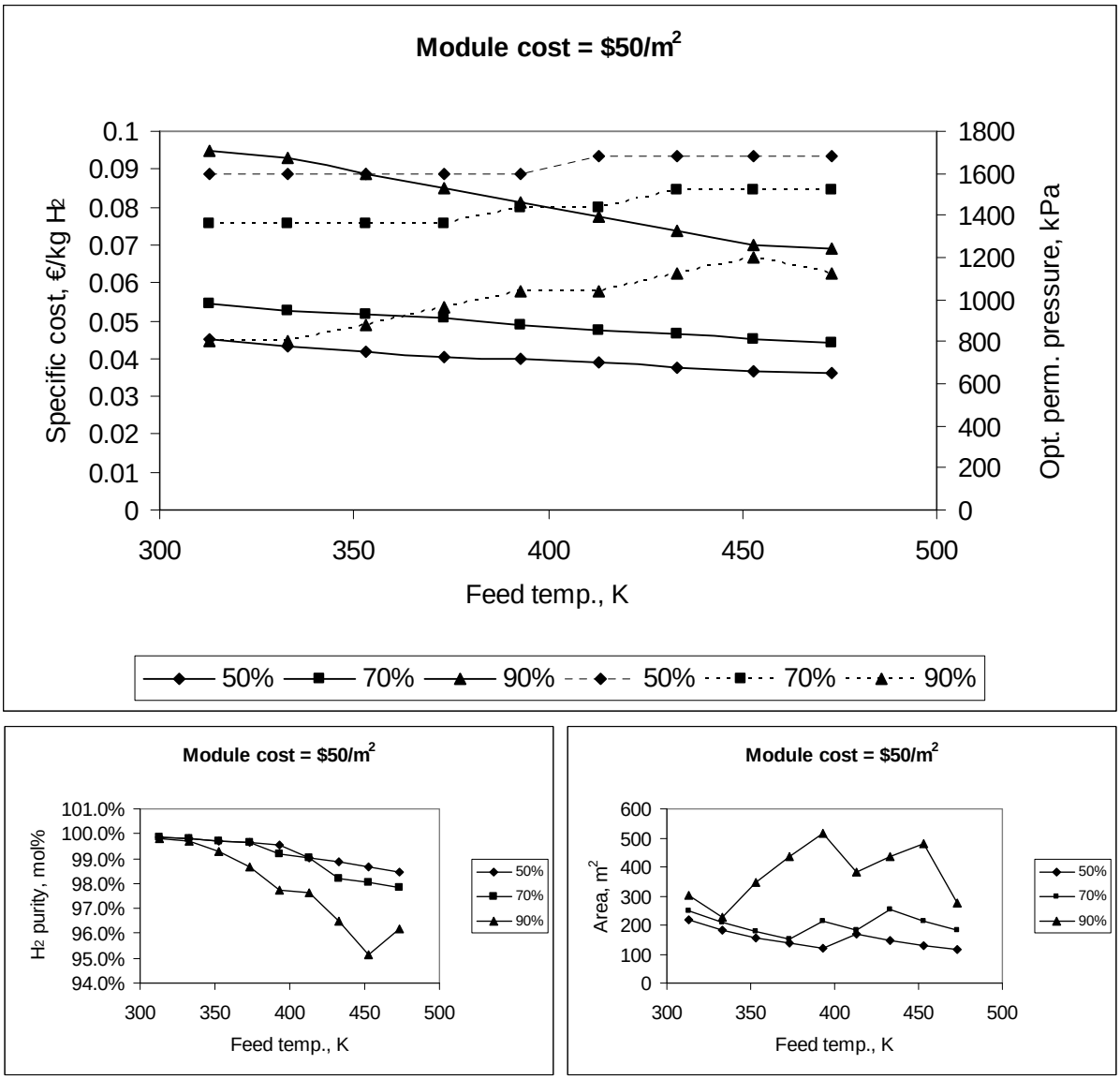

Figure 12-15. Results for the GO desulphurization case, CMSM module cost = $50/m^2. Top: Specific costs (—) and optimum permeate pressure (- - -). H_2 recovery included as a parameter. Purity limit met at 450 K for 90% rec. and permeate pressure forced down for 473 K

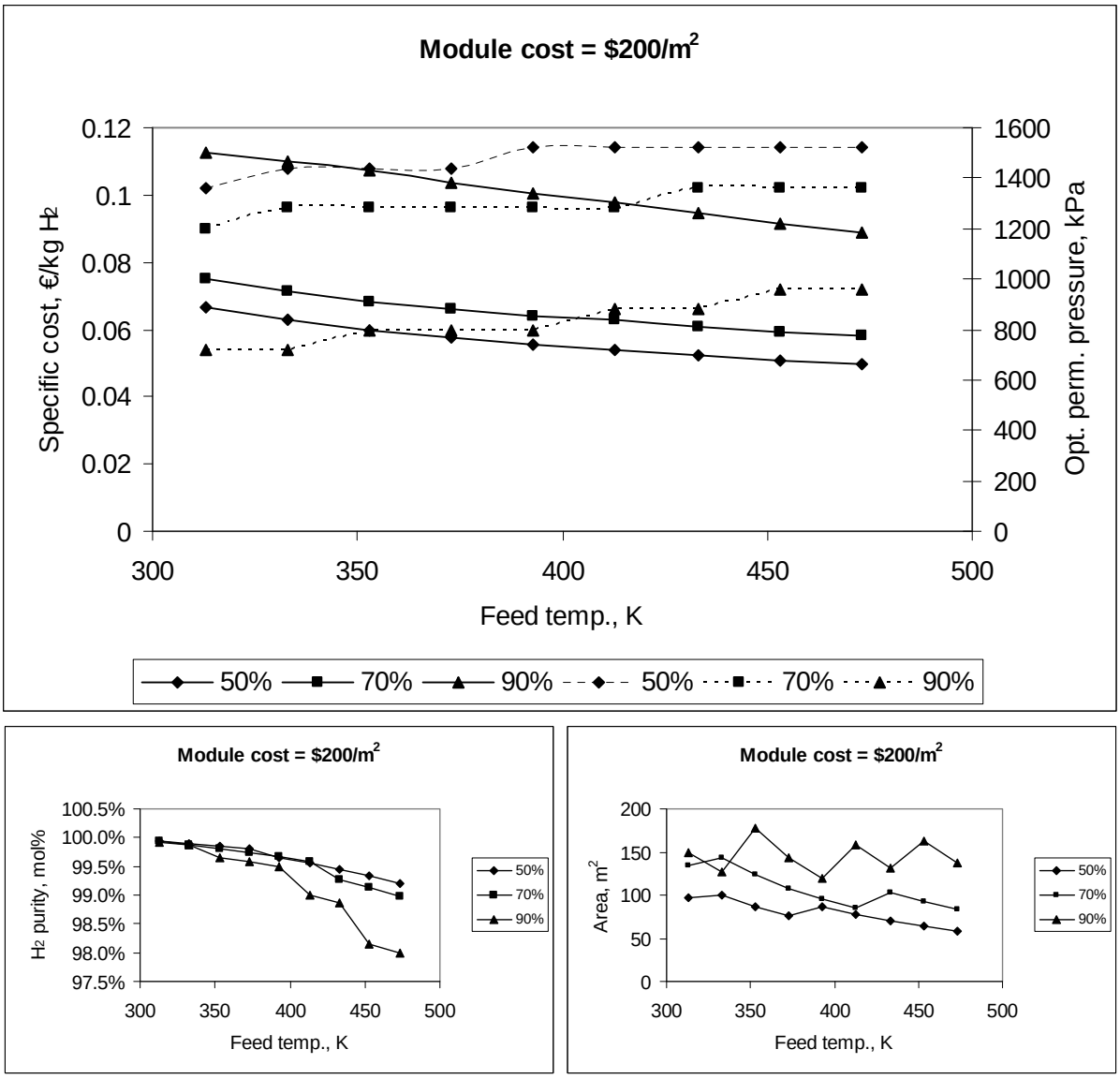

Figure 12-16. Results for the GO desulphurization case, CMSM module cost = $200/m^2. Top: Specific costs (—) and optimum permeate pressure (- - -). H_2 recovery included as a parameter

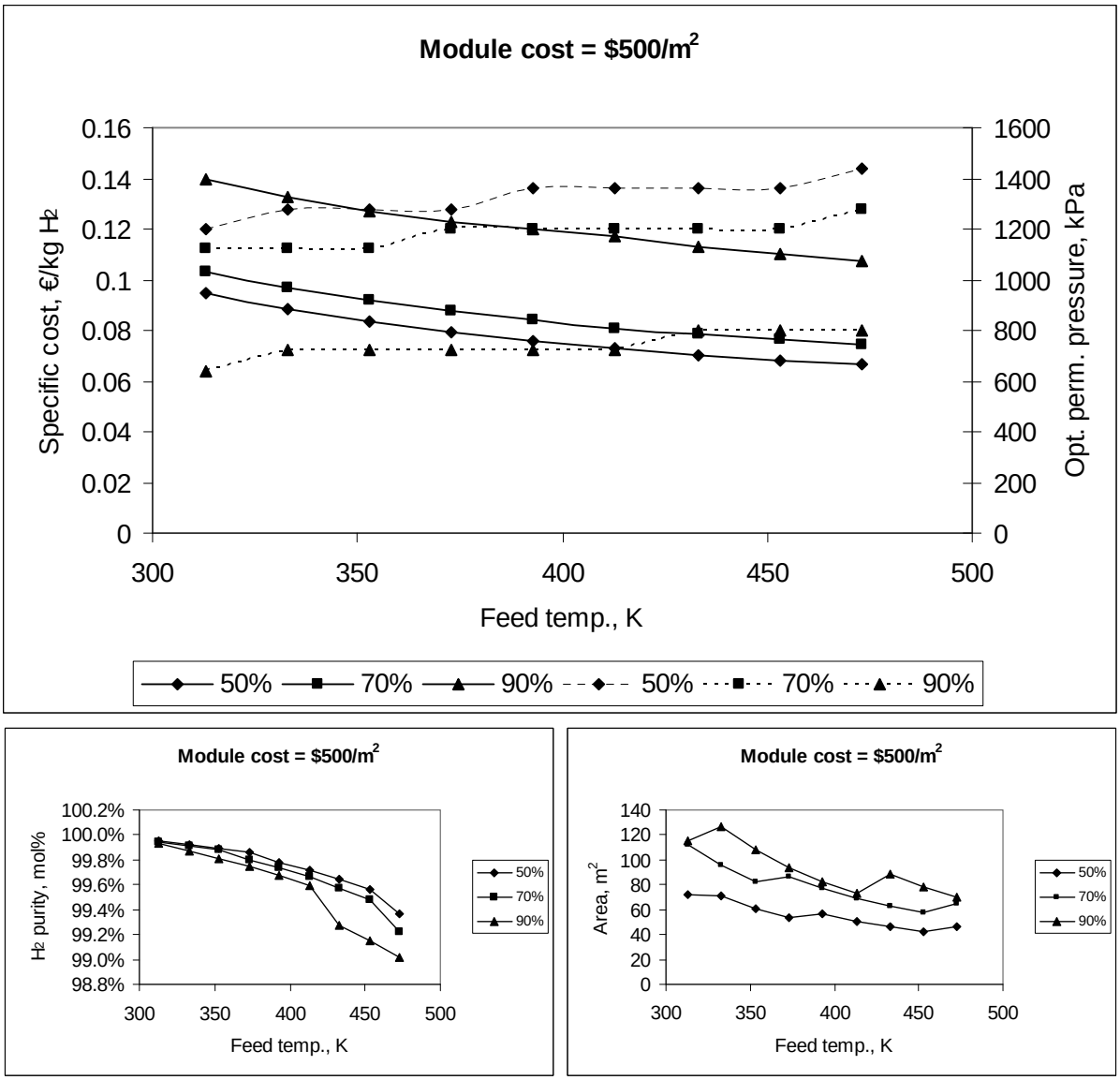

Figure 12-17. Results for the GO desulphurization case, CMSM module cost = $500/m^2. Top: Specific costs (—) and optimum permeate pressure (- - -). H_2 recovery included as a parameter

Polyimide membranes were not evaluated for this case because the feed conditions lie between the previous cases and no new conclusions were expected. The energy consumption in this process (Figure 12-18) was similar to that in the Naphtha case.

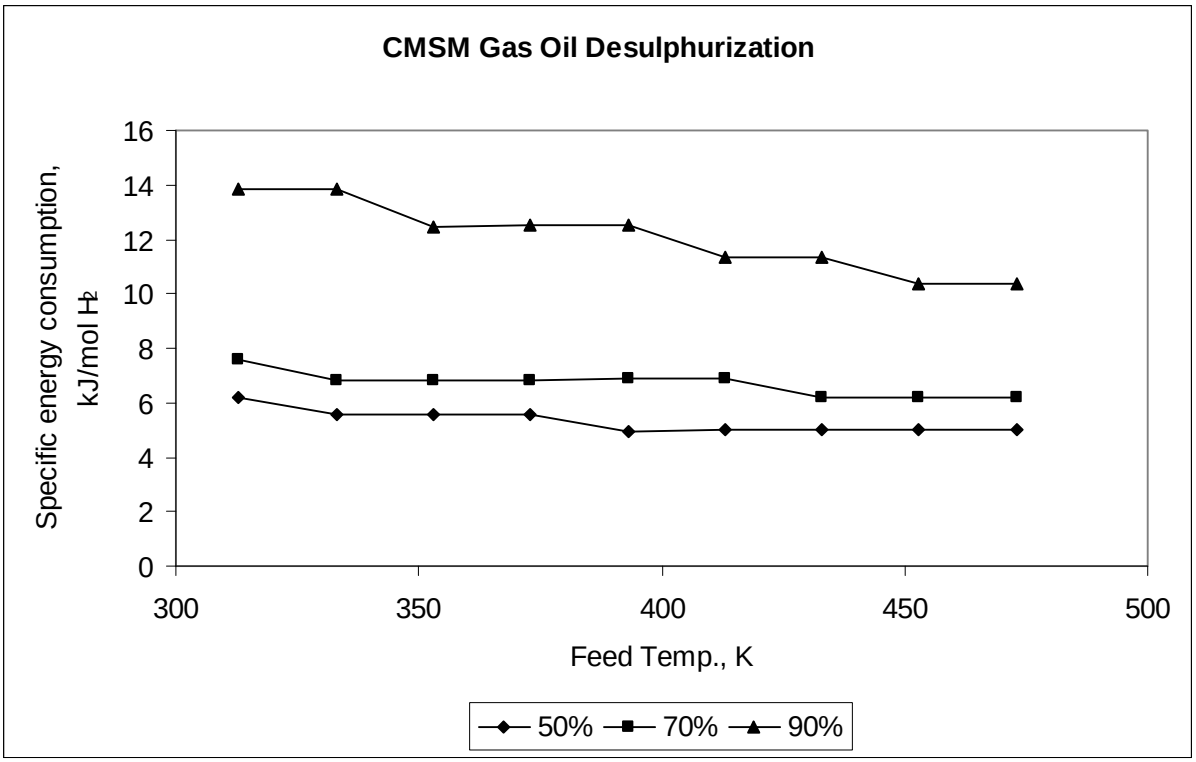

Figure 12-18. Energy consumption per mol H_2 produced in CMSM GO desulphurization process

12.6 Validation of Excel results with Hysys

Error in the Excel model will arise due to the assumption that the higher hydrocarbons have the same permeances as methane ("lumping") and because the model approximates cross-flow rather than counter-current flow. Any such error would be most apparent where the hydrogen driving force is lowest (i.e. the Hydrocracking case) because the relative fluxes of the other components are highest. Thus, the ChemBrane program was run for the CMSM hydrocracking cases over the temperature and recovery range for the module cost of \$200/m^2. ChemBrane was also run for the polyimide 1-stage cases between 50 and 80% recovery. The results are presented in Figure 12-19.

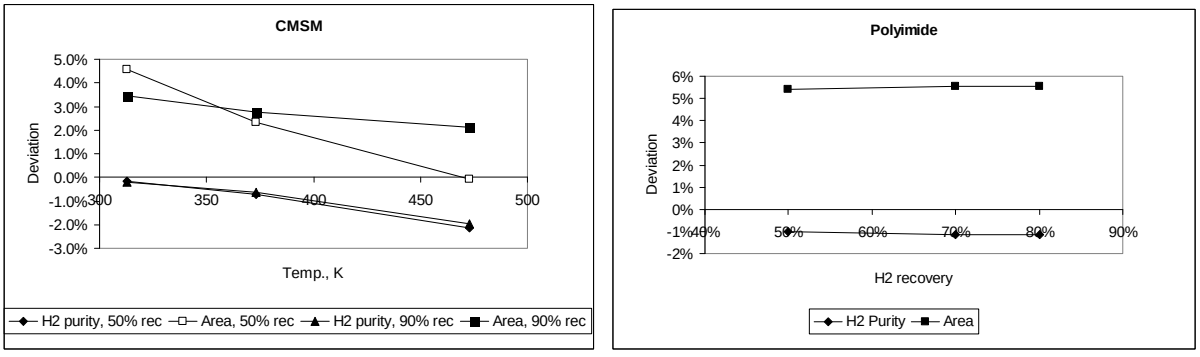

Figure 12-19. Excel model validation with Chembrane. Excel deviations from ChemBrane values

The graphs show the good approximation of the process by the Excel model, with deviations in required membrane area less than 6% for the polyimide process and 5% for the CMSM process. This means that the Excel model over-predicted the membrane area, as expected from the cross-flow model vs. the counter-current. The purity deviation in both cases is 0 to -

2%, meaning that ChemBrane calculated higher purities for the respective permeate pressure, to be expected from counter-current flow and also because the higher hydrocarbons actually permeate less than methane.

12.7 Conclusions

The evaluation shows that a one-stage carbon molecular sieve membrane easily achieves the separation specifications. Generally, this is done at higher permeate pressures than with the polyimide membrane, because the CMSM selectivity is so much higher. Consequently, the energy consumed by the CMSM processes is also lower. Finally, ultra-pure hydrogen can be achieved, particularly at lower operating temperatures.

13 Case 3: H_2 from CO_2 in an IGCC power plant

This study is based on the results of a similar study using a facilitated transport membrane, in which CO_2 is captured in an Integrated Gasification Combined Cycle (IGCC) power plant. The article describing that study is presented in Appendix C. In the most efficient route in the CO_2 capture concept, coal is gasified at 25 bar and 1500°C in a gasifier to produce syngas (Figure 13-1). The syngas is cooled, producing intermediate pressure steam, to 235°C before fly ash is removed by filtration and scrubbing. Steam is then added in a 2:1 H_2O:CO ratio and the stream passed over a sulphur-tolerant shift catalyst, to produce a mixture of mainly CO_2, H_2, H_2O and N_2 (Table 13-1). The H_2S present in the stream is removed by Selexol absorption and the excess water from the shift reaction removed by knockout. CO_2 is removed by the membrane and compressed to pipeline pressure (110 bar). The hydrogen retentate stream is humidified before being mixed with nitrogen in order to lower the combustion temperature in the gas turbine. The turbine exhaust gas, at 1.1 bar(abs) and 539°C, is routed to heat recovery and steam generation (HRSG) which raises and superheats HP steam (126 bar), IP steam (35 bar) and LP steam (6.5 bar). HP and IP steam produced in the gasification island are also superheated in HRSG. The steam is then routed through high, medium and low pressure turbines, before being condensed at 40 kPa and rejoining the water cycle.

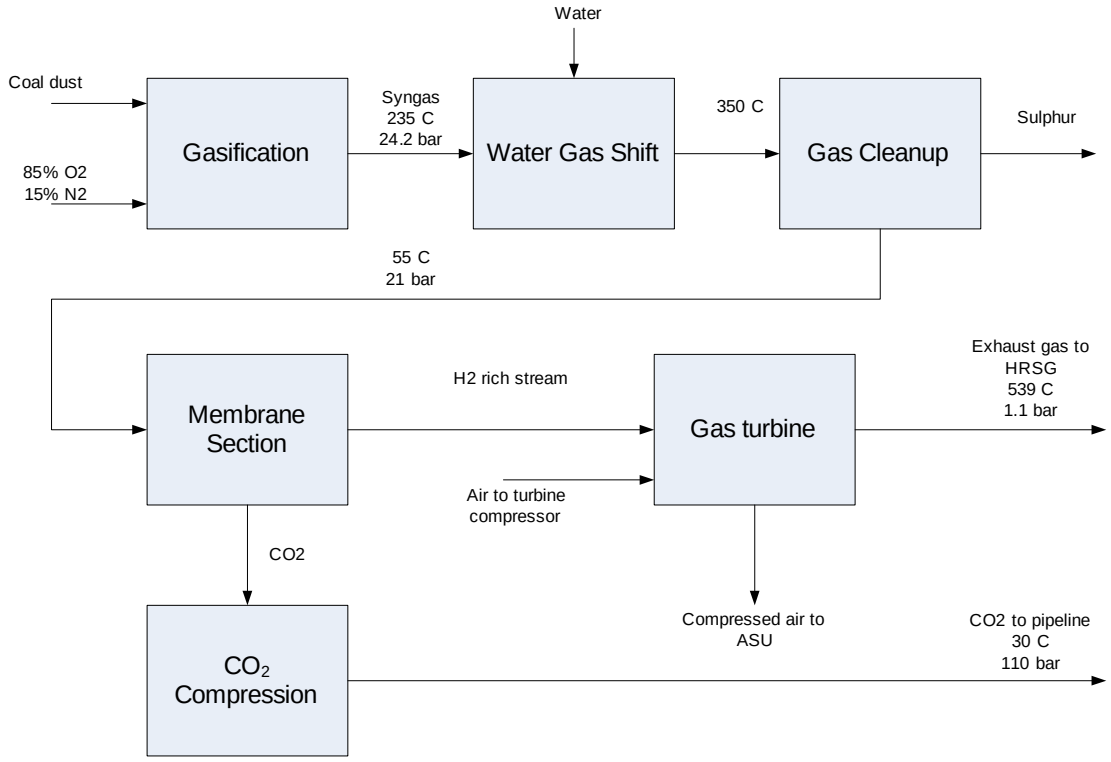

Figure 13-1. Block flow diagram of an IGCC process with CO_2 capture by membrane (ASU = air separation unit)

The facilitated transport membrane is a fixed site carrier (FSC) membrane formed by cross-linking polyvinyl amine (PVAm). This material permeates CO_2 and retains H_2 with both high selectivity (~100) and high fluxes (0.08 m^3(STP)/m^2.bar.h) at 35°C. However, the temperature of the gas stream from CO shift (shown in Table 13-1) is too high for the PVAm membrane and must be reduced to 35°C to achieve the optimum separation performance.

Component	Shifted sour syngas, mol% (dry basis)
CO	2.3
H_2	50.7
N_2 + Ar	7.3
CO_2	39.0
H_2S	0.7
COS	0.0
Temperature, °C	330
Pressure, bar	21

Table 13-1. Feed stream to membrane unit

Thus, although the FSC membrane achieves a sharper separation between CO_2 and H_2 than the carbon molecular sieves, there exist two advantages with CMSMs: 1) they can operate at much higher temperatures and 2) they should tolerate H_2S. H_2S should be retained and can be piped with the CO_2 to storage, eliminating the need for H_2S adsorption.

There exist two alternatives for integration of a carbon molecular sieve membrane. The first is to route the shift product, at 330°C and with the excess steam (which accounts for 30 mol% of the stream), directly through the membrane. This means that the hydrogen permeance would be high because of the high temperature, but has the disadvantages that the hydrogen partial pressure is lower and the water vapour may block the carbon ultramicopores (Jones and Koros, 1995a/b). The higher volume flow will also result in higher pressure drop along the membrane. The second alternative is to knock out most of the water by cooling to 90°C and then feed the 'dry' stream to the membrane. This is at a higher temperature than in the FSC process and still improves the process heat integration. The second alternative was evaluated in this study.

13.1 Design basis and methodology

The feed conditions were introduced in the previous section. The pressure of the feed will be 1 bar higher than the FSC case, however, because the Selexol absorption section is eliminated. Hence, 22 bar is available on the feed side. It was found in the FSC study that the most important variable affecting the total power plant efficiency is the loss of hydrogen to the captured CO_2. The loss needed to be restricted to less than 5% and preferably less than 3% for the technology to be competitive.

Unlike the FSC case, hydrogen is permeated and CO_2 and N_2 retained. This means that the hydrogen must be recompressed to 18 bar (the pressure of the N_2 that is added prior to entering the gas turbine combustor) and the CO_2 compressed from about 22 bar to 110 bar. In the FSC case, the hydrogen can be fed to the gas turbine without further combustion, but the CO_2 must be compressed from about 1 bar to 110 bar.

As with the previous cases, the optimisation study was first performed using the Excel model and the results validated with the ChemBrane. However, unlike in the other cases, the hydrogen purity was not fixed. The design target variables were the recovery of 90-99% of the H_2 and at least 70% of the CO_2. The purity of the H_2 was not directly important because the stream is to be mixed with nitrogen and excess air before the gas turbine, to limit the combustion temperature. Furthermore, by specifying a high H_2 recovery, the CO_2 will be relatively pure (but less so that in the FSC case, because N_2 is retained as well).

13.2 Results and discussion

It was impossible to capture more than 82% of the CO_2 and still recover more than 90% of the hydrogen because the selectivity of the carbon membrane is too low. The permeate pressure was dictated by the separation needs rather than cost and was less than 3 bar over the hydrogen recovery range (90-99%). This means that the membrane cost was less significant than the compression costs and the actual cost of the membrane (cost/m^2) had little impact on the overall separation costs. The separation cost (€/kg H_2 recovered) is shown in Figure 13-2. The actual cost of the separation is also less important than in the cases in Sections 11 and 12 because the membrane unit is a small part of the IGCC plant. Any loss of hydrogen in the membrane section represents the 'loss' of an equivalent percentage of the preceding plant, which costs many times more than the membrane unit. It is better to have a more expensive separation section and utilise the entire plant capital more effectively. Having stated that, however, the spreadsheet model still seeks the lowest cost for the given recovery of hydrogen, given the constraints.

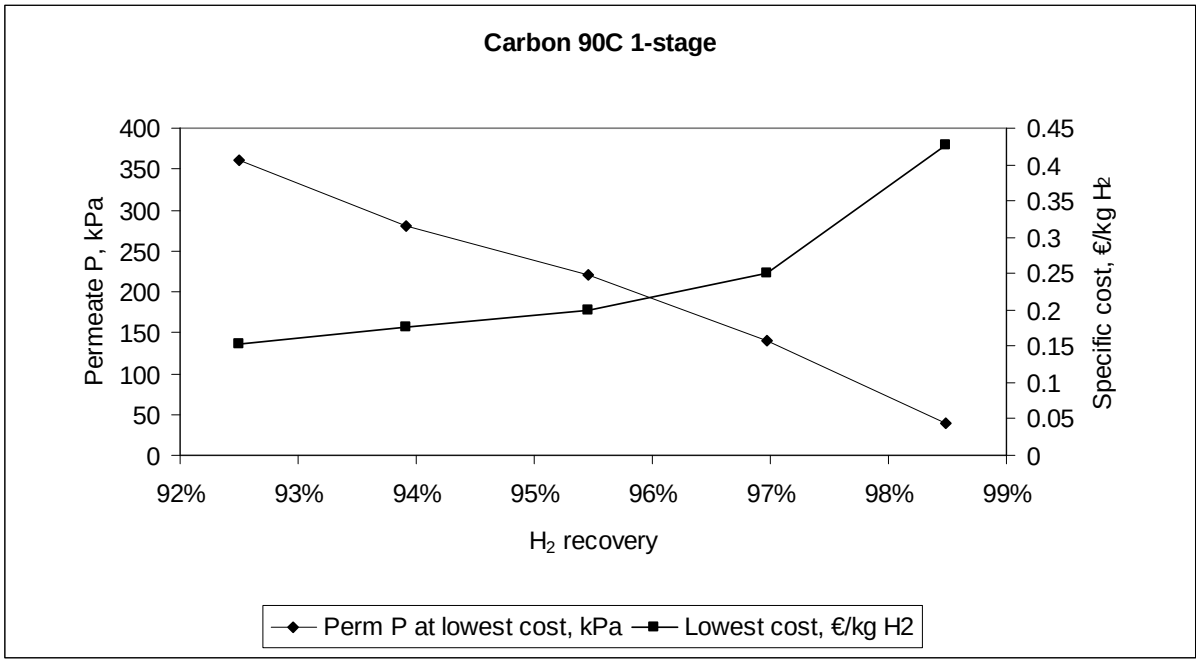

Figure 13-2. Specific separation cost at optimum recovery (Membrane cost= \$200/m^2, 70% CO_2 capture)

The separation cost increases as hydrogen recovery increases, unsurprisingly, because the recompression cost increases. The area decreased a little as the recovery increased, however, because the effect of the greater driving force at lower permeate pressure overwhelmed the usual inverse relationship between area and recovery (Figure 13-3). Because the amount of CO_2 captured is approximately constant and the hydrogen recovery increases, the CO_2 purity increases proportionally.

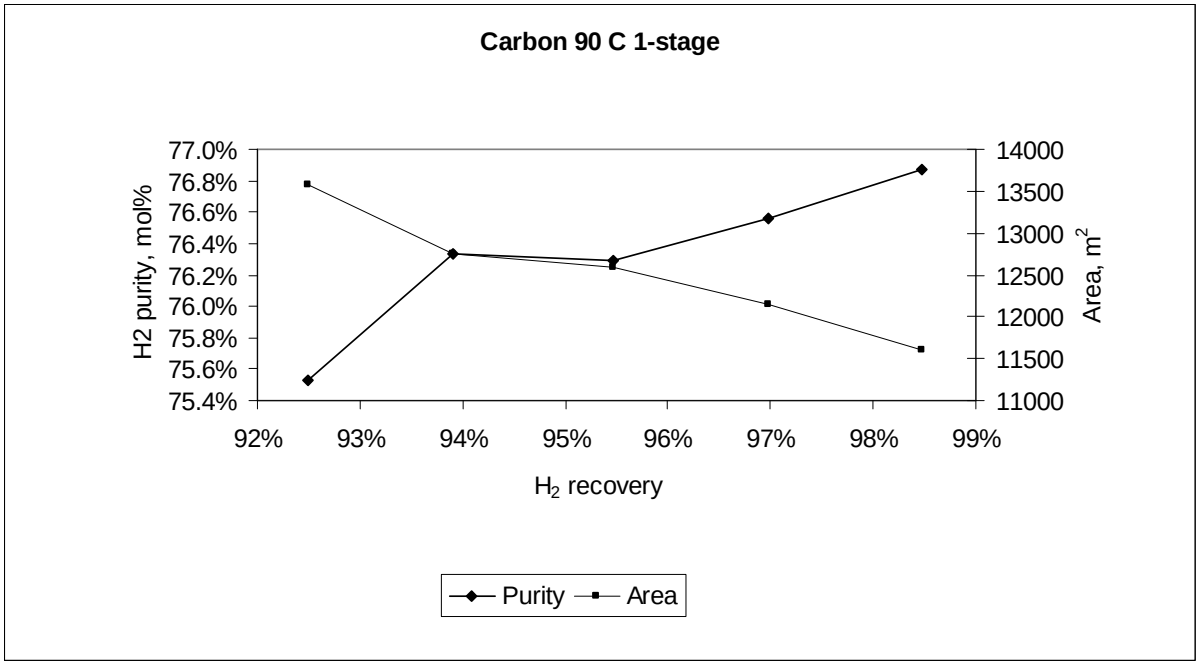

Figure 13-3. Area and hydrogen purity (Membrane = $200/m^2, 70% CO_2 capture)

The corresponding CO_2 recovery and purity is shown in Figure 13-4, for 70% capture of CO_2.

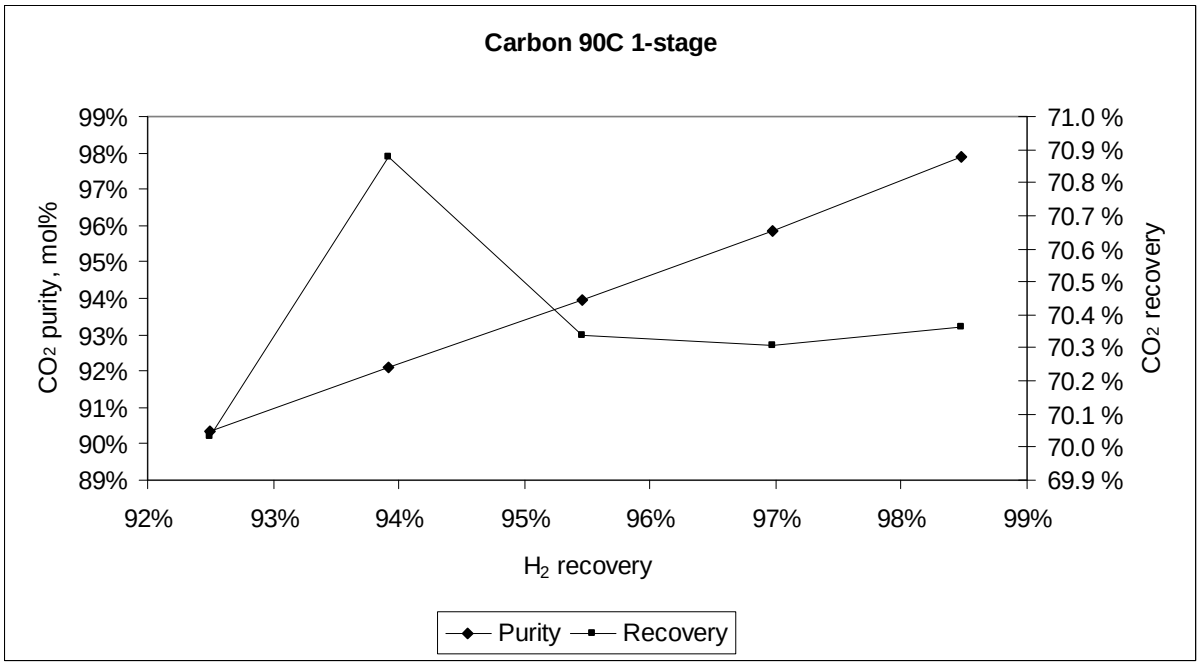

Figure 13-4. CO_2 product

A critical value is the energy consumed per mole of hydrogen produced in the separation unit because this affects the overall efficiency of the power plant. The consumption shown in Figure 13-5 includes the compression of hydrogen to 18 bar and CO_2 from 22 bar to 110 bar.

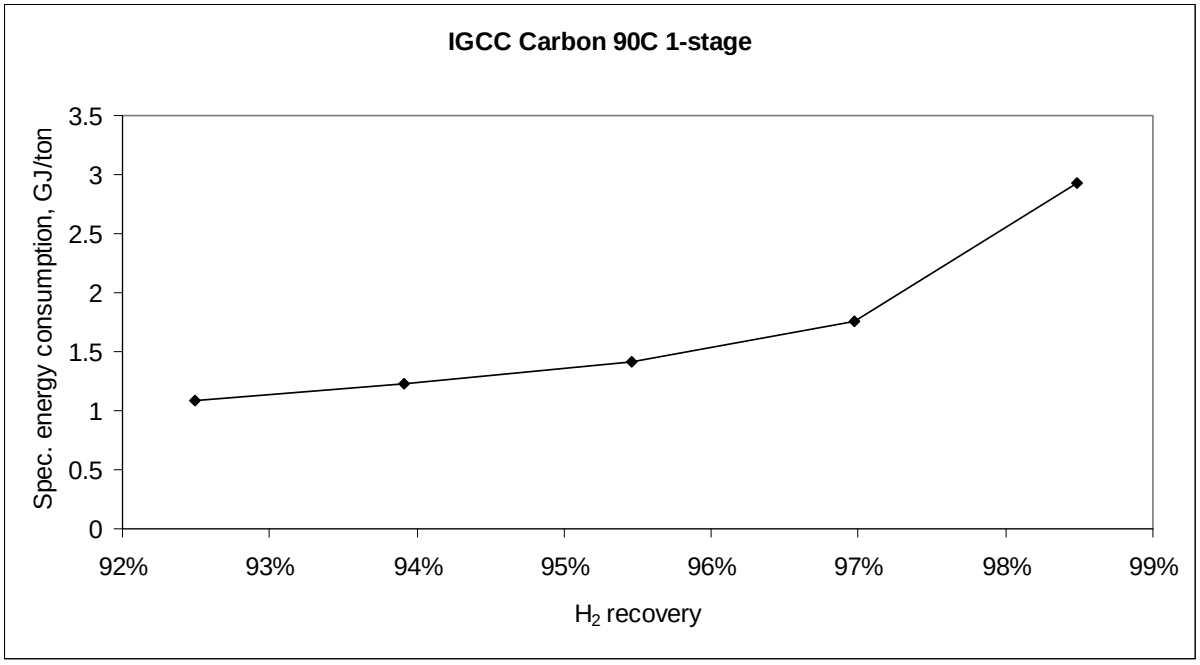

Figure 13-5. Specific energy consumption at 70% CO_2 recovery, equivalent to thermal units per ton of CO_2 capured. Membrane cost = \$200/m^2

13.3 Validation of Excel results with Hysys

The Hysys results, using a counter-current membrane model and actual feed composition, were close to the Excel results. The Hysys module was able to obtain higher CO_2 recovery with approximately 5% less membrane area, at the given H_2 recovery and permeate pressure.

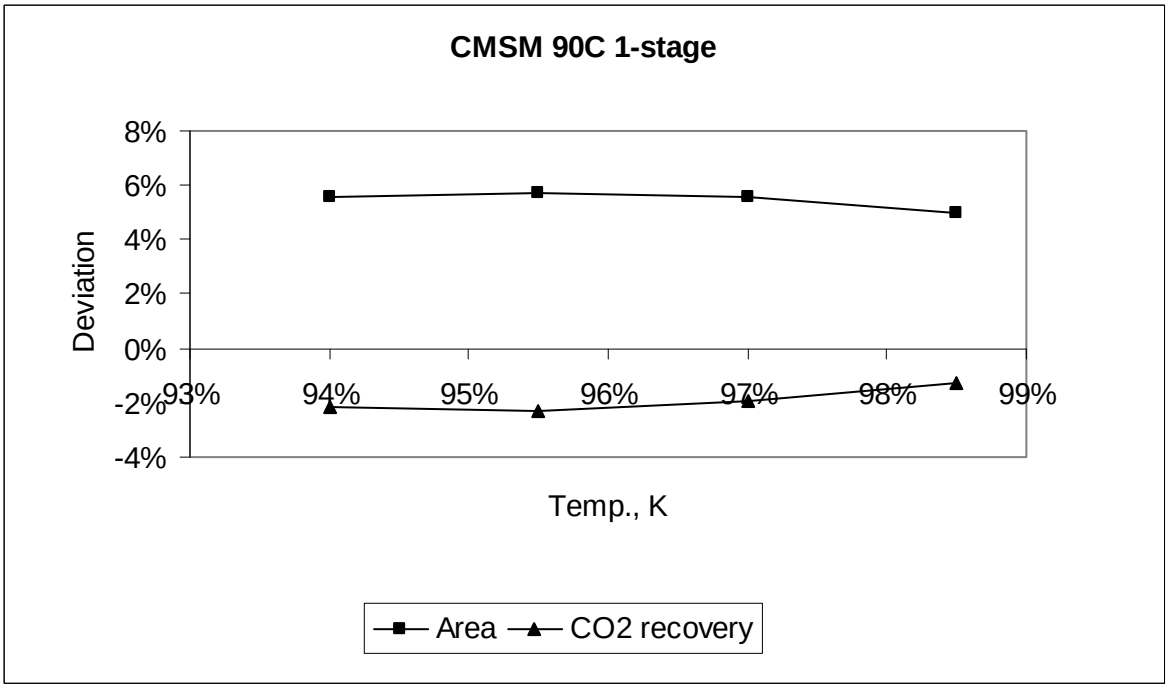

Figure 13-6. Deviation of Excel results from Hysys results

Because of the energy loss associated with the low permeate pressure and the low sensitivity of the separation cost to membrane price, it was decided to increase the 'optimum' permeate pressure in the Hysys simulation until approximately 70% CO_2 recovery was achieved. The new optimum values are shown in Table 13-2.

Table 13-2. Process parameters for Hysys CMSM process

H_2 recovery, %	94	95.5	97	98.5
Permeate press., kPa	350	270	180	60
Mem. area, m^2	13500	12880	12280	11430
CO_2 recovery, %	70.1	70.1	70.0	70.3

The composition of the retentate stream is given in Table 13-3 for the case where 98.5% of the hydrogen is recovered in the permeate stream. The purity of the CO_2 is lower than for the equivalent recovery with an FSC membrane (>95%) because the nitrogen and other impurities are retained with the CO_2, whereas they are retained with the H_2 in the FSC case. The lower purity of the CO_2 means that more impurities have to be compressed to 110 bar for storage and the pipeline must handle larger volumes. Of major importance is the high percentage of CO in the CO_2 stream. Due to the toxicity of CO, it may be necessary to send the stream through a combustor. Furthermore, this CO retention represents a significant loss of chemical energy in the power plant and strengthens the argument for including a low temperature shift (LTS) step to maximise the conversion of CO to H_2 and CO_2. It is important to state here that the above issues are common to all H_2 permeation membranes, also highly selective ones such as palladium membranes.

Table 13-3. CO_2 product composition for 98.5% hydrogen recovery

Component	**Mole %**
CO_2	68.0
N_2	17.6
CO	4.5
H_2S	1.8
H_2	2.0
H_2O	6.1

The modified process is shown in Figure 13-7.

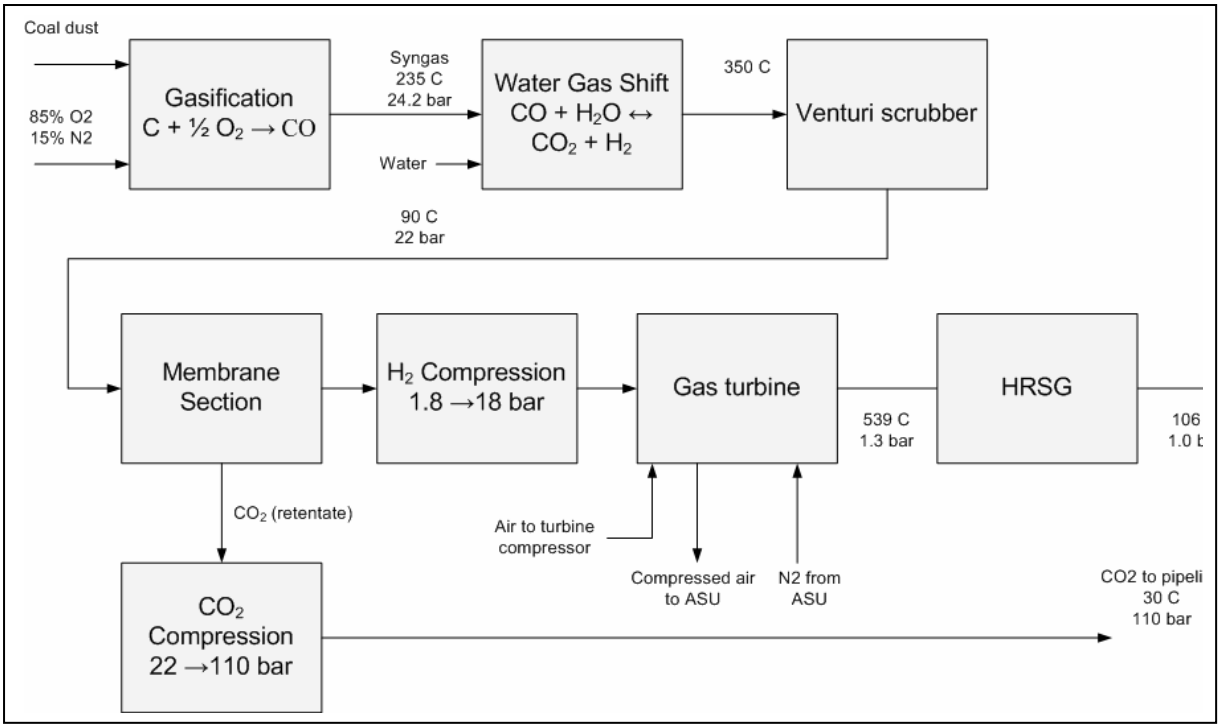

Figure 13-7. IGCC process with CO_2 capture by CMSM

13.4 Heat integration

A second challenge to hydrogen-permeating membranes involves heat integration. The effluent from the water-gas-shift reactors contains approximately 30 mol% H_2O at 330°C. The energy contained in this stream is recovered by first exchanging with the hydrogen permeate to heat it to about 250°C and then exchanging with condensate to produce steam for the steam turbines. In the FSC case, the stream is cooled to 35°C in the process of raising steam (Figure 13-8). The water in the process stream is condensed in this step and knocked out in the venturi scrubber.

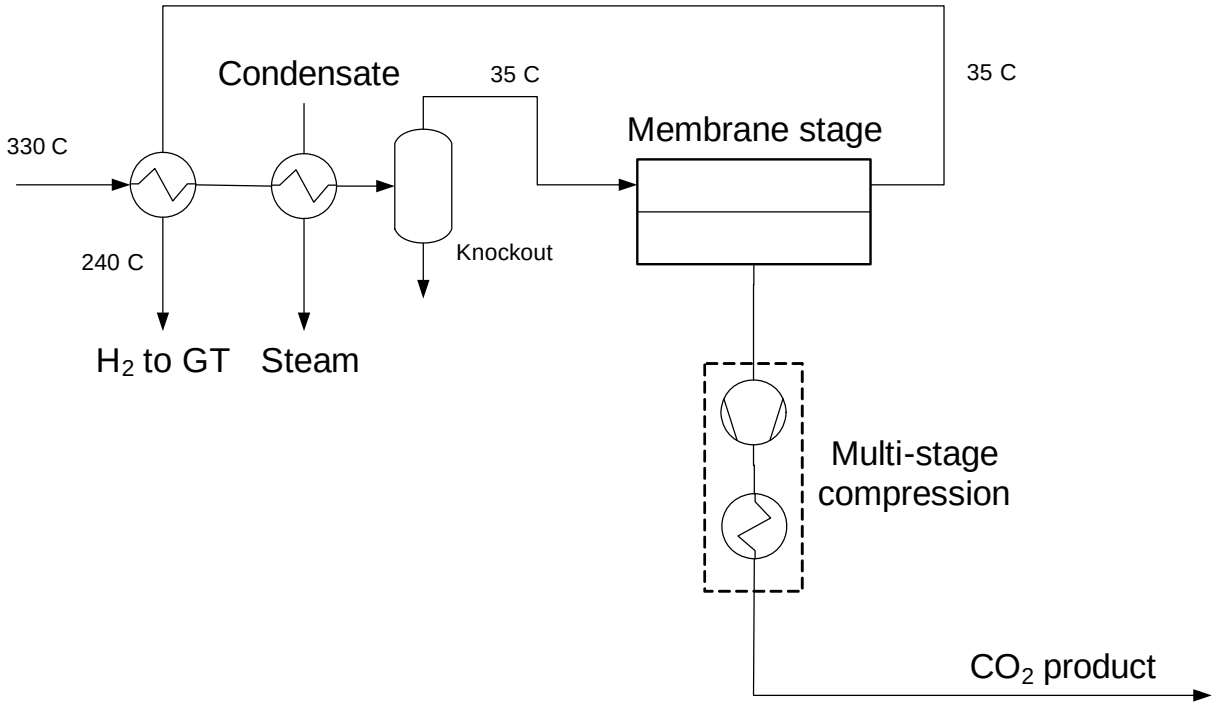

Figure 13-8. Heat integration scheme around CO_2-selective FSC membrane

In the CMSM case, the process stream is only cooled to 90°C before the venturi scrubber and membrane. However, the H_2 permeate compression proceeds through a number of stages with inter-cooling because the outlet temperature is typically limited to 150°C (Brannan (2005), pg 133). To minimise the number of stages and increase the compression efficiency of the first stage, it is beneficial to cool the permeate and retentate to 30°C directly after the membrane (Figure 13-9). In the case of the CO_2 product, first cooling the stream to 30°C allows the pipeline pressure of 110 bar to be achieved in one stage. From a heat integration perspective, this creates some challenges. If the permeate and retentate are cooled to 30°C, then the process then resembles the heat integration around the FSC membrane, with the final cooling step from 90°C to 30°C simply removed to after the membrane. Although this allows higher permeances due to the higher operating temperature, the process becomes more complicated because more cooling steps are involved. The energy transferred in the interstage coolers is also low value energy for steam production because the process stream is at 150°C. The stream from the final compression stage, at 150°C, is exchanged with the 330°C from CO shift.

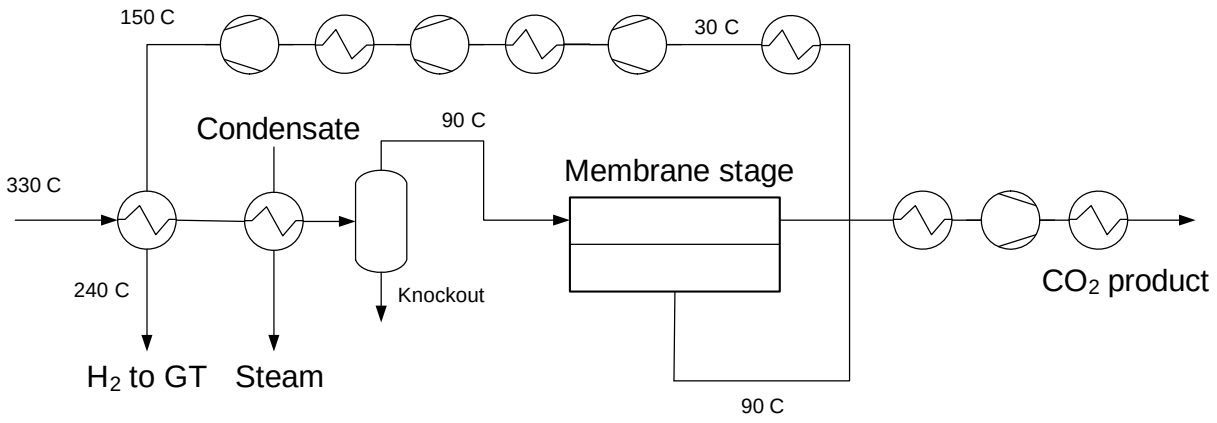

Figure 13-9. Heat integration scheme around H_2-selective membrane

In the case of high temperature (330°C) membrane operation, the permeate and retentate are certainly too hot for the compressors and must be cooled. Thus, the condensation of the water vapour in the process stream occurs after the membrane unit and so there is no heat integration benefit to using a high temperature membrane. A common criticism of polymeric membranes is that they are not suited to high temperature processes (Bredesen et al., 2004), but it is difficult to imagine a process without cooling to ambient temperature because of the compressors.

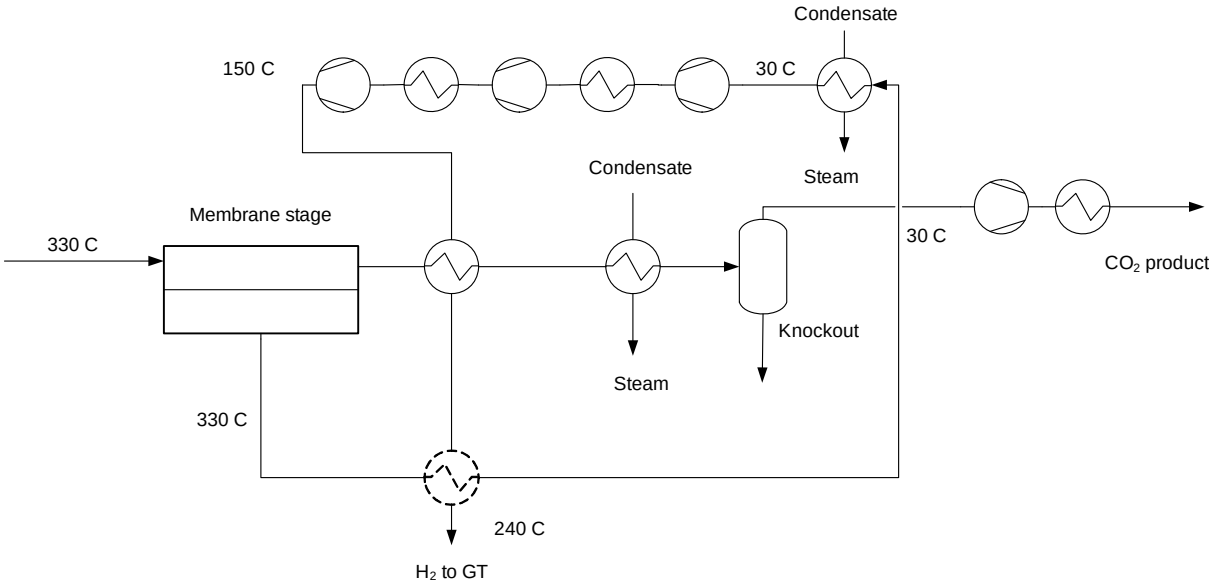

Figure 13-10. Heat integration scheme around high temperature H_2-selective membrane

The process performance of the CMSM case, compared with the base case without capture and the FSC process, is shown in Table 13-4. It was observed that the energy available for the steam turbines in the 98.5 % CMSM case was higher than in the FSC case, but that the energy available for the gas turbine was lower. The high compression costs for the CMSM cases make them uncompetitive.

Table 13-4. CMSM process performance (all membrane cases capture 70% of CO_2)

	Base case, no capture	CMSM, 98.5% H_2 recovery	CMSM, 97% H_2 recovery	FSC, 98.3% H_2 recovery
Thermal input, MW (LHV)	**668**	**668**	**668**	**668**
Gas Turbines, MWe	182	149	146	159
Steam Turbines, MWe	133	123	113	118
Gross power output, MWe	315	272	259	276
Auxiliary Electrical consumption, MWe	35	35	35	35
CO2 compression, MWe	0	60	28	16
NET power output	280	177	196	225
Equivalent shift consumption, MWe	0	28	28	28
Equivalent separation consumption, MWe	0	15	27	11
Gross efficiency (LHV)	**47.2%**	**40.7%**	**38.8%**	**41.3%**
Net efficiency (LHV)	**41.9%**	**26.5%**	**29.4%**	**33.7%**
CO2 purity	**-**	**68%**	**68%**	**97%**

13.5 Conclusions

Hydrogen-permeating membranes are faced with challenges in heat integration and in producing high purity carbon dioxide. Neither of these is a killer issue, as CMSM processes can clearly be developed that capture carbon dioxide and recover most of the hydrogen fuel. However, the CO_2 compression duties will always be higher than in the FSC process because the accompanying nitrogen must be compressed too. This also increases the CO_2 pipeline size because more gas must be transported. This challenge is faced by all hydrogen selective membranes, especially the highly selective ones such as palladium-based membranes.

The second challenge is that the hydrogen must be recompressed as well. This is a particular issue with the carbon molecular sieve, because the H_2/CO_2 permselectivity ratio at 90°C is only about 13 and so the permeate pressure must be low to achieve good separation. The conclusion is that the CMSM membrane cannot compete with the FSC membrane for CO_2 capture in IGCCs.

14 Overall conclusions

The membrane material provides the potential for a competitive technology in hydrogen recovery from natural gas distribution networks and from refinery off-gases. The goals in future development should be to realise this potential by fulfilling or bettering the assumptions made at the outset of the study – that is:

- Hollow-fibres of diameter 165 microns and wall thickness 16 microns can be manufactured in commercial quantities.
- That the dense layer responsible for mass transfer is approximately 1 micron thick (or less).
- That they can withstand pressure differences (feed to permeate) of at least 8 bar and preferably 40 bar.
- That they can be manufactured for less than $\$500/m^2$

Thus, the research effort in this field should be focussed on the practical issues of manufacturing modules and dealing with aging, as opposed to material development.

15 References

Avraham A and Dagan G. A method for potting or casting inorganic hollow fiber membranes into tube sheets. European patent EP 0 938 921 A1, 1999

Barsema JN, Balster J, Jordan V, van der Vegt NFA and Wessling M. Functionalised carbon molecular sieve membranes containing Ag-nanoclusters. J Mem Sci 219:47-57, 2003

Barton TJ, Bull LM, Klemperer WG, Loy DA, McEnaney B, Misono M et al. Tailored porous materials. Chem Mater 11: 2633-2656, 1999

Bradbury AGW and Shafizadeh F. Chemisorption of oxygen on cellulose char. Carbon 18:109-116, 1980

Bradbury AGW, Sakai Y and Shafizadeh F. A kinetic model for pyrolysis of cellulose. J Appl Polym Sci 23: 3271-3280, 1979

Brannan C. Rules of thumb for chemical engineers. 4th Ed. Elsevier Inc., 2005

Breck DW. Zeolite molecular sieves - Structure, chemistry and use. John Wiley and sons. New York, 1975

Bredesen R, Jordal K and Bolland O. High-temperature membranes in power generation with CO_2 capture. Chem Eng and Proc 43:1129-1158, 2004

Burggraaf AJ. Single gas permeation of thin Zeolite (MFI) membranes: theory and analysis of experimental observations. J Mem Sci 155:45-65, 1999

Burggraaf AJ and Cot L. Transport and separation properties of membranes with gases and vapours. In: Fundamentals of inorganic membrane science and technology. Elsevier Science, BV, 1996

Byrne JF and Marsh H. Introductory Overview, in Porosity in carbons; characterisation and applications. Ed. Patrick JW. Arnold, London, 1995

Centeno TA and Fuertes AB. Influence of separation temperature on the performance of adsorption-selective carbon membranes. Carbon 41:2016-2019, 2002

Coker DT, Freeman BD and Fleming GK. Modeling multicomponent gas separation using hollow fiber membrane contactors. Aiche J 44:1289, 1998

Dubinin MM. Water vapour sorption and the microporous structures of carbonaceous adsorbents. Carbon 18:355-364, 1980

Fan LT, Gharpuray MM and Lee YH. Cellulose hydrolysis. Springer Verlag, Heidelberg, 1987

Fick A. Pogg. Ann. 94, 59, 1885

Franklin RE. The interpretation of diffuse X-ray diagrams of carbon. Acta Crystallogr 3:107-121, 1950

Franklin RE. The structure of graphitic carbons. Acta Crystallogr 4:252-261, 1951

Geankoplis CJ. Transport processes and separation process principles. 4th Ed., Prentice Hall PTR, 2003

Geiszler VC and Koros WJ. Effects of polyimide pyrolysis conditions on carbon molecular sieve membrane properties. Ind Eng Chem Res 35:2999-3003, 1996

Gilron A and Soffer J. Knudsen diffusion in microporous carbon membranes with molecular sieving character. J Mem Sci, 209:339-352, 2002

Goodhew PJ, Humphreys J and Beanland R. Electron microscopy and analysis. 3rd Ed. Taylor and Francis, London, 2001

Groszek AJ, Avraham I, Danon A and Koresh JE. Interaction of O_2, N_2 and He at room temperature with carbon molecular sieves sensed by adsorption measurements. Colloids and Surfaces A: Physicochemical and Engineering Aspects 208:65–70, 2002

Hägg MB, Lie JA and Lindbråthen A. Carbon molecular sieve membranes. A promising alternative for selected industrial applications. Ann NY Acad Sci 984:329-345, 2003

Hallale N, Moore I and Vauk D. Hydrogen: Liability or asset? Chemical Eng Progress September 2002

Ho and Sirkar, Membrane Handbook. Springer, 1992 pg. 434

IUPAC Compendium of Chemical Terminology, Electronic version, http://goldbook.iupac.org/S05704.html

Jagtoyen M and Derbyshire F. Activated carbons from yellow poplar and white oak by H_3PO_4 activation. Carbon 36:1085-1097, 1998

Jones CW and Koros WJ. Carbon composite membranes: A solution to adverse humidity effects. Ind. Eng. Chem. Res. 34:164-167, 1995a

Jones CW and Koros WJ. Characterisation of ultramicroporous carbon membranes with humidified feeds. Ind. Eng. Chem. Res. 34:158-163, 1995b

Jones CW and Koros WJ. Carbon molecular sieve gas separation membranes – 1. Preparation and characterization based on polyimide precursors. Carbon. 32:1419-1425, 1994a

Jones CW and Koros WJ. Carbon molecular sieve gas separation membranes – 2. Regeneration following organic exposure. Carbon. 32:1427-1432, 1994b

Kaldis SP, Kapantaidakis GC and Sakellaropoulos GP. Simulation of multicomponent gas separation in a hollow fiber membrane by orthogonal collocation – hydrogen recovery from refinery gases. J Mem Sci 173:61-71, 2000

Kawamoto H, Murayama M and Saka S. Pyrolysis behavior of levoglucosan as an intermediate in cellulose pyrolysis: polymerization into polysaccharide as a key reaction to carbonized product formation. J wood Sci 49:469-473, 2003

Klemm D, Heublein B, Fink HP and Bohn A. Cellulose: Fascinating biopolymer and sustainable raw material. Angew Chem Int Ed 44:3358-3393, 2005

Koresh JE. On the flexibility of the carbon skeleton. J Chem Soc Faraday Trans 89:935-937, 1993

Koresh JE and Soffer A. Study of molecular sieve carbons. Part 1.- Pore structure, gradual pore opening and mechanism of molecular sieving. J Chem Soc Faraday Trans, 76:2457-2571, 1980

Koresh JE and Soffer A. Molecular sieve carbon permselective membrane. Part 1. Presentation of a new device for gas mixture separation. Sep Sci Techn 18:723-734, 1983

Koresh JE and Soffer A. Mechanism of permeation through molecular sieve carbon membrane. Part 1.- The effect of adsorption and the dependence on pressure. J Chem Soc Faraday Trans 82:2057-2063, 1986

Koresh JE and Soffer A. The carbon molecular sieve membranes. General properties and the permeability of CH_4/H_2 mixture. Sep Sci Techn 22:973-982, 1987

Koresh JE, Kim TH, Walker DRB and Koros WJ. Study of ultramicroporous carbons by high-pressure sorption. Part 5. –Isotherm and diffusion kinetics. J Chem Soc Faraday Trans, 86:2267-2270, 1990

Koros WJ and Mahajan R. Pushing the limits on possibilities for large-scale gas separation: which strategies? J Mem Sci 175:181-196, 2000

Lagorsse S, Campo MC, Magalhaes FD and Mendes A. Water adsorption on carbon molecular sieve membranes: Experimental data and isotherm model. Carbon 43:2769-2779, 2005a

Lagorsse S, Leite A, Magalhaes FD, Bischofberger FD, Rathenow J and Mendes A. Novel carbon molecular sieve honeycomb membrane module: configuration and membrane characterisation. Carbon 43:809-819, 2005b

Lewis IC and Singer LS. Electronic spin resonance and the mechanism of carbonization. In: Chemistry and physics of carbon. Vol 17. Eds Thrower PA, Walker PL. Marcel Dekker New York, pp 1-88, 1981

Lie JA. Synthesis, performance and regeneration of carbon membranes for biogas upgrading – a future energy carrier. Doctoral thesis at NTNU 2005:152, 2005

Lie JA and Hägg, M-B. Carbon membranes from cellulose and metal loaded cellulose. Carbon, 43:2600-2607, 2005

Lie JA and Hägg MB. Carbon membranes from cellulose: Synthesis, performance and regeneration. J Membrane Sci 284:79-86, 2006

Loeb S and Sourirajan S. Sea water demineralisation by means of an osmotic membrane. Saline Water Conversion-II, Advances in Chemistry Series no. 28, American Chemical Society, 1963

L'vov B. Kinetics and mechanism of thermal decomposition of silver oxide. Thermochimica Acta 333:13-19, 1999

Marsh H and Wynne-Jones WFK. Surface properties of carbon: I. The effect of activated diffusion in the determination of surface area. Carbon 1:269-279, 1964

Marsh H and Rodriguez-Reinoso. Activated carbon. Elsevier, 2006

Menendez I and Fuertes AB. Aging of carbon membranes under different environments. Carbon 39:733-744, 2001

Morrison IM and Stewart D. Plant cell wall fragments released on solubilisation in trifluoracetic acid. Phytochemistry 49:1555-1563, 1998

Mulder M. Basic principles of membrane technology. 2nd Ed. 1997

Murray KK, Boyd RK, Eberlin MN et al. Standard definitions of terms relating to mass spectrometry (IUPAC Recommendations 2006). IUPAC, 2006

Oak Ridge National Laboratory, Press Release: Carbon fiber cars could put U.S. on highway to efficiency. March 6, 2006.
http://www.ornl.gov/info/press_releases/get_press_release.cfm?ReleaseNumber=mr20060306-00

Pacalowska B, Whysall M and Narasimhan MV. Improve hydrogen recovery from refinery off-gases. Hydrocarbon Processing Nov. 1996

Perry RH and Green D. Perry's chemical engineers' handbook. 6th Ed. Mc.Graw-Hill, 1984

Peters MS and Timmerhaus KD. Plant design and economics for chemical engineers, 5th Ed. Mc.Graw-Hill, 2003

Pikulik A and Diaz HE. Cost estimating for major process equipment. Chem Eng 84:106-122, 1977

Rao MB and Sircar S. Nanoporous carbon membrane for gas separation. Gas Sep and Purification 7:279-284, 1993

Rao MB and Sircar S. Performance and pore characterisation of nanoporous carbon membranes for gas separation. J Mem Sci 110:109-118, 1996

Robeson LM. Correlation of separation factor versus permeability for polymeric membranes. J Mem Sci 62:165-185, 1991

Robeson LM, Burgoyne WF, Langsam M, Savoca AC and Tien CF. High performance polymers for membrane separation. Polymer 35:4970-4978, 1994

Rodrıguez-Reinoso F and Molina-Sabio M. Textural and chemical characterization microporous carbons. Adv Colloid & Interface Sci 76-77:271-294, 1998

Rodrıguez-Chong A, Ramirez JA, Garrote G and Vazquez M. Hydrolysis of sugar cane bagasse using nitric acid: a kinetic assessment. J Food Eng 61:143-152, 2004

Rouquerol F, Rouquerol J and Sing K. Adsorption by powders and porous solids. Academic Press, San Diego, 1999

Rouquerol J, Avnir D, Fairbridge CW, Everett DH, Haynes JH, Pernicone N et al. Recommendations for the characterisation of porous solids. Pure & Appl Chem 66:1739-1758, 1994

San Marchi C, Somerday BP and Robinson SL. Permeability, solubility and diffusivity of hydrogen isotopes in stainless steels at high gas pressures. Int J Hydrogen Energy 32:100-116, 2007

Sanborn Scott D. Fossil sources: Running out is not the problem. Int J Hydrogen Energy 30:1-7, 2005

Sauder C, Lamon J and Pailler R. The tensile behavior of carbon fibers at high temperatures up to 2400°C. Carbon 42:715-725, 2004

Saufi SM and Ismail AF. Fabrication of carbon membranes for gas separation – a review. Carbon 42:241-259, 2004

Sedigh MG, Onstot WJ, Xu L, Wildon LP, Tsotsis TT and Sahimi M. Experiments and simulation of transport and separation of gas mixtures in carbon molecular sieve membranes. J. Phys. Chem. A 102:8580-8589, 1998

Shafizadeh F, Furneaux RH, Cochran TG, Scholl JP and Sakai Y. Production of levoglucosan and glucose from pyrolysis of cellulosic materials. J Appl Polym Sci 23: 3525-3539, 1979a

Shafizadeh F and Lai YZ. Thermal Degradation of 1,6-Anhydro-β-D-glucopyranose. J Org Chem 37:278-284, 1972

Shafizadeh F and Sekiguchi Y. Development of aromaticity in cellulosic chars. Carbon 21:511-516, 1983

Shafizadeh F and Sekiguchi Y. Formation and structure of cellulosic chars. Abstr Pap Am Chem S 185:38-CELL, 1983b

Silverstein MS, Najary Y, Grader GS and Shter, GE. Complex formation and degradation in Poly(Acrylonitrile-co-Vinyl Acetate) containing copper nitrate. J of Polymer Science: Part B: Polymer Physics, 42:1023-1032, 2004

Singh A and Koros WJ. Significance of entropic selectivity for advanced gas separation membranes. Ind Eng Chem Res 35:1231-1234, 1996

Sircar S, Waldron We, Rao MB and Anand M. Hydrogen production by hybrid SMR-PSA-SSF membrane system. Sep and Purification Technol 17:11-20, 1999

Skoog DA, West DM and Holler FJ. Fundamentals of analytical chemistry. 7th Ed. Saunders College Publishing, 1996

Smith JM and Van Ness HC. Introduction to chemical engineering thermodynamics. 4th Ed. McGraw-Hill, 1987

Soffer A, Gilron J, Saguee S, Hed-Ofek R and Cohen H. Process for the production of hollow carbon fiber membranes. United States patent 5,925,591. 1999

Soffer A, Saguee S, Golub D, Cohen H and Azariah M. Selective clogging of failed fibres. United States patent 5,575,963. 1996

Speight JG and èOzèum B. Petroleum refining processes. Online edition, Marcel Dekker, c2002

Steel KM and Koros WJ. Investigation of porosity of carbon materials and related effects on gas separation properties. Carbon 41:253-266, 2003

Steel KM and Koros WJ. An investigation of the effects of pyrolysis parameters on gas separation properties of carbon materials. Carbon 43:1843-1856, 2005

Suda H and Haraya S. Carbon Molecular Sieve Membranes: Preparation, characterization and gas permeation properties. American Chemical Society Symposium Series, 2000

Tanihara N, Shimazaki H, Hirayama Y, Nakanishi S, Yoshinaga T and Kusuki Y. Gas permeation properties of asymmetric carbon hollow fiber membranes prepared from asymmetric polyimide hollow fiber. J Mem Sci 160:179-186, 1999

Verma SK and Walker PL. Carbon molecular sieves with stable hydrophobic surfaces. Carbon 30:837-844, 1992

Veziroglu TN. Editorial: IJHE grows with hydrogen economy. Int J Hydrogen Energy 32:1-2, 2007

Vieira-Linhares AM and Seaton NA. Pore network connectivity effects on gas separation in a microporous carbon membrane. Chem Eng Sci 58:5251-5256, 2003

Wankat PC. Large-Scale Adsorption and Chromatography. CRC Press, 1986

Wise J. The truth about hydrogen. Popular Mechanics, November 2006

Appendix A: Permeation rig temperature calibration

A heating jacket is used to raise and maintain temperatures in the permeation cell. The heating jacket thermocouple is situated in the jacket and measures, at best, the skin temperature of the permeation cell. The internal temperature had to be calibrated against the heating jacket set point temperature. Furthermore, the permeation cell represents a thermal mass that will take time to change from one temperature interval to another after the set point has been changed and this time needed to be quantified.

A Fluke K-Type 80-PK1 thermocouple (accurate to ±1.1°C) was connected to the retentate outlet port on the top of the cell, such that the thermocouple tip was near to the membrane (see Figure). The thermocouple was connected to a TES 1305 thermometer. The feed side was then charged with CO_2 while the permeate side was under vacuum, to mimic a permeation test.

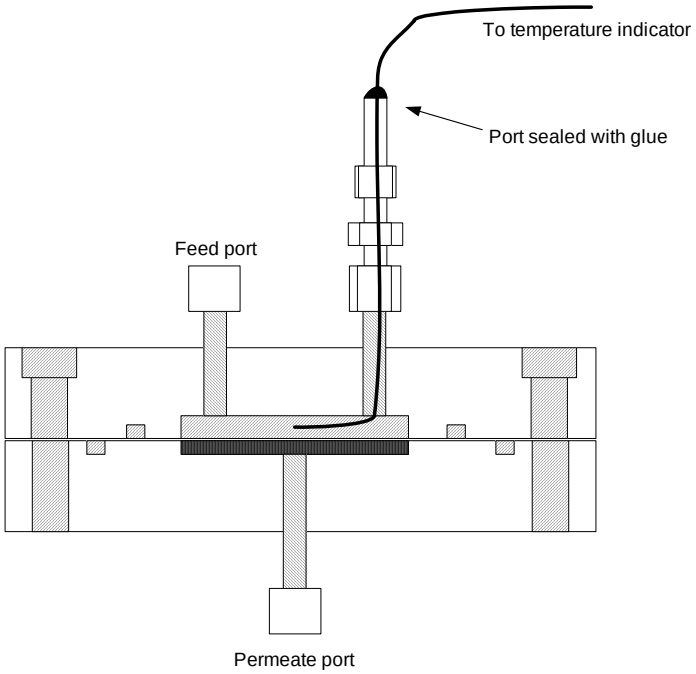

Figure 1. Thermocouple arrangement in permeation cell for internal temperature calibration

The set point was raised in intervals and the internal temperature recorded. It was observed that the steady state internal temperature was proportionally less than the jacket set point temperature. A calibration curve was obtained and is shown in Figure 2. This curve was found to be independent of the gas type present in the cell and jacket re-arrangement.

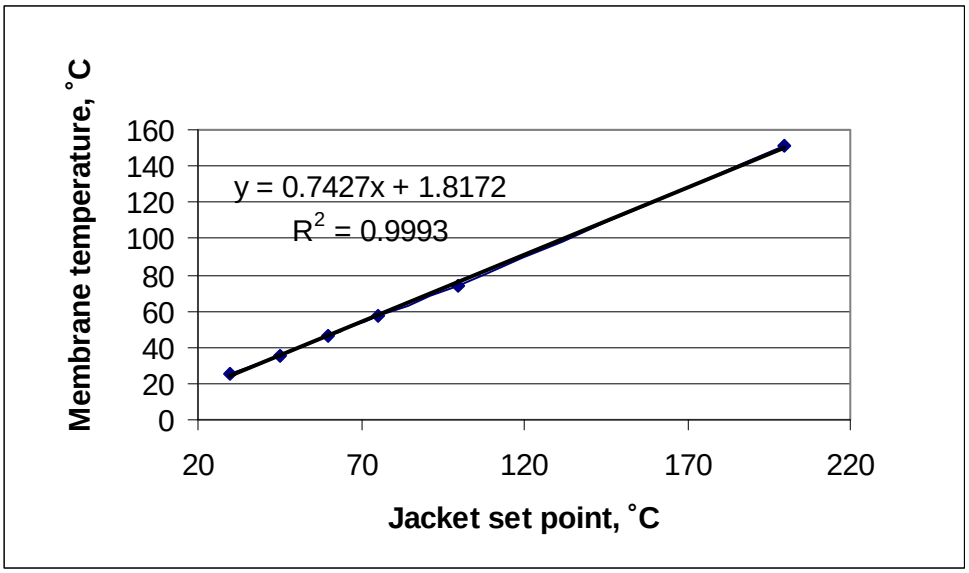

Figure 2. Calibration curve for internal (membrane) temperature

The lag time taken for the internal temperature to reach steady state was never seen to be more than 500 minutes, irrespective of the set point increase. An example is shown in Figure 3.

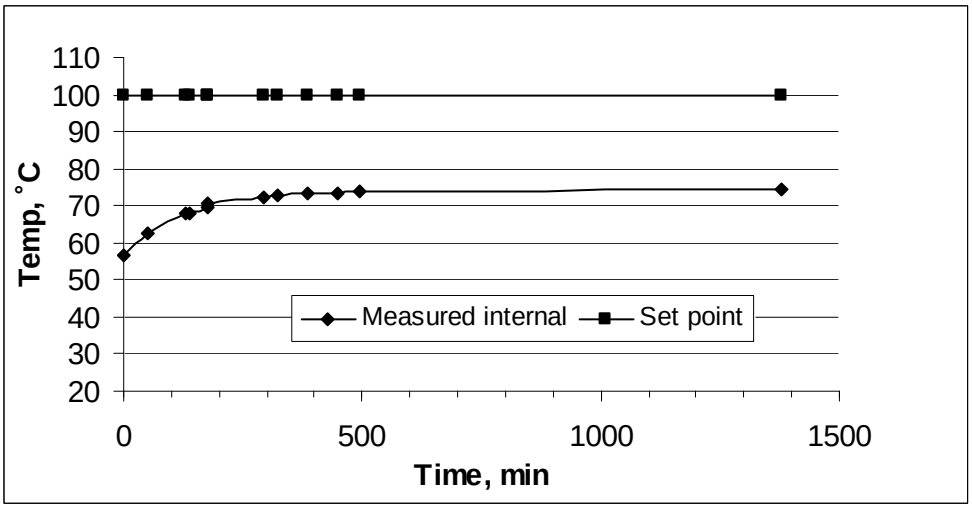

Figure 3. Curve showing time taken for internal temperature to stabilise when set point was changed from 75 to 100°C

Appendix B: Membrane model

A simple method for solving mixed-permeate and counter-current membrane models with multi-component feeds

1 Abstract

A novel method to solve counter-counter membrane models with multicomponent feeds is presented. The method makes use of a ‘start-up’ algorithm, in which the non-linear membrane model is first solved with a permeate pressure of zero, representing full vacuum. This decouples the system of differential equations and allows a permeate composition profile to be generated without an initial guess. The permeate pressure is then increased by an increment and the previous permeate composition profile used in the current iteration. This procedure is repeated until the steady-state permeate pressure is reached. The method was validated against the data from two published sources and found to produce similar results. The method does not require an initial estimate like most numerical methods and is easy to understand for the user, but can fail to converge at low feed pressure/permeate pressure ratios.

2 Introduction

As membranes for gas separation become more common in industry, so the need grows for accurate membrane models that can easily be integrated into commercial simulation packages. Because plant simulations often contain complicated flowsheets and may involve the iteration of material loops, the time taken for a membrane model to solve is an important parameter. Increasing the challenge is the large number of components found in many simulations, which increase the solution duration and can decrease algorithm stability.

A representation of membrane module configurations is shown in Figure 1-1. The permeate may flow in the same direction as the feed (a), be perfectly mixed (b), which is often used to represent cross-flow modules in gas separation (Mulder, 1997), or flow in the opposite direction to the feed (c). In practice, gas flow deviates to various extents from these ideals due to the geometry of the module, but these simple configurations will be adopted in this paper in order to introduce the proposed method of solving the molar balances.

a)

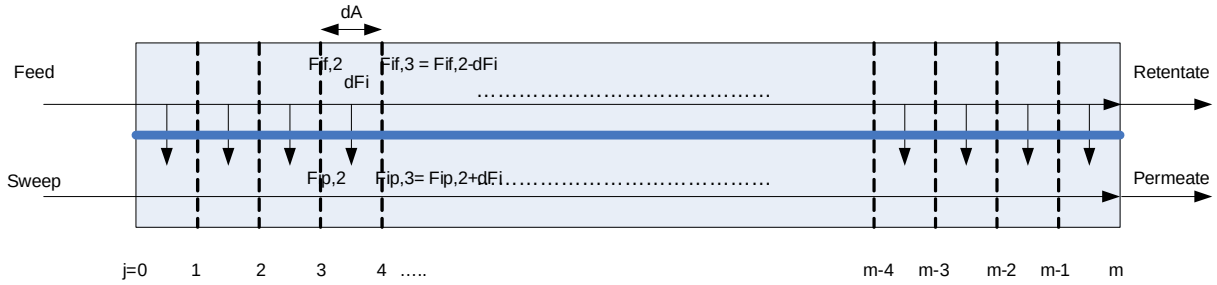

b)

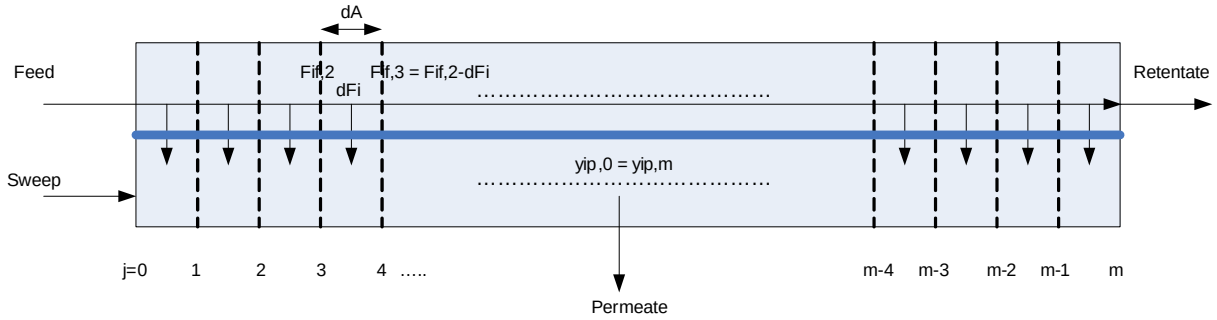

c)

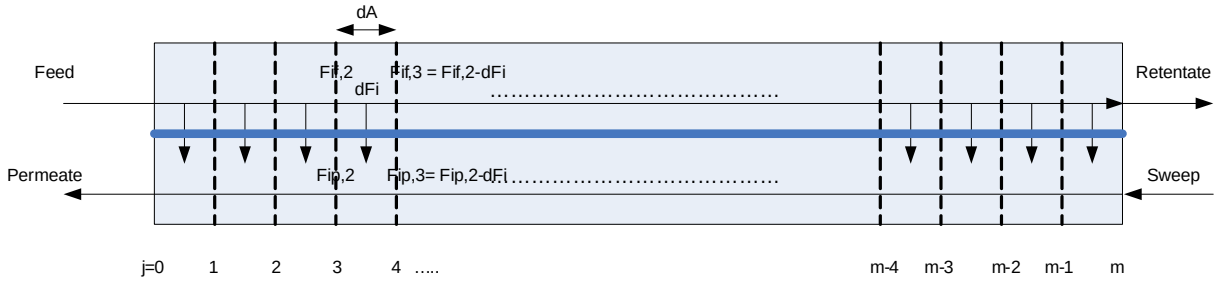

Figure 1-1. a) Co-current, b) mixed-permeate and c) counter-current

The membrane is divided into m equal area, perfectly mixed stages. Assuming a dense, symmetric membrane, the mole flux for the each component, i, on the feed side is given by:

$$dF_{if} = P_i.(P_h.y_{if} - P_l.y_{ip}).dA \quad \textbf{(53)}$$

where F_{if} is the molar flow of i in the feed, P_i is the permeance for i, P_h is the feed side pressure, P_l is the permeate pressure, y_{if} is the molar fraction of i in the feed side increment, y_{ip} is the molar fraction of i in the permeate side increment and A is the membrane area.

The simplest configuration to solve is co-current (a) because the inlet conditions are known for both feed and permeate, at the same point in the model. Assuming plug-flow on either side, the mole fraction of a component, i, in an increment, j, is

$$y_{ip,j} = \frac{F_{if,j}}{\sum F_{kf,j}} \quad \textbf{(54)}$$

where $\sum F_{kf,j}$ is the sum over all components in the feed side increment. Similarly for the molar fraction in permeate side increment:

$$y_{ip,j} = \frac{F_{ip,j}}{\sum F_{kp,j}} \qquad \textbf{(55)}$$

The permeate balance is:

$$dF_{ip,j} = -dF_{if,j} \qquad \textbf{(56)}$$

where $F_{ip,j}$ is the molar flow of i in the permeate. Thus, the model exists as a system of coupled non-linear differential equations. A fourth order Runga-Kutta algorithm, for example could be used to integrate the differential equations and obtain the final retentate. Components that are fed to the permeate side (i.e. sweep gases) participate in the system of equations and can also diffuse to the feed side if given a non-zero permeance.

A mixed-permeate configuration, with plug-flow on the feed side, is more complex to solve than the co-current because of the coupling of the permeate and feed molar fractions along the entire length of the membrane. In this case, the permeate concentration of a component is equal at all points and is calculated by:

$$y_{ip} = \frac{F_{ip,m}}{\sum F_{kp,m}} \qquad \textbf{(57)}$$

which is the composition of the outlet permeate. An initial estimate for the permeate composition and then iteration over this composition is required to solve for the final permeate fractions.

The counter-current configuration is even more complicated to solve, because a concentration profile exists on the permeate side and the permeate exit flows at j=0 are unknown. An initial estimate for the concentration profile is needed to solve the set of non-linear differential equations. Since the permeate and feed flows are in opposite directions:

$$dF_{if,j} = dF_{ip,j} \qquad \textbf{(58)}$$

The counter-current configuration provides the greatest separation efficiency and least membrane area, thus the need for a working model is greatest. Several algorithms to solve the counter-current model with multi-component feeds have been published in literature (Pettersen and Lien (1994), Coker et al. (1998), Thundyil and Koros (1997), Tessendorf et al. (1999) and Kaldis et al. (2000)). Good reviews of methods for solving the counter-current configuration are also provided by Kovvali et al. (1992) and Cruz et al. (2005). Most involve numerical methods, such as Newton-Raphson or successive substitution, to deal with the two-point value boundary problem presented by models and many are sensitive to the quality of the initial estimate of the permeate composition profile. Coker et al (1998) developed a robust model by dividing the membrane into N perfectly mixed stages (as done here) and solving the resultant system of tridiagonal matrices using the Thomas algorithm. An initial estimate of the flows for the algorithm was obtained by first solving a simpler cross-flow model to obtain an

initial estimate for their counter-current model, and converging by successive approximation. Orthogonal collocation is also a technique employed by investigators, but the convergence of these systems is very sensitive to the initial composition profile (Cruz et al, 2005). Others have made use of so-called 'shooting techniques', but these techniques can be cumbersome when there are more than two components and can become unstable at high recoveries (Coker et al, 1998).

The purpose of this study was to find a method that does not require the input of an initial estimate at any stage of the algorithm. This would be an advantage for models that are implemented in a simulation package, such as Aspen Hysys®. Simulations often have stream loops with multiple unit operations in them, including possible membrane units, which are iterated to converge the entire simulation. It is not desirable for user intervention for the membrane model for each loop iteration, for example.

3 The start-up method

An alternative method is proposed in this paper that moves away from the traditional approach of attempting to solve the system of coupled equations simultaneously at steady state conditions. Instead of requiring an initial estimate of the steady state concentration profile, it is proposed that the system first be solved with a total permeate pressure of zero in the first iteration, for which the solution of the mole balance Equation (53) is trivial (the value of the second term in parentheses is zero). The permeate flow in this iteration will also be the maximum, since the driving force is greatest for components. The permeate pressure is then increased by an increment. The concentration profile generated in the first iteration is used to solve the system in the second iteration. In this manner, the permeate pressure is increased until the actual (steady state) permeate pressure is reached, with small enough increments that the concentration profiles change slightly with each increment. The method is analogous to starting up a membrane module with full vacuum on the permeate side and allowing the pressure to rise by throttling the outflow of permeate. This method can also be applied to the simpler mixed-permeate case.

The permeate pressure profile can be tailored to reduce the number of iterations, yet maintain stability. It was observed that the pressure increments could be relatively large at low values of $P_{l,\,n}/P_{l,\,ss}$, where *n* and *ss* refer to pressure iteration *n* and steady state, respectively. As $P_{l,n}$ approaches $P_{l,ss}$, the increments (ΔP_n) need to be small in order to converge the system. The pressure profile we selected is based on the equation for a linear decrease in ΔP_n with slope *a*:

$$\Delta P_n = P_0 - a.n \qquad \textbf{(59)}$$

This is represented in Figure 1-2.

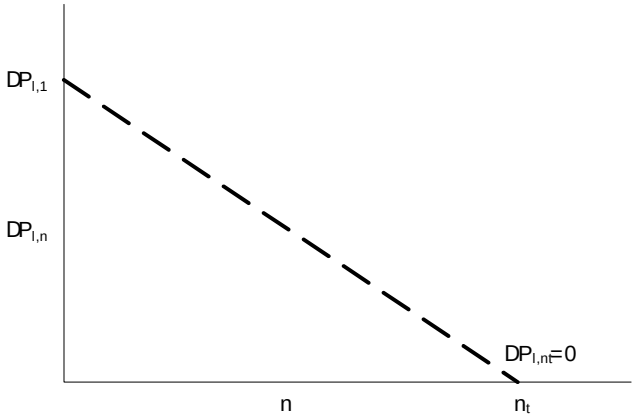

Figure 1-2. Linear decrease in ΔP_n with number of increments

The integral of Eq. (59) yields the permeate pressure for increment n:

$$P_{l,n} = P_0.n - \frac{a}{2}.n^2 \qquad \textbf{(60)}$$

Substituting $n = n_t$ (total number of iterations) and $\Delta P_n = 0$ in Eq. (60), we get

$$P_0 = a.n_t \qquad \textbf{(61)}$$

Combining Eq.'s (60) and (61):

$$a = \frac{P_{l,ss}}{0.5n_t^{\,2}} \qquad \textbf{(62)}$$

Given the total number of iterations, n_t, Eq. (60) yields pressure profiles such as those shown in Figure 1-3.

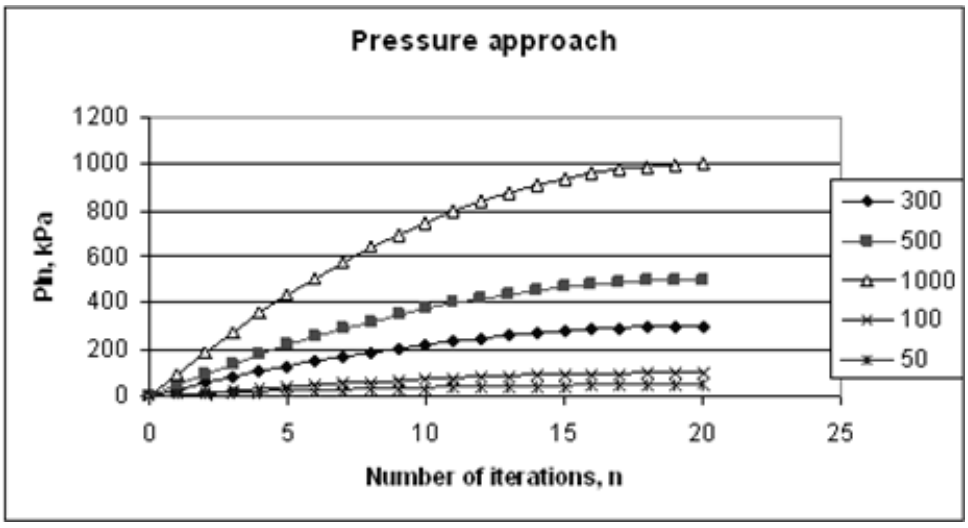

Figure 1-3. Permeate pressure profiles for nt = 20, $P_{l,ss}$ shown as parameter

Increasing the number of iterations, n_t, increases the number of points close to the steady state permeate pressure, resulting in more robust convergence, but clearly at the expense of longer computation time.

4 Implementation and validation

The counter-current model was implemented in an Aspen Hysys® User Op in Visual Basic 5.0. Any number of components can be entered, through the Simulation Basis Manager as per the usual procedure in Hysys®. The feed side molar flows were calculated using 4th order Runga-Kutta and the feed side compositions generated. The permeate mole fractions were calculated from the incremental mole balances and used in the following pressure iteration, as described in the previous section. It was found that for most applications, 300 area increments and 15 pressure increments were sufficient (beyond these values, there was no significant change in results). The final steady state pressure was repeated (iteration n_t+1) and the difference in the permeate mole flow of each component, between iteration n_t and n_t+1, was checked for convergence. In this case, the condition for convergence was set as

$$\frac{F_{i,p,nt+1} - F_{i,p,nt}}{F_{i,p,nt}} < 1 \times 10^{-3} \qquad (63)$$

The processing time taken to reach a solution was approximately 1 second on a 1 GHz Dell PC with 1 Gb of RAM.

The assumptions made for the model are: 1) The permeabilities are independent of pressure and temperature (they must be adjusted accordingly by the user). 2) There is negligible dispersion in the axial direction. 3) There is no concentration polarisation. 4) There is negligible pressure drop on the feed and permeate side. 5) Deformation of the hollow fibres under pressure is negligible.

Validation of the model was performed by comparing model results with published data. The first comparison was with membrane operating data that Kaldis et al. (2000) used to validate their orthogonal collocation method. A counter-current polyimide hollow-fibre module was used to generate the data. The feed and permeances are given in Table 1-1, but the reader is recommended to obtain the study for more details on the system. The permeate pressure was 1 bar in these tests.

Table 1-1. Component data for model validation, permeance at 40°C (Kaldis et al., 2000)

Component	Feed mole %	Permeance, $cm^3(STP)/cm^2.s.cmHg$[a]
H_2	67.5	2.9×10^{-4}
CO_2	16.7	0.93×10^{-4}
CH_4	4.3	0.037×10^{-4}
C_2H_6	11.5	0.0064×10^{-4}

[a] 1 $cm^3(STP)/cm^2.s.cmHg = 3.346 \times 10^{-4}$ $mol/m^2.s$ Pa

The comparison between operating data and our model results is shown in Figure 1-4 to Figure 1-6. It can be seen that good agreement is obtained between the model and the data, over the range of reported stage cut (θ = Permeate flow/Feed flow) and pressure.

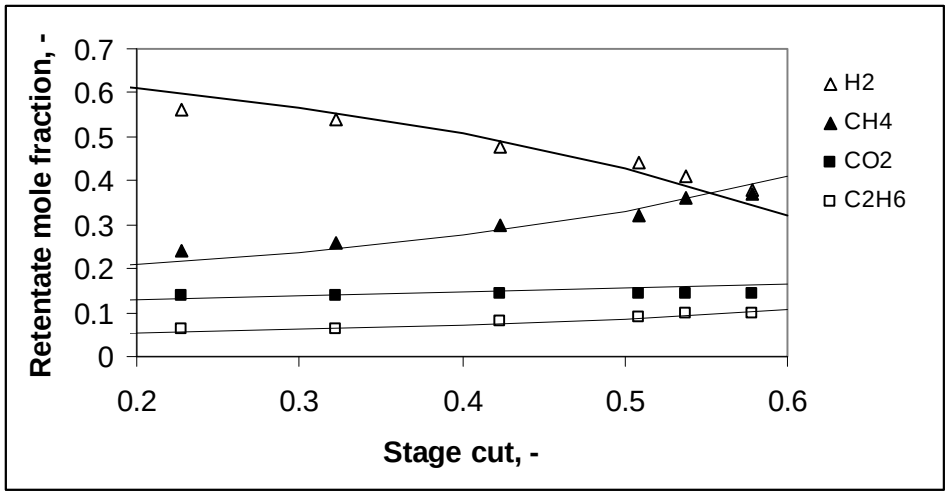

Figure 1-4. Model results (line) vs. polyimide membrane data (points) from Kaldis et al. (2000), for retentate. T=40°C, P_f=20 bar

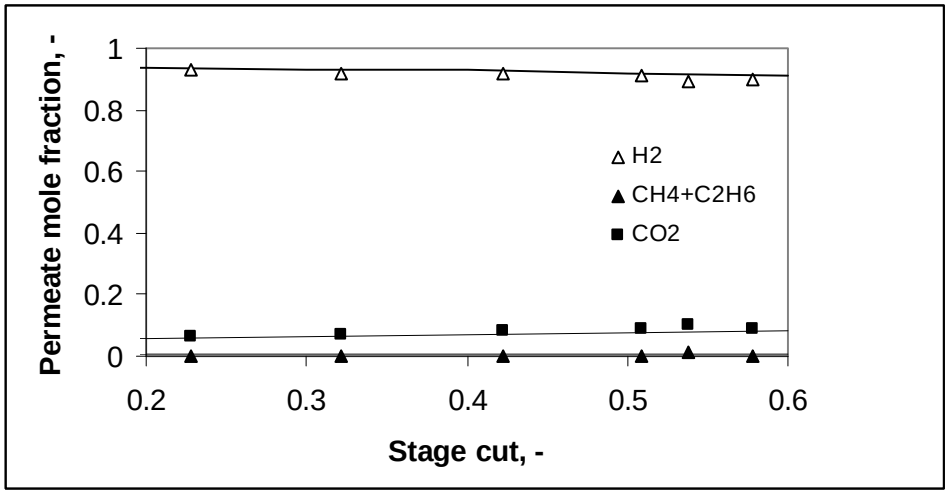

Figure 1-5. Model results (line) vs. polyimide membrane data (points) from Kaldis et al. (2000), for permeate. T=40°C, P_f=20 bar

Neither the model of Kaldis et al. nor the model presented here followed the curvature at low pressure observed in the experimental data for hydrogen and methane (see Figure 1-6).

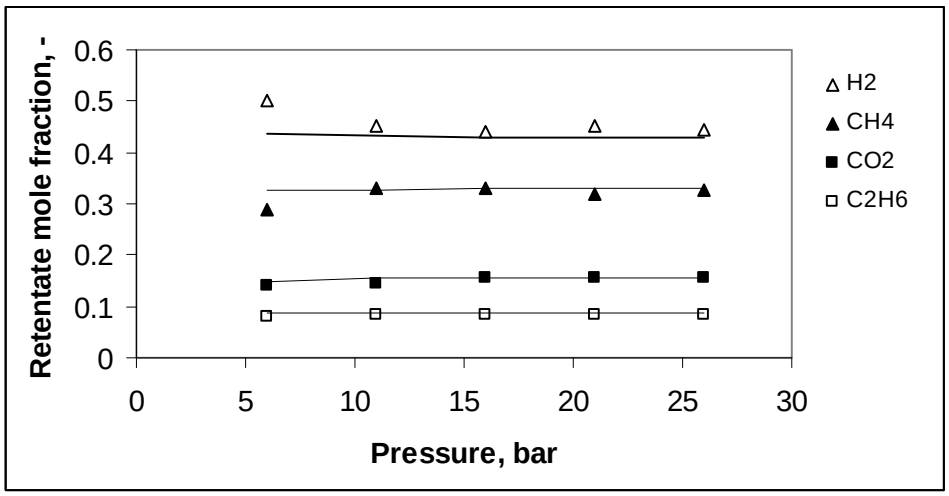

Figure 1-6. Model results (line) vs. polyimide membrane data (points) from Kaldis et al. (2000), for retentate. T=40°C, cut rate = 0.5

The model was also validated against results from Coker et al. (1998), who have published an often-cited study on multi-component membrane modelling. One of the cases presented in that paper dealt with the separation of hydrogen from hydrocarbons. The stream composition and permeances are given in Table 1-2.

Table 1-2. Component data for model validation, hydrogen separation (Coker et al., 1998)

Component	Feed mole fraction	Permeance, GPU[a]
H_2	0.650	100
C_2H_4	0.025	3.03
CH_4	0.210	2.86
C_2H_6	0.080	2.00
C_3H_8	0.035	1.89

[a] 1 GPU = 3.346×10^{-10} mol/m^2.s Pa

The comparison of the start-up method model with the results of the model presented by Coker et al. is shown in Figure 1-7. Coker et al. presented the permeate hydrogen fraction as function of hydrogen recovery for two pressure ratios (PR: feed pressure/permeate pressure); some points have been extracted from their curves for comparison. The models are in agreement for both pressure ratios, but the number of pressure increments needed to be increased from 15 to 300 in the PR=1.8 case for recoveries greater than 60%. The start-up model did not converge for recovery higher than 85% when PR=1.8. This is because the driving force for hydrogen transport becomes very small at the retentate end of the membrane (as j→m), leading to numerical instability. At this point, the separation becomes driven by partial pressure differences rather than selectivity. Coker et al. noted that the number of internal stages in their model needed to be increased from 100 to 1000 when stage cut was greater than 90% and that tests using shooting methods did not converge in high recovery cases where the partial pressure driving force for hydrogen became very small. Nevertheless, the conclusion must be that the start-up method is unstable at low pressure ratios where separation is dominated by partial pressure differences.

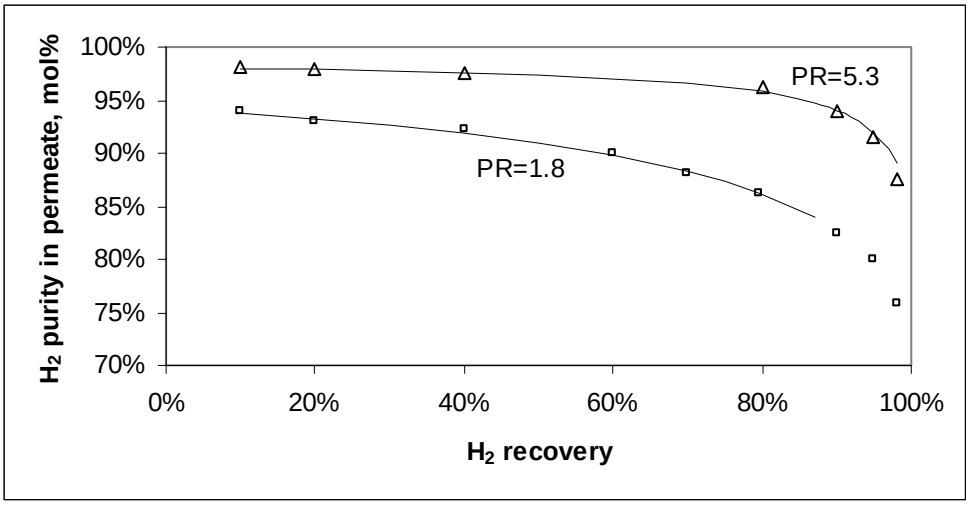

Figure 1-7. Model results (line) vs. Coker et al. (1998) model, for H_2 in permeate. PR = feed pressure/permeate pressure

The exercise was repeated for the air separation example given in Coker et al.

Table 1-3. Component data for model validation, nitrogen enrichment (Coker et al., 1998)

Component	Feed mole fraction	Permeance, GPU[a]
N_2	0.7841	3.57
O_2	0.2084	20
CO_2	0.0003	60
H_2O	0.0027	1000

[a] 1 GPU = 3.346×10^{-10} mol/m^2.s Pa

The feed pressure was 10 or 5 bara and the permeate pressure fixed at 1 bara. It can be seen in Figure 1-8 that the start-up model predicted higher purities than that of Coker et al., but that the general behaviour was similar.

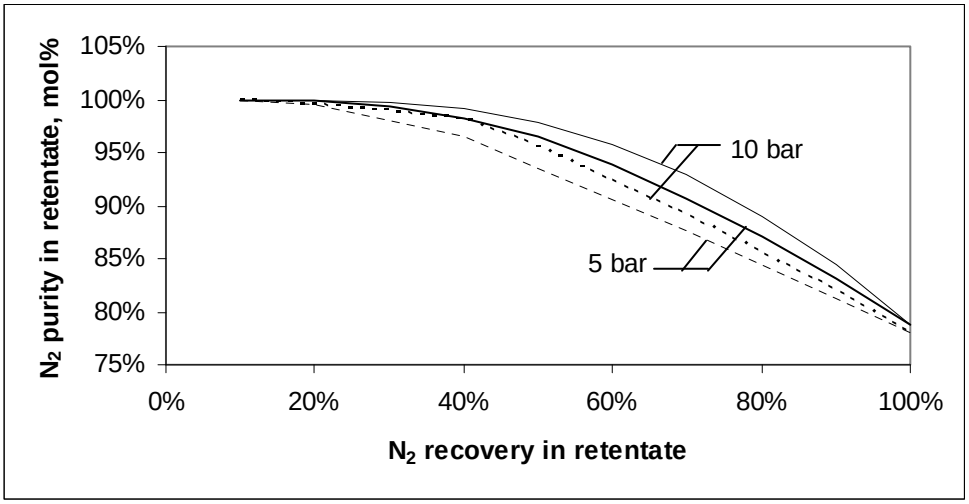

Figure 1-8. Model results (solid line) vs. Coker et al. (1998) model (dashed line), for N_2 in retentate. Feed pressure shown as a parameter

5 Conclusions

A novel method of dealing with the non-linearity of counter-current and mixed permeate membrane models has been proposed that does not need an initial estimate of the permeate flows or concentration profile. The technique produced results with reasonable processing time and stability, provided there is a sufficiently high pressure ratio.

6 Acknowledgements

Thanks and recognition are due to MSc student Kristian Holm Jensen for his work in validating the model against the data from Kaldis et al.

7 References

Coker DT, Freeman BD and Fleming GK. Modeling multicomponent gas separation using hollow fiber membrane contactors. Aiche J 44:1289, 1998

Cruz P, Santos JC, Magalhaes FD and Mendes A. Simulation of separation processes using finite volume method. Computers Chem Engng 30:83-98, 2005

Kaldis SP, Kapantaidakis GC and Sakellaropoulos GP. Simulation of multicomponent gas separation in a hollow fiber membraneby orthogonal collocation — hydrogen recovery from refinery gases. J Mem Sci 173:61-71, 2000

Kovvali AS, Vemury S, Krovvidi and Khan AA. Models and analyses of membrane gas permeators. J Mem Sci 73:1-23, 1992

Mulder M. Basic principles of membrane technology. 2nd Ed. Dordrecht: Kluwer Academic Publ; 1997

Pettersen and Lien KM. A new robust design model for gas separating membrane modules, based on analogy with counter-current heat exchangers. Computers Chem Engng 18:427-439, 1994

Tessendorf S, Gani R and Michelsen ML. Modeling, simulation and optimization of membrane-based gas separation systems. Chem Eng Sci 54:943-955, 1999

Thundyil MJ and Koros WJ. Mathematical modeling of gas separation permeators - for radial crossflow, countercurrent, and cocurrent hollow fiber membrane modules. J Mem Sci 125:275-291, 1997

Appendix C

Techno-economic evaluation of a PVAm CO_2-selective membrane in an IGCC power plant with CO_2 capture

Article in press, in *Fuel*

Available online at www.sciencedirect.com
ScienceDirect
Fuel xxx (2007) xxx–xxx
FUEL
www.fuelfirst.com

Techno-economic evaluation of a PVAm CO_2-selective membrane in an IGCC power plant with CO_2 capture

David Grainger, May-Britt Hägg *

Norwegian University of Science and Technology (NTNU), NO-7491 Trondheim, Norway

Received 14 December 2006; received in revised form 22 March 2007; accepted 27 March 2007
Available online 4 May 2007

Abstract

Published data for an operating power plant, the ELCOGAS 315 MWe Puertollano plant, has been used as a basis for the simulation of an integrated gasification combined cycle process with CO_2 capture. This incorporated a fixed site carrier polyvinylamine membrane to separate the CO_2 from a CO-shifted syngas stream. It appears that the modified process, using a sour shift catalyst prior to sulphur removal, could achieve greater than 85% CO_2 recovery at 95 vol% purity. The efficiency penalty for such a process would be approximately 10% points, including CO_2 compression. A modified plant with CO_2 capture and compression was calculated to cost €2320/kW, producing electricity at a cost of 7.6 € cents/kWh and a CO_2 avoidance cost of about €40/tonne CO_2.

Keywords: Membrane; Power; IGCC; CO_2 capture

1. Introduction

The International Energy Agency [1] predicts that use of the world's vast coal resources as a primary fuel will grow by roughly 30% between 2010 and 2030. Of the electricity produced in 2003, 40% was from coal. Considering that approximately 38% of the CO_2 emissions in 2003 stemmed from coal consumption, it is important to develop feasible CO_2 capture technologies to achieve the aims of agreements such as the Kyoto Protocol.

Integrated gasification combined cycles (IGCC) are considered one of the most environmentally friendly and potentially energy efficient means of power generation from coal [2]. These processes essentially consist of coal gasification to syngas, syngas clean-up, gas turbines, heat recovery and steam turbines. Present thermal efficiencies (lower heating value) are in the region of 46–47%, but in the future may be as high as 55% due to the implementation of new technology, as predicted by the IEA.

In a hybrid concept aimed at CO_2 capture, the syngas in an IGCC may be water–gas shifted (WGS) to produce a mixture of CO_2, H_2 and N_2:

Gasification	$C + 1/2\ O_2 \rightarrow CO$
	$C + H_2O \rightarrow CO + H_2$
WGS	$CO + H_2O \rightarrow CO_2 + H_2$

The high CO_2 content of the shifted gas presents an opportunity for membrane separation, since the driving force in membrane transport is a function of the CO_2 partial pressure,

$$dQ_i = dA(P_i/l) \cdot (\phi_{i,f} \cdot p_{i,f} - \phi_{i,p} \cdot p_{i,p}) \quad (1)$$

where dQ_i ((STP) m^3/h) is the volumetric flow rate of component i through the membrane in an area increment, P (m^3 (STP) m/m^2 bar h) is the permeability of component i in the membrane, dA (m^2) is an area increment, l (m) is the thickness of the membrane, p is the partial pressure of i, and subscripts f and p refer to the feed and permeate sides, respectively. ϕ is the fugacity coefficient of i.

With reference to Eq. (1), greater partial pressure differences produce a greater driving force and hence a lower area

* Corresponding author. Tel.: +47 7359 3138; fax: +47 7359 4080.
E-mail address: may-britt.hagg@chemeng.ntnu.no (M.-B. Hägg).

0016-2361/$ - see front matter © 2007 Elsevier Ltd. All rights reserved.
doi:10.1016/j.fuel.2007.03.042

requirement. In addition, the higher the ratio of the partial pressures ($p_{i,f}/p_{i,p}$), the purer the component with the highest permeability will be in the permeate stream – in this case CO_2. The ratio of two components' permeabilities in a membrane (P_i/P_j) is known as the ideal selectivity (α).

As the recovery of the target component increases, so the partial pressure of that component decreases along the membrane fibre length on the feed side. The fluxes of the remaining components become relatively larger, causing the permeate purity of the target component to decrease. Thus, higher recovery results in decreased product purity.

By using a facilitated transport membrane, such as the CO_2-selective polyvinlyamine (PVAm) referred to in the current paper, there will be an additional transport term based on the kinetics of the reversible reaction (shown below), where CO_2 is transported through the membrane as HCO_3^- and released again as CO_2 on the permeate side. The total resulting flux equation is stated in the following equation:

$$\begin{aligned} &CO_2 + H_2O \leftrightarrow HCO_3^- \\ &dQ_{CO_2} = dA \cdot (D_{CO_2}/l) \cdot (C_{CO_2,0} - C_{CO_2,1}) \\ &\qquad + dA \cdot \left(D_{HCO_3^-}/l\right) \cdot \left(C_{HCO_3^-,0} - C_{HCO_3^-,1}\right) \end{aligned} \quad (2)$$

Here D (m^2/h) is the diffusivity and C (mol/m^3) is the concentration of a species. Subscripts 0 and 1 refer to the membrane–gas interfaces. At high pressures, the membrane may become "saturated" at the active functional sites and Fickian diffusion may again become the dominating transport mechanism.

CO_2 separation before the gas turbine is termed pre-combustion capture, as opposed to post-combustion capture from flue gases which, in the case of membrane separation, suffers from low CO_2 partial pressures. IGCC flue gases tend to be near atmospheric pressure with CO_2 molar concentrations around 12%, while a CO-shifted stream may contain 40 mol% CO_2 and be at 20 bar. Göttlicher and Pruschek [3] concluded in their review of CO_2 capture alternatives that IGCC processes coupled with water–gas shift and membrane separation could attain higher efficiencies than processes coupled with other CO_2 capture technologies, but that further progress in membrane development was needed.

Kaldis et al. [4] evaluated hydrogen selective low-temperature polymer and high-temperature ceramic membranes for pre-combustion capture and obtained a plant efficiency 8–14% points lower than a plant without capture. Up to 57% of the CO_2 could be recovered at 88% purity with three polymer membrane stages. The study did not, however, include the significant pressure drops in equipment between the gasifier and the membrane system, which would lower the available separation driving force, and did not include the energy required to compress captured CO_2 to delivery pressure.

Corti et al. [5] simulated CO_2 separation in methane reforming power generation using PDMS membranes with a CO_2/H_2 selectivity of 6.4. The problems of low CO_2 purity in the product gas and an unacceptable loss of H_2 were encountered, even with two membrane stages. High-selectivity membranes such as PVBTAF (polyvinylbenzyl-trimethyl-ammonium fluoride), a facilitated transport membrane, were also discussed but were considered to have too low fluxes to be competitive. The conclusion of the authors was that current membranes could not compete with chemical absorption in terms of efficiency and specific CO_2 removal cost.

Bredesen et al. [6] reviewed inorganic membranes for CO_2 capture for various power generation cycles, with an emphasis on integrated membrane reactors for reforming or water–gas shift. They claimed that polymeric membranes did not achieve high enough fluxes or selectivities to be viable alternatives and, due to temperature constraints, were not compatible with pre-combustion separation. However, since cooling would also be necessary for a solvent-based CO_2 absorption system, the benchmark technology for such processes, there is no reason to disregard polymeric membranes on this basis. Furthermore, current palladium membrane reactors are poisoned by sulphur compounds [7]. Syngas from coal gasification often contains H_2S, meaning that gas cleanup, for which cooling is required, is still necessary before shift. The commercialisation of hot gas desulphurisation technology appears remote [8].

The aim of this study was to develop and evaluate a conceptual design for a highly selective CO_2/H_2 facilitated transport membrane. Developed at the Membrane Research Group (MEMFO) at the Norwegian University of Science and Technology, the membrane consists of a cross-linked polyvinylamine film supported on polysulfone [9]. The results of a preliminary screening of CO_2 capture in different types of power plants with this membrane identified IGCC as a promising application [10]. Capable of achieving CO_2/H_2 selectivities greater than 100 and a CO_2 permeance of 0.1 m^3 (STP)/m^2 bar h, the membrane offers superior performance to the CO_2-selective materials evaluated in previous design studies. An advantage of the CO_2-selective membrane is that the hydrogen fuel fraction, which constitutes 50% of the WGS product volume, is retained at the feed pressure while CO_2 permeates to the low pressure

Table 1
FSC membrane permeances

Components	Mixed gas permeances (10 bar), m^3 (STP)/m^2 bar h	Mixed gas permeances (20 bar), m^3 (STP)/m^2 bar h
CO_2	0.08	0.05
H_2	6×10^{-4}	5×10^{-4}
CO[a]	0.003	0.002
N_2	5×10^{-4}	4×10^{-4}
H_2O	5×10^{-4}	4×10^{-4}
H_2S	Assumed absent	Assumed absent
O_2	Assumed absent	Assumed absent
COS	Assumed absent	Assumed absent

[a] CO selectivity calculated on basis of single gas results.

Please cite this article in press as: Grainger D, Hägg M-B, Techno-economic evaluation of a PVAm CO_2-selective membrane ..., Fuel (2007), doi:10.1016/j.fuel.2007.03.042

side. With a hydrogen selective membrane, the hydrogen fraction must be re-compressed before combustion in the gas turbine. A summary of the membrane's performance is presented in Table 1. As the CO_2 permeance is influenced by the feed pressure, two sets of values are used for the different pressure levels in this study.

2. Process design

The process design in this study was based on published data from the Puertollano IGCC plant in Spain [11–14]. The existing plant was first simulated in Aspen Hysys® to provide a reference case for the CO_2 capture scenarios, and then new simulations were performed illustrating the various suggested modifications. The polytropic efficiency of the gas turbine was assumed to be 87%, in line with the study by Kaldis et al. [4]. Steam turbine efficiencies were assumed to be 75%.

In the base case process, a mixture of petcoke and coal is gasified at 25 bar and 1500 °C in a gasifier to produce syngas. The syngas is cooled, producing intermediate pressure steam, to 235 °C before fly ash is removed by filtration and scrubbing. The scrubbed gas then enters the sulphur removal section, which consists of a COS hydrolyser to convert COS to H_2S and an MDEA absorber unit to separate the H_2S. The clean syngas is humidified before being mixed with nitrogen in order to lower the combustion temperature in the gas turbine. The turbine exhaust gas, at 1.1 bar(abs) and 539 °C, is routed to heat recovery and steam generation (HRSG) which raises and superheats HP steam (126 bar), IP steam (35 bar) and LP steam (6.5 bar). HP and IP steam produced in the gasification island are also superheated in HRSG. The steam is then routed through high, medium and low pressure turbines, before being condensed at 40 kPa and rejoining the water cycle.

2.1. CO_2 capture

The composition of the raw and clean syngas is shown in Table 2, as well as the composition after WGS. To recover CO_2 from the process, the CO must first be shifted to CO_2 via water–gas shift. In industry this is often achieved in a high-temperature shift (HTS) stage using a FeCr-based catalyst and low-temperature shift (LTS) stage utilising a more sensitive CuZn-based catalyst. LTS is intended to mop up the remaining 1–2 mol% of CO that remains after HTS. In order to reduce pressure drop and equipment cost in the process, only the HTS is present in this design.

Table 2
Process gas design compositions [13]

Component	Raw syngas, mol% (dry basis)	Shifted sour syngas, mol% (dry basis)	Clean syngas, mol% (dry basis)	Shifted clean syngas, mol% (dry basis)
CO	61.3	2.3	60.5	2.2
H_2	22.3	50.7	22.1	50.4
$N_2 + Ar$	11.5	7.3	13.5	8.6
CO_2	3.7	39.0	3.9	38.8
H_2S	1.0	0.7	6 ppmv	Assumed 0
COS	0.2	0.0	6 ppmv	0.0

High-temperature shift is usually operated at 300–500 °C, with lower temperatures favouring H_2 yield. If H_2S is present, then the shift step is known as sour gas shift and a sulphur-tolerant catalyst is required. Both sour shift and sweetened gas shift were evaluated in this study, as the order of processing and the heat integration are affected. A Johnson–Matthey catalyst named Katalco 71-5, which operates between 290 °C and 350 °C, was used as an example for sweetened gas shift, while a Johnson–Matthey sulphur-tolerant catalyst designated Katalco K8-11 (260–500 °C) was used for sour shift [15,16].

2.2. Sour gas shift process

In order to avoid unnecessary heating and cooling of the syngas, the preferable process route would start with gasification, followed by CO shift over a sulphur-resistant catalyst, then cooling to 35 °C for the sulphur removal section and finally feeding to the membrane. This proposal is shown in the flowsheet in Fig. 1. An alternative proposal in which H_2S removal precedes WGS is shown in Fig. 2. The acid gas separation technologies are discussed in more detail in the section on gas clean-up.

Raw syngas from the candle filters, at 235 °C, is preheated in a WGS inter-cooler to 260 °C before being mixed with steam and fed to the first water–gas shift reactor. The steam is mostly raised from water that is boiled in the heat exchangers in the WGS section, with a make-up of IP steam from the HRSG. The temperature in the first bed is allowed to rise to 466 °C before cooling, while the temperature in the last is restricted to 336 °C to increase the yield of H_2. The CO content of the syngas is reduced from 61.3 mol% to 2.3 mol% (dry basis) in the WGS section. The Katalco K8-11 catalyst is also an effective hydrolyser of COS and eliminates the need for a separate hydrolysis reactor. The WGS effluent is then cooled, first by heat exchange with the membrane retentate stream and thereafter by raising steam for the WGS reaction, to 35 °C. After scrubbing of HCl, HF and ammonia with water in a venturi scrubber, the gas is passed through a Selexol wash to selectively absorb H_2S.

The stream is then humidified to 72% relative humidity as required by the FSC membrane. The feed enters the membrane at 21 bar and is assumed to experience a pressure drop of 0.2 bar through the membrane unit. The retentate, now mainly H_2, is reheated to 220 °C by heat exchange with the WGS product, saturated with water vapour and mixed with waste nitrogen from the air separation unit (ASU) before entering the gas turbine combustion chamber. From this point, the process is similar to the original base case, apart from the rerouting of some IP steam (1.1 tonnes/h) from HRSG to the WGS shift section. The

Please cite this article in press as: Grainger D, Hägg M-B, Techno-economic evaluation of a PVAm CO_2-selective membrane ..., Fuel (2007), doi:10.1016/j.fuel.2007.03.042

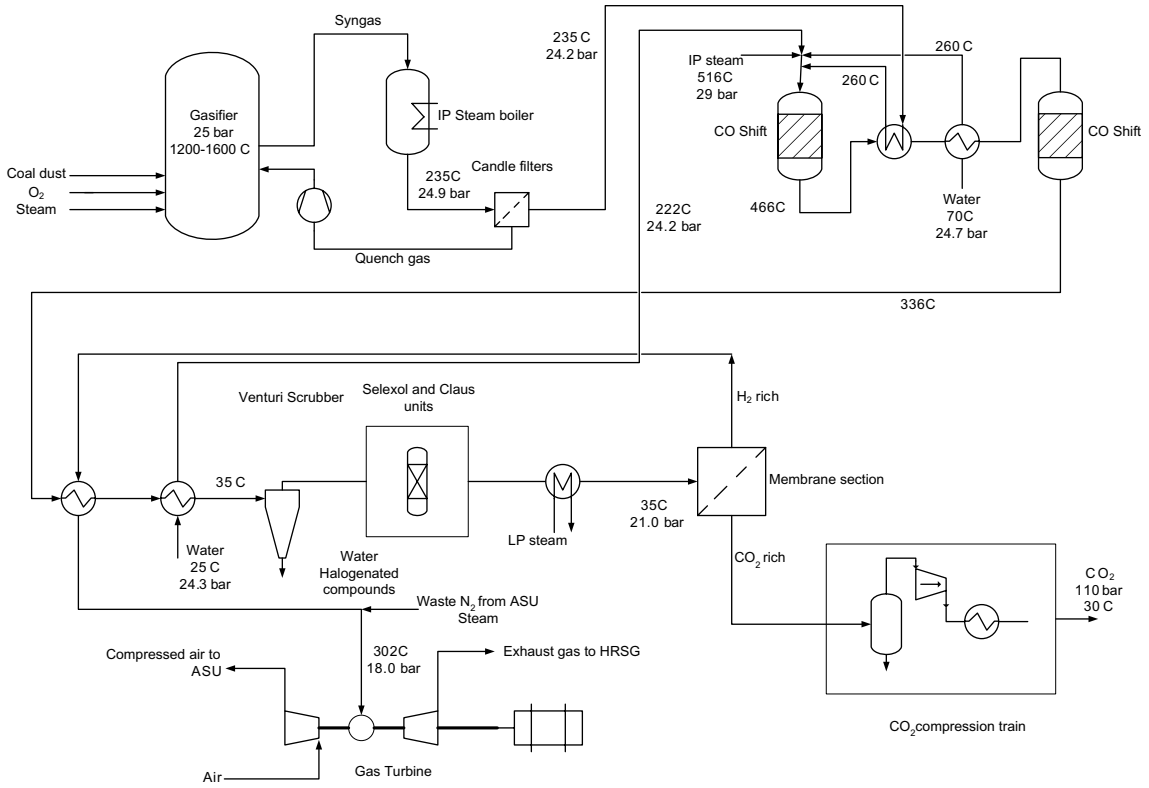

Fig. 1. Process diagram for sour water–gas shift.

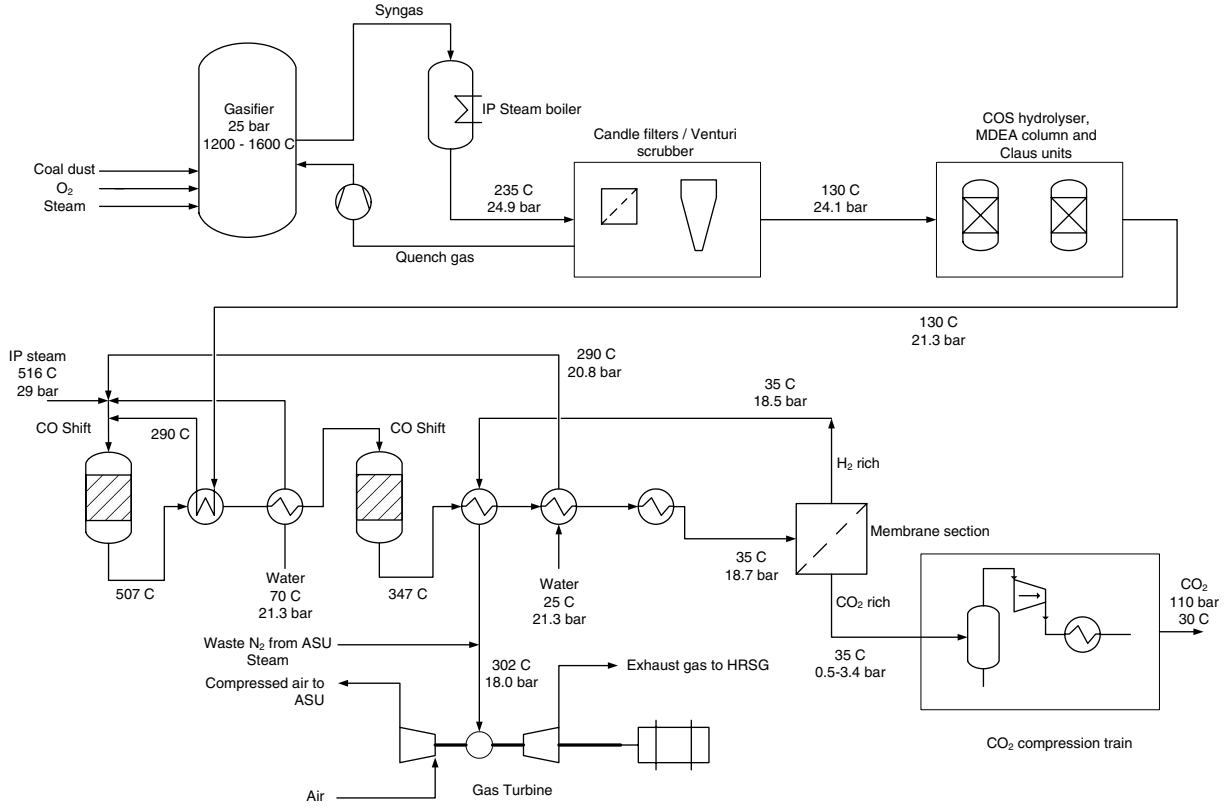

Fig. 2. Process diagram for clean gas shift.

Please cite this article in press as: Grainger D, Hägg M-B, Techno-economic evaluation of a PVAm CO_2-selective membrane ..., Fuel (2007), doi:10.1016/j.fuel.2007.03.042

permeate, mostly CO_2, is compressed to 110 bar delivery pressure in five stages with intercooling.

2.3. Clean gas shift process

The syngas from the gasifier is first filtered and subjected to amine scrubbing (see Fig. 2). After the MDEA sulphur removal section, the clean gas is heated from 130 °C to 290 °C and fed to the first shift reactor.

The effluent from the second reactor at 347 °C is cooled to 35 °C through successive exchangers, heating the retentate and raising steam before it enters the membrane section. The permeate stream, containing mostly CO_2, enters the compression train where it is compressed to 110 bar. The fuel gas stream is heated to 200 °C via heat exchange with the shift reactor effluent before being saturated, mixed with waste nitrogen from the ASU and entering the turbine combustion chamber.

3. Sensitivity study

The variables relevant to the separation process are the feed and permeate pressures, pressure drop through the membrane, membrane area and gas permeabilities. All of these affect CO_2 recovery, H_2 slippage, recovered CO_2 purity and compression, and hence the efficiency and economic performance of the process. A sensitivity study was therefore performed using the ranges shown in Table 3.

Process simulations were done using a membrane simulation module that has been developed within the MEMFO group for use in Aspen Hysys®. This module allows the simulation of co-current, counter-current and perfectly mixed permeate flow configurations, with or without a gas sweep on the permeate side. In this study, counter-current flow without a sweep was used. Any potential cooling due to the Joule–Thompson effect is also taken into account.

4. Results and discussion

4.1. General process

By introducing a shift section and CO_2 capture, the net efficiency of the plant (i.e. the electrical power delivered to the grid divided by the lower heating value (LHV) of the fuel fed to the plant) was, not surprisingly, found to decrease in five main ways: (1) by loss of some hydrogen to the CO_2 product stream, (2) through pressure drop in the process due to additional process equipment, (3) through loss of energy in the shift section, (4) by loss of the CO_2 product mass which would normally have passed through the turbine and (5) by compression of the CO_2 product stream to 110 bar. The efficiency was found to be a strongly dependant on the loss of hydrogen to the permeate, since this reduced the amount of energy available to the gas turbine and HRSG. Fig. 3 presents the total efficiencies for all the sour and clean shift cases in the sensitivity study, plotted against the hydrogen loss in those cases.

Higher recoveries, higher permeate pressures or lower selectivities led to more hydrogen loss and hence lower

Table 3
Design variable ranges for the membrane study

Design variable	Range
Scenarios	Sour shift, sweet shift
Membrane selectivity (P_{CO2}/P_{H2})	10–260
Permeate pressure	50–450 kPa
Membrane recovery (permeate CO_2/feed CO_2)	60–95%

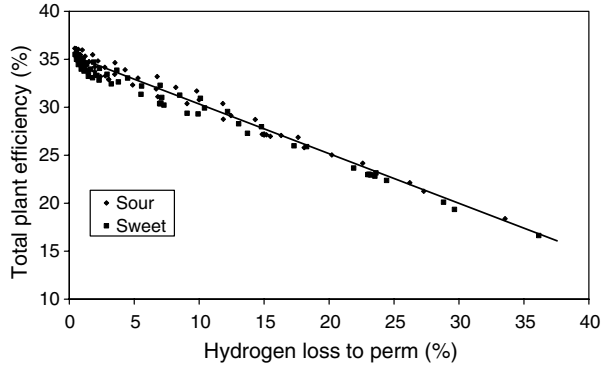

Fig. 3. Total plant efficiency as a function of hydrogen loss to CO_2 product.

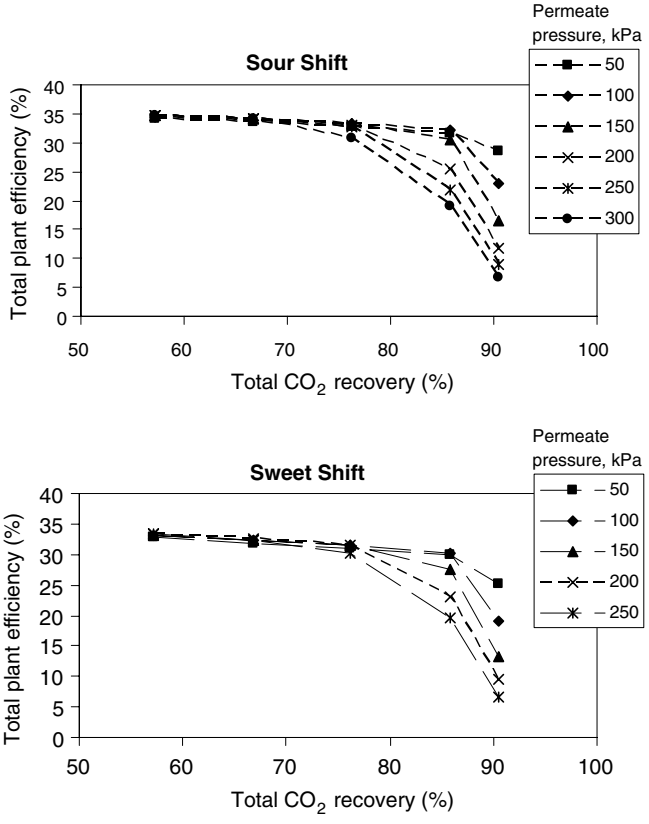

Fig. 4. Total plant efficiency (including CO_2 compression) as a function of CO_2 recovery and permeate pressure.

efficiencies. The results depicted in Figs. 4–6 are for a single membrane stage.

The total CO_2 recovery in the process is lower than the recovery in the membrane unit due to the existence of CO in the membrane feed stream, which is mostly retained. This CO is combusted in the gas turbine and emitted as CO_2. Eighty-nine percent CO_2 recovery in the membrane unit therefore produces an 85% recovery in the process. It can be seen in Fig. 5 that efficiency decreases with increasing recovery, declining rapidly above 80% recovery. Similarly, selectivities (α) below 60 produce a steeper drop in efficiency. Efficiency is less sensitive when selectivity is higher than 100.

Fig. 6 depicts the plant efficiencies for the two scenarios using the FSC membrane $\left(\alpha_{CO_2/H_2} \sim 100\right)$. The efficiency decreases sharply above 85% recovery; for this reason 85% recovery has been selected as the optimum. It was calculated that the sour shift scenario produced a slightly higher net electrical output and hence a higher net efficiency of 32.3% (see Table 5). With the CO_2 compression duty included, this represents a 9.6% point decrease from the no capture base case. The sweet case efficiency was 10.5% points lower than the base case. The better performance of the sour case can be explained by better heat integration and lower pressure drop in the process. The membrane feed pressure in the sour case was 21 bar (as opposed to 19 bar in the sweet case), which resulted in slightly lower H_2 slippage as well as less membrane area. The performance of a sour shift process capturing 70% of the CO_2 is also shown in Table 5 for comparison. The net efficiency and purity of the captured CO_2 for this case are significantly higher. The purity of the CO_2 product at 85% recovery was high (>95 mol%) for all the capture scenarios, because of the high permselectivity of the FSC membrane. The variation in purity between the scenarios is due to the differences in CO_2 partial pressure in the feed.

4.2. Membrane section

Permeate pressures in the range of 50–450 kPa were tested. Higher permeate pressures reduce the energy and capital required for recompression of the CO_2 product, albeit at the cost of higher membrane areas. Lower permeate pressures decrease the amount of hydrogen lost to the

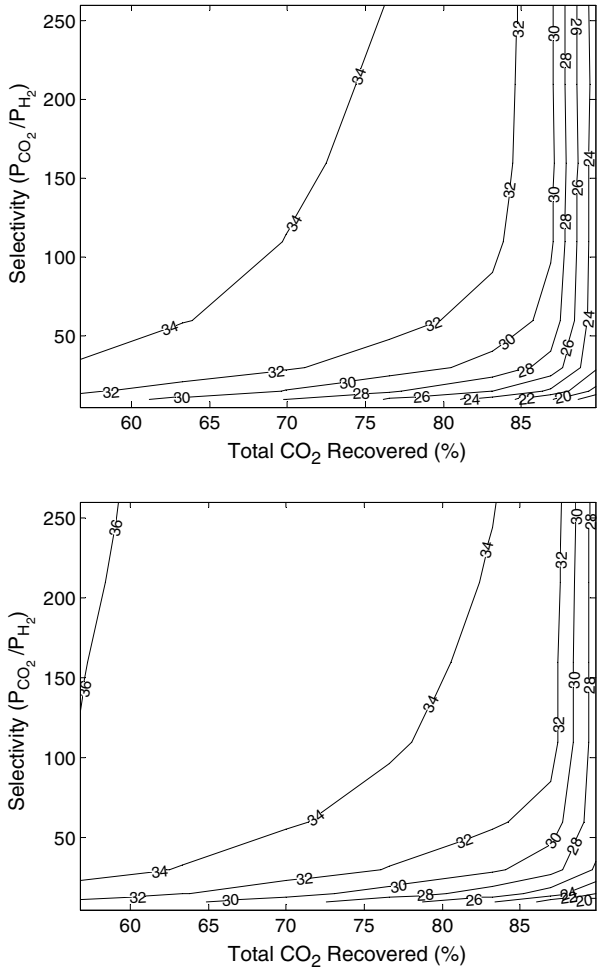

Fig. 5. Total plant efficiency (including CO_2 compression) for the sweet (top) and sour (bottom) shift scenarios (single membrane stage). Total plant efficiency shown as curve labels.

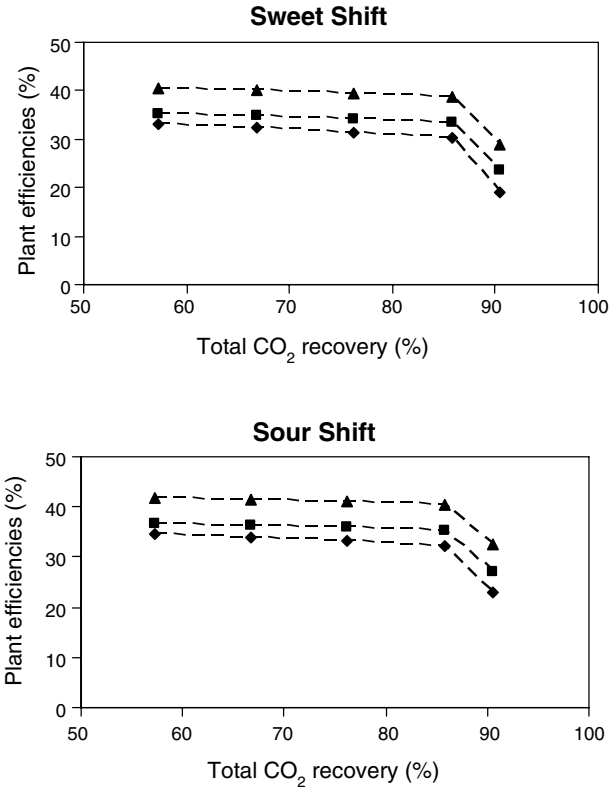

Fig. 6. Plant efficiencies for the scenarios with $\left(\alpha_{CO_2/H_2} = 100\right)$ and optimum permeate pressures. Gross efficiency (▲) is defined as the gross electrical output of the turbines divided by the LHV of the fuel. The plant efficiency excluding CO_2 compression (■) includes the auxiliary consumption of electricity within plant. Total plant efficiency (♦) includes CO_2 compression and auxiliary consumption.

Please cite this article in press as: Grainger D, Hägg M-B, Techno-economic evaluation of a PVAm CO_2-selective membrane ..., Fuel (2007), doi:10.1016/j.fuel.2007.03.042

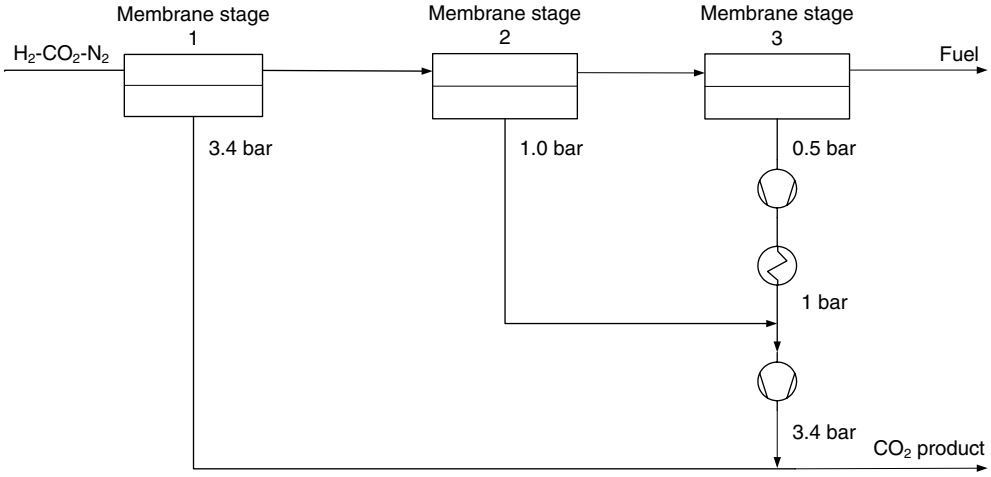

Fig. 7. Membranes in series.

CO_2 product, especially at high CO_2 recovery. A configuration of three membrane stages in series was chosen as the base case, where the first 35% of the CO_2 was recovered at a pressure of 3.4 bar(abs), the following 20% at 1 bar and the remaining 34% at 0.5 bar (see Fig. 7). The second and third stage permeates were re-compressed to 3.4 bar.

As this series arrangement resulted in a loss of 2.9%of the hydrogen to the CO_2 stream (see Table 4), an alternative configuration was investigated where a fraction of the CO_2 from the last stage in series was passed through a further membrane stage to recover some of the H_2. This alternative is designated as the ''Low Slip'' case (an example is given in Fig. 8 – note the permeate pressures).

As more CO_2 is recovered through stages 4 and 5, so the total membrane area and compression duty increases. The relative cost of the unit is plotted against H_2 loss in Fig. 9. The cost of the configuration shown in Fig. 7 was taken as the reference.

Table 4
CO_2 capture performance of a Selexol unit vs. FSC membrane unit (sour shift case)

CO_2 recovery case	Selexol	Sour, 85%	Sour lower slip, 85%	Sour, 70%
Feed pressure, bar	32	21	21	21
Feed CO_2 concentration, mol%	39	39	39	39
CO_2 product pressure, bar (abs)	3.4	3.4	3.4	3.4
CO_2 recovered in unit, %	99	89	89	89
CO_2 energy cost, GJ_{th}/tonne CO_2	0.9	0.3	0.3	0.2
H_2 loss, %	0.7	2.9	1.9	1.8
Membrane area requirement, m^2	–	600,000	650,000	400,000
Specific cost, €/kg CO_2/h[a]	260	237	282	263

[a] Costs calculated using AspenTech IPE. Selexol equipment documented in [18] also re-costed using AspenTech IPE. Membrane module cost assumed \$20/m^2 [21].

4.3. Gas clean-up and comparison with physical absorption

The choice of technology for H_2S clean-up is determined by the ratio of CO_2 to H_2S in the stream to be processed [17–20]. This ratio is low in the raw syngas before CO shift and a simple MDEA unit is suitable (Fig. 2). The selective separation of H_2S in an amine unit from a post-shift stream with a high CO_2 to H_2S ratio (Fig. 1) is less attractive due to a significant amount of co-absorption of CO_2. Previous studies have concluded that, for post-shift capture, commercial MDEA processes cannot produce H_2S streams of the required purity for a Claus unit (without an acid gas enrichment step) and separation using refrigerated Selexol is recommended. Due to the high partial pressure of CO_2 after shift, Selexol is also the preferred solvent for CO_2 capture. The performance of a membrane unit would therefore need to be compared with that of a Selexol unit. Data for the comparison has been adapted from studies by Doctor et al. [18] and Chiesa et al. [19].

Regeneration of the Selexol solvent in the H_2S recovery stage (Fig. 1) requires heat input to a stripper column, but in the CO_2 recovery stage regeneration is achieved simply by letting down the pressure of the CO_2-rich solvent in a series of flashes. Energy loss in the CO_2 section is mainly due to some refrigeration of the solvent, in solvent circulation pumps and compression of the CO_2 to a common pressure level. In the case chosen for comparison [18], the CO_2 is flashed from the solvent at 3.4, 1 and 0.3 bar(abs) and the latter two streams compressed to 3.4 bar.

In order to compare the Selexol process with the FSC process, the energy required to compress the CO_2-containing permeate to 3.4 bar must be taken into account (results are presented in Table 4). A power plant efficiency of 33% has been assumed for back conversion of electrical power to an equivalent thermal value.

Although the amount of CO_2 recovered is higher in the Selexol example (99% vs. 89%), the energy consumption by the membrane unit is less than half. The capital cost of the

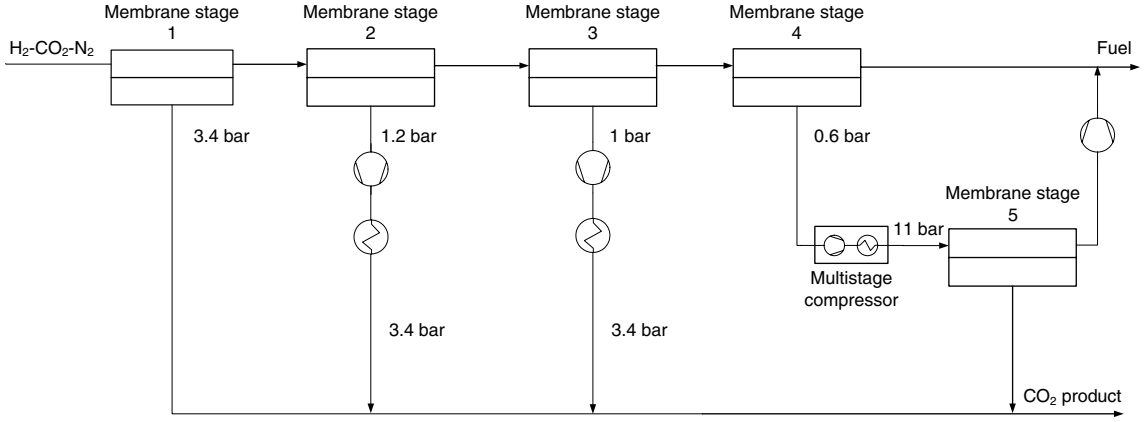

Fig. 8. Membranes in series and cascade.

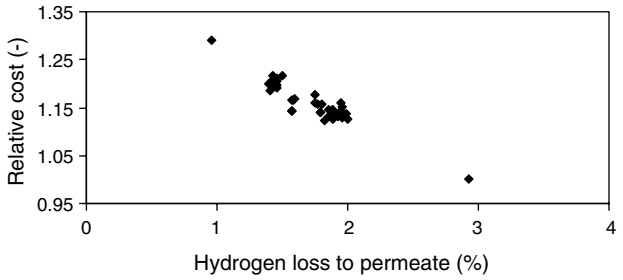

Fig. 9. Slip vs. relative cost of membrane section, including CO_2 compression to 3.4 bar. Results shown for different permutations of membrane configuration and intermediate stage pressures.

membrane section, normalised by the rate of CO_2 capture, is of a similar magnitude. The capital for the Selexol unit includes the inventory of solvent.

In the sour shift case, 2.9% of the hydrogen in the feed to the membrane unit is lost to the permeate. An IEA study [22] comparing CO_2 recovery options also found H_2 loss to be significant with glycol solvents, with 1.1% of the hydrogen fed to the unit lost to the CO_2 product for a similar unit feed stream. In the case presented by Doctor et al., approximately 0.7% of the H_2 is lost.

The column diameter and volume of the packing in the absorber was stated as being 3.6 m and 115 m^3, respectively [18]. The membrane area requirement was calculated to be 600,000 m^2 for the Sour 85% recovery case. For hollow fibre membranes, a typical range for packing density is 10,000–30,000 m^2/m^3 of module space [23]. Taking a conservative value of 10,000 m^2/m^3, the sour shift case with 89% capture in the membrane unit would need approximately 60 m^3 of module volume. With no other major equipment items, the footprint of the unit is significantly smaller than that of a Selexol unit.

4.4. Performance summary

Apart from CO_2 recompression, there is no direct consumption of power in the membrane unit, since neither feed compression nor sweep is required. However, the presence of a separation step is responsible for efficiency loss because of hydrogen slippage, CO_2 pressure loss over the membrane and loss of mass flow to the turbine. The equivalent power consumption in the membrane section has been calculated and is shown in Table 5. The presence of

Table 5
Process summary

	Base case, no capture	Sweet, 85%	Sour, 85%	Sour low slip, 85%	Sour, 70%
Thermal input (LHV), MW	668	668	668	668	668
Gas turbines, MWe	182	152	155	158	159
Steam turbines, MWe	133	112	116	117	118
Gross power output, MWe	315	265	271	275	276
Auxiliary electrical consumption[a], MWe	35	35	35	35	35
CO_2 compression, MWe	0	20	20	21	16
NET power output	280	210	216	219	225
Equivalent shift consumption, MWe	0	36	28	28	28
Equivalent separation consumption, MWe	0	15	16	12	11
Gross efficiency (LHV), %	47.2	39.6	40.6	41.1	41.3
Net efficiency (LHV), %	41.9	31.4	32.3	32.8	33.7
CO_2 purity, %	–	95	95	97	97
Calculated membrane area, m^2	–	710,000	610,000	655,000	407,000

[a] Auxiliary consumption value from [12].

a shift section also results in a decrease in power output, mostly due to consumption of some steam from HRSG section. This decrease was calculated as the difference in power output between the base case plant and a plant containing shift but no membrane section or CO_2 compression. The shift section is responsible for an efficiency loss of 4.3% points (LHV) in the sour shift case and 5.4 in the sweet shift case. CO_2 separation (this excludes any CO_2 compression) is responsible for 2.3% points of power loss and compression to 110 bar contributes the remaining 3% point loss.

4.5. Economic analysis

The Puertollano plant cost approximately 600 million euros [12] and delivers approximately 280 MWe to the grid, giving it a specific capital cost of €2140/kW. However, this is was a first-of-its-kind plant and recent estimates based on lessons learned range between €1000/kW and €1300/kW for a capacity in the region of 500 MWe [11,12]. Campbell et al. [11] calculated the capital cost of a 315 MW sized Puertollano plant to be 1500 €/kW, which was used as the reference in this study. The same methods and assumptions for calculating specific cost and cost of electricity (COE) were also used. The cost of electricity was defined to be the break even price, or electricity price that gives a plant with a life of 25 years a net present value (NPV) of zero. The CO_2 avoided cost was calculated using:

$$CO_2 \text{ avoided cost} = \Delta COE / \Delta CO_2 \text{ emitted} \quad (3)$$

where ΔCOE (€/kWh) is the difference in COE between the reference plant and the plant with capture and ΔCO_2 emitted (tonne CO_2/kWh) is the difference between the amount emitted in the reference case without capture and that emitted in the capture scenario. The cost of electricity is higher in the capture case due to both increased capital expenditure and reduction in power output because of efficiency loss. The CO_2 avoided cost is useful for comparison with other capture technologies, as well as carbon emission taxes that the power utility might pay or possible carbon trading credits gained. The purchased equipment costs for the shift, membrane and CO_2 compression train were calculated using AspenTech Icarus Process Evaluator™. The cost of existing Puertollano sections was assumed to be unaffected by the addition of CO_2 capture, except for the gas and steam turbines, which were scaled down with an index of 0.6. The additional equipment installed cost was calculated using an installation factor of 3 and a contingency of 10%.

The specific cost for power plants with CO_2 capture increased to approximately 2400 €/kW and 2320 €/kW for the sweet and sour shift cases, respectively, due to the addition of equipment and the decrease in power output (Table 6). The cost of avoided CO_2 was also lower for the sour shift process than the sweet shift. However, since cost estimates at this early stage typically have a margin of error of 30–50%, it is not possible to conclude that sour shift option is cheaper. The smaller membrane area, elimination of the hydrolysis reactor and higher overall efficiency are stronger arguments for selection of this process route.

The specific costs and electrical costs are lower for 70% recovery of the CO_2 than for 85%, mainly due to smaller equipment size and reduced H_2 slippage to the CO_2 product stream. However, since less CO_2 is recovered, the avoided cost is higher.

The lifetime of the evaluated membrane is presently unknown. A continuous run lasting 4 weeks indicated that the membrane is stable, but long-term testing with real gas feeds is required to establish the operating lifetime. It was assumed for the economics presented in Table 6 that the membrane modules must be replaced every 5 years. The sensitivity of the electricity price to this variable is shown in Fig. 10. The study also assumed a price of $20/m^2 for the membrane modules, based on estimates by Koros

Table 6
Economic summary for membrane cases at different CO_2 recoveries

	Base case[a], no capture	Sweet, 85%	Sour, 85%	Sour low slip, 85%	Sour, 70%
Capital costs, M€					
Solids reception, storage and prep	41	41	41	41	41
Air separation unit	36	36	36	36	36
Gasification	114	114	114	114	114
Gas cleaning	49	49	49	49	49
Gas turbines	73	65	66	67	67
HRSG	48	48	48	48	48
Steam turbines	43	39	39	40	40
Water treatment	15	15	15	15	15
Shift section and catalyst	–	26	29	29	29
Membrane section ($20/m^2)[b]	–	35	30	33	20
CO_2 compression train	–	33	33	40	29
Total installed cost, M€	419	502	501	511	488
Specific investment, €/kW	1496	2395	2322	2335	2170
COE, € cents/kWh[c]	5.0	7.8	7.6	7.6	7.1
CO_2avoided cost, €/tonne CO_2	–	43	39	40	41

[a] Based on data from Campbell et al. [11].
[b] Membrane module fabrication costs assume to be US$ 20/m^2.
[c] Discount rate of 7.5%, working capital = 2% of capital investment, capital fees = 2% of capital investment, fuel cost = €1.86/GJ_{LHV}, operating cost = 1.1% of capital investment, maintenance = 2.3% of capital investment, insurance = 2% of capital investment.

Fig. 10. Effect of membrane lifetime on COE (Sour 85% capture case).

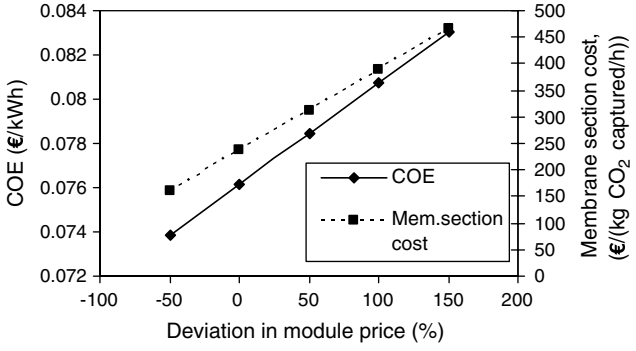

Fig. 11. Effect of module price on COE and membrane section cost.

[21]. The sensitivity of the COE to this variable is shown in Fig. 11.

5. Conclusions

Data from an existing power plant has been used as a basis for the simulation of an IGCC process with CO_2 capture. This process incorporated a fixed site carrier PVAm membrane, developed at MEMFO at NTNU, to separate the CO_2 from a CO-shifted syngas stream. It appears that the modified process, using a sour shift catalyst to convert CO to CO_2 before sulphur clean-up, could achieve 85% CO_2 recovery at an acceptable purity for liquefaction. The efficiency decrease for such a process would be approximately 10% points, including CO_2 compression to 110 bar(abs). The plant was calculated to cost €2320/kW, producing electricity at a cost of 7.6 € cents/kWh and with a CO_2 avoidance cost of €39/tonne CO_2.

The benefits presented by an FSC membrane unit are:

- Lower energy consumption than in a solvent unit.
- No solvent makeup or chemical inventory required.
- Smaller footprint.

The purpose of this exercise was to apply this new membrane technology using existing plant data so as to achieve as practical an evaluation as possible. There exist opportunities for improvement in performance. Improvement in the membrane CO_2 permeance at higher pressures would reduce the membrane area required and is the subject of ongoing research. Commercially available gasifiers running at higher pressures would allow lower membrane areas, less hydrogen slippage and higher permeate pressures.

Acknowledgements

The authors wish to acknowledge Dr. T.-J. Kim for excellent experimental work within the CEPEME Project. Further acknowledgement goes to Statoil and Alstom for their funding and invaluable support together with the Norwegian Research Council.

References

[1] Key world energy statistics. IEA; 2005.
[2] Control and minimisation of coal-fired power plant emissions. IEA working party on fossil fuels; 2003.
[3] Göttlicher G, Pruschek R. Comparison of CO_2 removal systems for fossil-fuelled power plant processes. Energy Convers Manage 1997;38:173–8.
[4] Kaldis SP, Skodras G, Sakellaropoulos GP. Energy and capital cost analysis of CO_2 capture in coal IGCC processes via gas separation membranes. Fuel Process Technol 2004;85:337–46.
[5] Corti A, Fiaschi D, Lombardi L. Carbon dioxide removal in power generation using membrane technology. Energy 2004;29:2025–43.
[6] Bredesen R, Jordal K, Bolland O. High temperature membranes in power generation with CO_2 capture. Chem Eng Process 2004;43:1129–58.
[7] Maurstad O. An overview of coal based integrated gasification combined cycle (IGCC) technology. Report MIT LFEE 2005-002 WP; 2005.
[8] Korens N, Simbeck D, Wilhelm D. Process screening analysis of alternative gas treating and sulphur removal for gasification. SFA Pacific Inc. Report; 2002.
[9] Kim T-K, Li B, Hägg M-B. Novel fixed-site-carrier polyvinylamine membrane for carbon dioxide capture. J Polym Sci, Pt B: Polym Phys 2004;42:4326–36.
[10] Grainger DR, Lindbråthen A, Hägg M-B. CO_2 capture from fossil-fuelled power plants using facilitated transport membrane technology. In: Proceedings of the eighth international conference on greenhouse gas control technologies; 2006.
[11] Campbell PE, McMullan JT, Williams BC. Concept for a competitive coal fired integrated gasification combined cycle power plant. Fuel 2000;79:1031–40.
[12] Coca MT. Integrated gasification combined cycle technology: IGCC – Its actual application in Spain. ELCOGAS Report. http://www.elcogas.es/shared/GICC%20tecnologia%20limpia%20del%20carbon_ en.pdf.
[13] IGCC Puertollano: A clean coal gasification power plant. ELCOGAS Report; 2000. http://www.elcogas.es/shared/thermie.pdf.
[14] Medez-Vigo I, Pisa J, Corte J, Schellberg W, Karg J. The Puertollano IGCC plant: status update. In: Gasification technologies conference; 1998.
[15] Johnson–Matthey catalysts brochure: Katalco K8-11 & K8-11/Sour CO shift catalysts; 2003.
[16] Personal communication with Ian Barton. Johnson–Matthey catalysts.
[17] Nicholas DM, Wilkins JT. Optimize acid gas removal. Hydrocarbon Process 1983;6:123–9.
[18] Doctor RD, Molburg JC, Thimmapuram PR. KRW oxygen-blown gasification combined cycle: carbon dioxide recovery, transport and

disposal. Argonne National Laboratory/ENS Report, ANL/ESD-34; 1996.

[19] Chiesa P, Consonni S, Kreutz T, Williams R. Co-production of hydrogen, electricity and CO_2 from coal with commercially ready technology. Part A: Performance and emissions. Int J Hydrogen Energy 2005;30:747–67.

[20] Kohl AL, Nielson RB. Gas purification. fifth ed. Houston: Gulf Publishing Company; 1997.

[21] Koros WJ. Membrane opportunities and challenges for large capacity gas and vapour feeds. EMS XX Summer School. Trondheim, Norway; 2003.

[22] Potential for improvement in gasification combined cycle power generation with CO_2 capture. IEA Report PH4-19; 2003.

[23] Mulder M. Basic principles of membrane technology. second ed. Dordrecht: Kluwer Academic Publishers; 1997.

Please cite this article in press as: Grainger D, Hägg M-B, Techno-economic evaluation of a PVAm CO_2-selective membrane ..., Fuel (2007), doi:10.1016/j.fuel.2007.03.042

Appendix D

Evaluation of cellulose-derived carbon molecular sieve membranes for hydrogen separation from light hydrocarbons

Journal of Membrane Science, accepted 08 September 2007

Evaluation of cellulose-derived carbon molecular sieve membranes for hydrogen separation from light hydrocarbons

David Grainger and May-Britt Hägg*

Norwegian University of Science and Technology (NTNU)
NO-7491 Trondheim, Norway
Tel: +47 7359 4030
Fax: +47 7359 4080
* may-britt.hagg@chemeng.ntnu.no

Abstract

Carbon molecular sieve membranes derived from cellulose-hemicellulose have been evaluated for hydrogen separation from light hydrocarbons. Copper (II) nitrate was added to the precursor in the range of 0-6 wt%, resulting in increased hydrogen/methane permselectivity at the expense of permeability. Carbonization temperature was varied from 400-700°C, with the best performance for membranes produced between 550°C and 650°C. Mixed gas tests with H_2, CO_2, C_1-C_4 and N_2 showed that these membranes tolerate light hydrocarbons and separated hydrogen with a permeability of about 480 Barrer and hydrogen/methane permselectivity >1000. Hydrogen/carbon dioxide permselectivity was found to be approximately 23 at 25°C. Transport was activated and an increase of 65°C from 25°C doubled the mixed gas hydrogen permeability. Performance was strongly influenced by exposure to air.

Key words: carbon, membrane, hydrogen, hydrocarbon, process

Introduction

Carbon molecular sieves have been shown to achieve excellent performance, with respect to hydrogen permeability and selectivity, in the separation of hydrogen from light hydrocarbons such as methane [1-8]. These membranes achieved performances above the trade-off curve (selectivity vs. permeability) reported by Robeson [9] for polymers. The objective of the work presented here was to build on these efforts by developing carbon membranes that are optimised for hydrogen/methane separation and to generate sufficient performance data that application in commercial cases could be simulated.

The main factors in the preparation of carbon molecular sieves are 1) precursor polymer [10], 2) precursor additives [2, 11], 3) final carbonization temperature [8, 10, 12], 4) carbonization environment [12], and 5) time spent at final temperature (soak time) [10]. The precursor in this work was an 80% cellulose-20% hemicellulose mixture, also used by Lie and Hägg [2, 3], which has produced promising results. Factors 2-4 were varied in order to characterize their

influence on performance, but soak time was kept to 2 hrs to reduce the number of time-consuming experiments.

As thermosetting polymers are carbonized, there occurs a process of pore creation as surface heteroatoms are eliminated from the carbon matrix and, as temperature increases further, a region of pore closure as carbon bonds shift to eliminate free radicals in the matrix [13]. Analysis of the permeabilities of hydrogen and methane by Koresh and Soffer [8] showed that they pass a maximum in cellulose-derived membranes at approximately 650°C.

Lie and Hägg [2] found that the nitrates of copper and silver were particularly effective in improving selectivity for the gas pairs nitrogen/oxygen and carbon dioxide/methane. Apart from the spacer effect of the additives, they also proposed that the gases released upon nitrate decomposition were porogens, in that they create pores by tunnelling through the material

Geiszler and Koros [12] found that carbon molecular sieves prepared under vacuum were more selective but less permeable than those produced under inert gas flow and concluded that pyrolysis was enhanced in an inert gas, due to improved mass and heat transfer. Oxygen also strongly influenced the membrane porosity; just 0.3 ppm of oxygen in the inert flow was found to produce more open membranes by oxidation.The aging of the membranes, or change in separation performance with time and exposure to air, was also investigated in this study as this can have a significant effect on productivity [14].

The effect of operating temperature and pressure on transport was considered, as well as the difference between single gas and mixed gas permeation results. The mechanism of separation in carbon membranes depends on the pore structure, gas species, mixture composition and conditions. These factors determine the degree of interaction between molecules and pores. Briefly, three regimes are important, which relate roughly to effective pore diameter: Knudsen diffusion (giving poor selectivity and prevalent in pores 2-100 nm in effective diameter [15]), selective surface flow (or competitive absorption in pores of 5-6 Å, which results in the more strongly adsorbing molecules permeating preferentially [16]) and molecular sieving (present in pores of 3-5 Å [17-19]), which is the desirable mechanism in this application. It is a kinetic-statistical mechanism incorporating size and shape exclusion of gas molecules by constrictions in the carbon pore network. Writing Fick's Law in terms of partial pressures for the flux of a gas through a membrane yields:

$$J_i = -D_i \frac{dC_i}{dp_i} \cdot \frac{dp_i}{dx} \qquad (1)$$

Here D is the diffusivity constant of gas i in a medium, p is the concentration of the gas and x is the distance over which diffusion is considered. The permeability, P, of a gas is then defined as:

$$P_i = -D_i \frac{dC_i}{dp_i} \qquad (2)$$

If Henry's law applies, $C_i = S_i.p_i$, where S is solubility; $dC_i/dp_i = S_i$ and hence $P_i = D_i \cdot S$. However, adsorption isotherms are typically of type I in carbons with a uniform, narrow pore size [8] and, if the Langmuir isotherm is adopted as an example, then Eq. 2 is more correctly written as:

$$P = D \cdot C_0 \cdot b/(1+bp)^2 \qquad (3)$$

where C_0 is the adsorption saturation capacity and b is an interaction parameter. A decrease in permeability is therefore expected for an increase in pressure, particularly for heavy gases for which the interaction parameter is large. If Henry's law holds (i.e. for a light gas with a dilute concentration in the membrane material), Eq. 2 can be rewritten to yield [19]:

$$P = D_0 S_0 \exp\left(\frac{-(E_s)}{RT}\right) \qquad (4)$$

where D_0 is the temperature-independent diffusivity constant, S_0 is the solubility constant, T (K) is temperature and R (J/mol.K) is the universal gas constant. E_s (J/mol) $= E_d + H_s$, where E_d is the activation energy required for diffusion to occur and H_s is the heat of sorption. The effect temperature has on the selectivity between two gases depends on the size of E_s. From Eq. 4, the ratio of permeabilities of a gas at two temperatures, $T_1 > T_2$, is given by

$$\frac{P_{T1}}{P_{T2}} = \exp\left[\frac{E_s(T_1 - T_2)}{RT_1T_2}\right] \qquad (5)$$

The implication of Eq. 5 is that, for molecular sieving materials, gases with a larger E_s than hydrogen will experience greater ratios of P_{T1}/P_{T2} and selectivity may decrease.

The membranes were also tested with minor fractions of C_2-C_4 in the feed, as an approximation of a real hydrocarbon feed, because hydrocarbons may hinder or even block the permeation of hydrogen by competitive adsorption in the ultramicropores [20]. Since the recovery of hydrogen in refineries is gaining in importance as crude stocks become heavier and fuel specifications stricter [21], one example of potential CMS application is the recovery of hydrogen from a hydrocracking purge gas containing 32 mol% hydrogen, 23 mol% methane, 17 mol% ethane, 18 mol% propane and butane and 9% hydrogen sulphide [23].

Another example is the recovery of hydrogen from a mixed natural gas-hydrogen distribution network [22]. If a hydrogen-based society were realised, the establishment of a hydrogen distribution system would be a lengthy and costly exercise; hence a transitional approach has been proposed to use existing natural gas (NG) networks to transport mixtures of hydrogen and NG. Critical to the success of the concept is the feasible separation of the hydrogen for end-use components requiring relatively pure hydrogen, such as fuel cells. In this concept, the fraction of hydrogen in the pipeline could range from 5 to 30 vol%. The principle gases in the separation are hydrogen and methane, with a minor fraction comprising C_2-C_4 hydrocarbons, carbon dioxide and nitrogen.

Experimental

Materials

Wood pulp (80-85% cellulose, 15-20% hemicellulose) from spruce and pine was supplied by Södra Cell Tofte, Norway. Trifluoroacetic acid (TFA, 99%) was supplied by Sigma-Aldrich (Germany) and copper (II) nitrate trihydrate by ACROS Organics (USA). Argon 5.0, CH_4 4.0, H_2 (>99.9%), N_2 5.0 and CO_2 4.0 were supplied by AGA AS, Norway.

Precursor solution and casting

Solutions were prepared by dissolving a sample of hemicellulose-cellulose (to give 1.5 wt%) and any metal nitrate in trifluoroacetic acid. Cellulose dissolved readily in TFA, usually forming a viscous solution within 3 days. The viscosity of the solution decreased steadily thereafter as depolymerisation occurred [2, 3]. The solution was then cast in a Teflon® dish and dried for three days.

Carbonization

Carbonization was carried out in two different ovens at the research group. The first was a horizontal Carbolite® TZF 12/100/900 (Hope Valley, UK) three-zone tube furnace, controlled by a Eurotherm 2408CP temperature regulator. The furnace tube was an alumina tube of 80mm ID, delivered by Chemi-Teknik AS, Oslo. The furnace tube was connected to a vacuum pump (RV5 from BOC Edwards, UK), allowing a vacuum of 0.34-0.41 mbar to be drawn during carbonization. The end caps were sealed using Viton® o-rings and gaskets, together with Molykote® heat-resistant grease. The pressure was measured using a MKS Baratron® 626 pressure transducer. The vacuum line passed through a liquid nitrogen dewar to trap volatiles from the pyrolysis process and prevent back-diffusion of oil vapour from the vacuum pump. The films to be pyrolysed were placed on a stainless steel grid (mesh size 3 mm).

The second furnace was a horizontal Carbolite® HZS 12/600E split three-zone tube furnace, also controlled by a Eurotherm 2408CP temperature regulator. The working tube was quartz and was constructed at the NTNU. The precursors were placed on a grooved quartz plate. The ends of the tube were sealed with stainless steel caps, one of which was connected to a vacuum pump while the other was connected to MKS Mass-Flo® flow-controllers. An Argon superficial velocity of ~1 cm/min was applied in the sweep cases. The flow-controller section could also be isolated with a diaphragm valve, allowing the furnace to be operated in vacuum mode. The pressure in the furnace was measured using a MKS Baratron® 626 pressure transducer (rated to 10 mbar) and found to be 0.02-0.05 mbar when at full vacuum. The heating procedure, for vacuum and inert gas flow, followed that used by Lie and Hägg [2, 3].

Characterisation

Thermogravimetric analysis of the carbonization procedure was carried out using a TA Q500 TGA (TA Instruments, USA). A Thermostar™ gas analysis system (Pfeiffer Vacuum GmBH, Germany) was coupled to the sample gas outlet on the furnace of the TGA. FE-SEM images were obtained with a ZEISS Supra-55 VP Field Emission Scanning Microscope (LV FE-SEM), manufactured by Carl Zeiss NTS GmBH, Germany.

Membrane area was obtained by scanning and image analysis with Scion Image (Scion Corp., MD, USA). Thickness was determined with a Mitutoyo 2109F thickness gauge (Mitutoyo Corp., Kanagawa, Japan) with a resolution of 1 micron. Relative standard deviation in the thickness was approximately 3%.

Gas permeation tests

The measurement of gas permeabilities was carried out in the apparatus shown in Figure 1. The membranes were mounted within the membrane cell using aluminium tape (3M 7940)

and epoxy (Devcon S-208/20845 (max. temp. 93°C) or Huntsman Araldite 2012 (max. temp. 200°C)) and a vacuum (~0.07 mbar) was drawn on the permeate side. After evacuation for a minimum of 12 hours to remove adsorbed species in the membrane and on equipment walls, the permeate side was isolated and feed gas at a specified pressure applied on the feed side. Due to equipment limitations, the maximum pressure in this work was 6 bar. The rate of pressure rise was measured using a MKS Baratron® 626 pressure transducer and logged using LabVIEW™ v6.1 (National Instruments, USA). The membrane cell temperature was regulated by means of a heating jacket and temperature regulator (HT MC1) provided by Horst GmbH, Germany.

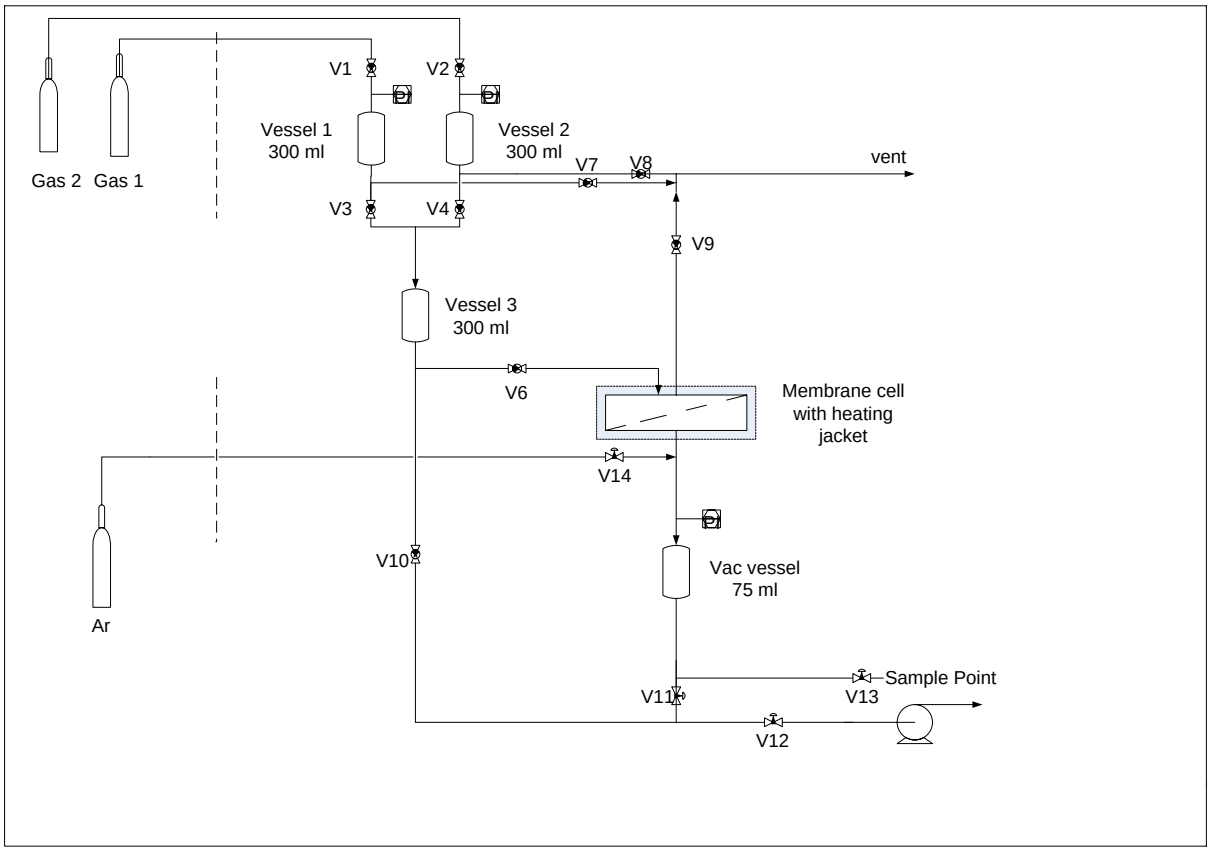

Figure 1. Gas permeation rig

The permeability of the gas through the membrane was calculated using

$$P_i = \frac{dp}{dt} \cdot \frac{T^o}{p^o} \cdot \frac{V_p}{T_p} \cdot \frac{l}{p_f} \cdot \frac{1}{A_m} \qquad \textbf{(6)}$$

Where *dp/dt* is the rate of permeate pressure rise, T^0 and P^0 are standard temperature and pressure respectively, V_p is the volume of the permeate side, T_p is the temperature of the permeate gas, l is the thickness of the membrane, p_f is the pressure of the feed gas and A_m is the membrane area. The permeate pressure, which was typically <0.5% of the feed pressure, is neglected in this expression. The leak rate, which was measured in a run without feed gas and subtracted from *dp/dt*, varied from about 10^{-5} to 10^{-4} mbar/min, which was sometimes on the same order as the methane permeation rate.

The permeabilities of gases in a mixture were determined with the same rig. Feed gas mixtures were obtained by charging vessels 1 and 2 with individual gases and then allowing them to mix by diffusion via vessel 3, or by purchasing ready-made mixtures from AGA AS (Norway). In the case of ready-mixed gases, the feed flowed continuously over the membrane and out through valve 9. The permeation rate of hydrogen was negligible compared to the feed rate (10 ml/min). After evacuating the permeate side, the permeate pressure rise was logged until a pressure of at least 20 mbar was reached. Argon was then allowed to flood the permeate side to a pressure of 2 bar. After 1 hour of mixing, the permeate gas mixture was bled to an Agilent Technologies 6890N GC system incorporating one mole sieve and one carbon PLOT column (Agilent Technologies Inc., USA) and the composition of the gases in the permeate measured. Because the permeate partial pressure of hydrogen could be a significant fraction of the feed partial pressure, and therefore affect the driving force, Eq. (7) was used to calculate permeability. This is derived from the dynamic molar balance over the system.

$$P_i = -\frac{l \cdot V_p}{B \cdot A_m \cdot R \cdot T_p \cdot t} \cdot \ln\left(\frac{p_{i,f^0} - B \cdot p_{i,p}}{p_{i,f^0}}\right) \qquad (7)$$

where l is membrane thickness, V_f is the feed volume, V_p is the permeate volume, $B = 1+V_p/V_f$, , t is time, superscript 0 refers to conditions at t = 0 and superscripts f and p refer to feed and permeate, respectively .

When no ready-mixed gas was available, continuous flow was approximated by performing a series of static experiments with mixed gas over several days. Once the rate and GC measurements of the permeate gas were completed, valve 6 was closed in order to isolate some feed gas in contact with the membrane. This was to allow the process of pore blocking, if occurring, to continue. The rest of the feed system was evacuated and a new feed mixture prepared, at 0.5 bar above the test feed pressure. After at least 5 hours of mixing, V6 was opened. The small volume between V6 and V9 meant that the total pressure was close to that of the newly prepared feed mixture. Valve 9 was then opened slightly and the feed side bled until the pressure decreased by 0.5 bar to the test pressure. This procedure caused fresh gas to flow into the membrane cell and the stale gas previously isolated above the membrane to be vented.

Results and discussion

A naming convention for the membranes has been adopted in this paper. The amount of copper nitrate (CuN) appears first, followed by the final carbonization temperature, oven type (TZF or HZS) and what sweep was used. For example, 4CuN650TZF had 4 wt% copper (II) nitrate (calculated without the waters of crystallization) added to the precursor and was carbonized at 650°C in oven TZF, without sweep (i.e. under vacuum). If more than one batch was prepared, then a batch designation was added (e.g. B3). If several distinct runs were executed with air exposure in between, then the run number is also noted (e.g. R3). The unit, Barrer, has been used for permeability in order to provide a convenient comparison with literature.

Carbonization

The evolution of pyrolysis gases is shown against the sample weight loss, in Figure 2. The onset of weight loss coincides with the increase in water, hydrogen and carbon dioxide. A nitrogen dioxide peak, from the decomposition of the $Cu(NO_3)_2$ to CuO, O_2 and NO_2, appears between 200 and 400°C. Whereas carbon dioxide evolution peaks in the temperature segment with the highest weight loss, hydrogen evolution rose steadily throughout carbonization. This is consistent with the conversion of aromatic sheets to graphene structures. Four distinct water peaks are present. The first, complete by about 140°C, corresponds to the evaporation of absorbed water from the polymer and removal of the waters of crystallization in the copper (II) nitrate. The following three are found within the main weight loss segment and are produced by the decomposition and aromatization processes, as -OH groups in the cellulose chain are eliminated. Carbon dioxide and water liberation was seen to rise again towards 800°C, perhaps as the more strongly bonded oxygens within the carbon matrix are ejected. The ion current signal for carbon monoxide, which is also a decomposition product, was masked by a declining residual ambient nitrogen signal in the furnace. The derivative of this signal with temperature, however, showed carbon monoxide evolution occurring between 200 and 300°C.

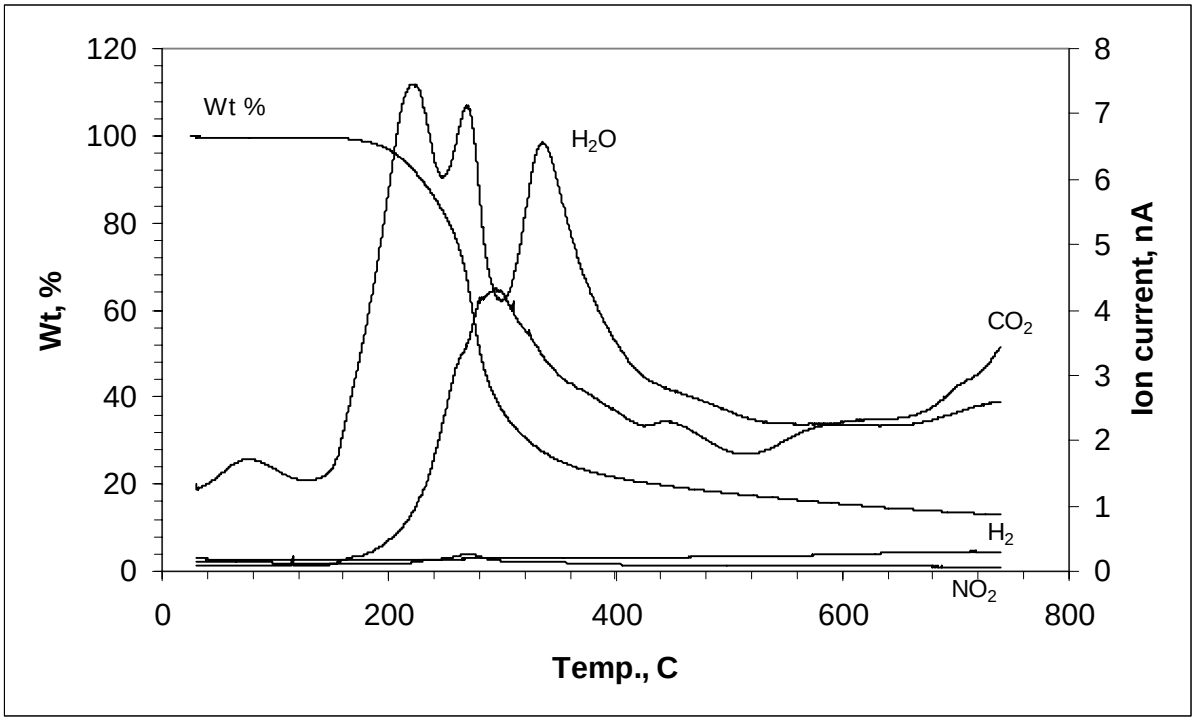

Figure 2. TGA and MS signals of the carbonization of a cellulose precursor doped with 4wt% copper(II) nitrate

Carbon film structure

Carbonization of the cellulose precursors produced flat sheets that appeared uniform to the naked eye. Generally, the sheets had a glassy side and a matt side reminiscent of graphite. At a magnification of 40X, it could be seen that this difference is due to the corrugations on the surface of the matt side (Figure 3), caused by ridges on the surface of the Teflon casting dish. These ridges appear to have been preserved during the carbonization process and the final carbon is a shrunken replica of the precursor, as is expected with a thermosetting polymer. TGA of the copper (II) nitrate confirmed the findings of Silverstein et al [24] that the stable

form is copper oxide in the carbonization range investigated here (400-700°C). SEM images show distinct clusters of the copper oxide embedded throughout the carbon material.

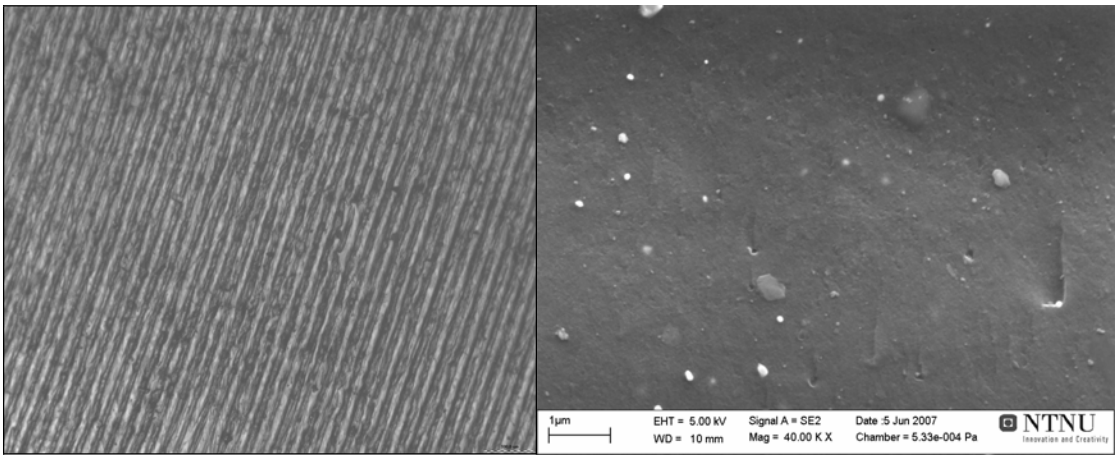

Figure 3. Magnified images (40X) of the matt (left) sides of a typical flat sheet carbon membrane (cellulose with 4 wt% copper (II) nitrate, carbonized at 650°C under vacuum). FE-SEM images of CuO clusters in 4CuN650HZS: Secondary electron (right) 40 000×magnification

Final carbonization temperature

When the ages of the membranes were similar, it was possible to elucidate the effect of the final carbonization temperature on the permeation properties. Figure 4 shows how the hydrogen and carbon dioxide permeabilities vary with final temperature, for a series of pure carbon membranes from the same precursor film. The membranes were allowed one day exposure to laboratory air at 22-26°C (since even short exposures are known to cause aging, it was decided to standardize contact time rather than attempt to avoid it). The graph shows a maximum permeability between 550 and 650°C for both gases, with the inferred peak being close to 650°C. The effect of carbonization temperature was also plotted for membranes that had had 4 wt% copper (II) nitrate added to the precursor. The preparation parameters for this series were not controlled as tightly as for the pure carbon series as the membranes were created from different precursor batches and tested after different aging times. Nevertheless, a similar trend is seen, with hydrogen and carbon dioxide permeability peaking between 550 and 650°C.

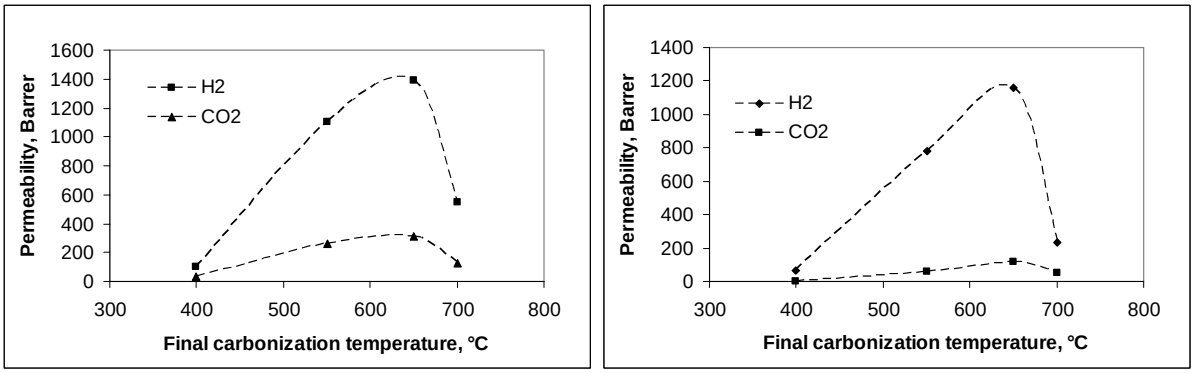

Figure 4. Hydrogen and carbon dioxide permeability plotted vs. carbonization temperature. Left: Pure carbon (no metal additives), produced in TZF oven under vacuum. Right: 4wt% copper nitrate added to precursor, prepared in TZF oven under vacuum. 1 Barrer = $3.34 \cdot 10^{-16}$ kmol·m/(m^2·s·kPa)

The permselectivity of the membranes for hydrogen vs. carbon dioxide is presented in Figure 5. The selectivity of the pure cellulose membrane increased from approximately 2 at 400°C to 4 at 550°C, and remained constant to 700°C. This surprising result implies that the ratio of porosity available to hydrogen vs. carbon dioxide was similar from 550°C to 700°C, even though the permeabilities decreased. The selectivity of the copper nitrate-doped membrane was higher than for the pure carbon membrane, decreasing as the final temperature increased. The copper oxide may have constricted the pores and increased selectivity.

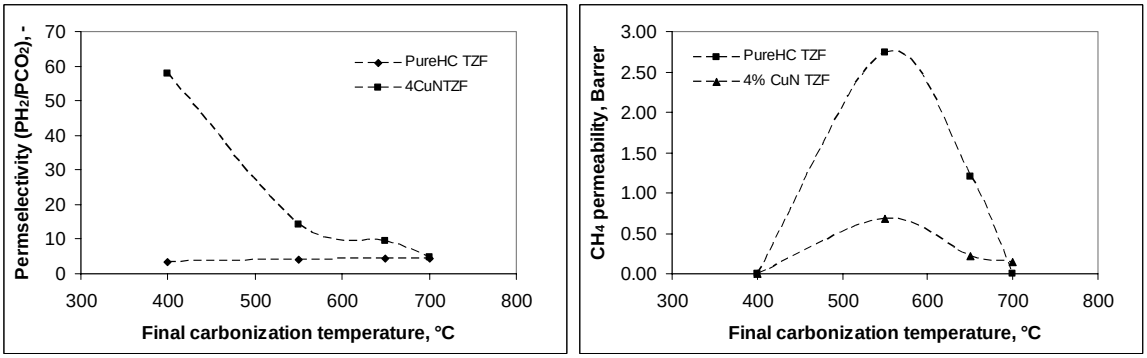

Figure 5. Hydrogen/carbon dioxide SG selectivity (left) and methane permeability (right) vs. final carbonization temperature. 1 Barrer = $3.34 \cdot 10^{-16}$ kmol·m/(m^2·s·kPa)

It was difficult to measure the low methane permeability for the 400°C and 700°C membranes. Normally, the leak rate was subtracted from the rate of pressure rise (*dp/dt*), but at the high and low temperatures the methane *dp/dt* was close to or even less than the measured leak rate. The permeability was set to zero in these cases. The methane permeability appeared to peak at a lower temperature (Figure 5), consistent with the shift in PSD proposed by Steel and Koros [10]. These trends are also in agreement with the findings of Koresh and Soffer [8].

Table 1. H_2/CH_4 SG selectivity vs. final carbonization temp

	Final carbonization temperature, °C			
	400	550	650	700
Pure HC TZF	V. large	402	1157	V. large
4CuN TZF	V. large	1227	4007	1550

The conclusion is that the maximum permeability is obtained for membranes carbonized at approximately 650°C (when the soak time is 2 hrs), whether or not copper (II) nitrate is added.

The selectivity is still high (Table 1) and hence this appears the best suited carbonization temperature for this application.

Copper (II) oxide addition

In the previous section, it was shown that the 4wt% copper nitrate-doped membranes were more selective than pure carbon ones. The analysis is extended in this section to all of the membranes doped with copper nitrate. There is some scatter in the graphs of permeability vs. metal salt wt%, but the general trend was that the permeability decreased as metal salt was added to the precursor (see Figure 6 and Figure 7). An exception was the HZS membranes, for which copper nitrate improved hydrogen permeability.

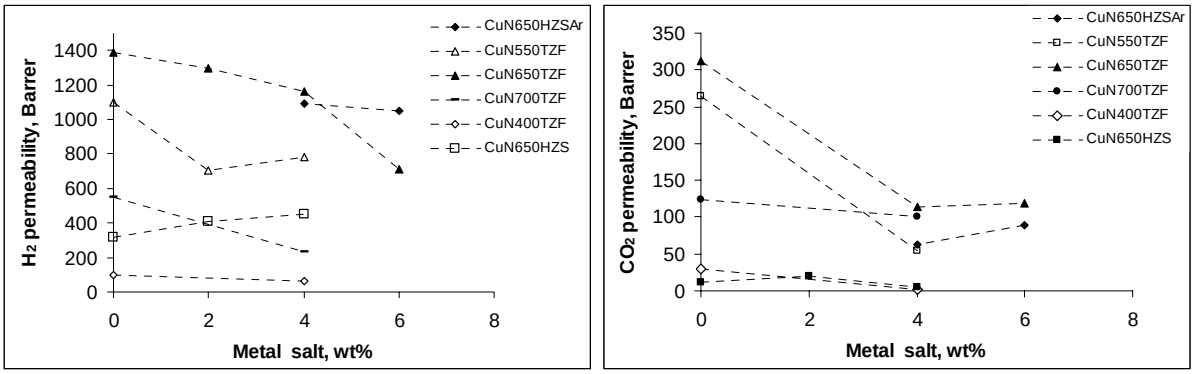

Figure 6. H_2 (left) and CO_2 (right) permeability vs metal nitrate wt% of cellulose precursor

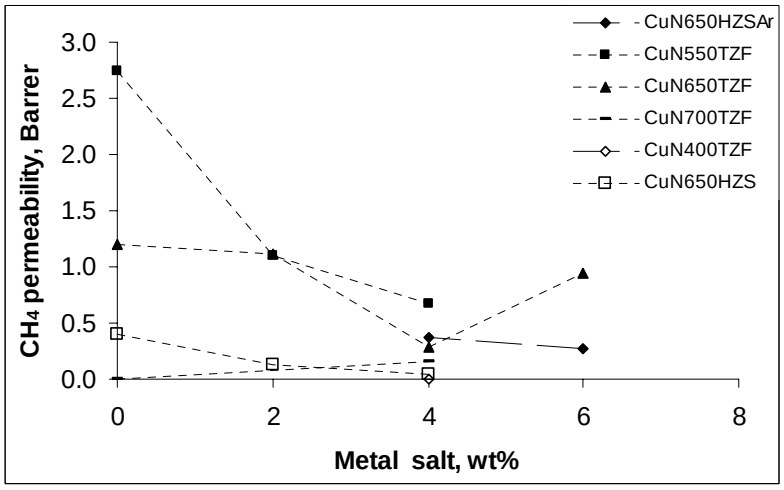

Figure 7. CH_4 permeability vs metal nitrate wt% of cellulose precursor

This behaviour is consistent with pore constriction by deposition of the metal oxide in the pores. There is little evidence of the metal nitrates acting as porogens (in that case one would expect an increase in permeability) and, generally, the hydrogen selectivity of membranes increased with metal addition (Figure 8). A loading of 6 wt% caused a surface layer to appear and the subsequent retardation of hydrogen caused the selectivity to decrease again.

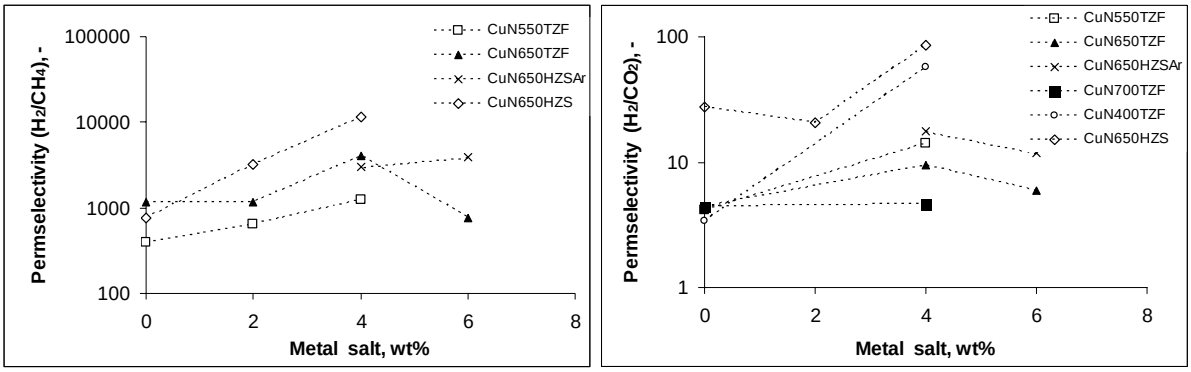

Figure 8. H_2/CH_4 (left) and H_2/CO_2 (right) permselectivity vs metal nitrate wt% of cellulose precursor

Carbonization environment

As described in the Experimental section, two ovens were available to prepare membranes, designated TZF and HZS. TZF operates under vacuum only whereas HZS is able to operate under vacuum or inert gas flow. It is seen in Figure 9 that these three environments produced significantly different membranes. The most hydrogen-permeable membranes were produced in the TZF oven, whereas vacuum pyrolysis in the HZS oven produced membranes with far lower permeabilities and higher selectivities, indicating lower porosity and a smaller apparent pore size. Operating the HZS oven with an inert flow produced membranes with similar hydrogen permeabilities and selectivities to the TZF furnace.

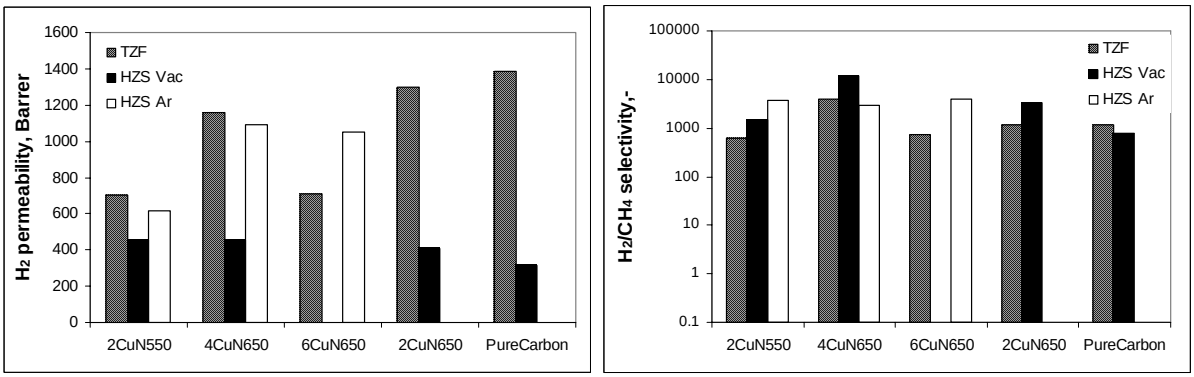

Figure 9. Comparison of membrane permeabilities (left) and selectivities (right) for different carbonization environments

The difference in results between vacuum and argon flow in HZS is explained by the increased mass and heat transfer provided by the inert sweep. The difference between the TZF and HZS results is likely due to the difference in vacuum level. The lowest absolute pressure in the TZF furnace tube (0.34-0.41 mbar) is higher than in the HZS oven (0.02-0.05 mbar). This implies that the oxygen partial pressure from air leaking into the tube is approximately 0.07-0.09 mbar in the TZF tube and only 0.004-0.011 mbar in the HZS. As reported by Geiszler and Koros [12], the presence of even 0.3 ppm of oxygen in an inert gas can increase porosity. 0.3 ppm oxygen in 1 bar argon flow is equivalent to a partial pressure of 0.0003 mbar, which is much lower than the levels present in the furnaces. It is accurate to say, then, that the membranes produced in both furnaces are influenced by oxidation, but that the effect is much more significant in the TZF furnace.

Summary of single gas results

The values in Figure 10 and Table 2 are for tests performed with 2 bar feed and at 25-30°C. Where possible, the values are shown for membranes that were tested within 1 month of being carbonized, to reduce the influence of aging. The membranes for which it was impossible to measure the methane permeability were assigned an arbitrary selectivity of 10^5, so that their position with respect to hydrogen permeability could also be shown. All other membranes exceeded the 1991 Robeson upperbound performance for polymers.

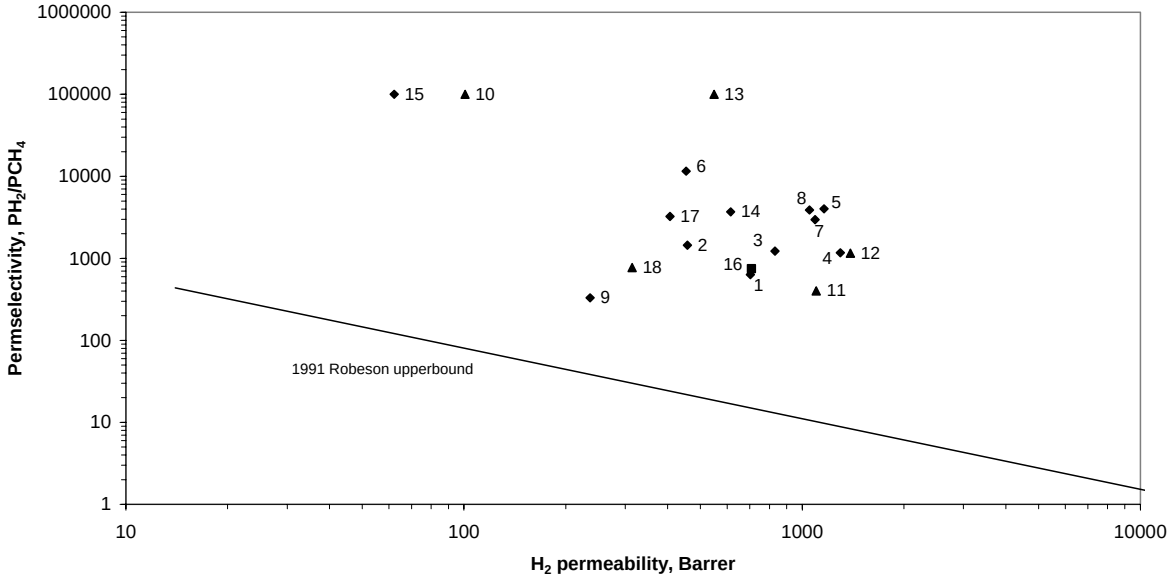

Figure 10. Robeson plot for single gas H_2/CH_4 pairs (■: silver nitrate ◆: copper (II) nitrate▲:no additive, see Table 2 for label key)

Table 2. Data for H_2/CH_4 Robeson plot

No	Designation	Carb. temp, °C	Oven	Additive	Wt% in precursor	Weight loss, %	Age, days	H_2 perm., Barrer	Selectivity, PH_2/PCH_4
1	2CuN550TZF	550	TZF	CuN	2	78.9%	17	703	636
2	2CuN550HZS	550	HZS	CuN	2	78.6%	19	458	1444
3	4CuN550TZFJ*	550	TZF	CuN	4	73.3%	19	830	1227
4	2CuN650TZF	650	TZF	CuN	2	85.2%	3	1296	1169
5	4CuN650TZFB3	650	TZF	CuN	4	83.7%	29	1161	4007
6	4CuN650HZS	650	HZS	CuN	4	83.7%	1	454	11544
7	4CuN650HZSAr	650	HZS, Ar	CuN	4	78.5%	5	1092	2969
8	6CuN650HZSAr	650	HZS, Ar	CuN	6	79.4%	10	1051	3894
9	4CuN700TZF	700	TZF	CuN	4	83.3%	100	236	331
10	Pure400TZF	400	TZF	-	-	80.5%	1	101	V. large
11	Pure550TZF	550	TZF	-	-	83.8%	1	1101	402
12	Pure650TZF	650	TZF	-	-	84.6%	1	1388	1157
13	Pure700TZF	700	TZF	-	-	84.8%	1	549	V. large
14	2CuN550HZSAr	550	HZS, Ar	CuN	2	85.4%	11	614	3690
15	4CuN400TZF	400	TZF	CuN	4	79.6%	1	62.22	V. large
16	6CuN650TZF	650	TZF	CuN	6	-	7	708.45	750
17	2Cun650HZS	650	HZS	CuN	4	80.8%	2	407	3242
18	Pure650HZS	650	HZS	-	-	81.2%	2	314	773

*Prepared by Lie [2]

Aging

The membranes were exposed to laboratory air between experimental runs. Some membranes were retested over a period of time and all exhibited signs of aging, in the form of permeability decrease (Figure 11). This occurred for all degrees of metal addition, carbonization procedures and ovens used. The original hydrogen permeability of a membrane was not recovered by evacuation or even heating to 150ºC (the limit tested), indicating that irreversible chemisorption was the cause. However, there was little aging during experiments, when the membrane was not exposed to air. A 4% copper (II) nitrate-doped membrane (designated 4CuN650TZFB3) was exposed to H_2, CH_4, N_2, CO_2, C_2H_8, C_3H_8 and i-C_4H_{10} at temperatures between 25°C and 90°C over three months without aging.

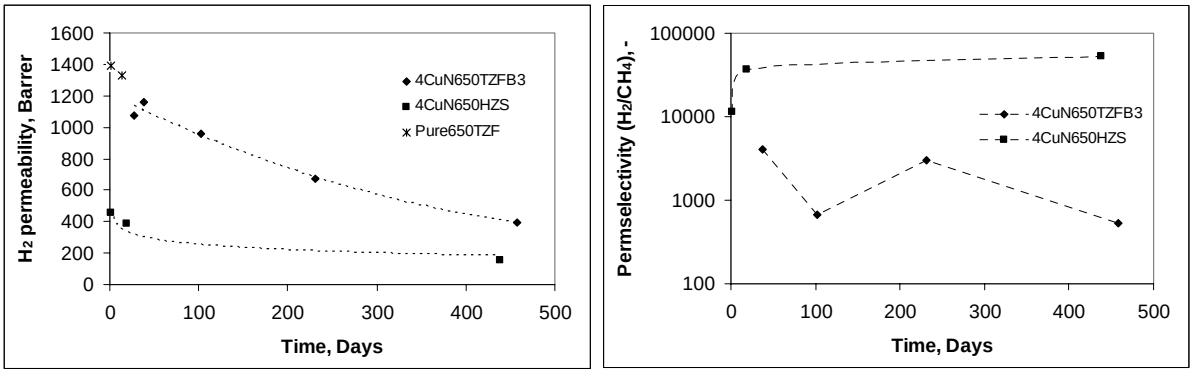

Figure 11. Hydrogen permeability and selectivity of membranes as a function of age. Test conditions: single gas, 2 bar, 25-30°C

Effect of operating temperature and pressure

Temperature was observed, in all the single gas cases, to increase the permeabilities of gases and decrease hydrogen selectivities in a manner consistent with Eq.'s 4 and 5. Pressure had little or no effect on hydrogen or carbon dioxide permeability in pure gas tests, but some effect was seen in the mixed gas tests, where increased pressure appeared to increase the hindrance of hydrogen transport by the more condensible gases. The permeabilities of carbon dioxide and methane were also insensitive to pressure in the range of 2-6 bar. A summary of results for pressure variation is shown in Table 3.

Table 3. Influence of feed pressure on pure CO_2 and CH_4 permeability for two different membranes

Test/membrane	Gas	Pressure, bar	Temperature, °C	Permeability, Barrer
4CuN650TZFB3 R3	H_2	2	25	672
		6	25	662
		2	60	930
		6	60	961
		2	90	1087
		6	90	1110
	CH_4	2	90	1.1
		6	90	1.2
	CO_2	2	25	26.7
		6	25	26.5
		2	90	105.1
		6	90	99.3
	N_2	6	90	1.5

In another example, a membrane prepared without additives and pyrolysed under vacuum in oven TZF at 650°C was tested with hydrogen and carbon dioxide at 2 bar from 25°C-150°C (Figure 12). In this temperature interval, the permeability of hydrogen increased from 1325 to 2255 Barrer and the selectivity halved. The regressed activation parameters for this membrane and a doped membrane are given in Table 4.

Table 4. Arrhenius parameters for pure gas tests

	P_0, Barrer	E_s, kJ/mol	Temp. range, °C	Regression R^2
HCPure650TZF				
H_2	8074	4.3	25-150	0.92
CO_2	17330	11.1	25-150	0.95
4CuN650TZFB3 R3				
H_2	16020	8.0	25-90	0.96
CO_2	78041	20.1	25-90	- (only 2 points)
CH_4	3372	24.3	25-90	- (only 2 points)

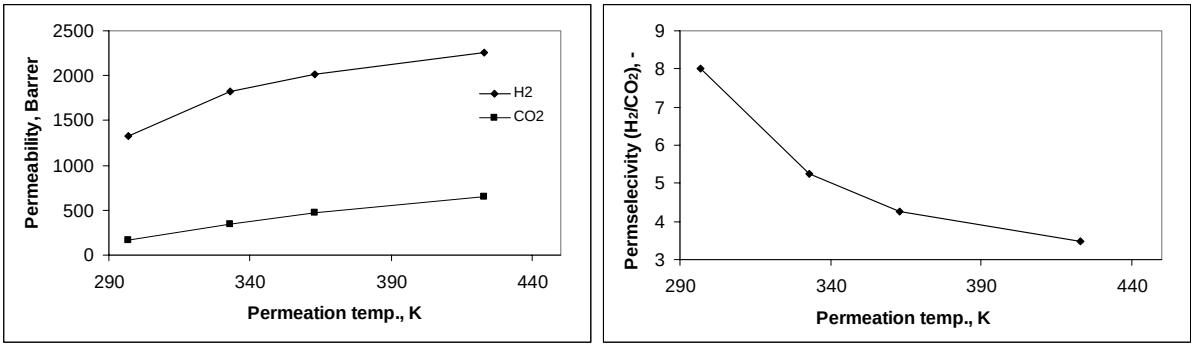

Figure 12. Effect of operating temperature on H_2 and CO_2 permeability (left) and permselectivity (right). Pure carbon membrane (HCPure650TZF)

A danger of characterising carbon membranes by single gas Robeson plots is that reverse selectivity due to competitive adsorption will not be identified. However, none of the cellulose-derived membranes here demonstrated competitive adsorption to the extent that selectivities were reversed – all of them functioned as molecular sieves. There was evidence, however, that the competitive adsorption by heavier gases reduced the permeability of hydrogen. Table 5 compares single gas with mixed gas permeabilities for the same run. A reduction in permeability was also seen for carbon dioxide and methane. This could be due to

the mutual hindrance of carbon dioxide and methane in the natural gas mixture and carbon dioxide and nitrogen in the 50% hydrogen-40% carbon dioxide CO_2-10% nitrogen mixture.

Table 5. Single gas vs. mixed gas results for the 4 CuN650TZF B3 R3

Membrane	Gas	Temp, °C	Gas mixture	Single gas perm, Barrer	Mixed gas perm, Barrer	%Change
4CuN650TZFB3 R3	H_2	24	H_2-CH_4	673	636	-5%
	H_2	60	H_2-CH_4	930	854	-8%
	H_2	90	H_2-CH_4	1087	999	-8%
	CO_2	90	50H_2-40CO_2-10N_2	105	77	-26%
	CO_2	25	30H_2-70 NG*	27	22	-16%
	CO_2	90	30H_2-70 NG*	105	84	-20%
	CH_4	25	H_2-CH_4	0.22	0.04	-82%
	CH_4	90	H_2-CH_4	1.09	1.01	-7%

*NG composition given in section on mixed gas testing

Mixed gas testing

The application of carbon membranes was simulated by running mixed gas tests with gases that approximated true feeds. The 4% copper (II) nitrate membrane designated 4CuN650TZFB3 was selected for simulated application testing because the membrane achieved an excellent performance for hydrogen/methane and reasonable performance for hydrogen-nitrogen and hydrogen- carbon dioxide separation. The membrane's aging history was also detailed and reasonable performance was still achieved after 7 months of air exposure. The following results are for a membrane age of 7-10 months (i.e. 3 months of testing).

Single gases were tested first, followed by binary mixtures (5-30% hydrogen in methane) and finally hydrogen mixed with a natural gas mixture. The effect of hydrogen gas concentration in methane, membrane temperature and total feed pressure is shown for binary mixtures in Figure 13. Hydrogen permeability increased strongly with temperature. This may be caused by a decrease in methane adsorption in the pores in addition to the activated transport effect. Also consistent with the former phenomenon is that the hydrogen permeability decreased slightly with increasing pressure (Figure 13), as a result of increased methane adsorption. The feed concentration of hydrogen was not significant.

Figure 13. Effect of feed pressure on H_2 permeability for membrane 4CuN650TZF (R3). Feed H_2 mole % and membrane temperature as parameters

Finally, hydrogen was mixed in situ with the natural gas mixture from AGA AS consisting of 81.7 mol% CH_4, 10% C_2H_6, 4.5% C_3H_8, 2% CO_2, 1.5% N_2 and 0.25% C_4H_{10}, to produce a 30

H_2:70 NG molar ratio. A series of tests was conducted at 6 bar, 25°C and 90°C over 320 hours (Figure 14, 15), following the approximated continuous flow method described in the Experimental section. The hydrogen-NG mixture was in contact with the membrane for this entire period. First, two tests were conducted at 90°C, in case ethane, propane or butane blocked the membrane pores at ambient temperature. Once it was established that this did not happen at 90°C, the temperature was reduced to ~25°C and a series of tests conducted until the permeabilities stabilised. The hydrogen permeability decreased from 586 Barrer to a steady value of about 480 Barrer, after 100 hours at 25°C. The membrane temperature was then raised to 90°C and three tests performed to check for consistency. The mixed gas selectivity is much lower at 25°C than in pure gas tests, but approaches the pure gas selectivity at 90°C. This could be due to 1) the adsorption of hydrogen at pore restrictions hindering methane transport. Adsorption is attenuated at 90°C and selectivity approaches pure gas values. 2) The methane concentration at 25°C (<100 molppm) being out of range for the calibration gas, which has a methane concentration of ~500 molppm. Uncertainty in GC accuracy should also be greater at this low concentration since measurement involves integration of very flat peaks. Ethane, propane and butane were not detected in the permeate.

From these results it can be concluded that some pore blocking by the heavier hydrocarbons occurred, particularly in the first 24 hours. However, the permeability eventually stabilised so this membrane appears suitable for the recovery of hydrogen from natural gas or refinery off-gases. The time taken for the permeability to decline could be explained by the slow, activated diffusion of the heavier gases into pores where they can adsorb and hinder hydrogen transport.

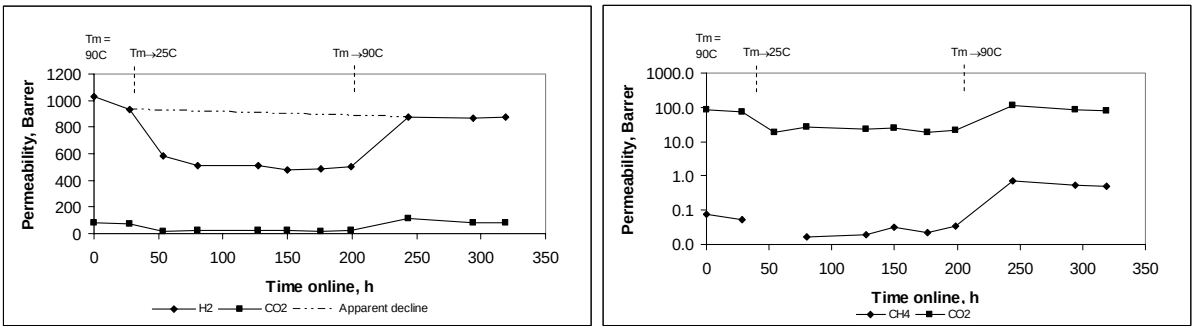

Figure 14. Medium-term testing with simulated natural gas

High permselectivities were calculated for hydrogen over methane, even at 90°C, where the permselectivity was approximately 1200-1800. The permselectivity of hydrogen over carbon dioxide was stable, with average values of 11 at 90°C and 23 at 25°C. Again, the larger gases benefited more than hydrogen from the temperature increase. Practically speaking, this is not an issue for hydrogen separation from methane, since the permselectivity is still very high. If hydrogen/carbon dioxide selectivity is to be maximised, then operation at ambient temperature is recommended.

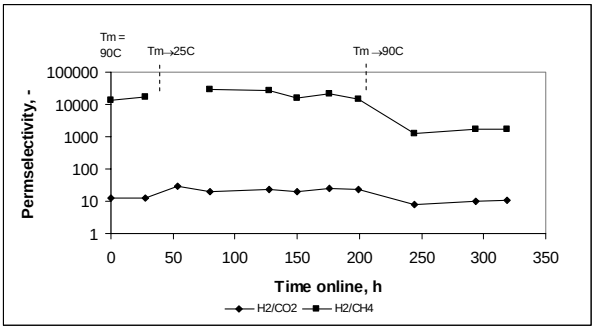

Figure 15. Medium-term testing with simulated natural gas – H_2/CO_2 and H_2/CH_4 permselectivities

The activated transport parameters, regressed over all mixed gas results for this membrane in this run, are shown in Table 6. E_s for hydrogen is similar to the single gas value (see Table 4), but the methane value is higher. Considering the low concentrations of methane in the permeate gas at 25°C and the associated uncertainty, this value is probably too high.

Table 6. Activate transport parameters for 4CuN650TZFB3 R3

	P_0, Barrer	E_s, kJ/mol	Temp. range, °C	Regression R^2
H_2	14820	8.0	25-90	0.95
CH_4	2844790	45.5	25-90	0.92

Conclusions

Carbon molecular sieves derived from a cellulose-hemicellulose precursor are very selective towards hydrogen and achieve high permeabilities, both for single gases and mixtures approximating real feeds. The addition of copper (II) nitrate increased the selectivity at the expense of some productivity. Since the hydrogen selectivity of the pure carbon membranes is already high (1400 for the membrane carbonized in oven TZF at 650°C), it is better not to dope membranes for applications if separation is easy i.e. when the feed concentration of hydrogen is high and/or the purity specification is not severe. When carbon dioxide is present in the mixture, the feed hydrogen partial pressure is low or ultra-pure hydrogen is required, there is a benefit to doping the membrane. The separation performance of membranes is strongly dependent on exposure to air, as has been reported by other researchers using different precursors. This phenomenon makes comparison with published results difficult and can mask the effect of other preparation parameters. Performance is not a static quality, and this should be accounted for when designing a carbon membrane process.

Acknowledgements

The authors are grateful for the funding from the NTNU-SINTEF Gas Technology Centre and the NaturalHy project.

References

[1] S.M. Saufi and A.F. Ismail, Fabrication of carbon membranes for gas separation – a review, Carbon, 42 (2004) 241.

[2] J.A. Lie and M.-B. Hägg, Carbon membranes from cellulose and metal loaded cellulose, Carbon, 43 (2005) 2600.

[3] J.A. Lie and M.-B.Hägg, Carbon membranes from cellulose: Synthesis, performance and regeneration, J. Membrane Sci., 284 (2006) 79.
[4] J.E. Koresh and A. Soffer, The carbon molecular sieve membranes. General properties and the permeability of CH_4/H_2 mixture, Sep. Sci. Techn. 22 (1987) 973.
[5] C.W. Jones and W.J. Koros, Carbon molecular sieve gas separation membranes – 1. Preparation and characterization based on polyimide precursors, Carbon, 32 (1994) 1419.
[6] M.G. Sedigh, W.J. Onstot, L. Xu, L.P. Wildon, T.T. Tsotsis and M. Sahimi, Experiments and simulation of transport and separation of gas mixtures in carbon molecular sieve membranes, J. Phys. Chem. A, 102 (1998) 8580.
[7] N. Tanihara, H. Shimazaki, Y. Hirayama, S. Nakanishi, T. Yoshinaga and Y. Kusuki, Gas permeation properties of asymmetric carbon hollow fiber membranes prepared from asymmetric polyimide hollow fiber, J. Membrane Sci., 160 (1999) 179.
[8] J.E. Koresh and A. Soffer, Mechanism of permeation through molecular sieve carbon membrane. Part 1.- The effect of adsorption and the dependence on pressure, J. Chem. Soc. Faraday Trans., 82 (1986) 2057.
[9] L.M. Robeson, Correlation of separation factor versus permeability for polymeric membranes, J. Membrane Sci., 62 (1991) 165
[10] K.M. Steel and W.J. Koros, An investigation of the effects of pyrolysis parameters on gas separation properties of carbon materials, Carbon, 43 (2005) 1843.
[11] J.N. Barsema, J. Balster, V . Jordan, N.F.A. van der Vegt and M. Wessling, Functionalised carbon molecular sieve membranes containing Ag nanoclusters, J. Membrane Sci., 219 (2003) 47.
[12] V.C. Geiszler and W.J. Koros, Effects of polyimide pyrolysis conditions on carbon molecular sieve membrane properties, Ind. Eng. Chem. Res., 35 (1996) 2999.
[13] H. Marsh and F. Rodriguez-Reinoso, Activated carbon, Elsevier, 2006 pp 30-34.
[14] I. Menendez and A.B. Fuertes, Aging of carbon membranes under different environments, Carbon, 39 (2001) 733.
[15] A.J. Burggraaf and L. Cot, Transport and separation properties of membranes with gases and vapours, In: Fundamentals of inorganic membrane science and technology, Elsevier Science, 1996.
[16] M.B. Rao and S. Sircar, Performance and pore characterisation of nanoporous carbon membranes for gas separation, J. Membrane Sci. 110 (1996) 109
[17] J. Koresh and A. Soffer, Study of molecular sieve carbons. Part 1. Pore structure, gradual pore opening and mechanism of molecular sieving, JCS Faraday I, 76 (1980) 2457.
[18] A. Singh and W.J. Koros, Significance of entropic selectivity for advanced gas separation membranes, Ind. Eng. Chem. Res., 35 (1996) 1231.
[19] H. Suda and S. Haraya, Carbon Molecular Sieve Membranes: Preparation, characterization and gas permeation properties, American Chemical Society Symposium Series, 2000.
[20] C.W. Jones and W.J. Koros, Carbon molecular sieve gas separation membranes – 2. Regeneration following organic exposure. Carbon, 32 (1994) 1427.
[21] B. Pacalowska, M. Whysall and M.V. Narasimhan, Improve hydrogen recovery from refinery off-gases, Hydrocarbon Processing, Nov. 1996.
[22] http://www.naturalhy.net
[23] S.P. Kaldis, G.C. Kapantaidakis and G.P. Sakellaropoulos, Simulation of multicomponent gas separation in a hollow fiber membrane by orthogonal collocation – hydrogen recovery from refinery gases, J. Membrane Sci., 173 (2000) 61.

[24] M.S. Silverstein, Y. Najary, G.S. Grader and G.E. Shter, Complex formation and degradation in Poly(Acrylonitrile-co-Vinyl Acetate) containing copper nitrate, J. Polymer Sci.: Part B: Polymer Physics, 42 (2004) 1023.

Appendix E

The recovery by carbon molecular sieve membranes of hydrogen transmitted in natural gas networks

Submitted to *International Journal of Hydrogen Energy*

The recovery by carbon molecular sieve membranes of hydrogen transmitted in natural gas networks

David Grainger and May-Britt Hägg*

Norwegian University of Science and Technology (NTNU)
NO-7491 Trondheim, Norway
Tel: +47 7359 4030
Fax: +47 7359 4080
* may-britt.hagg@chemeng.ntnu.no

Abstract

The recovery of hydrogen from gas mixtures with hydrocarbons may provide a commercial niche for carbon molecular sieve membranes. A potential application is the recovery of hydrogen transmitted with natural gas in a mixed network in a hydrogen economy scenario. Performance data measured on the bench-scale was applied to a techno-economic evaluation of hydrogen recovery and the results were compared to a commercial polyimide membrane's performance. The carbon membranes produced higher purity hydrogen, consumed less energy in separation and achieved competitive specific separation costs. Recovery of 90% of the hydrogen from a feed stream containing 5 mol% hydrogen was feasible in a single stage.

Key words: carbon, membrane, hydrogen, hydrocarbon, process

Introduction

If a hydrogen-based society were realised, the establishment of a hydrogen distribution system would be a lengthy and costly exercise; hence, a transitional approach has been proposed to use existing natural gas (NG) networks to transport mixtures of hydrogen and NG. This concept is being investigated by the NaturalHy Integrated Project, financed by the 6th EU Framework Programme [1]. The project involves 39 partners including the Norwegian University of Science and Technology (NTNU) and will test the effect of hydrogen addition to the natural gas on all critical components of a pipeline. In this concept, the fraction of hydrogen in the pipeline could range from 5 to 30 vol%. Critical to the success of the concept is the feasible separation of the hydrogen for end-use components requiring relatively pure hydrogen, such as fuel cells.

Carbon molecular sieve membranes (CMSMs) are prepared by the carbonization of thermosetting polymers at temperatures of 400-1000°C and separate components by means of their microporosity, which discriminates between molecules according to their size, shape and strength of interaction with the pore surfaces [2-9]. Carbon molecular sieves have been shown to achieve excellent performance, with respect to hydrogen permeability and selectivity, in the separation of hydrogen from light hydrocarbons such as methane. CMSM's derived from the

carbonization of cellulosic films have been further developed at NTNU for the purpose of hydrogen recovery, by evaluating the effect of copper (II) nitrate addition to the cellulose precursor, carbonization temperature and carbonization environment on carbon molecular sieve membrane performance. For more details on the study and the methods used to generate the data used here, see the article by Grainger and Hägg [10]. CMSMs were shown to perform better than polymeric membranes for hydrogen/methane separation in terms of the Robeson trade-off curve [11], which plots membrane productivity (often represented by permeability) against selectivity. Sufficient performance data was also generated to simulate these membranes in the separation of hydrogen and natural gas components.

Membrane principles

The mole flow of a gaseous component through the membrane in an area increment is calculated by:

$$dF_i = dA\frac{P_i}{l}(p_{i,f} - p_{i,p}) \qquad (1)$$

where P is the permeability of component i in the membrane, A is the area, l is the active membrane layer thickness, p is the partial pressure of i, and subscripts f and p refer to the feed and permeate sides, respectively. The permselectivity (used interchangeably with 'selectivity' in this paper) is defined as the ratio of two gas permeabilities. Permeance is the permeability normalised by the membrane active layer thickness, P_i/l.

If Henry's law holds for the sorption of gases into the carbon pore network (i.e. for light gases with a dilute concentration in the membrane material), the permeability of gases in molecular carbon sieve membranes can be written as [12]:

$$P_i = D_{0i}S_{0i}\exp\left(\frac{-(E_{s,i})}{RT}\right) \qquad (2)$$

where D_0 is the temperature-independent diffusivity constant, S_0 is the solubility constant, T (K) is temperature and R (J/mol.K) is the universal gas constant. E_s (J/mol) $= E_d + H_s$, where E_d is the activation energy required for diffusion to occur within the pores and H_s is the heat of sorption on the pore walls. Thus, for positive values of E_s, permeability will increase with increasing temperature.

As hydrogen is withdrawn from the feed side, so the partial pressure and permeation rate of hydrogen decrease. The relative rate of transport of methane increases and the purity of hydrogen in the permeate subsequently decreases. Higher recoveries, therefore, tend to result in lower product purity. The ratio of feed- to permeate pressure is also an important parameter – the purity of the component with the highest permeability increases as this ratio increases.

NaturalHy design basis

This concept involves the injection of hydrogen from a large source into the network, to be conveyed to the end-users. Two end-use pressure levels are considered, representing

industrial and residential segments of the network – 40 bar (medium pressure) and less than 8 bar (low pressure). Due to equipment constraints, the membranes at NTNU have been tested up to 6 bar (abs), but Tanihara et al. [8] successfully tested asymmetrical carbon hollow fibres at pressures up to 50 bar, so it is assumed for the sake of this exercise that cellulose-derived carbon membranes can also be applied in the 40 bar segment of the pipeline. A natural gas composition, which was used in the experimental work to measure gas permeabilities from a typical mixture, is presented in Table 1. This composition was also used in simulations. It was assumed for the sake of the simulations that the gas feed to the membrane unit was 25°C, which was the lowest temperature applied in the experiments. Lower temperatures in the field would decrease component permeabilities according to Eq. (2), but this was ignored here.

Table 1. Representative natural gas composition.

Gas	i-Butane	N_2	CO_2	Propane	Ethane	Methane
Mole %	0.254	1.5	2	4.52	10	81.7

The separated hydrogen was assumed to be consumed in a PEM fuel cell and the total impurity fraction, including carbon dioxide and nitrogen, was set to <5 mol%. Carbon monoxide and other PEM poisons are expected to be absent. Delivery pressure was 1.5 bar (abs), sufficient for PEM fuel cells. The proposed hydrogen production rate was from 100 Nm^3/h for a hospital fuel cell to 1000 Nm^3/h for industrial use.

The membrane unit performance depends on the following variables:

1. The mole fraction of hydrogen in the pipeline, y_{H2pipe}
2. The pressure of the pipeline gas
3. The hydrogen flow rate in the pipeline relative to the end use requirement, F_{H2use}/F_{H2pipe}. This determines the required recovery since the closer the ratio to 1, the closer recovery must be to 100%. The ratio also sets the difference between the partial pressure of hydrogen in the feed and retentate of the membrane and hence the driving force for separation. The lower the ratio F_{H2use}/F_{H2pipe}, the easier the separation from a driving force point of view.
4. The price and area of the membrane unit
5. Membrane temperature, which affects productivity. Heating can be accomplished by combusting natural gas, preferably from the retentate to reduce the loss of hydrogen from the network
6. Permeate pressure. The higher the ratio, p_{feed}/p_{perm}, the purer the product, but at the expense of more gas recompression to achieve 1.5 bar

Performance data

It was shown in the developmental work [10] that the hydrogen permeability in cellulose-derived molecular sieve membranes is strongly reduced by pore blocking through chemisorption of oxygen from air, decreasing by about 50% after one year of exposure. The strategies to deal with this could be:

- Preventative: blanketing of the module with an inert such as nitrogen
- Adaptive: adding new modules, increasing the driving force or increasing operating temperature as productivity declines
- Conservative: Designing the process based on the steady state, fully-aged performance

- Regenerative: Periodically applying an electrical current to the membrane to regenerate performance [4]

In this case, a conservative approach was adopted and data from measurements on a membrane exposed to air for 7 months was used in the simulations. This membrane was prepared by doping a cellulose-hemicellulose precursor derived from wood pulp with 4wt% copper (II) nitrate, and carbonizing it at 650°C to form a flat carbon sheet. The membrane in these simulations, however, was assumed to be in the form of hollow-fibres with a wall thickness of 16 microns. The thickness of the dense selective layer in the asymmetric fibre wall was taken to be 1 micron, a typical value observed in the cellulosic carbon hollow fibres spun at the NTNU.

The permeabilities and permeances used in this study are shown in Table 2. These were derived from measurement of the permeation rates of the components in Table 1 from gas mixtures or pure gases on the feed side of the membrane. Since C_2-C_4 hydrocarbons are significantly slower permeating than methane and were not detected in mixed gas permeation tests in the lab, they were assigned permeances of 0. Nitrogen was also not detected in the permeate in mixed gas experiments because of its combined low permeability and feed fraction, but should permeate faster than methane and so was assigned the permeability measured in tests with pure N_2 feed. Pure gas permeabilities were also used for methane because very low methane concentrations were detected in the mixed gas permeate, leading to large uncertainty in the calculated mixed gas methane permeability.

Table 2. Gas transport data (average values from H_2-natural gas runs for H_2 and CO_2)

10].

Gas	H_2	i-Butane	N_2	CO_2	Propane	Ethane	Methane
Permeability 25°C, m^3(STP)·m/m^2·bar·h (Barrer)	$1.40\cdot10^{-6}$ (514)	0	$4.1\cdot10^{-9}$ (1.5)	$7.1\cdot10^{-8}$ (26)	0	0	$5.5\cdot10^{-10}$ (0.2)
Permeability 90°C, m^3(STP)·m/m^2·bar·h (Barrer)	$2.49\cdot10^{-6}$ (909)	0	$4.1\cdot10^{-9}$ (1.5)	$2.2\cdot10^{-7}$ (80)	0	0	$2.7\cdot10^{-9}$ (1.0)
Permeance 25°C, m^3(STP)/m^2·bar·h	1.4	0	0.004	0.07	0	0	0.00055
Permeance 90°C, m^3(STP)/m^2·bar·h	2.5	0	0.004	0.20	0	0	0.00270

The mixed gas tests showed that pressure affects the separation only slightly in the range 2-6 bar and permeances are assumed independent of pressure. The activated transport parameters for hydrogen that were calculated from tests with hydrogen-methane mixed feeds and the activated transport parameters for methane from pure gas tests are shown in Table 3.

Table 3. Activated transport parameters for 4CuN650TZFB3 R3 ($P_0 = S_0 \cdot D_0$)

	E_s, kJ/mol	P_0, Barrer	Temp. range, °C	Regression R^2
H_2	8.0	14820	25-90	0.95
CH_4	24.3	3372	25-90	0.92

1 Barrer equates to 2.74×10^{-3} m^3(STP) /m^2·bar·h for thickness of 1 micron

Comparison with a commercial polymer

The performance of the CMSM was compared with data on a commercial polyimide membrane manufactured by UBE Industries Ltd, Japan [13]. The hydrogen permeance of the polymer membrane is approximately half that of the CMSM at 25°C and has a hydrogen/methane selectivity an order of magnitude lower (Figure 1).

According to Kaldis et al. [13], the polyimide membrane can operate up to 100°C. The influence of temperature on both CMSM and polyimide performance is shown in Figure 1; the permeance increases for both as temperature is raised, but the selectivity decreases for the carbon molecular sieve and increases for the polyimide membrane.

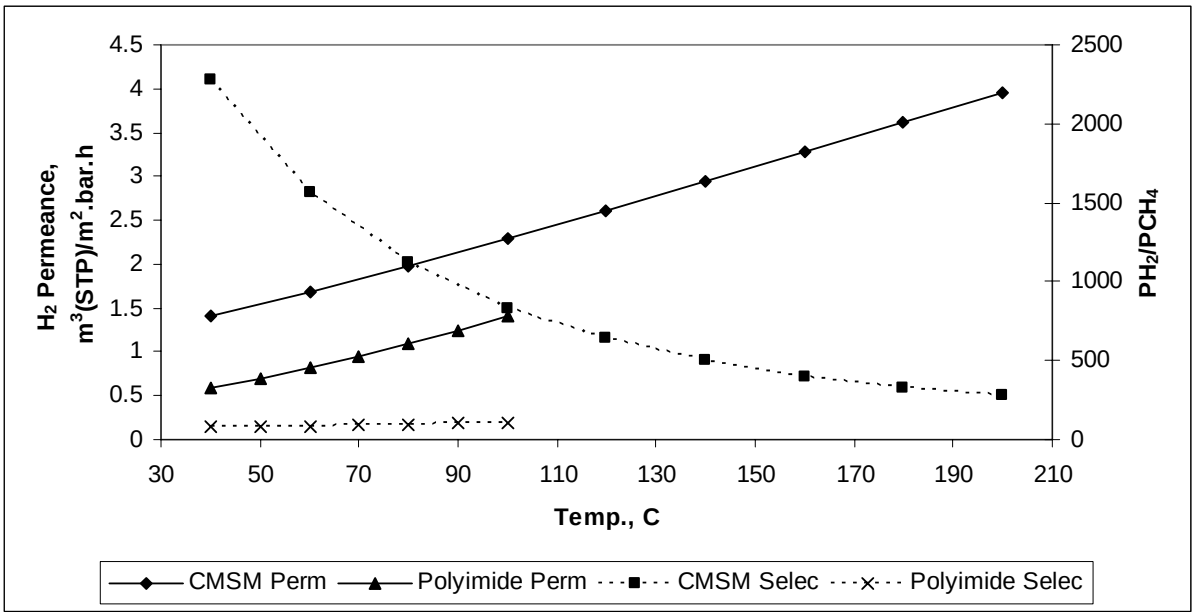

Figure 1. Influence of temperature on membrane performance, based on activated transport parameters

Carbon membrane module cost

Polymeric hollow-fibre membranes cost roughly \$20-50/m^2 [14] and a cost of \$20/m^2 is assumed for the polyimide. Predicting the cost of carbon membrane modules is difficult because of the lack of commercial precedent. Koros and Mahajan [15] stated that carbon, glass, zeolite and other inorganic membranes could cost between one- and three-orders of magnitude more per unit of membrane area compared to polymeric membranes, which places a lower limit on the CMSM cost of \$200/m^2.

The cost of the raw material, cellulose from wood pulp, is about \$520 per air dried ton [3]. However, the cost of the precursor is only a small fraction of the module cost, the rest being manufacturing. Assuming self-supported 16 micron thick hollow-fibres like those provided by Carbon Membranes Ltd [16], the cost of cellulose per m^2 of fibre is calculated to be approximately \$0.05. A commercial analogue for carbon hollow fibres is graphitic carbon fibres, produced by carbonizing PAN, Rayon or pitch spun fibres at 2400°C or more [17]. One source [18] states the cost of commercial grade carbon fibres as being \$8-10/lb (\$17.6-22/kg). Using a density of 1750 kg/m^2 for carbon fibre of 165 microns in diameter and \$22/kg

to calculate the carbon fibre cost per m^2 gives \$2/m^2. The difficulty of assembling a module with fragile carbon hollow fibres is of course not reflected in these figures, but they are much lower than the lowest suggested cost of \$200/m^2. The cost was therefore varied from \$50-500/m^2 in this study in order to gauge its effect on the process economics.

Methodology

Simulation

Simulation was performed with Aspen Hysys® 2004.2. A multicomponent, counter-current membrane model was integrated in Hysys® and able to interface with the Adjust function, enabling the manipulation of membrane area or operating pressure to achieve given product recoveries or purities. The membrane model, which is a non-linear, two-point Boundary Value Problem, was based on a series of perfectly mixed stages and solved by successive approximation of permeate flows.

The membrane unit process is shown in Figure 2. Since the natural gas is of a commercial grade, it will be filtered, dew-pointed and dehydrated before entering the gas network and pre-treatment before the membrane is unnecessary. The major equipment items influencing the capital cost are therefore the membrane and compressor. If heating of the feed is required, then a gas-fired heater must also be installed.

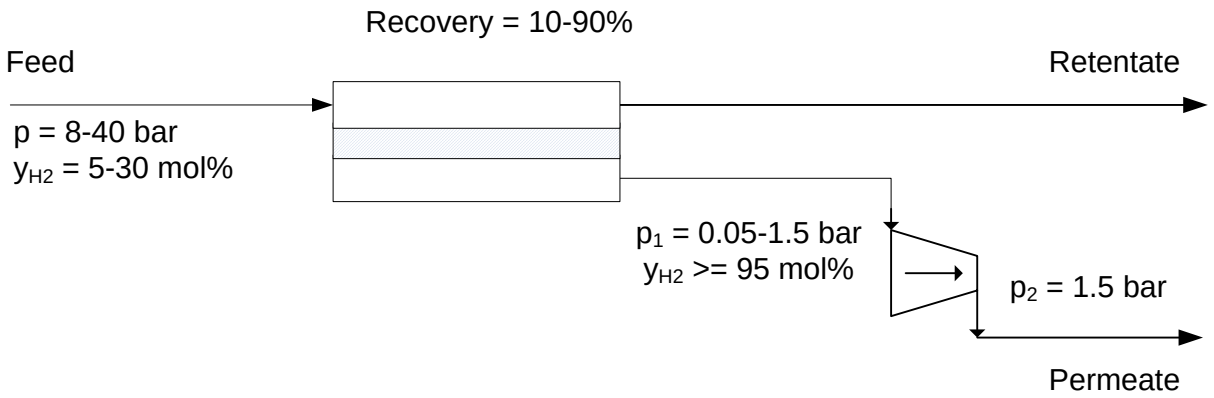

Figure 2. Simple 1-stage membrane process

Sensitivity analysis and optimisation

The many variables in these processes (feed pressure, permeate pressure, temperature, hydrogen feed fraction and hydrogen recovery) make the results data set large. As a simplification, feed compression was not considered so that separation occurred at pipeline or off-gas stream pressure. The assumption was also made that the feed mixture can be approximated by hydrogen and methane only, with all other components lumped with methane. This is reasonable because methane constitutes 82 mol% of the natural gas. Methane permeability is larger than those of the larger hydrocarbons, so this assumption is conservative with respect to eventual product hydrogen purity. Although CO_2 is much more permeable than methane, it is only 2 mol% of the natural gas fraction. The reduction of the

stream to a binary mixture then allowed the separation to be solved using the analytical solution provided by Mulder [19, pg. 496] for binary gas separation under cross-flow conditions.

A Microsoft® Office Excel spreadsheet was then developed that could simultaneously generate and analyse many cases. The spreadsheet calculates, for each case, the area required for separation and the mass balance. The costs of the two main equipment items – the membrane and the compressor – were estimated from the cost per unit area of the former and the calculated adiabatic power of the latter. The graphical method of costing compressors provided by Peters and Timmerhaus [20] was fitted to a log function that could be entered into the spreadsheet. The compressor material was assumed to be stainless steel (for hydrogen use). Fired heaters were costed using Aspen's Icarus Process Evaluator. Other economic parameters are presented in Table 4.

Table 4. Economic factors for Excel-based performance analysis

Factor	
Installation factor for purchased equipment	4
Annual operating time	8000 hours
Fixed costs	
Capital charge	15% of installed capital cost
Module replacement frequency	Every 5 years
Maintenance	2% of installed capital cost, excluding module replacement
Insurance	1% of installed capital cost
Variable cost	
Electrical power	€0.035/kWh
Natural gas price	$7/MMBTU
$:€ euro exchange rate	1.3

Excel was then used to generate the membrane area, mass balance, energy consumption and operating cost simultaneously over the recovery (10-90%) or temperature, and permeate pressure ranges. The permeate pressure that produced the lowest specific operating cost (€/kg H_2 separated) and met the purity specification for a certain recovery was selected and the corresponding membrane area and energy consumption recorded.

The objective function subject to minimisation was:

$$\textit{Annual specific separation cost} = (C_{\textit{capital charge}} + C_{\textit{Module replacement cost/yr}} + C_{\textit{maintenance}} + C_{\textit{insurance}} + C_{\textit{electricity consumption}} + C_{\textit{natural gas combusted/yr}})/\textit{Mass } H_2 \textit{ recovered per year}$$

where *C* is cost. Capital charge was calculated as 15% of the total installed cost of equipment, per year. Module replacement cost was taken as a 20% of the module purchased cost, per year, based on the replacement frequency.

The costs calculated by the spreadsheet model and those derived from simulations in Hysys will differ slightly because 1) the rigorous model can operate in counter-current mode, which produces higher average driving forces and purer product and 2) ethane and propane permeate very little relative to methane. Lumping ethane and propane with methane will therefore overestimate the amount of methane in the permeate. However, the spreadsheet approximation is a useful way to map the system. The difference between Excel and the rigorous model results was later checked for the optimum values to verify that the correct conclusions were drawn.

Recovery from a mixed hydrogen-NG network

Eight cases were developed, covering feed pressure (8 and 40 bar), H_2 concentration (5 and 30 mol%) and temperature (25 and 90°C), but for the sake of brevity, not all are presented here. The results for the feed boundary cases, representing the highest and lowest feed hydrogen partial pressures, are shown in Figure 3 and Figure 4 for 25°C operation. The end use was assumed to be a hospital fuel cell requiring 100 Nm^3 H_2/h. The following was found:

- Carbon molecular sieved membranes can meet PEM fuel cell specifications in a simple one-stage process, even when the feed concentration of hydrogen is only 5 mol%.
- The lowest costs are obtained for low hydrogen recovery from a feed of 40 bar and 30% hydrogen. The last two factors provide the highest driving force, leading to smaller membrane areas and higher permeate pressures. As recovery increases, so the driving force decreases per unit of recovery and the membrane area required increases per unit of recovery.
- Product purity decreases with increasing recovery and decreasing feed hydrogen concentration. In the separation at 25°C, purity was met for all recoveries up to 90%. At 90°C, the selectivity of the membrane is lower and the minimum purity could not be achieved at high recoveries for the 5 mol% hydrogen feed.
- The optimum permeate pressure decreased as recovery increased and as feed pressure or hydrogen concentration decreased. The steps seen in some of the pressure graphs are due to the 5 kPa interval used to generate the results. Smaller increments would produce a smooth curve.
- The cost of the membrane influences the optimum permeate pressure. If the membrane costs more, the optimum moves towards lower permeate pressures to increase the driving force and reduce the necessary membrane area.

Overall, the conclusion is that the choice of permeate pressure is influenced by all the variables and any unit will be adapted according to conditions in the field. There is no single cost of separation for a carbon molecular sieve unit, even if the cost/m^2 of membrane is fixed.

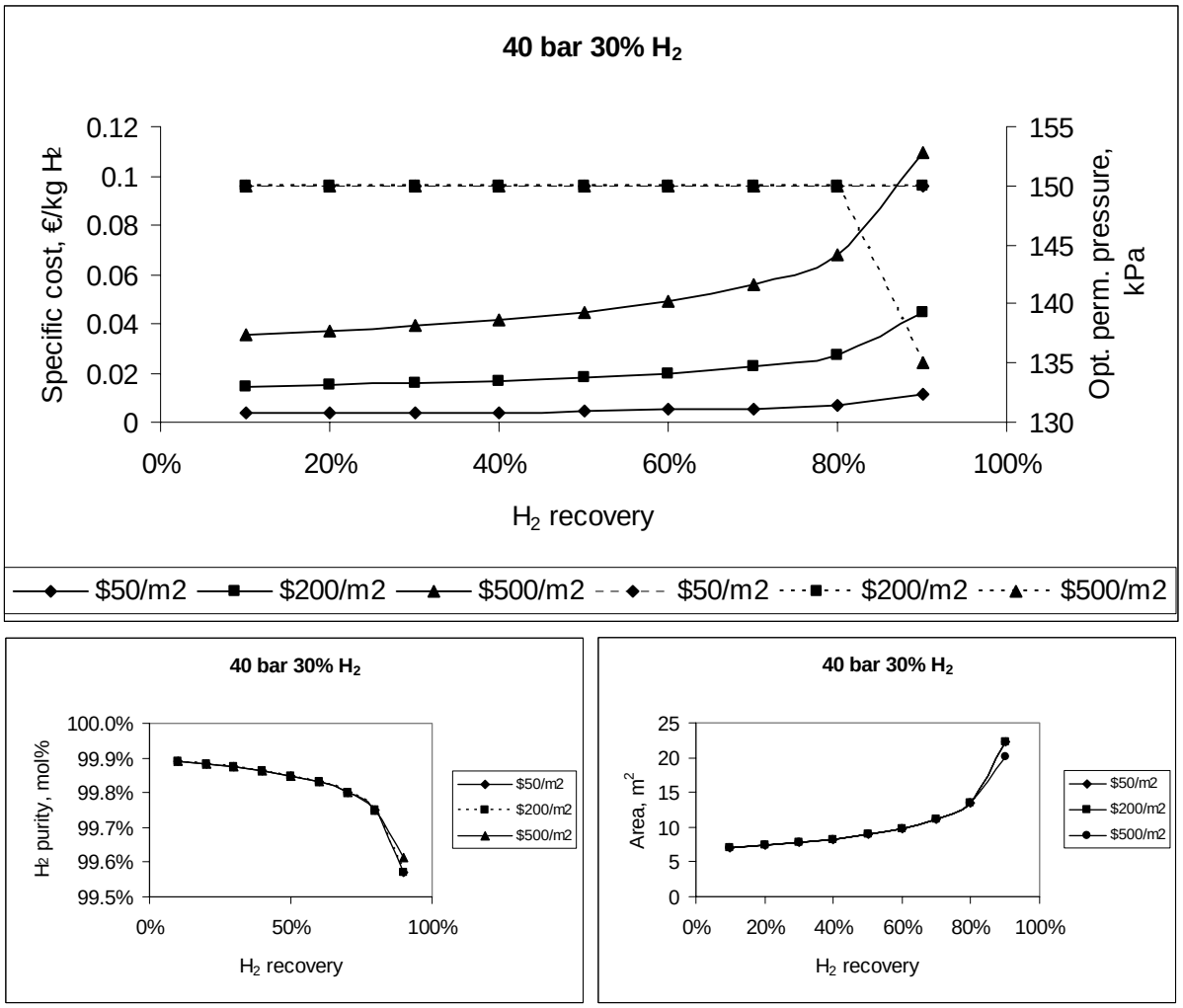

Figure 3. 40 bar feed pressure, 30% H_2 at 25°C. Left graph: Specific costs (—) and optimum permeate pressure (- - -); right: H_2 purity (- - -) and membrane area (—).H_2 partial pressure is high and permeate pressure is held constant at 1.5 bar over most of the recovery range. Purity is high, but decreases slightly, while area and cost follow the same upward trend

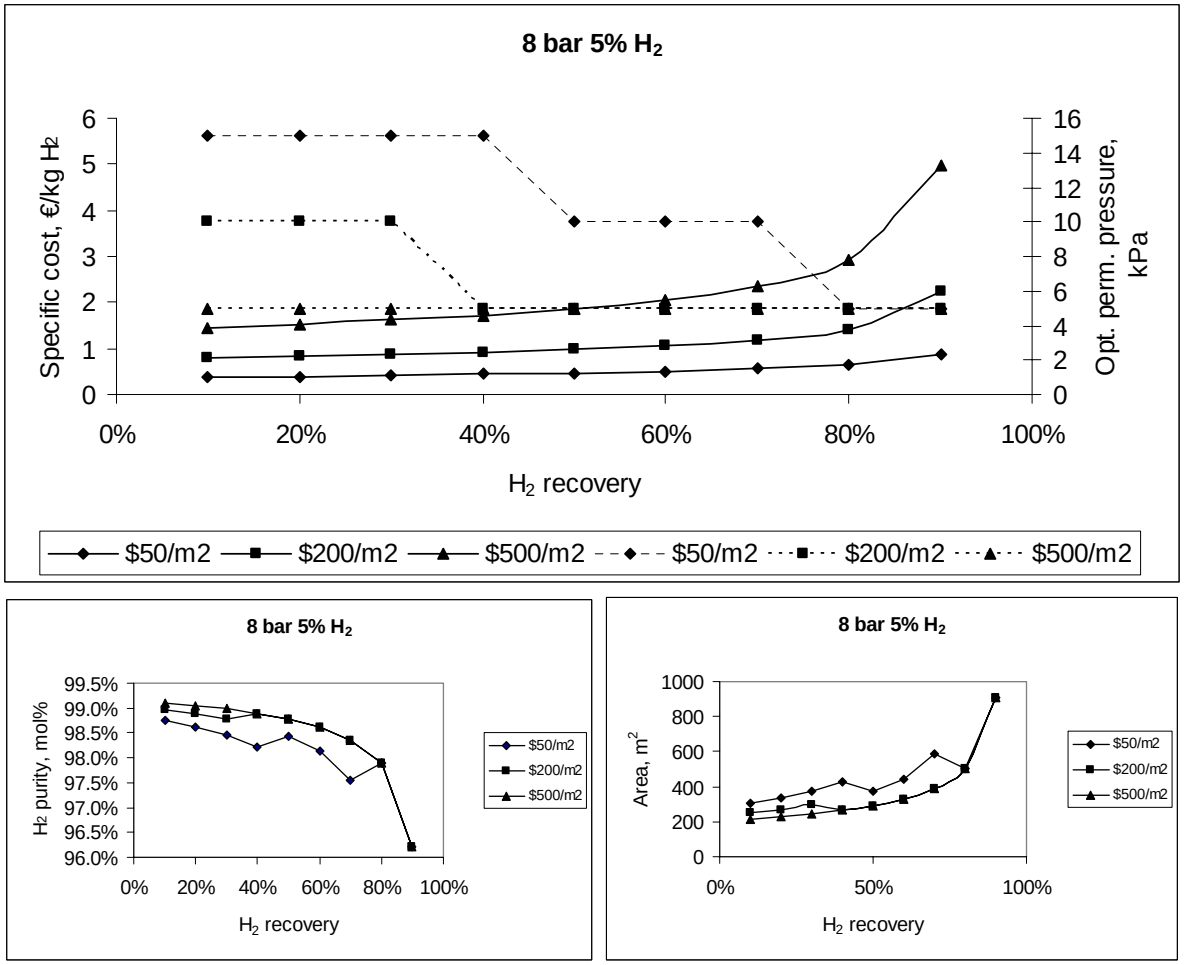

Figure 4. 8 bar feed pressure, 5% H_2 at 25°C. Top: Specific costs (—) and optimum permeate pressure (- - -); bottom: H_2 purity (left) and membrane area (right). H_2 partial pressure is lowest and membrane area influences costs. Permeate pressure is v. low to meet purity and reduce membrane cost

The extra costs for a fired heater (and the associated NG consumption) are offset by the higher permeation rate and lower membrane capital cost. Thus, if membrane area is a dominating cost, it may be worthwhile heating the feed. In the 40 bar, 30% hydrogen case, for which membrane cost is a minor contributor, there is no cost benefit to heating to 90°C until the membrane cost is as high as \$4000/m^2. The membrane cost is more important in the 8 bar, 5% hydrogen case, but heating is still only advantageous when the membrane module cost is greater than \$500/m^2. The conclusion, therefore, is that there is no benefit to heating the feed for the module cost range. There was also no economy-of-scale benefit to increasing the capacity of a membrane unit unless a fired heater was present. Equipment cost is often scaled with the equation

$$C_1 = C_2 \left(\frac{S_1}{S_2} \right)^n \qquad (3)$$

where C is the purchase cost, S is capacity and n is an index that is unique to the equipment type [21]. Cost is proportional to area for membranes and nearly proportional to power for

centrifugal compressors (n ~ 0.93) [20]. Only furnaces show some economy of scale, with an index of 0.8 [21].

Comparison with a polyimide membrane

The performance of the polyimide membrane is shown in Figure 5. Despite the low polyimide module cost, separation is more economic with the carbon molecular sieve at higher recoveries. This is because the permeate pressure must be lower for the polyimide to produce hydrogen of 95 mol% purity, whereas the CMSM does not need permeate recompression for the full range of recovery. The polyimide process is cheaper for recovery below 40%.

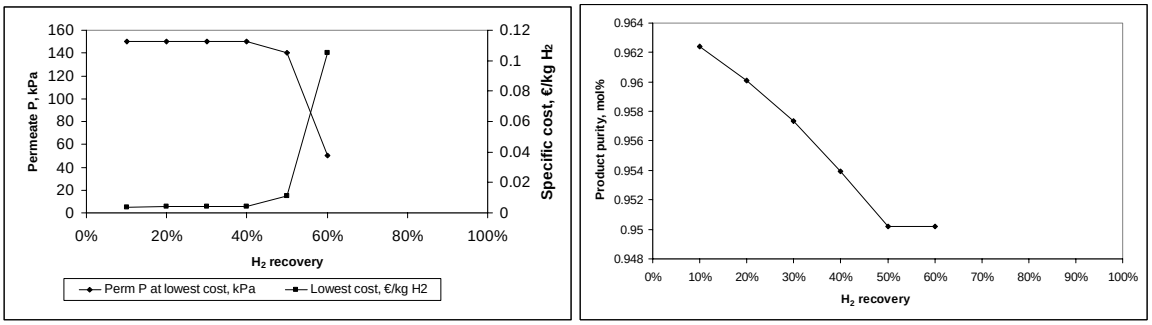

Figure 5. Performance of polyimide membrane at 40 bar, 30% H_2 feed (T=25°C)

The spec cannot be met at all for recoveries higher than 60% and the product must be purified in a further membrane stage (Figure 6). If the hydrogen content in the feed is less than 20 mol%, then the spec cannot be achieved in one stage for any recovery and a two-stage process is required.

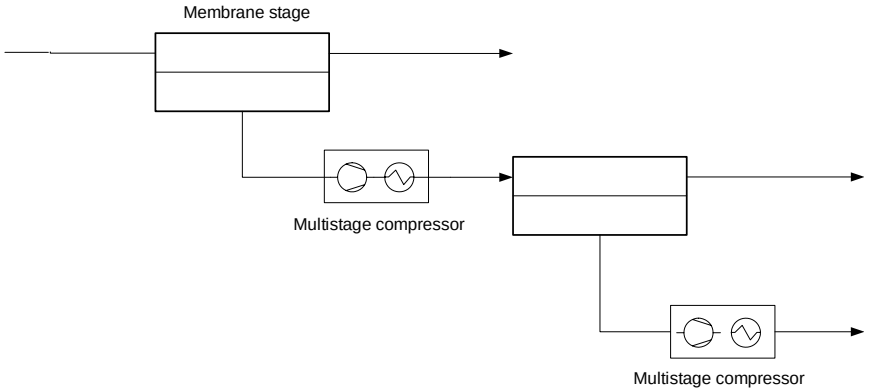

Figure 6. Two stage polyimide membrane process

The permeate pressures of both stages were set equal to simplify the sensitivity study, whereas the feed pressure (compressor outlet) for the second stage was varied to find the lowest cost. It was found that 400 kPa provided this. Since the product rate is fixed (~4.5 kmol/h for a hospital fuel cell), the feed size will vary according to the overall recovery (or usage ratio, $F_{H2product}/F_{H2feed}$). This relationship is seen in Eq. (4).

$$F_{feed} = F_{product} \cdot y_{H2,product} / (R \cdot y_{H2,feed}) \qquad (4)$$

where R is overall recovery. R is the product of the two stage recoveries, i.e.

$$R = R_1 \cdot R_2 \qquad (5)$$

And hence, for stage 2, the size of the feed stream is determined by

$$F_{feed,\ stage\ 2} = F_{feed} \cdot y_{H2,feed} \cdot R_1 / y_{H2,\ feed\ stage\ 2} \qquad (6)$$

The relationship between R_1 and R_2 has a large impact on the cost and energy consumption of the process, because the larger R_1, the larger the compression duty for the same amount of overall product. The goal is therefore to minimise the recovery in the first stage and still meet the requirements of Eq. (5) and the purity specification. It was found that setting $R_1 = 1.05 \cdot R$ satisfied these conditions. Heating the feed stream was not beneficial, mostly because the polyimide membrane is relatively cheap and area savings were not as important. For a feed of 8 bar, 5% hydrogen, the 2-stage polyimide process is slightly cheaper than the CMSM because membrane area dominates costs, due to the low driving force.

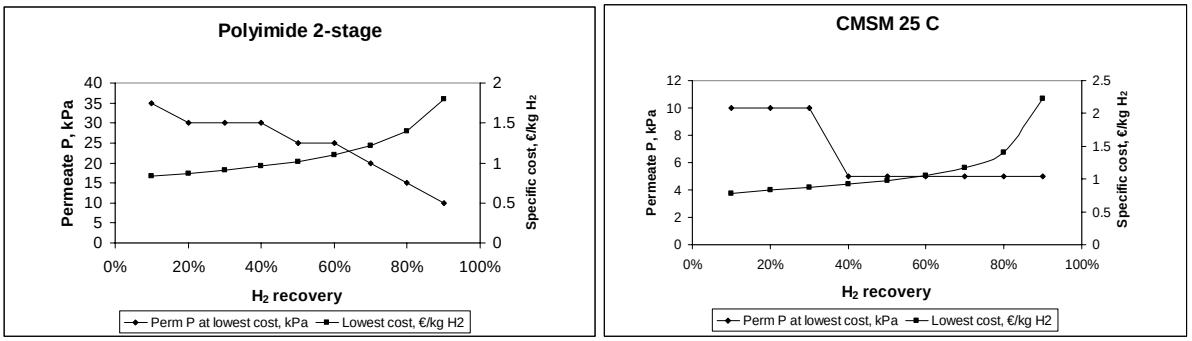

Figure 7. Comparison of membranes for 8 bar feed, 5% H_2 (CMSM Mod. cost = \$200/m^2)

The estimation of specific cost is subject to many assumptions, not least of all the cost of the modules. Another point of comparison is the energy consumption per mole of hydrogen, shown in Figure 8. These are thermal equivalent values, obtained by converting electrical consumption in compressors to thermal consumption by multiplying by 3 (representing an energy conversion process with 33% efficiency) and adding any heating duty. Bearing in mind that the lower heating value (LHV) of hydrogen is 242 kJ/mol, the energy consumption of the polyimide 1-stage process is low. With 2 stages, however, the extra interstage compression causes the energy consumption to be a significant fraction of the LHV of H_2.

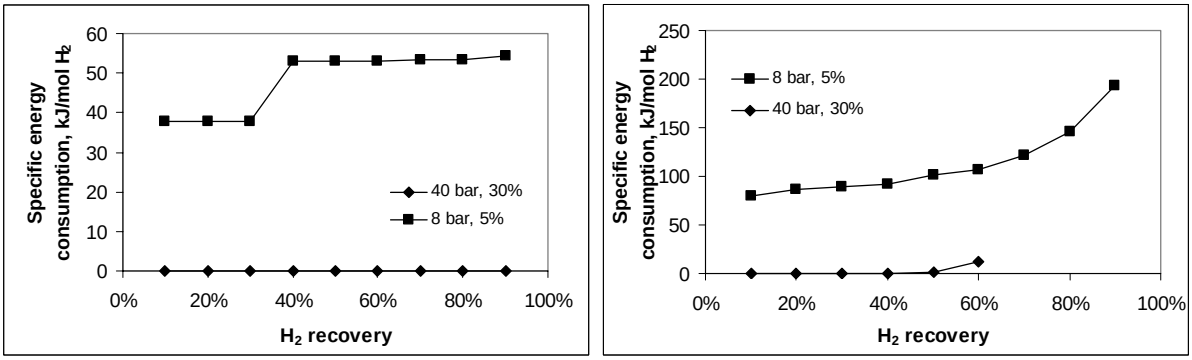

Figure 8. Energy consumed per mole of hydrogen produced in CMSM (left) and polyimide membrane (right) processes

The energy consumption for the CMSM (25°C) process is lower for both 30% and 5% hydrogen feed cases, because less permeate recompression is required. In the 30% case, the CMSM permeate is at 1.5 bar and no recompression is required. This is a result of the higher

selectivity of the membrane – separation can be achieved in one stage and permeate pressures are higher.

Validation of Excel results and conclusions

The optimum cases were run in Hysys using the multicomponent membrane module, and it was found that the relative area difference, $(A_{Excel\ model}-A_{multcomp.model})/A_{Excel\ model}$, was less than 7% and the relative product purity difference was greater than -2%. Considering that this study is only a preliminary techno-economic evaluation of the process, and typically subject to ±30% error [21], the difference between models does not change the conclusions in this paper.

Carbon molecular sieve membranes offer great potential for hydrogen recovery from hydrocarbons. They produce purer hydrogen from leaner streams with lower energy consumption. Single-stage carbon molecular sieve membranes easily achieve separation specification at higher permeate pressures than the polyimide membrane because the CMSM selectivity is higher.

The performance and optimum process parameters depend on the feed conditions and the cost of a CMSM module. In the studied cost range ($50-500/m^2), however, CMSMs can be competitive. Furthermore, with hollow fibre modules packing values of 10 000-30 000 m^2 of membrane per m^3 of module volume [19], the small carbon membrane areas required to effect the separation mean that these modules will have a small footprint. For example, a volume less than 250 litres would be able to service a hospital fuel cell from streams with 5 mol% hydrogen content. Further development should focus on methods of large-scale manufacture, particularly on the challenges in mounting relatively brittle carbon hollow fibres in a module, and on assembling a reliable estimate of module costs.

Acknowledgements

The authors are grateful for the funding from the NTNU-SINTEF Gas Technology Centre and the NaturalHy 6th EU Framework Programme.

References

[1] http://www.naturalhy.net
[2] S.M. Saufi and A.F. Ismail, Fabrication of carbon membranes for gas separation – a review, Carbon, 42 (2004) 241.
[3] J.A. Lie and M.-B. Hägg, Carbon membranes from cellulose and metal loaded cellulose, Carbon, 43 (2005) 2600.
[4] J.A. Lie and M.-B.Hägg, Carbon membranes from cellulose: Synthesis, performance and regeneration, J. Membrane Sci., 284 (2006) 79.
[5] J.E. Koresh and A. Soffer, The carbon molecular sieve membranes. General properties and the permeability of CH_4/H_2 mixture, Sep. Sci. Techn. 22 (1987) 973.
[6] C.W. Jones and W.J. Koros, Carbon molecular sieve gas separation membranes – 1. Preparation and characterization based on polyimide precursors, Carbon, 32 (1994) 1419.

[7] M.G. Sedigh, W.J. Onstot, L. Xu, L.P. Wildon, T.T. Tsotsis and M. Sahimi, Experiments and simulation of transport and separation of gas mixtures in carbon molecular sieve membranes, J. Phys. Chem. A, 102 (1998) 8580.
[8] N. Tanihara, H. Shimazaki, Y. Hirayama, S. Nakanishi, T. Yoshinaga and Y. Kusuki, Gas permeation properties of asymmetric carbon hollow fiber membranes prepared from asymmetric polyimide hollow fiber, J. Membrane Sci., 160 (1999) 179.
[9] J.E. Koresh and A. Soffer, Mechanism of permeation through molecular sieve carbon membrane. Part 1.- The effect of adsorption and the dependence on pressure, J. Chem. Soc. Faraday Trans., 82 (1986) 2057.
[10] D. Grainger and M.B. Hägg, Evaluation of cellulose-derived carbon molecular sieve membranes for hydrogen separation from light hydrocarbons, J. Membrane Sci., *Accepted 08 September 2007*
[11] L.M. Robeson, Correlation of separation factor versus permeability for polymeric membranes, J. Membrane Sci., 62 (1991) 165
[12] H. Suda and S. Haraya, Carbon Molecular Sieve Membranes: Preparation, characterization and gas permeation properties, American Chemical Society Symposium Series, 2000.
[13] S.P. Kaldis, G.C. Kapantaidakis and G.P. Sakellaropoulos, Simulation of multicomponent gas separation in a hollow fiber membrane by orthogonal collocation – hydrogen recovery from refinery gases, J. Membrane Sci., 173 (2000) 61.
[14] W. Ho and K. Sirkar, Membrane Handbook, 1992 pp. 434.
[15] W.J. Koros and R. Mahajan, Pushing the limits on possibilities for large-scale gas separation: which strategies?, J. Membrane Sci., 175 (2000) 181.
[16] J.A. Lie, Synthesis, performance and regeneration of carbon membranes for biogas upgrading – a future energy carrier, Doctoral thesis at NTNU 2005:152, 2005.
[17] C. Sauder, J. Lamon and R. Pailler, The tensile behavior of carbon fibers at high temperatures up to 2400°C, Carbon 42 (2004) 715.
[18] Oak Ridge National Laboratory News Release. Carbon fiber cars could put US on highway to efficiency. March 2006
[19] M. Mulder, Basic principles of membrane technology, 2nd Ed., Springer, 1997.
[20] M.S. Peters and K.D. Timmerhaus, Plant design and economics for chemical engineers, 5th Ed., Mc.Graw-Hill, 2003.
[21] R.K. Sinnot, Coulson and Richardson's Chemical Engineering Vol. 6, 2nd Ed., 1996.